

**Simultaneous in situ and ground-based common-volume  
measurements for the investigation of the formation mechanism of  
Polar Mesosphere Winter Echoes**

**Dissertation**

**zur**

**Erlangung des akademischen Grades  
doctor rerum naturalium (Dr. rer. nat.)  
an der Mathematisch-Naturwissenschaftlichen Fakultät  
der Universität Rostock**

VORGELEGT VON:

Tristan Staszak,  
geb. am 07.06.1989 in Kamen

GUTACHTER:

Prof. Franz-Josef Lübken  
(Leibniz-Institut für Atmosphärenphysik)

Prof. Gerald Lehmacher  
(Clemson University, South Caroliner, US)

EINGEREICHT:

16.08.2021 (v.1.0)

VERTEIDIGT:

10.12.2021

KORRIGIERT:

10.02.2022 (v.1.1)

[https://doi.org/10.18453/rosdok\\_id00003541](https://doi.org/10.18453/rosdok_id00003541)



**Abstract:** Relatively strong radar returns from mesospheric heights (~55–85 km) in the winter polar region have been detected by radar since the late 1970s. These observations result from coherent structures of electrons and are called Polar Mesosphere Winter Echoes (PMWE). Since the annual season of PMWE observations is relatively long, and PMWE detections cover an extensive altitude range, these echoes have an enormous potential for utilization as a tracer for geophysical processes. However, the formation mechanism of this phenomenon is not understood.

All relevant parameters potentially involved in the PMWE formation were measured in a common volume and subsequently analyzed for the first time. The combined results of rocket-borne and ground-based measurements of two rocket flights conclusively show that coherent structures are created by a turbulent process involving tiny charged MSPs. By analyzing the background winds, it could be shown that a braking gravity wave most likely created the turbulent structures. Another result of this thesis is that the intensity of turbulence varies by approximately one order of magnitude within only a few buoyancy periods (i.e., minutes) and thereby essentially influences whether PMWE is formed or not.

**Kurzfassung:** In polaren Breiten werden seit den späten siebziger Jahren während der Wintersaison relativ starke Radarsignale aus Höhe der Mesosphäre (~55–85 km) empfangen. Diese Echos entstehen durch Reflexionen von kohärenten Strukturen und werden Polar Mesosphärische Winter Echos (PMWE) genannt. PMWE werden über einen ausgedehnten Höhenbereich beobachtet und decken einen Großteil der Mesosphäre ab. Kontinuierliche Radarbeobachtungen von PMWE haben können somit einen wesentlichen Beitrag zum Verständnis für geophysikalische Prozesse in dieser ansonsten schwierig zu vermessenden Atmosphärenschicht liefern. Erstmals wurden alle relevanten Parameter, die für den Entstehungsprozess von PMWE potentiell entscheidend sind, in einem gemeinsamen Volumen mittels raketenge tragenen in situ Messungen und bodengebundenen Instrumenten untersucht. Obwohl zwei Raketenflüge unter sehr unterschiedlichen geophysikalischen Bedingungen durchgeführt wurden, ergeben die Messungen ein einheitliches Bild: Turbulenz erzeugte in Verbindung mit geladenen Meteorstaubteilchen kohärente Strukturen, die mit dem Radar beobachtet wurden. Die weitergehende Analyse des Hintergrundwindes deutet darauf hin, dass diese Turbulenz von einer brechenden Schwerewelle erzeugt wurde. In dieser Arbeit wurde deutlich, dass die Stärke der Turbulenz mit einer Größenordnung innerhalb weniger Auftriebsperioden (d.h. Minuten) variiert und darüber entscheidet, ob PMWE entstehen oder nicht.



# Contents

<b>1</b>	<b>Introduction</b>	<b>4</b>
1.1	Introduction to the MLT . . . . .	4
1.2	Radar echoes in the D-region/MLT . . . . .	7
1.3	Open Questions and Outline . . . . .	8
<b>2</b>	<b>Theoretical Preconiderations</b>	<b>10</b>
2.1	Coherent radar scattering . . . . .	10
2.1.1	Refractive Index . . . . .	11
2.1.2	Potential refractive index gradient . . . . .	12
2.1.3	Bragg scattering . . . . .	13
2.1.4	Volume scattering . . . . .	14
2.1.5	Partial reflection . . . . .	16
2.2	Turbulence . . . . .	17
2.2.1	Energy spectrum . . . . .	18
2.2.2	Scalar spectrum . . . . .	20
2.3	Investigations of PMWE at VHF . . . . .	22
2.3.1	Statistical Properties . . . . .	22
2.3.2	Influence of electron density . . . . .	25
2.3.3	Role of the neutral atmosphere background . . . . .	27
2.3.4	Turbulent structuring mechanism . . . . .	28
2.3.5	Meteor Smoke Particles . . . . .	30
2.3.6	Viscous waves . . . . .	32
2.4	Conclusions and Hypotheses . . . . .	34
<b>3</b>	<b>Analysis methods</b>	<b>38</b>
3.1	Turbulence from radar measurements . . . . .	38
3.1.1	Power method . . . . .	38
3.1.2	Spectral width method . . . . .	39
3.2	Turbulence from rocket measurements: The spectral model technique for scalar tracers . . . . .	40
3.2.1	Spectral Models . . . . .	41
3.2.2	Data processing . . . . .	43
3.2.3	Derivation of turbulence dissipation rate . . . . .	45
3.2.4	Variance dissipation rate . . . . .	45
3.2.5	Derivation of the $Sc$ number . . . . .	46

3.3	Ascertain aerosol radii from the $Sc$ number . . . . .	47
3.4	Absolute neutral density and temperature . . . . .	48
3.4.1	Calibration . . . . .	49
3.4.2	Aerodynamic correction . . . . .	50
3.4.3	Deriving temperature . . . . .	52
3.5	Absolute Electron density . . . . .	52
3.6	Calculated radar volume reflectivity . . . . .	53
3.6.1	Derivation from turbulence spectral models . . . . .	53
3.6.2	Derivation from a measured power spectrum . . . . .	54
<b>4</b>	<b>PMWE – Sounding rocket project</b>	<b>55</b>
4.1	Ground-based instruments . . . . .	56
4.1.1	MAARSY . . . . .	56
4.1.2	Saura radar . . . . .	56
4.1.3	EISCAT-VHF . . . . .	57
4.1.4	RMR lidar . . . . .	58
4.2	Payloads instrumentation . . . . .	58
4.2.1	PMWE1F–FIONA . . . . .	59
4.2.2	PMWE1D–DUSTIN . . . . .	60
<b>5</b>	<b>Results from the PMWE-1 sounding rocket campaign</b>	<b>63</b>
5.1	Results from PMWE1F . . . . .	63
5.1.1	Launch conditions . . . . .	64
5.1.2	In situ measured atmospheric background . . . . .	68
5.1.3	Small scale fluctuations . . . . .	72
5.1.4	Comparison of volume reflectivity from radar and in situ soundings	78
5.1.5	Radar measurements of turbulence . . . . .	80
5.1.6	Evolution of the PMWE layer . . . . .	80
5.1.7	Discussion and Conclusions . . . . .	84
5.2	Results from PMWE1D . . . . .	86
5.2.1	Launch conditions . . . . .	87
5.2.2	Neutral background . . . . .	89
5.2.3	Estimation of necessary turbulence dissipation rates for the onset of PMWE . . . . .	90
5.2.4	Discussion and Conclusions . . . . .	92
5.3	Verification of the viscous waves theory . . . . .	95
5.4	Artificially induced radar echoes . . . . .	96
<b>6</b>	<b>Summary and Outlook</b>	<b>97</b>
	<b>Appendices</b>	<b>101</b>
<b>A</b>	<b>Viscous wave theory for the D-region case</b>	<b>101</b>
A.1	Potential refractive index gradient at 2, 53.5, and 224 MHz . . . . .	101
A.2	Parameters for infrasound for ~50 and 224 MHz . . . . .	104

---

<b>B</b>	<b>CONE Calibration curves</b>	<b>106</b>
<b>C</b>	<b>Uncertainties</b>	<b>108</b>
C.1	Error estimations of background parameters . . . . .	108
C.1.1	Density . . . . .	108
C.1.2	Temperature . . . . .	110
C.1.3	Viscosity . . . . .	110
C.1.4	Buoyancy frequency . . . . .	112
C.2	Uncertainty of energy dissipation rates and $Sc$ number derived from the spectral model technique . . . . .	112
C.3	Potential electron density/ refractive index gradient . . . . .	113
<b>D</b>	<b>A new aerodynamic correction approach for axis symmetric payloads</b>	<b>115</b>
<b>E</b>	<b>PMWE-1 launch informations</b>	<b>119</b>
E.1	Vehicle and flight informations . . . . .	119
E.2	Trajectory . . . . .	120
<b>F</b>	<b>PMWE-1 Spectra</b>	<b>121</b>
F.1	PMWE1F spectra for neutral- and electron density fluctuations (CONE) . . . . .	121
F.2	PMWE1D spectra for neutral density fluctuations (Turb3D) . . . . .	125
	<b>References</b>	<b>127</b>
	<b>Acknowledgements</b>	<b>155</b>
	<b>Declaration of authorship</b>	<b>157</b>

# 1 | Introduction

Polar Mesosphere Winter Echoes (PMWE) are relatively strong radar returns, observed in both hemispheres in an altitude range of ~55–85 km, namely in the mesosphere and lower thermosphere (MLT) of the Earth’s atmosphere.

Before starting the detailed investigation of this phenomenon, a brief introduction to unique features of the MLT region should be given, shortly depicting our current understanding of radar echoes in the MLT, present in summer and winter, and motivating following investigations. Finally, a scientific question is formulated, and an outline of this thesis is given.

## 1.1 Introduction to the MLT

The MLT is the atmospheric region extending from the stratopause to above the mesopause (~50–110 km). It consists of the whole mesosphere and the lower part of the thermosphere. Whereas the stratosphere and thermosphere are characterized by an overall positive temperature gradient, the mesosphere has a negative lapse rate and therefore is generally statically unstable. Despite the fact that >99 % of the atmosphere’s mass is below the MLT, this region is of particular scientific interest due to its unique dynamics that couple small-scale dynamical processes on scales of ~meters to hundreds of meters. In particular, these processes are turbulence on the one end, and pole-to-pole circulations, on the other. In between these scales, waves (e.g., generated by orography, or thunderstorms at low altitudes) propagate through the atmosphere, transport and deposit momentum, and therefore couple atmospheric layers vertically (e.g., [Nappo, 2002](#)). Moreover, this region considerably overlaps with the lower part of the Earth’s ionosphere (e.g., [Schunk and Nagy, 2009](#); [Kelley, 2009](#)) and is the place where most of the meteoroids ablate, subsequently re-condensate and ultimately deposit material as tiny meteor smoke particles (MSP, [Rosinski and Snow, 1961](#); [Hughes, 1997](#); [Janches et al., 2006](#); [Mathews et al., 2008](#)). One of the most salient consequences of the MLT dynamics is the unexpected thermal structure of the atmosphere that is far different from the state that would be expected considering radiative processes only.

This becomes even more evident when comparing high-latitude temperature profiles at summer and winter poles ([Lübken et al., 1999](#)). In Fig. 1.1 winter and summer temperature profiles from model are shown for two cases: While the first only considers radiative processes (dashed lines), the second, and more realistic profile is obtained by additionally considering wave dynamics (solid lines). In contrast to what we would expect from solar radiation, the winter mesopause is up to 90 K warmer and the summer mesopause is 60 K



colder than the state that would be reached by merely considering radiative processes only. (e.g., [Holton and Alexander, 2000](#)). In fact, with temperatures down to  $\sim 120$  K during the summer the mesopause becomes the coldest place in the entire atmosphere (e.g., [Theon et al., 1967](#); [Lübken, 1999](#)).

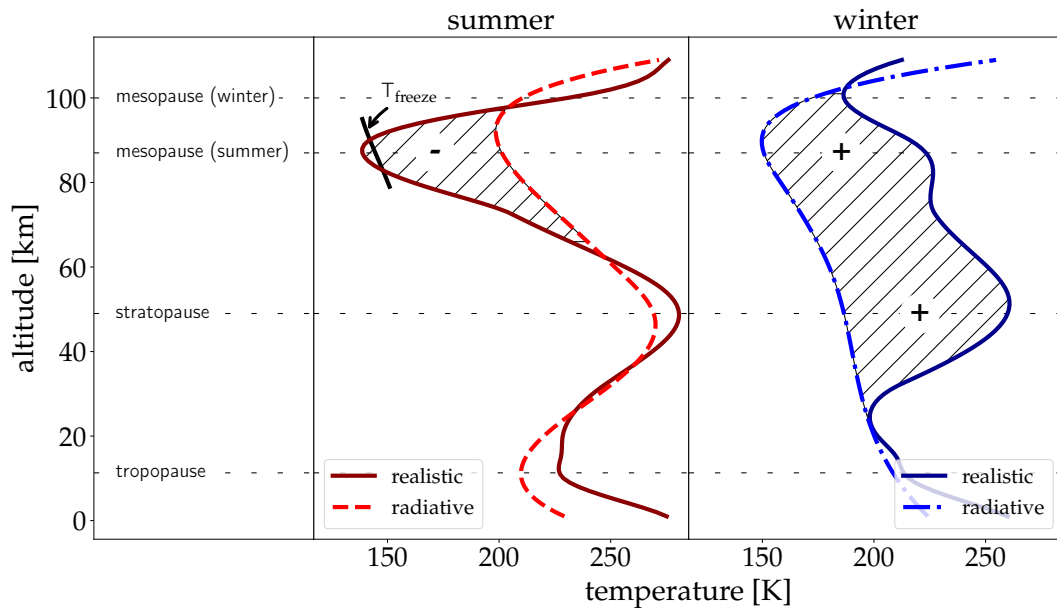


Figure 1.1. Thermal structure of the atmosphere ( $69^\circ\text{N}$ ,  $16^\circ\text{E}$ ) in summer and winter from the realistic model NRLMSISE-00 ([Picone et al., 2002](#)) and radiative temperature profiles, adapted from zonal mean temperature contours ([Becker, 2012](#)). Realistic model temperature profiles are mean profiles for July 2018 and November 2017 to February 2018. Realistic summer mesopause temperatures are below frost point temperatures ( $T_{\text{freeze}}$ ), derived for a water mixing ratio of 5 ppm (see [Marti and Mauersberger, 1993](#)). Shaded areas indicate the divergence between realistic and radiative temperatures. The summer mesopause is much colder  $\ominus$ , the winter meso- and stratopause are much warmer  $\oplus$  than expected from only considering radiative processes.

These differences can only be explained by the influence of gravity waves (GWs) originating from lower parts of the atmosphere. Gravity waves propagate upwards, and due to energy conservation and decreasing atmospheric density, their amplitudes grow until they become unstable and break by depositing momentum to the background flow and creation of turbulence (e.g., [Rapp, 2004](#)). A natural limit of turbulence is the turbopause ( $\sim 110$  km), where molecular diffusion equals eddy diffusion of turbulence, and turbulent structures do not persist.

Momentum deposition of GWs to the zonal wind in the mesosphere ultimately drives a summer-to-winter flow. The upward motion of air over the summer pole causes adiabatic cooling of the mesopause, whereas adiabatic downwelling heats the winter mesosphere. This circulation pattern is called residual circulation (e.g., [Holton and Hakim, 2013](#); [Garcia and Solomon, 1985](#); [Becker, 2012](#)). The direction of drag by GW momentum deposition is closely related to the lower atmosphere's structure since filtering of upward propagating GWs occurs in the stratosphere and troposphere (e.g., [Lindzen, 1981](#); [Taylor et al.,](#)

1993). Thus, the mesosphere is coupled vertically to the entire atmosphere via GW filtering and propagation, and globally through summer-to-winter pole flow. Consequently, changes in lower atmospheric parts of the winter hemisphere cause changes in the summer hemisphere's mesosphere (e.g., Rapp, 2004; Becker, 2004; Goldberg, 2004; Fritts, 2004; K ornich and Becker, 2010).

Besides the dynamical characteristics of the MLT, a part of the atmosphere is charged and forms the ionospheric plasma.<sup>1</sup> This plasma around the Earth creates the so-called ionosphere. The ionosphere in the MLT shows several distinct layers, which are named D- (>50–90 km), E- (90–150 km), F<sub>1</sub>-region (150–250 km), and F<sub>2</sub>-region (around 300 km). While in the D-region, molecules are mainly ionized by the Lyman- $\alpha$  line (121.57 nm), and also by particle precipitation, the E-region is formed by influence of extreme ultraviolet (EUV,  $10 < \lambda < 120$  nm) and X-ray ( $\lambda < 10$  nm). While in MLT, neutral constituents are mainly N<sub>2</sub>, O<sub>2</sub>, and O, the D-region ionosphere consists of negative and positive ions. Below ~85 km cluster ions are formed via hydration of mainly NO<sup>+</sup> and O<sub>2</sub><sup>+</sup>. In the E-region ion chemistry is simpler and NO<sup>+</sup>, O<sub>2</sub><sup>+</sup>, and N<sub>2</sub><sup>+</sup> are most abundant. In the F-region the degree of ionization rises and ion-atom interactions become more critical, with peak ionization around the F<sub>2</sub>-layer (~10<sup>12</sup> m<sup>-3</sup>). Atomic species of O and O<sup>+</sup> are most dominant in these regions (e.g., Schunk and Nagy, 2009). Fig. 1.2 shows model examples of the day and nighttime electron density profiles and the corresponding degree of ionization (i.e.,  $N_e/N_n$ ). It is clear that due to the low level of ionization—there are 10<sup>10</sup> neutrals for each

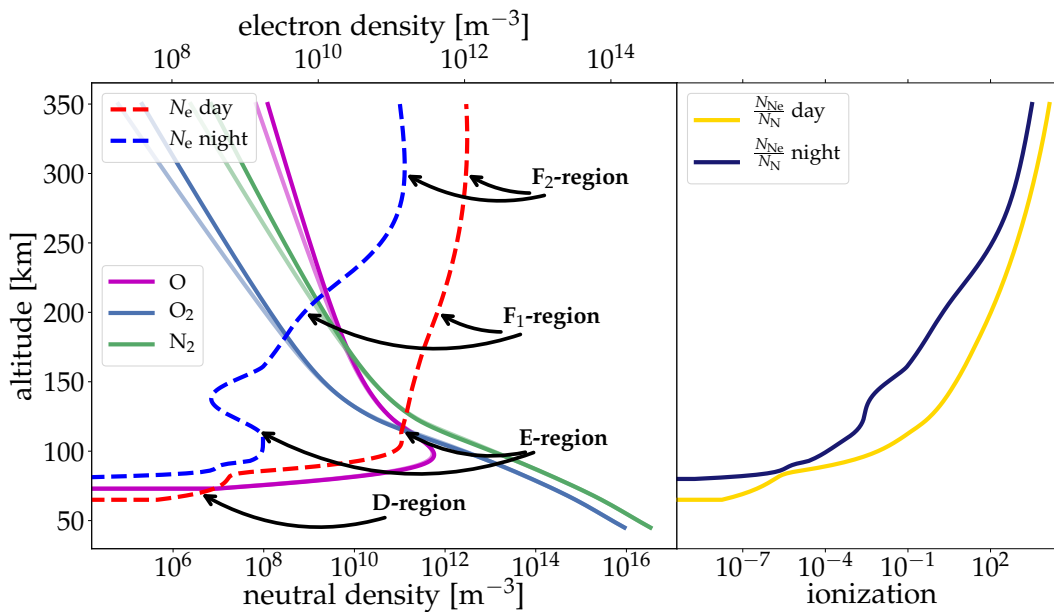


Figure 1.2. Left panel: Mean densities of neutrals and electrons at night and daytime for the winter season 2017/18 (i.e., September to May), derived by NRLMSISE-00 (Picone et al., 2002) and IRI2016 (Bilitza et al., 2014, 2016). The right panel shows the degree of ionization (ratio of electron density to neutral density).

<sup>1</sup> In atmospheric science it has become established practice to only call the charged part of the atmosphere a plasma. In that sense it is differentiated between neutrals and plasma. Since it is expected that most readers are from atmospheric physics, this definition is mainly used in this work, well knowing that plasma in a strict sense generally consists of both neutral and ionized species (e.g., Saha, 1920)

electron in the lower MLT- the dynamics of the plasma are dominated by the neutrals. Even in the F<sub>2</sub>-region there remain 100 neutrals per electron. Especially near the Earth's poles the MLT's characteristics form exciting phenomena, such as the well-known Aurora and Noctilucent Clouds (NLCs), visible to the naked eye. NLCs are layers of ice particles at ~83 km altitude, illuminated by the Sun when the Sun is below the horizon and does not illuminate the troposphere (e.g., [Fiedler et al., 2009](#)). Another group of phenomena in the MLT became visible only thanks to the development of radar technology in the last century. Radar, an abbreviation for radio detection and ranging, utilizes radio waves of wavelengths  $\lambda \gtrsim 10$  cm, and has been used for meteorology since its invention. Apart from weather radars monitoring the troposphere, several radars are operated to observe the MLT region.

## 1.2 Radar echoes in the D-region/MLT

Coherent radar returns at very high frequency (VHF) (i.e., band from 30–300 MHz) from the MLT/D-region were first reported more than half a century ago by measurements at ~40–50 MHz ([Bowles, 1958](#); [Flock and Balsley, 1967](#)). After that, also observations of radar echoes from the MLT region at equatorial, mid- and polar latitudes were reported ([Woodman and Guillen, 1974](#); [Czechowsky et al., 1979](#); [Ecklund and Balsley, 1981](#)). [Czechowsky et al. \(1979\)](#) and [Ecklund and Balsley \(1981\)](#) already noted a profound difference between echoes in winter and summer at polar latitudes. While in summer the majority of echoes were detected from 80–92 km altitude with a strong signal-to-noise ratio (SNR), echoes in winter were observed from 55–82 km altitude with significantly lower SNR. Furthermore, echoes in the summer season were often observed during day and night, while winter echoes most likely occur during the daytime (e.g., [Ecklund and Balsley, 1981](#)). With growing understanding of the MLT it turned out that these echoes were not only different from a phenomenological perspective but also their mechanism of formation must be different. Consequently, in order to differentiate between them, they were named (Polar) Mesosphere Summer and Winter echoes, (P)MSE ([Röttger et al., 1988](#); [Hoppe et al., 1988](#)) and (P)MWE ([Kirkwood et al., 2002b](#)).

Summer radar echoes have been studied intensively, both on a theoretical level (e.g., [Hocking, 1983, 1985](#)) as well as on experimental approach (e.g., [Röttger et al., 1988](#); [Hoppe et al., 1988](#); [Lübken et al., 1994b](#); [Rapp and Lübken, 2004](#); [Rapp et al., 2008](#)). Based on sounding rocket measurements, evidence of the formation mechanism was found (see, e.g., [Ulwick et al., 1988](#); [Kelley et al., 1990](#); [Lübken et al., 1993](#); [Havnes et al., 2001](#)).

The explanation of (P)MSE formation due to turbulence structuring of charged ice particles that influence the refractive index has become widely accepted. Moreover, it has been shown that these radar echoes are strongly connected to the previously mentioned NLC (see e.g., [Kaifler et al., 2011](#), for a recent study). Briefly, our understanding of (P)MSE is that water vapor nucleates (either on hydrated ions or MSP) and starts freezing in the cold summer mesopause. By interaction with ionospheric plasma, these ice particles become charged and interact with free electrons, which subsequently reduces the electrons mobility, alter the radio refractive index and ultimately become observable via VHF radar. Often, ice particles grow further, sediment downwards, and thus become visible as NLC

(see, e.g., [Rapp and Lübken, 2004](#); [Baumgarten et al., 2008](#); [Hervig et al., 2009](#)). However, in the MLT region, these conditions are only met in the cold summer mesopause, whereas it is much too warm in winter (cf. Fig. 1.1).

Since the creation mechanism of (P)MSE is widely understood, summer echoes are used as a tracer for studies of the complex MLT dynamics. This includes wind profilers, studies on waves and tides utilizing spectral shift or spaced antenna techniques (e.g., [Röttger and Larsen, 1990](#); [Stober et al., 2012](#); [Hoffmann et al., 2008, 2010](#)), and turbulence (e.g., [Strelnikova and Rapp, 2010](#); [Strelnikov et al., 2017](#)). The advantage of radar measurements is that the atmosphere can be sampled quasi-continuously, independent of tropospheric weather conditions.

Compared to radar echoes in summer, winter echoes are much weaker. In addition, they are rare, and have, for a long time, only been observed occasionally, with observation occurrence rates of 0.3 % (mid-) and 2.9 % (polar latitudes) during the season ([Zeller et al., 2006](#)). With development of the powerful MAARSY (Middle Atmosphere Alomar Radar System, [Rapp et al., 2011a](#); [Latteck et al., 2012](#)), the occurrence rate of observations increased dramatically (~16%, [Latteck and Strelnikova, 2015](#)). Considering that the D-region ionosphere, where the radar echoes occur, is dominated by collisions of neutrals and only weakly ionized, the creation mechanism is most probably an effect of the atmosphere's dynamics. Depending on the underlying dynamical process, (P)MWE may have enormous potential for utilization as a tracer for MLT dynamics. This connection is potentially much more direct since the involved charged particles are most probably much smaller than those connected to (P)MSE formation. Even though seasonal occurrence rates are lower compared to echoes in summer, (P)MWE are observed over a much more extended period, i.e., from September to May (8 months). The (P)MSE season instead lasts only from mid- or end of May to September (3–4 months). At this time, occasionally also radar echoes -identical to (P)MWE- are observed ([Latteck et al., 2021](#)), but are not always identified as (P)MWE (e.g., [Havnes et al., 2018](#)). Moreover, altitude coverage of winter observations from 55–85 km is much broader than (P)MSE, which can almost exclusively be found between 80–92 km.

### 1.3 Open Questions and Outline

To use (P)MWE as a tracer for dynamical processes in the MLT region, it is fundamental to understand their formation mechanism in detail. However, the formation process of PMWE is still an open scientific question. Therefore the following question has to be answered:

Q: What is the formation mechanism of PMWE?

The thesis is structured as follows: After an introduction to the MLT-region and radar echoes, coherent radar scattering, the potential of small-scale dynamical processes, and the role of the background are discussed in a theoretical part. Based on this, the hypothesis to be proven in this work are formulated. The first methodological part focuses on analysis tools, while in the second part the instrumental setup is explained, and a description of the

first sounding rocket campaign is given. Subsequently, the results of the first two sounding rocket flights are presented and discussed. A short summary is given at the end of this thesis and a brief outlook on further scientific projects following this work.

## 2 | Theoretical Preconiderations

This chapter includes the theoretical and observational basis of this work. The current understanding of the topic will be summarized and shortly discussed to form hypotheses to be proven in this work. First, the principle of coherent radar scattering is introduced. This is done by defining the most critical terms, e.g., refractive index ( $n$ ), potential refractive index/electron density gradient ( $M_n/M_e$ ), Bragg scale ( $\lambda_B$ ), volume reflectivity, and scatter cross section ( $\eta/\sigma$ ). Also, the principle of partial reflection is explained shortly. While this part discusses these topics only briefly, detailed information can be found elsewhere (e.g., [Hocking et al., 2016](#); [Schunk and Nagy, 2009](#)).

A second part is dedicated to turbulence, with a focus on spectral theory. After that, our current understanding of PMWE is summarized. Starting from phenomenology of PMWE, all relevant investigations made are subsequently outlined and discussed, and main geophysical contributors to PMWE formation are identified.

It will be shown that some scientific insights have been gained, most by means of radar with different sounding frequencies, but also in situ. However, these insights are often anything but conclusive, and no complete picture of all relevant aspects exists. Ultimately, based on the previous sections, hypotheses are derived in the last section.

### 2.1 Coherent radar scattering

A radar sends out electromagnetic waves that is influenced by the refractive index  $n$  of the medium. If the refractive index differs substantially from one place to another, phase speed is altered. Subsequently, the wave gets deflected, a part is reflected and returns to the receiver. In the ionosphere, where free electrons are available, these electrons are displaced in the plane of the electric field of an electromagnetic (radio)wave, hereby sending an electromagnetic wave of the same frequency. A part of this radio wave reflects. This scattering mechanism is called Thomson scattering. If the electrons can move completely freely, the backscattered signals are uncorrelated in time due to the high velocity of electrons. The signal received by the radar is called incoherent. If, in turn, electrons cannot diffuse freely and are bound to the more inert species (i.e., to ions), the received signal from pulse-to-pulse is correlated in time. The received signal is called coherent. The advantage of these coherent signals is that they can be integrated over several pulses in order to increase the signal-to-noise ratio (SNR). This data-processing method is often referred to as coherent integration.

Since PMWE are coherent radar returns from mesospheric heights, the main concepts in connection to coherent scattering are described below.

### 2.1.1 Refractive Index

A general formulation, valid for the refractive index in the ionosphere, including the effects of collisions, and magnetic field was derived from magneto-ionic theory by Appleton and Hartree (e.g., Appleton, 1932; Friedrich, 2016):

$$n^2 = 1 - \frac{X}{1 - iZ - \left( \frac{Y_T^2}{2(1-X-iZ)} \right) \pm \sqrt{\left( \frac{Y_T^4}{4(1-X-iZ)^2} \right) + Y_L^2}} \quad (2.1)$$

In this formula,  $i^2=-1$  denotes the imaginary number,  $X=\omega_p^2/\omega^2$  is the ratio of plasma frequency  $\omega_p$  to sounding frequency  $\omega$ .  $Y = \omega_g/\omega$ ,  $Y_L = \omega_g \sin(\theta)/\omega$ , and  $Y_T = \omega_g \cos(\theta)/\omega$  are given by the ratio of absolute, longitudinal and transversal parts of gyro-frequency  $\omega_g$  to sounding frequency, with respect to the angle between propagation vector and magnetic field  $\mathbf{B}$ , denoted by  $\theta$ . Due to the interaction of the sounding wave with gyro motions (with  $\omega_g$ ) of the charged particles, these wave modes experience a different refractive index, denoted by  $\pm$  in Eq. 2.1 (see, e.g., Friedrich, 2016, for more details).

The ratio of collision frequency between electrons and inertial particles (i.e., neutrals)  $\nu_e$  to sounding frequency is defined by  $Z=\nu_e/\omega$ . Plasma frequency  $\omega_p$  is given by:

$$\omega_p = \sqrt{\frac{N_e e^2}{\epsilon_0 m_e}}, \quad (2.2)$$

where  $N_e$  is the electron number density,  $\epsilon_0$  is the dielectric vacuum constant,  $e$  is the elementary charge, and  $m_e$  is the electron mass. The other frequency to be defined is gyro-frequency:

$$\omega_g = \frac{eB}{m_e}, \quad (2.3)$$

with the magnetic field strength  $B$ . This formula generally applies to every charged particle. In this case,  $e$  is replaced by the particle's charge  $q$  and its corresponding mass. Furthermore, the collision frequency can be defined as:

$$\nu_c = \frac{v}{\lambda} = N A v, \quad (2.4)$$

i.e., the ratio of (thermal) velocity  $v$  to the mean free path  $\lambda$  (i.e., the mean path a molecule travels between collisions), or directly as the product of number density  $N$ , collision cross-section  $A$ , and (thermal) velocity. In contrast to the simple case of pure neutral molecule collision (e.g., Bird, 2003), the case of electron collisions is not straight forward, since the collision cross section depends on the electron speed, ultimately relating the collision frequency to:  $\nu \propto v^2$  (see, e.g., Budden, 1965, and references therein).

In the MLT, Eq. 2.1 becomes much simpler since the components in the denominator are small compared to unity.

$$n^2 = 1 - X = 1 - \frac{\omega_p^2}{\omega^2} \quad (2.5)$$

In this case, collision frequency  $\nu_e$  is neglected. If  $\nu_e$  should be taken into account,  $\omega^2$  is replaced by  $(\omega^2 + \nu_e^2)$ . Inserting Eq. 2.2 and wavelength  $\lambda=2\pi c\omega^{-1}$  in Eq. 2.5 yields:

$$n^2 = 1 - \frac{N_e e^2}{\epsilon_0 m_e \omega^2} = 1 - \frac{N_e e^2}{\epsilon_0 m_e} \left( \frac{\lambda}{2\pi c} \right)^2 = 1 - \frac{r_e N_e \lambda^2}{2\pi}, \quad (2.6)$$

where the classical electron radius  $r_e = \frac{1}{4\pi\epsilon_0} \frac{e^2}{m_e c^2}$  is introduced. This expression is valid for non-magnetized and collisionless electron gas, and appropriate for free-electron gas. A semi-empirical formula for radio refractive index in air, developed from series expansion, was proposed and improved by [Essen and Froome \(1951\)](#) and [Smith and Weintraub \(1953\)](#). Inclusion of the effect of the ionosphere (Eq. 2.6) reveals a formula that is applicable in the MLT region (e.g., [Balsley and Gage, 1980](#); [Röttger, 1980](#)):

$$n - 1 \approx \frac{3.73 \cdot 10^{-1} e}{T^2} + \frac{77.6 \cdot 10^{-6} p}{T} - \frac{40.32 N_e}{f^2}, \quad (2.7)$$

where  $T$  is temperature in K,  $e$  is the partial pressure of water vapor in mbar,  $p$  is air pressure in mbar, and  $f=\omega/(2\pi)$  is sounding radar frequency. The right-hand terms (from left to right) are called “wet”, “dry” and “ionospheric” terms. Where the “wet” term is dominant in the troposphere, “wet” and “dry” terms in the stratosphere, and the “ionospheric” term dominates in the ionosphere, from approximately 50–100 km altitude.

## 2.1.2 Potential refractive index gradient

Refraction appears where the refractive index sufficiently changes along the path of an electromagnetic wave within spacial scales smaller than the wavelength. In a stationary atmosphere, a change of the refractive index perceived by an electromagnetic wave (considering radio range) traveling vertically from the ground into the atmosphere would be small, and thus no noteworthy refraction would appear. However, internal atmospheric waves and turbulence are key players in the mixing process of the atmosphere. These processes can transport parcels of air vertically and if the change of state is sufficiently fast (e.g., heat transfer is negligible), the refractive index of the vertically displaced air parcel ( $n_0$ ) significantly differs from its surrounding refractive index ( $n_1$ ) by  $\Delta n$ :

$$\Delta n = n_1 - n_0 \quad (2.8)$$

It is important to note that  $n_0$  is not the same as the refractive index at an altitude  $z_0$ , because the vertically displaced air parcel will exchange energy during displacement. It is assumed that the air parcel moves relatively fast, so an adiabatic change of state (i.e., no transfer of heat,  $\delta Q=0$ ) emerges. The total differential  $n(N_e)$  is denoted by (according to [Hocking, 1981, 1985](#)):

$$dn = \frac{\delta n}{\delta N_e} \cdot \frac{\delta N_e}{\delta z} dz \quad (2.9)$$

where the most interesting part is  $\delta N_e/\delta z$ . The expression  $\delta N_e/\delta z$  is often referred to as potential electron density gradient and depends on the (potential) temperature ( $\theta$ ,  $T$ ), neutral density-  $\rho$ , and absolute electron  $N_e$  density profiles. With the assumption that



the ratio of electron density to total density inside the parcel is unchanged during vertical motion, Eq. 2.9 forms to (Hocking, 1981):

$$M_n = \frac{dn}{dz} = \frac{\delta n}{\delta N_e} \underbrace{\left( \frac{N_e}{T} \cdot \frac{d\theta}{dz} - \frac{dN_e}{dz} + \frac{N_e}{\rho} \cdot \frac{d\rho}{dz} \right)}_{\delta N_e / \delta z}. \quad (2.10)$$

$M_n$  is called potential refractive index gradient. With the introduction of the characteristic-quantities Brunt-Väisälä frequency  $\omega_B$  and scale heights of neutral density  $H_N$  and electron density  $H_e$ , defined as:

$$\begin{aligned} \omega_B^2 &= \frac{g}{T} \cdot \frac{dT}{dz} + \frac{g}{c_p} \\ \frac{1}{\rho} \frac{d\rho}{dz} &= \frac{1}{N} \frac{dN}{dz} = -\frac{1}{H_N} \\ \frac{dN_e}{dz} &= -N_e \cdot \frac{1}{H_e}, \end{aligned} \quad (2.11)$$

inserting Eq. 2.11 into 2.10 reveals

$$M_n = \frac{\delta n}{\delta N_e} \cdot N_e \underbrace{\left( \frac{\omega_B^2}{g} - \frac{1}{H_e} + \frac{1}{H_N} \right)}_{\delta N_e / \delta z = M_e}, \quad (2.12)$$

where  $g$  denotes the acceleration due to gravity,  $N$  the neutral number density, and  $c_p$  the specific heat capacity at constant pressure. All terms inside the brackets of  $\delta N_e / \delta z$ , or  $M_e$  in Eq. 2.12, are of the same order of magnitude in the lower ionosphere. Therefore, none of them is negligible. Hocking (1981) simplified this formula further, assuming a constant value of  $H_N \approx 7$  km from an atmospheric model (Sissenwine et al., 1962). Today, it is widely known that neutral density is noticeably modulated by, e.g., propagating gravity waves; consequently, the assumption of a constant neutral scale height was not made here. For high-frequency radio waves  $\omega$  (i.e., VHF in our cases)  $\delta n / \delta N_e$  is obtained by assuming  $n \approx 1$ . Thus, considering  $n$  in Eq. 2.6, for  $r_e N_e \lambda^2 \pi^{-1} \rightarrow 0$ , the first element of series expansion of Eq. 2.6 around  $N_e = 0$  is

$$\frac{\delta n}{\delta N_e N_e=0} \approx -\frac{r_e \lambda^2}{2\pi}, \quad (2.13)$$

and therefore constant for a constant sounding frequency  $\omega$  and independent of  $N_e$ .

### 2.1.3 Bragg scattering

The term Bragg scattering goes back to experiments by Bragg (senior and junior), determining the structure of several crystals by use of X-ray scattering on planes of atoms (Bragg and Bragg, 1913). They showed that the maximum backscatter appears under a specific condition,

$$\lambda i = 2\delta \cdot \sin(\theta) \quad (2.14)$$

with wavelength  $\lambda$ , grid-distance  $\delta$ , the angle between atom grid plane and X-ray  $\theta$ , and multiple integer  $i$ . Later this expression was named, in honor of its discoverers, Bragg-condition. The underlying individual scattering process of the atom-bound electrons with the X-ray photons is the elastic Thomson-scattering, which is the low energy case of the more general Compton-scattering. The same principle can be applied to the scattering of radar waves on structures of refractive index, i.e., structures of electrons in the case of non-magnetized and collisionless plasma. For the case of mono-static radars (i.e., co-located transmitter and receiver), the angle  $\theta$ , denoting angle between the incident and the scattered wave, is  $\pi/2$  and consequently,

$$\frac{\lambda i}{2} = \delta = \lambda_{\text{BC}} \quad (2.15)$$

where the original variable  $\delta$  denoting the distance from the crystal planes is replaced by  $\lambda_{\text{BC}}$  to follow the established notation used in the context of radars. For radar applications,  $i$  is set to unity (cf. [Tatarski et al., 1961](#); [Ottersten, 1969a](#)). The relation of radar Bragg scale  $\lambda_{\text{BC}}$  and radar frequency is given by

$$\lambda_{\text{BC}} = \frac{1}{2} \lambda = \frac{c}{2f}, \quad (2.16)$$

where  $c$  is the speed of light, and  $f$  is the radar frequency.

In reality, the arrangement of free electrons in the ionosphere's plasma differs substantially from bound electrons in crystals. If the electrons are not coupled to a structure, these free electrons move very fast compared to the time resolution of the radar. Hence, the back-scattered signal relies on the Bragg scattering principle. The returning pulse-to-pulse signal phases are uncorrelated in time due to phase-shift differences of the moving electrons. This kind of scattering, where only amplitudes but not phases are correlated, is named incoherent scatter (IS). This process is used to determine electron density from intensity, ion-drift velocity from Doppler shift, and temperatures from Doppler broadening of the received signal (see, e.g., [Mathews, 1984](#)). Even though radar scattering generally relies on scattering on Bragg scales, the term Bragg scattering is commonly used for scattering due to periodic structures on scales of half-sounding wavelength. Those structures in the refractive index are persistent over several pulses and, therefore, correlated and coherent. Coherent scattering on radar Bragg scale enables averaging techniques and allows the use of less sensitive radars.

#### 2.1.4 Volume scattering

Volume reflectivity  $\eta$  is a quantity, relating received signal power to properties of the scatter itself. It gives the ratio of scatter cross section  $\sigma_s$  per volume  $V$ . It is crucial to interpret backscatter signals from various radars, independent of the observation volume and other technical aspects of the respective radar system.

$$\eta [\text{m}] = \sigma_s [\text{m}^2] / V [\text{m}^3] \quad (2.17)$$

### Scatter cross section and volume reflectivity of electrons

The quantity of scatter cross section  $\sigma$  describes an effective area that scatters an incident Poynting-vector  $\mathcal{S}_{\text{in}}$  isotropically. If a radar sends out  $\mathcal{S}_{\text{in}}$ , which is subsequently reflected by an object (with the cross section  $\sigma$ ) by scattering  $\mathcal{S}_{\text{sc}}$ , the radar receiver gets back a power  $P_{\text{rec}}$  of  $\mathcal{S}_{\text{sc}} \cdot 4\pi r^2$ . The term  $4\pi r^2$  denotes the surface area of a sphere with radius  $r$  denoting the distance between object and receiver. Consequently, the cross section is given by:

$$\sigma = \frac{\overbrace{\mathcal{S}_{\text{sc}} \cdot 4\pi r^2}^{=P_{\text{rec}}}}{\mathcal{S}_{\text{in}}} \quad (2.18)$$

For a single electron  $\sigma$  is the Thomson cross section:

$$\sigma_{\text{T}} = \frac{8\pi}{3} r_0^2 \approx 6.65 \cdot 10^{-29} \text{ m}^2. \quad (2.19)$$

A radar, sounding the ionosphere, receives scattering from multiple ( $n$ ) electrons. Thus, the received power increases by:

$$P_{\text{rec}} = n \cdot \sigma_{\text{T}} \cdot \mathcal{S}_{\text{in}}. \quad (2.20)$$

Note that  $n$  (only here) is the absolute number of electrons, and should not be confused with the refractive index. The radar's sounding volume  $\Delta V$  is defined as

$$\Delta V = \Delta l \cdot \pi (r\Delta\theta) \quad (2.21)$$

with the pulse length ( $\Delta l$ ), beamwidth  $\Delta\theta$ , and distance from radar (transmitter/receiver) to the sampled volume  $r$ . Note that  $\Delta V$  can be approximated to be cylindrical since  $\Delta l \ll r$ . Received power (and therefore the detected number of electrons  $n$ ) depends on the sampling volume  $\Delta V$ . This volume is different for each radar, and, consequently, a normalization to  $\Delta V$  is helpful to be able to compare radar returns from various radar-systems. Analog to Eq.2.18 the volume-independent quantity, volume reflectivity  $\eta$  is obtained by:

$$\eta = \frac{\mathcal{S}_{\text{sc}} \cdot 4\pi r^2}{\mathcal{S}_{\text{in}} \Delta V} = \frac{\sigma}{\Delta V} \quad (2.22)$$

### Volume reflectivity of spatially distributed tracers

The scattered signal  $\mathcal{S}_{\text{sc}}$  from randomly distributed tracers in the sampling volume  $\Delta V$  returned to the receiver can also be described by the power density of a spectrum  $\Phi$  at radar Bragg wavenumber  $k_{\text{BC}}$ . In analogy to Eq. 2.20, scattered power from electrons is related by:

$$P_{\text{rec}} = \mathcal{S}_{\text{sc}} \cdot 4\pi r^2 \propto \sigma_{\text{T}} \mathcal{S}_{\text{in}} \cdot \Phi_{\text{Ne}}(k_{\text{BC}}) \Delta V \quad (2.23)$$

For radar applications, the tracers generally are refractive index fluctuations. A detailed review of the original derivation of a quantitative spectral formulation of [Tatarski \(1971\)](#) can be found in [Hocking et al. \(2016\)](#), where the spectral formulation is derived for the

dielectric constant (i.e.,  $\epsilon' = \epsilon(\omega)/\epsilon_0$ , as in the original), which is closely related to the refractive index ( $n^2 = \epsilon'$ ). The received Poynting-vector  $\mathcal{S}_{sc}$ , is then given by (Hocking et al., 2016):

$$\mathcal{S}_{sc} = \frac{\pi k^4}{2r^2} \mathcal{S}_{in} \Delta V \Phi_{\epsilon'}(k_{BC}). \quad (2.24)$$

Subsequently, volume reflectivity  $\eta$  can be derived by inserting Eq. 2.24 in Eq. 2.22.

$$\eta = 2\pi^2 k^4 \Phi_{\epsilon'} \quad (2.25)$$

For conversion from  $\eta_{\epsilon'}$  to  $\eta_n$ , the spectrum of the refractive index must be multiplied by  $(dn/d\epsilon')^2$ , yielding:

$$\Phi_{\tilde{\epsilon}} = 4n^2 \Phi_n. \quad (2.26)$$

Consequently, volume reflectivity of the refractive index is written as:

$$\eta = 8\pi^2 k^4 n^2 \Phi_n. \quad (2.27)$$

Since received scattering essentially results from structures on Bragg scale, the wavenumber  $k$  is substituted by  $\kappa = k/2$ . Further, taking into account that the refractive index  $n$  in the atmosphere is usually very close to unity, this produces a modified version of Eq. 2.27

$$\eta = \frac{\pi^2}{2} k^4 \Phi_n. \quad (2.28)$$

This relation is widely used (see e.g., Ottersten, 1969a; Rapp et al., 2008; Lübken, 2014).

### 2.1.5 Partial reflection

When electromagnetic waves pass from a medium with a particular refractive index to another medium with a refractive index different from the first, refraction and reflection occur on the boundary surface. In radar science, the terms partial reflection or Fresnel reflection are used equivalently (e.g., Fukao and Hamazu, 2014). The contribution of partial reflection to atmospheric science with radars is briefly reviewed in Fukao and Hamazu (2014) (and references therein). Since the atmosphere is known to be stratified, electromagnetic waves in the frequency band of 2–100 MHz get partially reflected (Hocking et al., 1991; Hocking, 2003). The boundaries on which reflection occurs can be idealized as planar mirrors, with a reflection coefficient  $|R|^2 \leq 1$ .

The reflection coefficient  $|R|^2$  generally depends on the altitude profile of the refractive index  $n$ , layer thickness  $l$ , and the sounding Bragg wavenumber vector  $\kappa = k/2 = 4\pi\lambda^{-1}$ .

$$|R|^2 = \frac{1}{4} \left| \int_{-l/2}^{l/2} \frac{1}{n} \frac{dn}{dz} e^{-j\kappa z} dz \right|^2 \quad (2.29)$$

This equation can be further simplified by assumptions of the shape of the refractive index profile (also see Fukao and Hamazu, 2014, and references therein). Another important aspect is the horizontal extension of the layer. To get sufficient backscatter, this has to

be larger than a certain limit, denoted by a circular area with Fresnel radius, defined by (Hocking et al., 2016) as

$$r_F = \sqrt{r \cdot \lambda} \quad (2.30)$$

where  $r$  and  $\lambda$  denote the radial distance between radar and target and the radar wavelength, respectively. This radius  $r_F$  spans a surface perpendicular to the radio wave, in which the radial distance changes by  $\lambda/2$  at the edges. For VHF radars at  $\sim 50$  and  $\sim 220$  MHz, respective Fresnel radii are 600–700 m and 290–340 m for altitudes of 60 or 80 km.

## 2.2 Turbulence

Turbulence is a widely known phenomenon from everyday experience, e.g., often associated with uncomfortable air travels. From a scientific view, turbulence is of continued interest since it is a crucial mechanism of energy transfer and mixing.

To answer the question what turbulence is, usually its characteristics were listed (e.g., Pope, 2000; Lesieur, 2008): random, multi-scale, rotational, dispersive, and develops at a high Reynolds number  $Re$ .  $Re$  is a dimensionless characteristic number, describing the ratio of inertia to viscous forces of a flow:

$$Re = \frac{L \cdot u}{\nu}, \quad (2.31)$$

where  $\nu$  is the kinematic viscosity of the fluid,  $u$  is velocity, and  $L$  is a characteristic length scale. The latter is defined by the geometry of flow, e.g., the diameter of a cylinder, length of a channel, or vortex size.  $Re$  is one of the fundamental characteristic numbers in fluid mechanics and allows scaling (viscosity, velocity, dimension) of fluid mechanical problems and, therefore, e.g., its investigation in laboratories. Moreover, the concept of dimensionless characteristic numbers (some more will be introduced later) leads to universality of scientific findings in the field of turbulence (e.g., L'vov, 1998), from galactic scales of  $10^{16}$ – $10^{18}$  km, hundreds of meters to meters in the MLT, down to centimeters and millimeters in the kitchen sink.

Mathematically, flows can be described by the Navier-Stokes-Equations (NSE). Reynolds (1895) further introduced a decomposition of flow quantities:

$$u = \bar{u} + u', \quad (2.32)$$

describing the velocity  $u$  as the sum of a slowly changing mean velocity  $\bar{u}$ , superimposed by velocity fluctuations  $u'$ . Finally, a combination of both yields the Reynold-Averaged-Navier-Stokes-Equation (RANSE, e.g., Prandtl, 2012; Hinze, 1975; Lesieur, 2008):

$$\rho \frac{D\bar{u}_i}{Dt} = F_i - \frac{\delta \bar{p}}{\delta x_i} + \mu \nabla^2 \bar{u}_i - \frac{\delta}{\delta x_j} \overline{\rho u'_i u'_j}. \quad (2.33)$$

For Eq. 2.33 Einstein summation convention is used, where  $i$  or  $j$  denotes the component (e.g.,  $i$  for x-direction). Variables  $t$  and  $x$  represent time and space, respectively. Variable  $F_i$  denotes body force (e.g., due to gravity). Variables  $\rho$ ,  $p$ , and  $\mu$  are mass density, pressure, and dynamic viscosity. The most exciting term is  $-\frac{\delta}{\delta x_j} \overline{u'_i u'_j}$ , called Reynolds

stress tensor ( $R_{ij}$ ). This term indicates a loss of momentum, is non-linear and induces a closure problem. However, numerous models exist to approximate  $R_{ij}$ . From simple one-point closure models, e.g., introducing an eddy viscosity and utilizing the mixing-length concept (Prandtl, 1925), and more elaborated two-point closure models, using two-point correlation and the spectrum concept (with pioneering works, e.g. from Kolmogorov, 1941; Obukhov, 1949; Taylor, 1935; Weizsäcker, 1948; Heisenberg, 1948) to describe the turbulent fluctuations in  $R_{ij}$  (e.g., Lesieur, 2008).

## 2.2.1 Energy spectrum

The distribution of kinetic energy  $E(k)$  of turbulent fluctuations in a fluid with respect to wavenumber  $k$  (or spatial scales  $\lambda$ ) can be expressed by an energy spectrum, as shown in Fig. 2.1.

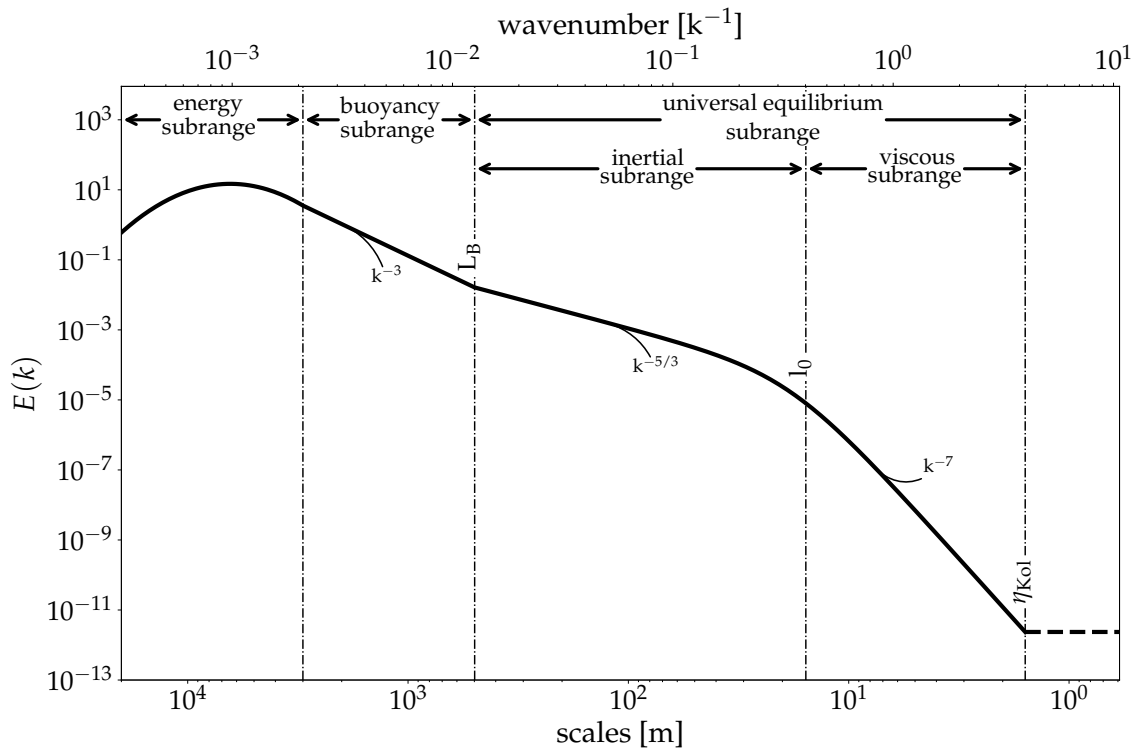


Figure 2.1. Vertical energy spectrum for representative values of the polar mesosphere in  $\sim 75$  km in spring/autumn ( $\omega_B = 0.02 \text{ s}^{-1}$ ,  $\nu = 0.5 \text{ m}^2 \text{ s}^{-1}$ ,  $\epsilon = 20 \text{ mW kg}^{-1}$ ). Scales and wavenumber are shown on bottom and top abscissa, respectively. Their energy contribution to the spectrum is plotted on the ordinate. Different subranges labeled in the upper part are delimited by characteristic scales, indicated with vertical dashed lines. The universal equilibrium subrange is derived using the Heisenberg (1948) model.

This spectrum can be split into several subranges. Beginning at the largest scales (lowest wavenumber): The energy subrange is the part of the spectrum, where energy in the form of large eddies (e.g.,  $\sim 2.5\text{--}7.5$  km, from GW with  $\sim 5\text{--}15$  km vertical wavelength) is induced to the spectrum. Further following the energy cascade, the energy gets transferred into

the buoyancy subrange, with a slope of  $k^{-3}$ , where buoyancy forces dominate. At the Buoyancy scale ( $L_B$ ), buoyancy subrange passages to the universal equilibrium subrange, which includes inertial and all smaller scales. The Buoyancy scale is denoted by (e.g., [Lübken, 1993](#), and references therein):

$$L_B = 9.97 \cdot \sqrt{\frac{\varepsilon}{\omega_B^2}}, \quad (2.34)$$

with buoyancy frequency  $\omega_B$  and energy dissipation rate  $\varepsilon$ . Note that  $L_B$  is not necessarily defined (i.e., for  $\omega_B^2 > 0$ ), e.g., in the case of convective turbulence, where  $\omega_B^2 < 0$  (e.g., [Hocking, 1985](#)).

The smallest scale, i.e., where kinetic energy finally dissipates, is approximately given by the Kolmogorov microscale (e.g., [Pope, 2000](#); [Hinze, 1975](#)):

$$\eta_{\text{Kol}} = \left( \frac{v^3}{\varepsilon} \right)^{1/4} \quad (2.35)$$

In the inertial subrange, where inertial forces dominate, the 1D kinetic energy spectrum is given by the Kolmogorov-Obukhov law:

$$E(k) = C_{\text{KO}} \varepsilon^{2/3} k^{-5/3}, \quad (2.36)$$

where  $\varepsilon$  is the kinetic energy dissipation rate,  $k$  is the wavenumber, and  $C_{\text{KO}}$  is the Kolmogorov-Obukhov constant. Due to its  $k^{-5/3}$  dependency, the Kolmogorov-Obukhov law is often called -5/3-power-law and has been found to describe various measurements accurately (e.g., [Grant et al., 1962](#); [Gibson and Schwarz, 1963](#); [Grant et al., 1968](#); [Champagne et al., 1977](#); [Nastrom and Gage, 1985](#), and others). The -5/3-power-law precisely describes the energy spectra down to approximately a scale called inner scale  $l_0$ , corresponding to a wavenumber  $k_0 = 2\pi/l_0$ . At smaller scales, viscous forces start to dominate over inertia and, consequently, the spectrum reveals a steeper drop-off. Thus at scales  $\ll l_0$ , the subrange is called viscous. In contrast to the consensus on the -5/3-spectral-form of the inertial subrange, there are several different suggestions on how to describe the spectral form of the viscous subrange (e.g., [Heisenberg, 1948](#); [Kovaszny, 1948](#); [Novikov, 1961](#); [Grant et al., 1962](#); [Tchen, 1973](#); [Driscoll and Kennedy, 1981](#); [Driscoll, 1983](#); [Smith and Reynolds, 1991](#)). Those authors suggest a spectral slope of either  $k^{-7}$  ([Heisenberg, 1948](#)) or exponential drop-off (e.g., [Tatarski, 1971](#); [Driscoll and Kennedy, 1981](#)), or even a combination of both ([Tchen, 1973](#)).

A general formulation for the 1D kinetic energy spectrum in the universal equilibrium subrange is given by:

$$E(k) = C_{\text{KO}} \cdot \varepsilon^{2/3} k^{-5/3} \varphi(k, \eta_{\text{Kol}}) \quad (2.37)$$

where  $\varphi(k, \eta)$  describes the viscous subrange, and is e.g.,  $\propto \exp(k^{-2})$  or  $\propto k^{-7}$ .

The 1D form is of particular interest since most instruments such as balloons, but also wind channel measurements, e.g., utilizing constant temperature anemometers (CTA), measure along a trajectory rather than sampling a 3D volume.

Finally, it is crucial to note that several assumptions were made to derive the 1D spectral formulation of turbulence that is: **stationarity**, meaning that the energy input at  $\sim L_B$

equals the dissipation of energy at  $\sim\eta_{Kol}$ , **local isotropy**, i.e., no preferred direction exists, and **local homogeneity**; thus, the turbulent field is the same at arbitrary points. Of course, the reality in the MLT is very different from that, and it is well known that turbulence appears in layers of large horizontal and small vertical extent, and, due to the dynamic of its sources (e.g., a breaking GW), is not stationary (see, e.g., [Fritts and Wang, 2013](#); [Strelnikov et al., 2017](#); [Staszak et al., 2021](#)). However, the spectral models remain applicable in most cases, and it has been shown that they are a reliable tool for in situ investigations in the atmosphere ([Lübken et al., 1992](#); [Lübken, 1997](#); [Lübken et al., 1993, 2002](#); [Rapp and Lübken, 2004](#); [Strelnikov et al., 2003, 2013](#); [Staszak et al., 2021](#)).

## 2.2.2 Scalar spectrum

Since direct and precise measurement of the kinetic energy spectrum (i.e., of velocity fluctuations) is often unachievable in the mesosphere, fluctuations of scalar quantities like temperature or densities of various species are measured instead. Thus, formulations of the spectrum for scalar quantities are needed.

Spectral distribution of a scalar quantity, in the subrange where inertia forces dominate, is described by an equation of a similar form to Eq. 2.36, derived by [Obukhov \(1949\)](#) and [Corrsin \(1951\)](#):

$$E_{\theta}(k) = K_{CO} \cdot \chi_{\theta} \varepsilon^{-1/3} k^{-5/3}, \quad (2.38)$$

where  $K_{CO}$  is the Corrsin-Obukhov-constant, and  $\chi_{\theta}$  denotes the effect of “dissipation” of fluctuations of the scalar quantity, called the total rate of dissipation of scalar quantity ([Corrsin, 1951](#)) or variance dissipation rate ([Lübken, 1992](#)). The variable  $\varepsilon$  is the energy dissipation rate and  $k$  the wavenumber. Depending on the tracer (temperature or density), this spectrum is called either inertial-conductive or inertial-diffusive (e.g., [Lesieur, 2008](#); [Hinze, 1975](#)). This is since inertial forces of the velocity field dominate over viscous forces, and the scalar quantity is transported either by convection (density) or conduction (temperature). Analog to the velocity spectrum, this spectrum describes a spectrum down to the inner scale  $l_0$ , where other forces start to dominate.

A spectrum describing the scalar spectrum down to the smallest scales is called the universal-equilibrium range and is defined by:

$$E_{\theta}(k) = K_{CO} \cdot \chi_{\theta} \varepsilon^{-1/3} k^{-5/3} \varphi(k, \eta, Sc|Pr), \quad (2.39)$$

with the dimensionless function  $\varphi(k, \eta_{Kol}, Sc|Pr)$ , which equals unity in the inertial-convective subrange, and additionally depends on dimensionless numbers  $Sc$  or  $Pr$ , in the case of density or temperature spectrum.  $Sc$  or  $Pr$ , called Schmidt number and molecular Prandtl number, giving the ratio of the kinematic viscosity  $\nu$  to diffusion of material  $D_{\theta}$  or thermal diffusion  $\alpha$ , respectively, are described by:

$$Sc = \frac{\nu}{D_{\theta}} \mid Pr = \frac{\nu}{\alpha}, \quad (2.40)$$

where  $\nu$ ,  $D_{\theta}$  and  $\alpha$  are conceptually similar, describing either the balance-mechanism of momentum, concentration or temperature differences.

[Batchelor et al. \(1959\)](#) developed the theory for three different cases:  $Sc|Pr=1$ ,  $Sc|Pr>1$ , and  $Sc|Pr<1$ .



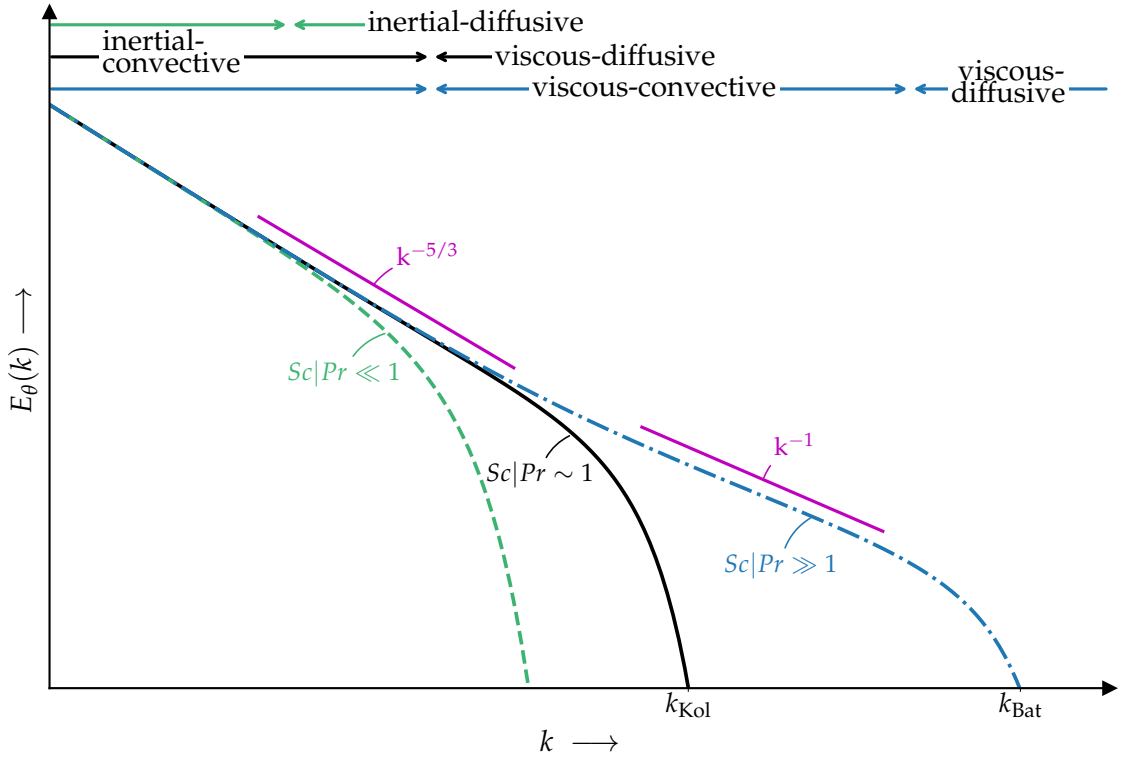


Figure 2.2. Schematic of a scalar spectrum for density fluctuations. On the abscissa, the wavenumber is shown. Their energy contribution to the spectrum is plotted on the ordinate. Both are on a logarithmic scale. Three different cases,  $Sc|Pr \approx 1$  (black, solid),  $> 1$  (blue, dashed-dotted), and  $< 1$  (green, dashed), are shown. Respective subranges and transitions are illustrated on top of the panel. Wavenumbers, associated with the Kolmogorov-scale (from kinetic energy) and the Batchelor-scale are indicated on the abscissa.

In all cases of  $Sc|Pr$ , the inertial-convective range will develop for fully developed turbulence. However, following the energy cascade to smaller scales, the spectra differ for different values of  $Sc|Pr$ . If  $Sc|Pr < 1$ , the diffusive/conductive mechanism dominates the spectrum and the scalar spectrum shrinks to smaller wavenumbers (larger scales). In this case, the smallest scales of the scalar spectrum  $\eta_\theta$  are larger (smaller wavenumber) than those of the kinetic energy spectrum, denoted as  $\eta_{Kol}$ .

$$\begin{aligned} \eta_\theta &> \eta_{Kol} \\ k_\theta &< k_{Kol}, \quad \text{if } Sc|Pr < 1 \end{aligned} \quad (2.41)$$

If  $Sc|Pr > 1$ , the spectrum expands to higher wavenumbers (smaller scales), forming the viscous-convective subrange, with a slope of  $k^{-1}$ . Batchelor et al. (1959) showed that this subrange expands until a specific wavenumber, and then the spectrum decreases exponentially. In this case, the smallest scale is given by:

$$\eta_{Bat} = \left( \frac{\nu^3}{\varepsilon} \right)^{1/4} \cdot Sc^{-1/2} = \eta_{Kol} \cdot Sc^{-1/2}, \quad (2.42)$$

referred to as the Batchelor scale. Predictions by Batchelor et al. (1959) have been verified experimentally by (e.g., Gibson and Schwarz, 1963; Grant et al., 1968). For  $Sc|Pr > 1$ ,  $\eta_{Bat}$

is smaller than the Kolmogorov microscale:

$$\begin{aligned} \eta_{\text{Bat}} &< \eta_{\text{Kol}} \\ k_{\text{Bat}} &> k_{\text{Kol}}, \quad \text{if } Sc|Pr > 1. \end{aligned} \quad (2.43)$$

In the case of neutral density fluctuations  $Sc \approx 1$ , but can exceed values of 1000 for electron density measurements in the MLT (Rapp et al., 2008). Similar to the form of viscous subrange (energy spectrum), no uniform description for a spectral form of  $\varphi(k, \eta_{\text{Kol}})$  exists (e.g., Hill and Clifford, 1978; Driscoll and Kennedy, 1985).

Fluctuations are generally caused by the difference of state due to adiabatic displacement and the background. This is in analogy to the explanations of the potential refractive index as laid out in Sec. 2.1.2.

A mathematical formulation of spectral models used in this work (Heisenberg, 1948; Tatarski, 1971; Driscoll and Kennedy, 1985) and notes on the influence of the background gradient for the tracers utilized for this work are presented in Ch. 3.

## 2.3 Investigations of PMWE at VHF

First coherent radar returns from the D-region at very high frequency band (VHF) have been reported from equatorial latitudes (Jicamarca Radar Observatory, Lima, Peru) by Flock and Balsley (1967). The first observations of mesospheric winter echoes at mid-latitudes (Max-Planck-Institute for Aeronomy, Katlenburg-Lindau, Germany,  $\sim 51.5^\circ\text{N}$ ) have been reported by Czechowsky et al. (1979). They already found distinct differences between mesospheric echoes during summer and non-summer (i.e., autumn and winter) periods. Subsequently, Ecklund and Balsley (1981) showed a cycle of radar echoes from the MLT/D-region at polar latitudes of almost two years, investigating the seasonal variation of signal-to-noise ratio (SNR), occurrence height, and correlation with the Sun's inclination. This has hence been the first report on observations of polar mesosphere winter echoes (PMWE). All these investigations were made with mesosphere, stratosphere, troposphere (MST) radars, operating at  $\sim 50$  MHz (except the one of Flock and Balsley (1967), using  $\sim 40$  MHz), corresponding to a Bragg scale  $\lambda_{\text{BC}}$  of 3 m. It turned out, however, that PMWE can also be observed by VHF radars operating at much higher frequencies, e.g., EISCAT at 224 MHz (Kirkwood et al., 2002a; Strelnikova and Rapp, 2011; Belova et al., 2013, 2018). In this section, examples of PMWE observations from 53.5 and  $\sim 224$  MHz are presented accompanied by a phenomenological description and a discussion of differences between observations at various frequencies and to PMSE. After that, a short description of annual and diurnal statistical properties follows. Subsequently, the influence of all relevant parameters and possible dynamical processes are worked out based on an extensive review of the literature. These findings are concluded in Sec. 2.4 and hypotheses to be investigated in the frame of this work are formulated.

### 2.3.1 Statistical Properties

Fig. 2.3 shows two representative examples of PMWE as observed by EISCAT-VHF and MAARSY, at 224 and 53.5 MHz respectively, where the color indicates volume reflectivity. Most PMWE appear at sunlit conditions with an occurrence maximum around local

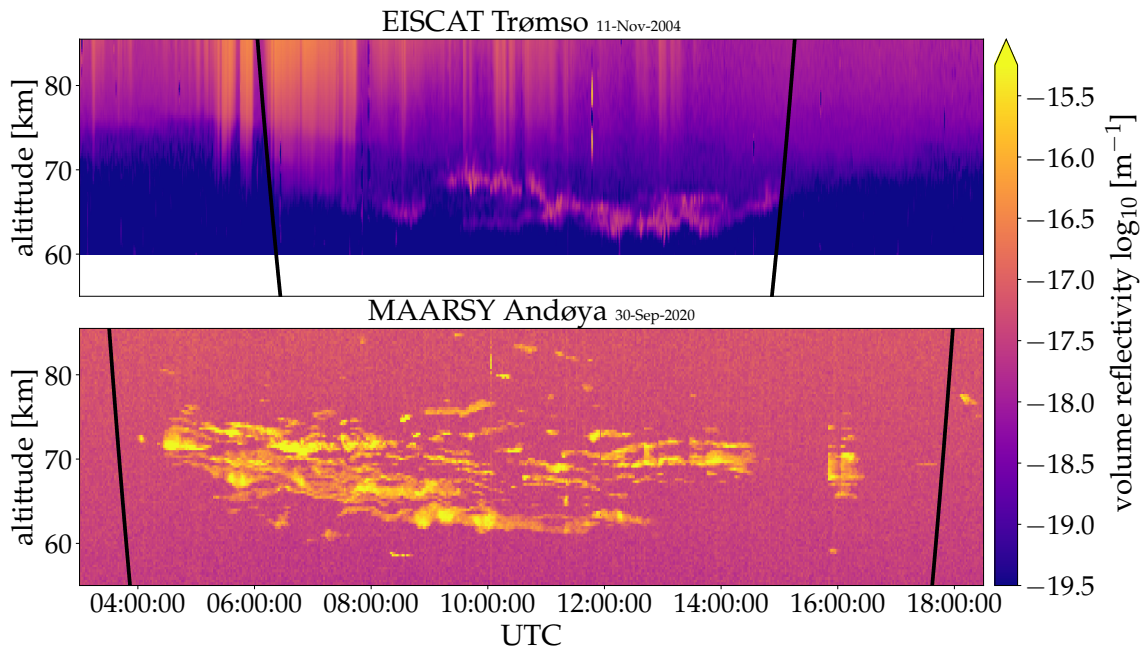


Figure 2.3. Observations of PMWE on 224 MHz and 53.5 MHz by EISCAT-VHF and MAARSY, on top and bottom panel, respectively. The color indicates volume reflectivity over altitude (ordinate) and time (abscissa). The black lines indicate dusk and dawn at the corresponding altitude.

noon. Observations at nighttime are scarce and were only made during exceptional ionization due to solar proton events or particle precipitation (e.g., Zeller et al., 2006; Kirkwood et al., 2002b). A common morphological feature is that the echoes appear as layers in different altitudes at the same time. Revealing both large scale “drift” of all layers on scales of several kilometers, over time periods of hours, as well as small “oscillations” of single layers of only hundreds of meters on periods of minutes.

The right panel of Fig. 2.4 shows the diurnal mean occurrence rate for 53.5 MHz MAARSY, and 224 Mhz EISCAT-VHF observations. Despite the fact that the database of PMWE events detected by EISCAT-VHF is limited (32.5 h, cf. Strelnikova and Rapp, 2013), while MAARSY observations are continuous over nine seasons from 2011–2020, occurrence rates are in qualitative agreement – both time and altitude-wise, although EISCAT-VHF observations are limited to a smaller height and time range. Very few PMWE have been observed below 60 km<sup>1</sup>, and only one echo has been detected from above 75.5 km. MAARSY measurements reveal a larger extend over altitude (~55–85 km) and time. They are also elucidating the altitude dependence to local time, i.e., the position of the Sun that is controlling the ionization. Altitudinal occurrence rates are plotted on the left panel of Fig. 2.4, revealing a median of the PMWE observations from ~77 km and ~70 km for day and nighttime measurements, respectively (see also Latteck et al., 2021), where daytime records dominate the mean profile.

<sup>1</sup> Note that statistical analysis for EISCAT-VHF data must be carried out with care since different operation modes limit or prohibit PMWE observation. See, for example Fig. 2.3, where data was cut off below 60 km.

A comparison of volume reflectivity measured by the MAARSY radar (see [Latteck et al., 2008](#), for details on absolute calibration) and calculated from (equivalent) electron density measurements by the EISCAT-VHF yields mean values of  $\sim 10^{-16.5}$ – $10^{-15.5}$   $\text{m}^{-1}$  for MAARSY-MST ([Latteck and Strelnikova, 2015](#)) and  $\sim 10^{-18.5}$ – $10^{-17.5}$   $\text{m}^{-1}$  for the EISCAT radar, respectively. Thus, a difference of 1–2 orders of magnitude in echo strength is observed between 53.5 MHz and 224 MHz measurements.

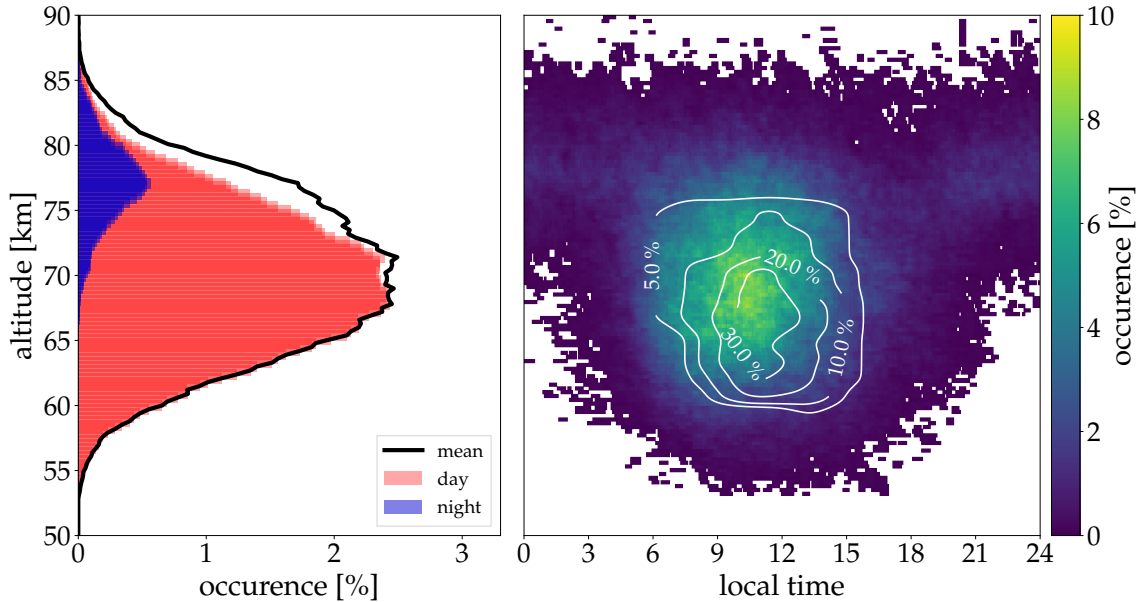


Figure 2.4. Left panel: Mean altitude distribution of all PMWE seasons (black line) and distributions for day and nighttime measurements (red and blue bars, respectively). Right panel: Mean diurnal variation from MAARSY and EISCAT-VHF. MAARSY occurrence frequencies (threshold  $\eta \geq 10^{-17}$   $\text{m}^{-1}$ ) are color-coded. The color plot is an updated version from [Latteck and Strelnikova \(2015\)](#) for continuous winter period observations from 2011–2020. White contour lines represent EISCAT-VHF PMWE occurrence frequencies of all PMWE events reported by [Strelnikova and Rapp \(2013\)](#) (i.e., 32.5 h of PMWE).

An analysis of seasonal statistics by [Latteck and Strelnikova \(2015\)](#), reveals a seasonal occurrence rate of PMWE of 14 %, much more than was calculated from the former ALWIN radar (ALOMAR Wind radar, [Latteck et al., 1999](#)), which revealed an occurrence rate of 2.9 % at similar sounding frequency ([Zeller et al., 2006](#)). This is mainly due to improvements in sensitivity (i.e., detection limits are  $\sim 10^{-16}$   $\text{m}^{-1}$  (ALWIN) and  $\sim 10^{-17.5}$   $\text{m}^{-1}$  (MAARSY)), which is accompanied by an increased altitude coverage of PMWE, ranging from  $\sim 57$  km to 83 km, reported by [Zeller et al. \(2006\)](#), to  $\sim 50$  to 87 km for recent MAARSY data. Fig. 2.5 elucidates seasonal occurrence rate statistics. On the top panel, seasonal-diurnal dependency is shown. It is apparent that most observations have been made when the Sun ionizes the background atmosphere. On the lower panel of Fig. 2.5 the seasonal variation of occurrence is shown, revealing the maxima of PMWE observations in periods of the end of September to mid-October and another less pronounced period from mid-February to mid-April. This is the period where the D-region is ionized by the Sun for a long time range ( $\sim 12$  h) and after or before PMSE season onset (see [Latteck et al., 2021](#), for recent statistics on mesospheric radar echoes).

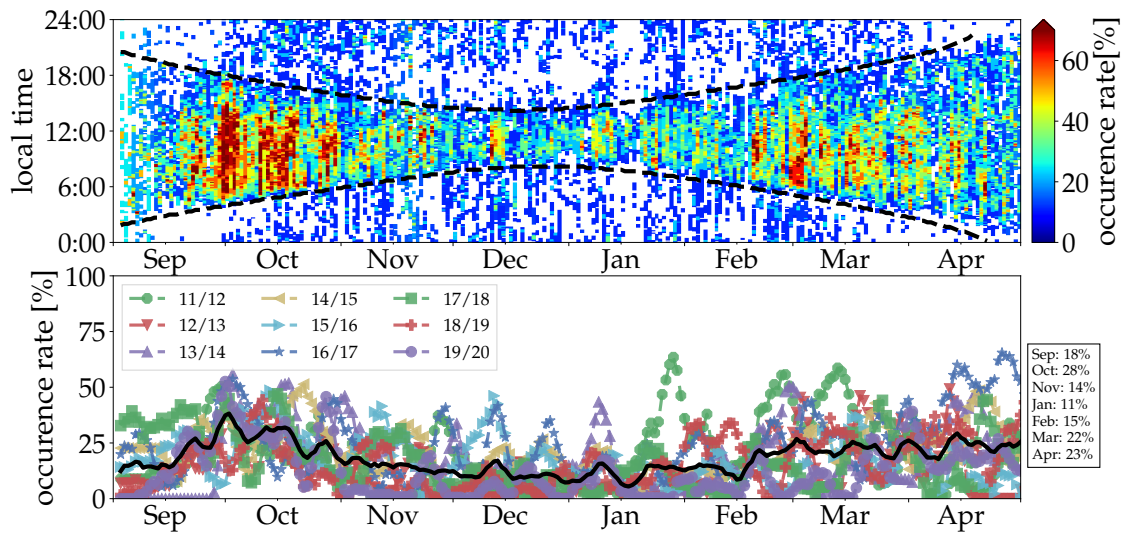


Figure 2.5. Seasonal variation of PMWE observation from 9 seasons, measured by MAARSY. The top panel shows the occurrence rate for local time. Sunrise and sunset are indicated by dashed black lines for altitudes of 55 and 83.5 km, respectively. Seasonal occurrence rates are given in the lower panel (mean as solid black line, single seasons as colored lines). The right-hand side box beside the lower panel indicates the mean monthly occurrence rate. This is an updated version of [Latteck and Strelnikova \(2015\)](#) for continuous winter period observations 2011–2020.

### 2.3.2 Influence of electron density

In Sec. 2.1.1, it was shown that electron density is a main contributor for the (potential) refractive index. Radar reflections are caused by changes in the refractive index. As is apparent from Sec. 2.1.1, these changes are proportional to the absolute change of  $N_e$  in the MLT region (i.e., in the D-region). Consequently, the refractive index  $n$  in the altitude range of PMWE observations is defined by the profile of electron density along the sampling volume. Fig. 2.6 shows electron density derived by the partial reflection radar located near Saura, on the island of Andøya, Norway (hereafter called Saura radar), which is only 17 km south of the location of MAARSY. Simultaneous PMWE measurements by MAARSY are indicated as black contour lines. The congruence between high electron density and PMWE signatures shows that  $N_e$  must reach a certain limit for PMWE to be observable by radar.

This is confirmed directly by remote sensing studies of PMWE ([Belova et al., 2005](#); [Kirkwood et al., 2006](#); [Lübken et al., 2007](#)) and by in situ measurements (see [Lübken et al., 2006](#)). Or indirectly through cosmic noise absorption (CNA) measurements as substitute for electron density ([Nishiyama et al., 2015, 2018](#)).

According to these studies, background electron density can vary over a wide range, starting below  $10^{-8} \text{ m}^{-3}$  and can reach values of less than  $10^{-11} \text{ m}^{-3}$  at a reference height of  $\sim 70 \text{ km}$  (cf. [Nishiyama et al., 2015](#); [Kirkwood et al., 2002b](#)). However, most observations were made during at least “enhanced” electron density ([Kirkwood et al., 2002b,a](#); [Stebel et al., 2004](#); [Belova et al., 2005](#); [Lübken et al., 2006, 2007](#)).

Nonetheless, PMWE can be absent even in regions of high electron density, as is also ap-

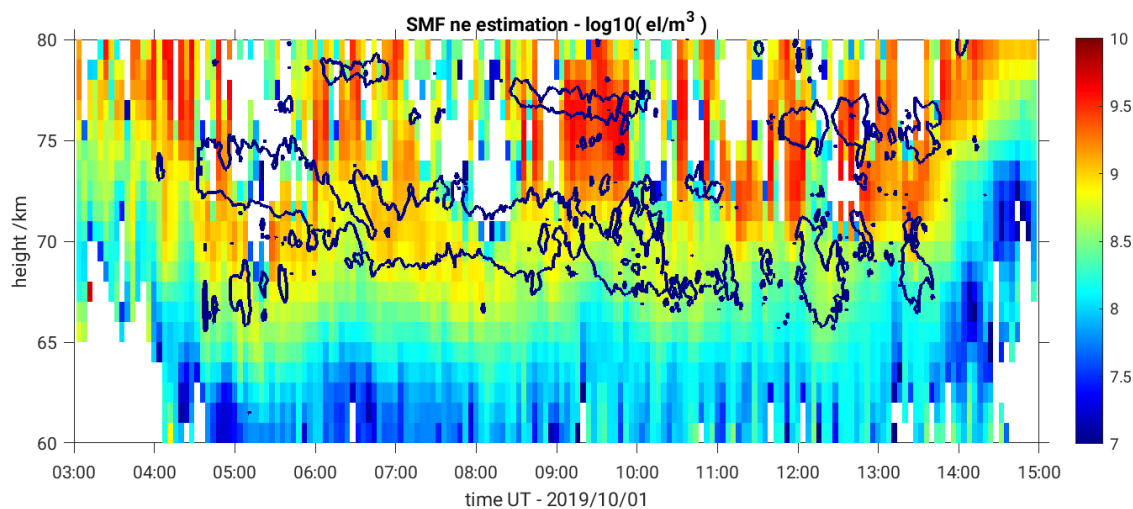


Figure 2.6. Height-time electron density plot, derived by Saura radar measurements (color-coded). Contour lines indicate simultaneous PMWE observations by MAARSY. PMWE only occurs where  $N_e$  is sufficiently high ( $\gtrsim 2 \cdot 10^8 \text{ m}^{-3}$ ). Reprinted from [Renkwitz et al. \(2021\)](#).

parent from Fig. 2.6. This behavior highlights the role of absolute change in the electron density profile. Statistical studies of [Zeller et al. \(2006\)](#) show that there is no significant correlation with Ly- $\alpha$ , which is, together with NO (nitric oxide), the dominant source of ionization in the D-region. The Ly- $\alpha$  flux in the D-region can be approximated by the  $F_{10.7}$  flux and is mainly controlled by the Sun's activity ([Friedrich, 2016](#)). The vertical electron density gradients are expected to be rather smooth and therefore they do not necessarily form a favorable ionospheric background for PMWE observations. Observations of PMWE simultaneous to measurements of high electron densities even suggest that there is an upper density limit for the existence of PMWE, since electron's diffusivity gets too strong and coherent structures cannot exist (e.g., [Nishiyama et al., 2018](#)). At high (geomagnetic) latitudes, ionization by particles guided along the Earth's magnetic field lines (i.e., particle precipitation) can be another input source of ionization. This mechanism, compared to ionization by Ly- $\alpha$  is sporadic and shows a strong dependence on the energy of particles and altitude of ionization, as higher energetic particles are able to penetrate deeper into the atmosphere. These particles start a complex ion chemistry, ultimately ionizing the atmosphere and hence increasing the electron density (e.g., [Schunk, 1987](#); [Jackman and McPeters, 1987](#); [Rees, 1987](#); [Schunk and Nagy, 2009](#)). The process of particle precipitation correlates with the geomagnetic index  $K_p$  ([Friedrich, 2016](#)). [Zeller et al. \(2006\)](#) showed a strong correlation of PMWE observations and the geomagnetic index. Also other authors noted a connection with e.g., solar wind speed and proton fluxes, which are also related to particle precipitation (see also [Kirkwood et al., 2015](#); [Belova et al., 2020](#)). Summarizing these findings, high electron density alone is not a necessary condition for PMWE. And it is the potential electron density gradient  $M_e$  (see Eq. 2.12) which is a critical prerequisite for the formation of coherent radar echoes, as has been pointed out by [Lübken et al. \(2006, 2007\)](#) and [Lübken \(2014\)](#).

### 2.3.3 Role of the neutral atmosphere background

Coherent radar returns ultimately depend on fluctuations of electron density. These fluctuations can be the consequence of the vertical displacement of an air parcel by dynamical processes. Since this displacement is fast compared to collisional accommodation and molecular diffusion, the change of state (c.o.s.) is adiabatic (i.e., no heat is transferred over the displacement). This situation is shown schematically in Fig. 2.7. Since the par-

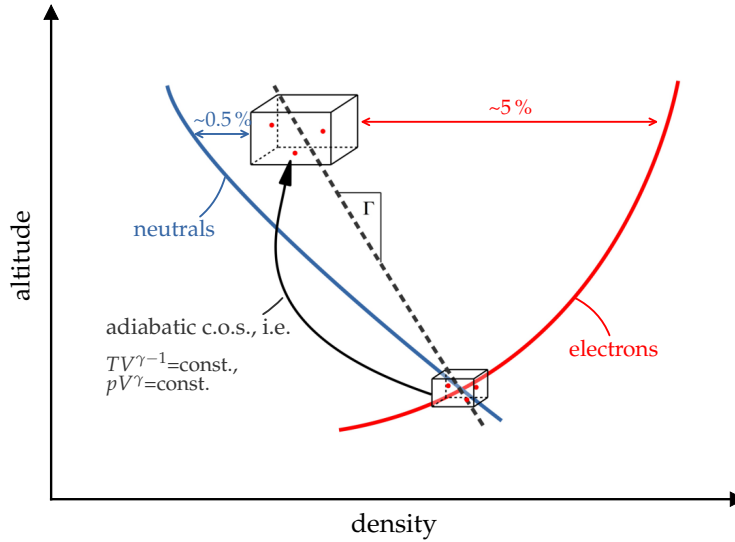


Figure 2.7. Schematic of a vertical displaced air parcel with adiabatic change of state (c.o.s.). If the parcel is lifted upwards, it expands (adiabatically). The total number of particles, either electrons or neutrals is constant inside the parcel. Subsequently, the number density decreases.

cel expands (compresses) for upward (downward) displacements whereas the total particle number inside the parcel remains constant, the number density consequently decreases (increases).

With the use of scale height  $H_N$  and buoyancy frequency  $\omega_B$  (see Eq. 2.11), potential gradients for neutral- and electron density are defined by:

$$M_N = \frac{\Delta N}{N} / \Delta z \approx \left( \frac{1}{H_N} - \frac{1}{\gamma H_p} \right) \approx \frac{\omega_B^2}{g} \quad (2.44)$$

$$M_e = \Delta N_e / \Delta z \approx N_e \left( \frac{\omega_B^2}{g} - \frac{1}{H_e} + \frac{1}{H_N} \right).$$

where  $\Delta z$  denotes a small vertical displacement ( $\Delta z \ll H_N, H_p$ ),  $H_p$  is the pressure scale height and  $\gamma$  is the isentropic expansion coefficient.  $M_N$  was derived by [Thrane and Grandal \(1981\)](#). Note that  $M_N \rightarrow 0$ , if the background profile is already adiabatic, i.e.,  $H_N = \gamma H_p$ . The definition of  $M_e$  was already implicitly given in Eq. 2.12 that shows the dependence of  $M_e$  to the neutral background via buoyancy frequency  $\omega_B$  and neutral scale height  $H_N$ . Moreover, electron as well as neutral density and temperature influence the resulting potential electron density gradient by the same order of magnitude for PMWE

altitudes. In many PMWE related works, at least one of these quantities is assumed to be constant (e.g., Hocking, 1985; Stebel et al., 2004; Belova et al., 2005) or is not directly measured (Kirkwood et al., 2006). However, Lübken (2014) emphasized the importance of  $M_e$  for radar scattering in the MLT and stated that  $N_e$  or its gradient does not solely define it. It should be noted that, as a consequence of Eq.2.44, fluctuations of electrons from vertical displaced air parcels can exist, even if the neutral background equals the adiabatic gradient. They can also exist if there is no  $N_e$ -gradient and the neutral background is not layered adiabatically.

Another crucial parameter in the context of dynamical processes is the kinematic viscosity  $\nu$ . Kinematic viscosity can be interpreted as the diffusion coefficient of momentum of the molecules and becomes important when dynamics of small scales (i.e., low  $Re$ ) are considered. For example, it relates the smallest scale of turbulence  $\eta_{Kol}$  to energy dissipation rate  $\epsilon$  as was shown before in Sec. 2.2. But it is also the starting point for the viscous-wave theory, as is reviewed below.

The kinematic viscosity  $\nu$  is defined by temperature  $T$  and mass density  $\rho$  (Sutherland, 1893):

$$\begin{aligned} \nu &= \frac{\mu}{\rho} \\ \mu &= \frac{\beta \cdot T^{3/4}}{T + S}, \end{aligned} \tag{2.45}$$

with dynamic viscosity  $\mu$ , constant  $\beta=1.458 \cdot 10^{-6} \text{ kg s}^{-1} \text{ m}^{-1} \text{ K}^{-0.5}$  and Sutherland's constant  $S=110.4 \text{ K}$ .

Profiles of neutral quantities (i.e.,  $N_N$ ,  $T$ , and related quantities) are modulated by signatures of dynamical processes (e.g., propagating GW), especially in the winter polar mesosphere. These quantities, in turn, sufficiently alter the potential electron/refractive index gradient and thereby influence the radar returns' strength. Consequently, all quantitative discussions about dynamical processes forming the PMWE phenomenon remain ambiguous as long as actual values of temperature and neutral density are not considered and only typical values are employed instead.

### 2.3.4 Turbulent structuring mechanism

Since radars are sensitive to scattering on the Bragg scale, a mechanism creating fluctuations of the refractive index at these scales is needed to explain relatively strong radar returns from the mesosphere. Furthermore, this process should be dominated by neutral dynamics since  $N_N \gg N_e$ . Fig. 2.8 illustrates the process of radio wave reflection on turbulent whirls at Bragg scale  $\lambda_{BC}=\lambda/2$ , ultimately forming coherent structures, detectable by radar (see Sec. 2.1.3). Tatarski (1971) and Ottersten (1969a,b) discussed turbulence as a mechanism to create such small-scale fluctuations, forming mesosphere (D-region) radar echoes observed with MST radars operating at frequencies  $\sim 50 \text{ MHz}$  (Woodman and Guillen, 1974; Czechowsky et al., 1979; Röttger et al., 1979). Hocking (1985) showed on the basis of estimates of turbulence strength and background (i.e., kinematic viscosity) that scales of  $\sim 3 \text{ m}$  (i.e.,  $\lambda_{BC}$  for 50 MHz radars) could theoretically be within the inertial-convective subrange of the turbulence spectrum.



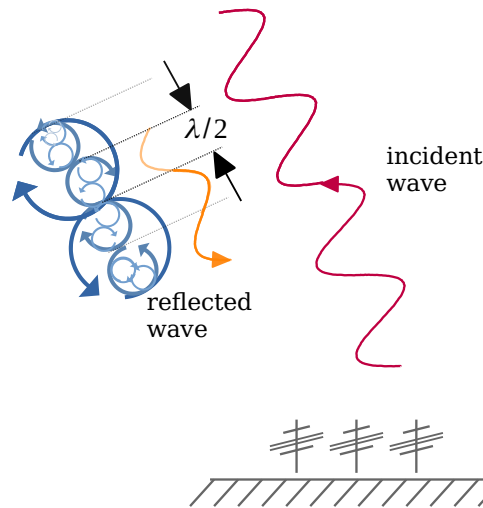


Figure 2.8. Schematic view of the volume scattering mechanism, caused by structures of turbulence on radar Bragg scale  $\lambda/2$ .

In situ measurements of electron density fluctuations at equatorial latitudes revealed that turbulence spectra could explain the observed radar echo strength (Royrvik and Smith, 1984).

Radar echoes at polar latitudes during the winter season (i.e., PMWE) were first reported by Balsley et al. (1983). The formation process is still under debate. Lübken et al. (2006) and Brattli et al. (2006) presented indicators for active turbulence in the presence of PMWE, such as an adiabatic lapse rate in temperature profiles, a low  $Ri$  number, spectral broadening (obtained from radar measurements), and turbulent spectra revealed from in situ ion density fluctuations. However, the instrument measuring ion density fluctuation was insensitive at the relevant scale of  $\sim 3$  m. Lübken et al. (2006) demonstrated that turbulence indeed could explain the observed echo strength by means of typical background values and assumptions on the electron density gradients. Nonetheless, since PMWE was not the main objective of those experiments, relevant parameters like  $N_e$  fluctuations (mainly defining the refractive index in the D-region) and background parameters were not measured, or not measured consistently (i.e., simultaneously and in common volume). Therefore, their findings are not definite universal statements that are valid for any PMWE.

Moreover, PMWE were also observed on much higher frequency by the EISCAT-VHF radar (i.e., at 224 MHz), resulting in a Bragg scale of 0.67 m (e.g., Collis et al., 1992; Kirkwood et al., 2002a; Belova et al., 2005; Strelnikova and Rapp, 2013). Creating such small scales through “pure” neutral turbulence (i.e. without considering the influence of charged MSPs) would require unreasonably high dissipation rates.

This problem can be overcome if charged heavy constituents (e.g., MSPs) are taken into account. Such particles, due to inertia, lower the mobility (i.e., diffusivity) of electrons. Thus increasing  $Sc > 1$  and extending the turbulence spectrum to smaller scales (see Fig. 2.2). Such a mechanism was found to be responsible for the creation of polar mesosphere summer echoes (PMSE). In the cold polar summer mesopause the high  $Sc$  effect originates from ice particles of up to 100 nm size (e.g., Baumgarten et al., 2008; Hervig et al., 2009). For more details on PMSE theory, the reader is referred to Rapp and Lübken (2004).

However, in winter season, the mesopause is much too warm to create such ice particles. Another plasma constituent comes into play, namely meteor smoke particles, discussed in the next section.

### 2.3.5 Meteor Smoke Particles

A constant input of cosmic dust from comet trails and meteoroids from the asteroid belt impacts the Earth's atmosphere. Because of collisions with high relative velocity, they ablate within the MLT. Thereby, material is deposited in the MLT in the form of metal and other atoms. Subsequently, these molecules and atoms re-condensate and thereby form meteor smoke particles (MSPs) (Rosinski and Snow, 1961; Hunten et al., 1980). The exact ablation and re-condensation process is somewhat more complex due to chemical reactions with the ambient atmosphere (see Plane, 2003) and proposed to take place between 100–80 km altitude where MSPs start to sediment further downwards into the stratosphere. These MSPs serve as nucleation cores for water, sulfur acids, or nitric acids and ultimately can form NLCs or PSCs (Polar Stratospheric Clouds) under temperature conditions below the frost-point in the summer mesopause and winter stratopause, respectively (e.g., Schreiner et al., 1999; Carslaw et al., 1998).

First experimental evidence for MSPs in the MLT region was found by use of a rocket-based three-mode (ion<sup>+</sup>, ion<sup>-</sup>, neutrals) cryogenic mass-spectrometer (Arnold et al., 1977): These (daytime) measurements (at 78 and 90 km) revealed that MSPs are charged negatively. An essential step to reliable robust measurements was made by developing the Faraday-Cup technique (Havnes et al., 1996). A sophisticated version of the Faraday-Cup, the ECOMA-instruments, measures charged and neutral MSPs (Rapp and Strelnikova, 2009). Another concept, with a coarse mass resolution of 5 mass-bins, is used by the MASS (Mesospheric Aerosol Sampling Spectrometer) instrument (Robertson et al., 2009, 2014). A recent review of in situ MSP measurements is given by Baumann et al. (2013), see Fig 2.9. Additionally, Friedrich et al. (2012) showed that MSPs are an important charge carrier in the D- and lower E-region.

In situ measurements of MSP, however, remain challenging due to aerodynamic effects on the instruments of the supersonic flight (e.g., Horányi et al., 1999; Gumbel, 2001a; Hedin et al., 2007; Strelnikova et al., 2009; Staszak et al., 2017). This is why measurements shown in Fig 2.9 are restricted to altitudes above a lower cut-off around 75–85 km. The majority of PMWE is observed in this altitude range. Other evidence for MSP existence came from radar techniques. Strelnikova et al. (2007) and Rapp et al. (2007) both showed that charged MSPs exist by analyzing the spectral form from IS radar data. Moreover, these authors state that MSPs should have sizes >0.5 nm to be able to significantly influence (by narrowing) radar spectral width (Rapp et al., 2007).

Another argument that supports the role of MSP in radar echo formation is the so-called heating experiment (Kavanagh et al., 2006; La Hoz and Havnes, 2008; Kero et al., 2008; Havnes et al., 2011). Similar experiments were also applied for PMSE studies (e.g., Chilson et al., 2000; Belova, 2003; Chen and Scales, 2005; Biebricher and Havnes, 2012; Senior et al., 2010, 2014). The essence of these experiments is summarized as follows: While an MST or IS radar observes radar echo (e.g., PMWE), a high frequency (HF) radio wave transmitter radiates into the observational volume, thereby heating free electrons. This

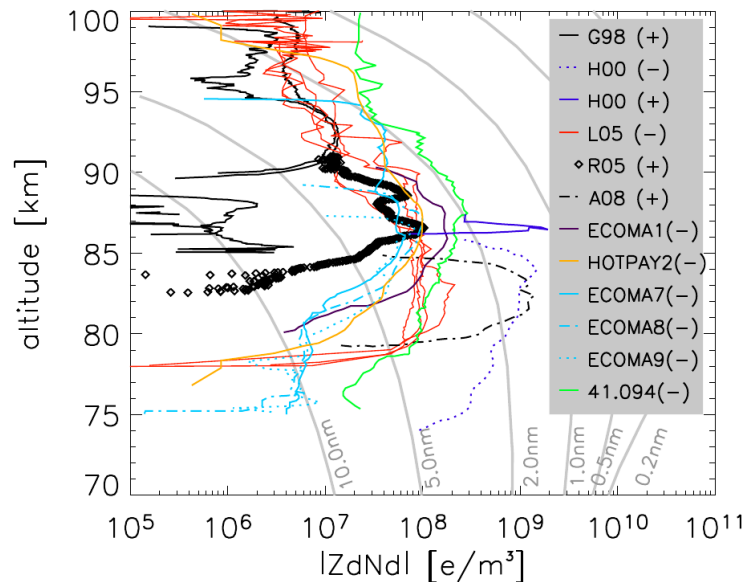


Figure 2.9. In situ MSP density measurements during nighttime, updated version from [Rapp et al. \(2007\)](#) and [Friedrich and Rapp \(2009\)](#), gray contours show MSP number densities after [Hunten et al. \(1980\)](#). Measurement details to be found in [Baumann et al. \(2013\)](#). Reprinted from [Baumann et al. \(2013\)](#).

heating drastically enhances the diffusive properties of the electrons, and, subsequently, the echo disappears. When the heater is switched off, the echo appears again with an even stronger amplitude. By switching the heater on and off and precisely measuring the change of echo intensity in time, it is possible to make conclusions on the diffusive properties of the plasma (e.g., [Rietveld et al., 1993](#); [Chilson et al., 2000](#)). Thus, [Belova et al. \(2008\)](#), [Kero et al. \(2008\)](#), [La Hoz and Havnes \(2008\)](#), [Havnes et al. \(2011\)](#) concluded that only the presence of charged MSP could explain the results of the PMWE heating experiment. Since MSP are immersed in the ionospheric plasma, a part of them becomes charged (e.g., [Chen, 2016](#); [Shukla, 2001](#); [Shukla and Mamun, 2015](#)). Three major charge mechanisms can be identified:

- Attachment of negative ions ( $\text{ion}^-$ ), free electrons ( $e^-$ ), or positive ions ( $\text{ion}^+$ ), ([Rapp, 2000](#))
- Detachment and emission of photo-electrons from neutrals and negative MSP, ([Knappmiller et al., 2011](#))
- Secondary electron emission induced by energetic electrons from the magnetosphere, ([Baumann et al., 2016](#))

The attachment mechanism based on collisions is dominant in the lower part of the ionosphere (e.g., 60 km), whereas other means become more critical at higher altitudes. Since the plasma in the lower ionosphere is only weakly ionized and highly collisional, neutral flow controls the overall motion. As a consequence, global-scale models, including charged MSPs, might reveal a higher concentration of larger MSPs at the winter poles

(Megner et al., 2006). This is simply explained by transport within global residual circulation in the mesosphere towards winter poles. Larger MSPs also have a larger collision cross section and therefore are transported more effectively. On small scales, the charged portion of MSP and ions are coupled to electrons through Coulomb-forces, controlling electron's mobility, i.e., diffusivity  $\propto D_e$  (e.g., Chen, 2016). Naturally, these MSP and ions are also dominated by the neutral flow.

The ratio of “diffusion of momentum” ( $\alpha\nu$ ), brought by the neutrals, to the diffusion of electrons ( $\propto D_e$ ) is quantified by the Schmidt number  $Sc$  (see Eq. 2.40). It is believed that inert charged MSP lower the diffusion coefficient  $D_e$  and subsequently increase  $Sc$ . In contrast, a decrease of  $Sc$  can be expected, if  $D_e$  increases. This might be the case if much more negative constituents (i.e., electrons, ion<sup>-</sup>) are abundant to effectively shield the influence of MSP.

The  $Sc$  number is quantified by comparison of turbulent spectra of electron- and neutral-density fluctuations (see Sec. 2.2.2). Subsequently, one can use this  $Sc$  number to estimate an effective mean MSP radius.

Based on the theory by Cho et al. (1992), Asmus et al. (2017) derived the mean radii (and the size distribution) from in situ soundings in the winter mesosphere, and extracted mean radii of 0.1–0.8 nm (i.e.,  $1 \lesssim Sc \lesssim 7$ ).

### 2.3.6 Viscous waves

Radar echo observations were made on various latitudes in the tropo- and mesosphere with properties contradicting the explanation that echoes origin from isotropic turbulence: slow fading (Röttger and Liu, 1978), narrow spectra (Hocking et al., 1991), aspect sensitivity (Czechowsky et al., 1989; Czechowsky and Ruster, 1997), and observation of active turbulence nearly exclusively in the upper part of radar echoes in summer ( $\geq 85$  km) (Rapp and Lübken, 2003).

The proposed mechanism includes GWs propagating into the atmosphere and partially refracting on critical levels, e.g., on rapid changes in the Buoyancy frequency or winds. As a result of this refraction, viscosity waves are formed with a wavelength on Bragg scale. These waves are heavily dampened by viscous effects and therefore die out after approximately one wavelength. The viscosity waves ultimately form a very thin layer that is highly visible for radar and –as discussed within the theory of partial reflection, see Sec. 2.1.5– could explain observations made in the troposphere at  $\sim 50$  MHz and mesospheric echoes, observed by 2 MHz radar systems. However, GWs as a source to create radar echoes at 50 MHz fails since much shorter vertical wavelength are necessary (Hocking et al., 1991). Subsequently, this theory was modified (Hocking, 2003) to also explain VHF radar observations in the mesosphere at higher frequencies. This modification led to the exclusion of Buoyancy waves since the resulting wavelength (tens of meters) does not fulfill the Bragg condition ( $\lambda_{BC} \sim 3$  m) and therefore is not detectable at 50 MHz. Instead, temperature steps with a depth of  $\sim 100$  m were introduced as an effective “critical layer”. It was speculated that infrasound waves with periods of 1–10 s (corresponding to 300 m–3 km wavelength), (partially) reflecting on temperature steps, could induce viscosity waves on scales of meters. These waves are heavily dampened by viscosity and therefore evanescent within  $\sim 1$  period. Moreover, they can only propagate in absolute laminar conditions, as additional

turbulence would diffuse these waves rapidly.

The main characteristics of this viscosity wave mechanism are briefly summarized below (Hocking et al., 1991; Hocking, 2003):

- vertical extent  $\sim 1/8 - < 1/2$  of radar wavelength (scattering structure)
- horizontal extent over at least on Fresnel zone, cf. Eq. 2.30 (scattering structure)
- pre-existing temperature gradient needs to occur over scales smaller than vertical wavelength of the incident wave, e.g., in the order of  $\sim 100$  m depth (infrasound wave – viscous wave interaction layer)
- viscous waves can only exist in laminar regions

If a wave (e.g., infrasound), described by momentum equations, passes a “critical” layer, the viscous term of momentum equations for small vertical wavelength becomes dominant:

$$\begin{aligned}\frac{\delta u'}{\delta t} &= \nu \nabla^2 u' \\ \frac{\delta w'}{\delta t} &= \nu \nabla^2 w'.\end{aligned}\tag{2.46}$$

With velocity perturbations in horizontal and vertical directions,  $u'$ ,  $w'$ , and kinematic viscosity  $\nu$ ,  $\nabla^2$  denotes the second derivative of horizontal and vertical space,  $\delta^2/\delta x^2$  and  $\delta^2/\delta z^2$ , respectively. Solving Eq. 2.46 with wave ansatz  $u' = u_0 \cdot \exp\{i(kx + mz - \omega t)\}$  for the vertical wavelength  $\lambda_z = 2\pi/m$ , provides the connection of incoming infrasound wave frequency  $\omega$ , or period  $T$ , and the background viscosity  $\nu$  to the resulting viscous wave vertical wave length:

$$\lambda_z = 2\sqrt{\nu \cdot Sc^{-1} \cdot T}.\tag{2.47}$$

Where  $Sc$  is the Schmidt number which is unity for viscous,  $Sc < 1$  for diffusive, and  $Sc > 1$  for the convective case. In consequence, to obtain the same  $\lambda_z$  (e.g., fulfilling Bragg condition) a shorter period  $T$  is needed for  $Sc \ll 1$  or a longer period  $T$  for  $Sc \gg 1$  (see, Kirkwood et al., 2006, for discussion). The solution of full momentum equations, plus the incompressible continuity equation, again using a wave ansatz delivers a relation of density perturbation with respect to vertical and horizontal wavenumber  $m$ ,  $k$ , respectively:

$$\frac{\rho'}{\rho_0} \approx \frac{i\omega}{g} \left[ 1 + \frac{i\nu}{\omega} (m^2 + k^2) \right] \text{ for } m \gg k,\tag{2.48}$$

where  $g$  denotes acceleration by gravitation and  $i = \sqrt{-1}$ . Further, an approximation for the expected electron density deviation  $N'$  is formulated by consideration of a vertical displaced parcel by a wave acting on a background potential electron density gradient  $M_e$ , (see Eq. 2.12):

$$N'_e = -\frac{w'}{i\omega} \cdot M_e = \frac{u'k}{im\omega} M_e\tag{2.49}$$

Eq. 2.49 relates velocity fluctuations  $u'$  and  $w'$  to the electron density deviation. And it is further used to derive effective reflection coefficient  $R$ .  $R$ , in turn, is used to calculate

the expected received power by radar (see Sec. 2.1.5). For the D-region (at 70 km) typical values of  $\sim M_e = 2 \cdot 10^4 - 2 \cdot 10^5 \text{ m}^{-4}$ ,  $v = 0.1 \text{ m}^2 \text{ s}^{-1}$ , and the Bragg wavelength for 2 MHz radars ( $\lambda_{\text{BC}} = 75 \text{ m}$ ), near-horizontal wavefronts (tilt  $1^\circ$ ,  $k/m = 0.02$ ), and a horizontal velocity  $u' = 1 \text{ ms}^{-1}$  reveal an electron density deviation  $N_e'$  between  $0.2 - 0.6 \text{ cm}^{-3}$ , or  $0.2 - 0.25\%$  in relative terms of fluctuations. Hocking (2003) noted that there was an error in the calculations reported by Hocking et al. (1991). Therefore, the values above were updated using the same sources, see Ap. A. These values reveal a reflection coefficient  $R$  of  $\sim 6 \cdot 10^{-7} - 1.6 \cdot 10^{-6}$  for 2 MHz radars and are below or at the lower limit of typical values<sup>2</sup> of  $R = 10^{-6} - 10^{-4}$ , reported by Hocking et al. (1991) and references therein. This example assumes GWs as the primary wave, subsequently producing viscous waves, and can only explain the observation of echoes for the lower VHF (i.e.  $\sim 2 \text{ MHz}$ ) regime. For higher radar frequencies, values of  $R$  are even lower, i.e.,  $\sim 10^{-11} - 10^{-10}$  for 53 MHz and  $\sim 10^{-13} - 10^{-12}$  for 224 MHz. Hocking (2003) proposed that infrasound waves with periods of 1–10 s could be sufficient to create viscous structures on respective Bragg scales, but this has not been proven quantitatively (cf. Hocking, 2003).

Kirkwood et al. (2006) applied the proposals of infrasound viscosity wave interaction by Hocking et al. (1991) and Hocking (2003) to explain simultaneous measurements of PMWE by ESRAD (52 MHz) and EISCAT (224 MHz). Some data presented to support the viscous wave approach could also be interpreted as an indicator for turbulence, e.g., spectral broadening inside the echo, compared to outside. Also, it is questionable if spectral-width histograms (revealing a broader spectrum outside of PMWE than inside) are well comparable since sampled volumes (i.e., altitude spans) are quite different. The most striking aspect in the argumentation for the existence of viscosity waves is the extremely high horizontal drift velocity of  $300 - 500 \text{ m s}^{-1}$ , derived by the Full Correlation Analysis (FCA) method (e.g., Briggs, 1984). However, even though the coherence between Saura-radar (3.17 MHz) Doppler wind profile and ESRAD winds is strong over the largest part of the observed altitude range, Saura observations in the range where ESRAD yields extremely high velocities (in a range of  $\sim 300 \text{ m}$  at  $\sim 67.8 \text{ km}$ ), does not observe such large winds. Measurements from Saura rather reveal a smooth profile with similar values above and below  $\sim 67.8 \text{ km}$ .

## 2.4 Conclusions and Hypotheses

At the beginning of this chapter (Sec. 2.1), the mechanisms of radar scattering relevant for PMWE investigation were recapitulated. It has been shown that it is the quantity of the potential refractive index  $M_n$  that should be used, as long as neutral dynamical processes, related to vertical motions of air, are considered to be responsible for the coherent radar echo formation.

Generally, radars are sensitive on scales fulfilling the Bragg condition. Received signals are either uncorrelated in phase (incoherent scatter, IS) or correlated in phase and persist over a certain time period (coherent scatter), allowing for averaging techniques, and therefore are detectable also with relatively low-powered MST-radars, cf. Sec. 2.1.3. These persisting structures could be explained either by volume scattering from periodic structures,

<sup>2</sup> calculation of  $R$  is given in Ap. A.

constructively interfering at Bragg scale, see Sec. 2.1.4, or partial reflection of radar waves on a thin layer of drastic change in the potential refractive index, described in Sec. 2.1.5.

In the last part of this chapter, current investigations of PMWE were briefly reviewed, and main findings were recapitulated. Statistically, PMWE most often occur during the daytime, around local noon in an altitude range between 55–83 km, with annual enhanced occurrence rates during March and April, and also at the end of September and October, see Sec. 2.3.1.

It was shown that the background given by electron density, neutral density and temperature is crucial for PMWE observations, but is often unknown due to the lack of simultaneous measurements of PMWE and the full background. In fact, none of the previous studies draws a complete picture of the background state, thus falling back on model parameters or “typical-value” estimates, not to mention simultaneous measurements of fluctuations on radar Bragg scale. Whilst the importance of background is common sense, the possible formation mechanism to create structures of refractive index (i.e., electrons in MLT) is under debate. Two lines of argumentation exist.

The first one is based on volume scattering and introduces turbulence as a formation mechanism: Turbulence was shown to be a key player in the formation of radar echoes in the troposphere (e.g., Ottersten, 1969a; Nastrom and Gage, 1985) and the summer mesosphere (e.g., PMSE Rapp and Lübken, 2004). Inserting a spectral model similar to the one of Eq. 2.39 into Eq. 2.28 reveals the volume reflectivity  $\eta$  as a function of radar wavenumber  $k$ , see Fig. 2.10.

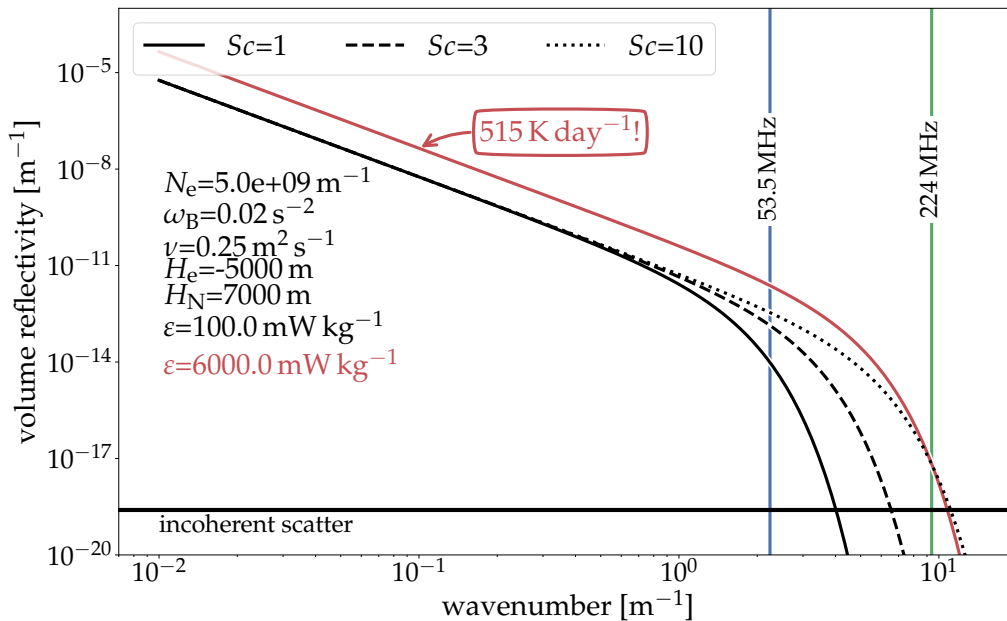


Figure 2.10. Volume reflectivity  $\eta$  for theoretical turbulent spectra (ordinate), as a function of wavenumber (abscissa). The horizontal black line indicates the value for incoherent scatter at a given  $N_e$ , cf. Eq. 2.22. The vertical lines mark wavenumber for Bragg condition on 53.5 MHz and 224 MHz. Turbulent spectra for typical values of atmospheric background and turbulence are given by black curves for  $Sc=1, 3,$  and  $10$ . The red graph shows hypothetical case of  $\epsilon=6 \text{ W kg}^{-1}$  and  $Sc=1$ .

Examples in Fig. 2.10 show spectra for typical background conditions at  $\sim 75$  km for  $Sc=1, 3, 10$ . In the case of  $Sc$  around unity, electrons are supposed to be directly bound to ions, which are collisionally coupled to the flow. As shown in Sec. 2.3.4, neutral turbulence can explain PMWE observations with radar systems  $\sim 50$  MHz, i.e.,  $\sim 3$  m Bragg scale, or  $k \approx 2$ . Also, the example of Fig. 2.10 shows  $\eta = 10^{-14} - 10^{-15} \text{ m}^{-1}$  at  $k \approx 2$  (vertical blue line). This leads to the formulation of hypothesis H1.1.

Observations of PMWE at a higher frequency, i.e., 224 MHz, corresponding to  $\lambda_{BC} \approx 0.7$  m or  $k \approx 9$ , reveal that applying hypothesis H.1 does not provide a possible explanation for the same “typical background” conditions, see Sec. 2.3.4. For typical background conditions, a turbulent dissipation rate of  $\epsilon = 6 \text{ W kg}^{-1}$  is necessary to explain observations at 224 MHz by pure turbulence. Ultimately resulting in a heating of  $> 500$  K per day, where an order of 10 K per day would be realistic.

This complication can be solved, if MSPs are taken into account. Numerous in situ experiments have repeatedly obtained MSP densities of  $10^7 - 10^9 \text{ m}^{-3}$  in the winter mesopause region (see, e.g., [Baumann et al., 2013](#), for a recent review). These heavy and inert particles could sufficiently lower the electron diffusion and subsequently enhance  $Sc$  (cf. Sec. 2.3.5). The effect of reduced diffusivity to the (electron density) spectrum is shown as dashed and dotted black lines in Fig. 2.10. Obtained by means of typical background conditions, nominal  $\epsilon$  and  $Sc$  correspond to a MSP size of  $\sim 1$  nm. Moreover, MSP are a natural plasma constituent in the mesosphere and compulsorily affect turbulence spectrum. These assumptions provide the basis to formulate hypothesis H1.2.

Summarizing the previous argumentation, the first branch of hypothesis is formulated, claiming that structures of turbulence are responsible for the PMWE.

### Hypothesis 1:

Small-scale structures in the refractive index were formed by the action of turbulence.

H1.1: Irregularities in the refractive index, which is nearly solely defined by electron density, are linked to neutral-density irregularities, caused by turbulence, through ions<sup>+</sup>.

H1.2: The coupling of the neutral and electron density field is indirect. Through heavy charged aerosols (e.g., MSP) the diffusivity of electrons is sufficiently altered. This ultimately leads to fluctuations at much smaller scales as those of neutral density.

The second hypothesis introduces a different dynamical mechanism, resulting in partial reflection. This alternative mechanism is fostered by characteristics, seemingly contradicting theories of isotropic turbulence, and introduces an infrasound wave–viscosity-wave–interaction on layers of sharp temperature steps with  $\sim 100$  m vertical extent, explained in detail in Sec. 2.3.6. The resulting rapidly-evanescent viscosity waves are thought to create structures on Bragg scale, with fast horizontal drift velocities of  $300 - 500 \text{ ms}^{-1}$ . Conse-



quently, hypothesis H2 is formulated to be proven within this thesis:

**Hypothesis 2:**

H2: Small-scale structures in the refractive index are formed by viscosity waves, generated by the reflection of infrasound waves on steps of temperature.

## 3 | Analysis methods

This section is dedicated to the discussion of analysis methods in order to deduce geophysical parameters. In the first part (Sec. 3.1), two different ways to derive turbulent parameters from radar measurements are given since these observations deliver time-resolved measurements. Only the relative change of these radar measurements will be used later on since absolute values of derived  $\varepsilon$  are relatively uncertain compared to in situ measurements. Turbulent parameters from in situ measurements are based on the spectral method described in section (3.2). The most relevant parameters deduced from this method are the energy dissipation rate  $\varepsilon$ , the  $Sc$  number, and the variance dissipation rate  $\chi$ , defined mainly by the atmospheric background. Subsequently, an approach to derive ( $Sc$ -equivalent) MSP radii in Sub. 3.3 is given, mainly to illustrate the more abstract quantity of  $Sc$ . Key points of this analysis were shown by [Staszak et al. \(2021\)](#) and are discussed here in more detail. After that, methods are introduced to derive absolute background densities of electrons (Sec. 3.5) and neutrals (Sec. 3.4). The measurement of absolute density is crucial, also since other parameters, e.g., temperature, viscosity, and buoyancy frequency, are derived from the absolute density profile. To obtain an absolute density measurement, the instruments are calibrated in the laboratory with a reference sensor. Moreover, the effect of aerodynamics is corrected by means of computational flow simulations. The general procedure to derive absolute density is introduced in the text, whereas a detailed discussion of uncertainties can be found in the appendix (Ap. C). Finally, two methods to derived volume reflectivity are introduced. First, a method based on a spectral model is formulated by using input parameters from in situ measurements. Then, a technique to derive volume reflectivity directly from fluctuations of electron density is presented. Both methods enable a direct comparison between in situ measurements and radar observations.

### 3.1 Turbulence from radar measurements

Turbulent parameters, particularly the turbulent energy dissipation rates  $\varepsilon$ , can be derived from radar measurements by different methods. One uses the back-scattered power; the other utilizes spectral broadening of the received signal.

#### 3.1.1 Power method

For the power method (described in [Hocking, 1985](#)), a three-dimensional description of the inertial subrange of the turbulence spectrum  $\Phi$  is related to the volume reflectivity  $\eta$

(see Eq. 2.28). The spectrum  $\Phi$  includes the structure-function constant  $C_\xi$ , which is connected to  $\varepsilon$  through the outer scale of turbulence  $L_0$ . Since the received power of a radar depends on the volume reflectivity, a mean dissipation rate  $\bar{\varepsilon}$  inside the volume, spanned by the cross area of radar cone and pulse length  $\Delta V$ , can be derived. However, this method has some substantial drawbacks:

1. Radar Bragg scale  $\lambda_{BC}$  must be within the inertial subrange, which is often not the case for altitudes above 60 km.
2. Several uncertainties were introduced by approximation of  $Ri$  (Richardson number), often taken as  $Ri = Ri_{crit} = 1/4$ , and taking “typical” values of  $\omega_B$  (e.g.,  $0.02 \text{ s}^{-1}$ ), but are known to be highly variable due to the action of, e.g., GW. Note that  $\bar{\varepsilon} \propto \omega_B^3$  and  $\bar{\varepsilon} \propto Ri^{-3/2}$ .
3. Values of scale heights  $H_N$ ,  $H_e$ , and absolute electron density  $N_e$  are required, though often not measured and taken from models instead. These quantities are connected to  $\bar{\varepsilon}$  via the potential refractive index gradient  $M_n$  (Eq. 2.12), where  $\bar{\varepsilon} \propto M_n^2$ .
4. A further challenge is that only a mean dissipation rate is measured inside the volume. Turbulence, however, often has a patchy nature of layers with relatively thin vertical and large horizontal extent. Therefore, the volume without any turbulence contributes to the mean. This circumstance is considered by introducing a beam-filling factor  $F$ . However, this factor can be only estimated imprecisely and subsequently introduces further uncertainties, with  $\bar{\varepsilon} \propto F^{-1/2}$ .

### 3.1.2 Spectral width method

Another approach is to use the spectral-broadening effect of turbulence to overcome the difficulties that come with the power method (Hocking, 1983, 1985). The core of this concept is the connection between spectral broadening and root mean velocity fluctuations caused by turbulence. The mean velocity fluctuations  $\overline{v'^2}$  on scales  $> l_{BC}$  or wavenumbers  $< k_{BC}$  can be observed by radar. By considering a theoretical turbulence spectrum, a connection to  $\overline{v'^2}$  can be made via integration from  $k_{BC}$  to the largest scales of turbulence, at a wavenumber denoted by  $k_B$ :

$$\frac{1}{2} \overline{v'^2} = \int_{k_B}^{k_{BC}} E(k) dk + \int_{-k_{BC}}^{-k_B} E(k) dk. \quad (3.1)$$

Integration for  $E(k) \propto \varepsilon^{2/3} k^{-5/3}$  (inertial sub-range) reveals a relation between  $\overline{v'^2}$  and the turbulence dissipation rate  $\varepsilon$ :

$$\varepsilon \simeq c_L \overline{v'^2}^{3/2} / \left( L_B^{2/3} - \lambda_{BC}^{2/3} \right)^{3/2} \stackrel{L_B \gg \lambda_{BC}}{\simeq} c_L \overline{v'^2}^{3/2} / L_B, \quad (3.2)$$

with the constant  $c_L \approx 3.5$  (Hocking, 1985). Applying the definition for the “outer scale”  $L_B$ , Eq. 3.2 forms to:

$$\varepsilon \simeq c_\omega \overline{v'^2} \omega_B. \quad (3.3)$$

With the constant  $c_\omega \approx 0.4 \dots 0.49$  and buoyancy frequency  $\omega_B$  (Hocking, 1983). The “outer scale”  $L_B$  determines the transition between inertial and buoyancy subrange, was established by Weinstock (1978), and is identical to the buoyancy scale (see Eq. 2.34). Since it

differs from the commonly-known outer scale by [Tatarski \(1971\)](#). [Hocking \(1983, 1985\)](#) derived a relationship between both scales:  $L_o = 0.035 \cdot L_B$ . [Weinstock \(1981\)](#) used  $L_B$  as the integration limit for studies in stratified turbulence.

Note that within this method, it is also assumed that  $\lambda_{BC}$  lies inside the inertial subrange of turbulence. But in contrast to the power method, an integral with bounds from  $\lambda_{BC}$  to  $L_B$  is applied. Since the contribution of energy from small scales is much less than that from larger scales, this method should be applicable, if  $\lambda_{BC}$  is not too far inside the viscous sub-range. A correct choice of the outer scale is much more important, since it contains the majority of energy.

Considering an appropriate measure of  $\overline{v'^2}$ , considerable uncertainties are introduced by the choice of  $c_\omega$  and  $\omega_B$ , if absolute values of  $\varepsilon$  are concerned. The mean fluctuations can be estimated by the Doppler-radar technique using the HPHW (half-power half-width) frequency  $f_{HPHW}$ :

$$\overline{v'^2} = \lambda_{BC}^2 f_{HPHW}^2 / 2 \ln 2 \quad (3.4)$$

The spectral width is not only defined by turbulent velocity fluctuations but rather by a sum of different contributions from gravity waves, wind shears, and beam geometry (see, e.g., [Hocking, 1983](#), for discussion). The most important effect on the studies presented here has the beam broadening, i.e., even a vertically directed radar beam with a width  $\gtrsim 2^\circ$  obtains Doppler contributions from horizontal moving structures. Shear broadening can be a major contributor for tilted beams and large observation volumes  $\Delta V$ . For zenith beam observations it therefore does not play a major role in non-turbulent contributions. Additionally, MAARSY has a particularly narrow beam ( $3.6^\circ$ , see Sec. 4.1) that shrinks the observation volume and is therefore beneficial for turbulence analysis. The contribution of vertical r.m.s. from, e.g., GW could be viable if the resolution is worse than  $L_B$ . Suppose one is only interested in the relative value  $\varepsilon_{rel}$  instead of absolute  $\varepsilon$  values and the contribution of a non-turbulent mechanism can be assumed to be negligible, the following relation can be used:

$$\varepsilon_{rel} \propto f_{HPHW}^2 \quad (3.5)$$

Assuming that spectral broadening, quantified by  $f_{HPHW}$ , is mainly due to turbulence, the spectral width correlates with the received power. This is due to the reasons given by the explanation of the power method and maybe becomes more vivid considering the examples of spectra for different turbulence strength shown in Fig. 2.10.

## 3.2 Turbulence from rocket measurements: The spectral model technique for scalar tracers

[Lübken \(1992\)](#) developed a method to derive the energy dissipation rate  $\varepsilon$  by fitting a model to the measured spectrum of scalar quantities. Tracers used for the spectral model technique are density fluctuations of neutrals, electrons, ions, and charged aerosols (e.g., [Asmus, 2018](#), and references therein).

The energy dissipation rate is directly obtained from the inner scale  $l_0$ , i.e., the transition scale between inertial and viscous subrange. The advantage of this approach is that the

normalization of the spectrum does not affect the results for  $\varepsilon$ . In other words, there is no need for precise measurements of absolute values of fluctuations.

A significant assumption allowing the connection of spectral models of turbulence to the measurements is the frozen-field hypothesis, which is shortly explained hereafter. The spectral models used in the data analysis are also described subsequently. This includes descriptions of the models for neutral density fluctuations and models for the application of electron density.

### 3.2.1 Spectral Models

#### Frozen field

Since turbulence measurements are often records of single-point measurements over a time period, where either the turbulent field passes the sensor or the sensor passes the turbulent field, the Fourier-transformed record depends on frequency  $\omega$  and not wavenumber  $k$ . Taylor (1938) formulated the connection between wavenumber-dependent and frequency-dependent spectrum,  $E(k)$  and  $W(\omega)$ . To derive  $W(\omega)$ , Lübken (1993) used the following equation (see Tatarski, 1971):

$$W(\omega) = 2\pi/v_R \int_{|\omega|/v_R}^{\infty} \Phi(k)k dk \quad (3.6)$$

Where  $\Phi(k)$  is the 3D spectrum and  $v_R$  is the sensor velocity, i.e., the rocket's velocity in this case. Thereby, the frozen-field, or frozen-turbulence, hypothesis was introduced, which can be applied, if the relative velocity of the sensor  $v_R$  is large compared to the turbulent velocity  $v_{\text{turb}}$ , i.e.,  $v_R \gg v_{\text{turb}}$ . Thus, it is assumed that turbulence patterns remain unchanged during the measurement, which is a good approximation for typical values of  $v_R \approx 1000 \text{ m s}^{-1}$  and  $v_{\text{turb}} \approx (v\varepsilon)^{-1/4} \approx 1 \text{ m s}^{-1}$ .

#### Heisenberg model

A first model used in the following work is referred to as the Heisenberg (H) model (Heisenberg, 1948). Originally it was formulated for velocity fluctuations. The model was adapted for the use of scalar tracers by Lübken (1993) and can be identified with Eq. 2.39 with  $\varphi = \varphi(k, \eta_{\text{Kol}}) \propto k^{-7}$ . The complete formulation for the 1D spectrum is given by Lübken et al. (1993):

$$W(\omega) = \frac{\Gamma(5/3)\sin(\pi/3)}{2\pi v_R} \cdot a^2 \chi_\theta \varepsilon^{-1/3} f_\alpha \frac{(\omega/v_R)^{-5/3}}{\left(1 + [(\omega/v_R)/k_0]^{8/3}\right)^2} \quad (3.7)$$

Where  $\omega$  is the cyclic frequency,  $\chi_\theta$  is the variance dissipation rate,  $\Gamma$  stands for the gamma function, and  $f_\alpha$  and  $a^2$  are numerical constants, chosen to be 2 and 1.74 (Lübken et al., 1993). The wavenumber  $k_0$  denotes the transition scale  $l_0$ ,  $k_0 = 2\pi/l_0$ . The relation of  $l_0$

and  $\eta_{\eta_{\text{Kol}}}$  is crucial for the derivation of  $\varepsilon$  and is given by:

$$l_0^{\text{H}}/\eta_{\text{Kol}} = 2\pi \left( \frac{9f_\alpha a^2 \Gamma(5/3) \sin(\pi/3)}{16Pr_{\text{N}}^{\text{mol}}} \right)^{3/4} = 9.9. \quad (3.8)$$

This relation was derived by investigation of the behavior of the structure function around its origin and the relation to the spectrum and therefore is model dependent. Hence, the inner scale for the H model is betoken by  $l_0^{\text{H}}$ . This scale further depends on the dimensionless number  $Pr_{\text{n}}^{\text{mol}}$ , called molecular Prandtl number. If the scalar tracer is number density (N),  $Pr_{\text{N}}^{\text{mol}}$  is defined as the ratio of kinematic viscosity to the molecular diffusion coefficient and, hence as  $Pr_{\text{N}}^{\text{mol}}=0.83$  for diatomic gases (see [Lübken, 1993](#), and reference therein).

### Tatarski model

Another model is based on the work of [Novikov \(1961\)](#), described in [Tatarski \(1971\)](#), finally used for the spectral model technique by [Lübken \(1992, 1997\)](#) and referred to as the Tatarski model. The 1D formulation is:

$$W(\omega) = \chi_\theta \tilde{\varepsilon}^{-3/4} \left( \frac{2\pi}{v_{\text{R}}} \right) b^{5/6} \int_{|y|}^{\infty} y^{-8/3} \exp(-y^2) dy \quad (3.9)$$

where the normalized dissipation rate is defined by  $\tilde{\varepsilon}=\varepsilon/A^3$  with a constant  $A=0.033a^2$  ( $a$  was defined before). The integration variable  $|y|$  is given by:

$$|y| = k/k_{\text{m}}. \quad (3.10)$$

Other parameters and constants are condensed in variable  $b$ , obtained by:

$$b = \{3f_\alpha \pi \Gamma(5/3)\}^{3/2} \cdot \left( \frac{\nu}{Pr_{\text{N}}^{\text{mol}}} \right)^{3/2}. \quad (3.11)$$

The constant  $f_\alpha$ ,  $\Gamma(5/3)$ , kinematic viscosity  $\nu$ , and molecular Prandtl number were defined before. Wavenumber  $k_{\text{b}}^2=\varepsilon^{1/2}/b$  is the wavenumber where the transition from inertial (-convective) to viscous (-diffusive) subrange occurs. The corresponding inner scale  $l_0^{\text{T}}$  is related to the micro scale  $\eta_{\text{Kol}}$  via:

$$l_0^{\text{T}}/\eta_{\text{Kol}} = 2\pi \left\{ \frac{3f_\alpha a^2 (5/3) \Gamma(5/3)^2 \sin(\pi/3)}{4\pi Pr_{\text{N}}^{\text{mol}}} \right\}^{3/4} = 7.06, \quad (3.12)$$

derived similarly to Eq. 3.8.

### Driscoll and Kennedy model

Another spectral model is needed to analyze electron density fluctuations since the  $Sc$  number of electron density fluctuations can substantially differ from unity. For  $Sc > 1$ , an additional subrange emerges intermediate the inertial (-convective) and the viscous (-diffusive)- subranges (see Sec. 2.2.2). A model description was given by [Driscoll and Kennedy \(1985\)](#) and subsequently modified for use with in situ measurements, applying Eq. 3.6 and normalization ([Giebeler, 1995](#)). The resulting normalized spectra is given by:

$$W^{D\&K}(y) = \frac{1}{2v_R} A_1 \beta \epsilon_\theta \epsilon^{-1/3} \eta_{Kol}^{5/3} \cdot \int_y^\infty (y^{-8/3} + y^{-2}) \cdot \exp \left\{ A_{3\theta} \left( \frac{3}{2} y^{4/3} + y^2 \right) \right\} dy$$

with :

$$\begin{aligned} y &= Q^{3/2} \eta_{Kol} \cdot k \\ A_1 &= \alpha Q^{5/2} \\ A_{3\theta} &= \frac{\alpha}{Q^2 \cdot Sc} \\ \epsilon_\theta &= \frac{4\pi \cdot A \cdot \chi_\theta}{\alpha \cdot \beta} \end{aligned} \quad (3.13)$$

With constants  $A=0.033 \cdot a^2$ ;  $a^2=1.74$ ,  $\alpha=0.83$ ,  $\beta=1$ ,  $Q=2$ , and variance dissipation rate  $\chi_\theta$ .

The inner scale is given in implicit form ([Lübken et al., 1994a](#)):

$$\frac{1}{e^2} \left( \frac{1}{y_0} + \frac{3}{5} y_0^{-5/3} \right) = \int_{y_0}^\infty \left( \frac{1}{y^2} \right) \exp \left\{ -A_{3\theta} \left( \frac{3}{2} y^{4/3} + y^2 \right) \right\} dy \quad (3.14)$$

Thus, defining the value of  $y_0$ , where the power law for slopes  $-5/3$  and  $-1$  drops by a factor of  $1/e^2$ . The relation of  $y_0$  and wavenumber  $k_0$  is given by  $y=Q^{3/2}\eta_{Kol}\cdot k$ . Finally, by conversion to inner scale  $l_0^{D\&K} = 2\pi/k_0$ , the inner scale of the Driscoll&Kennedy (D&K) model can be derived by:

$$l_0^{D\&K} / \eta_{Kol} = 6.66. \quad (3.15)$$

### 3.2.2 Data processing

For extraction of turbulent parameters from density measurements, the data must be reduced to residuals, transformed into frequency space, normalized, and finally a spectral turbulence model is fitted to the measured spectrum.

#### Residuals

Currents obtained by electrostatic probes (e.g., [Blix et al., 1990](#)) and ionization gauges ([Giebeler et al., 1993](#)) are proportional to the local number density of the measured species

since sensor sensitivity, and aerodynamic effects are supposed to vary only slowly with altitude (e.g. Hillert et al., 1994). Residuals  $r(t)$  are derived by:

$$r(t) = \frac{\Delta N_\theta(t)}{\langle N_\theta \rangle} = \frac{I(t) - I_{\text{mean}}(t)}{I_{\text{mean}}(t)}, \quad (3.16)$$

where  $\Delta N_\theta(t)$  is the difference of actual density to the mean density  $\langle N_\theta \rangle$ . The actual current is denoted by  $I(t)$  and the mean current by  $I_{\text{mean}}(t)$ . This mean is derived either by a polynomial fit (e.g., Lübken, 1992, Hillert et al., 1994) or running average technique (e.g., Blix et al., 1990). An example of this conversion is shown in Fig. 3.1, with measured  $I(t)$  and fitted  $I_{\text{mean}}(t)$  on the left panel and extracted residuals on the right panel.

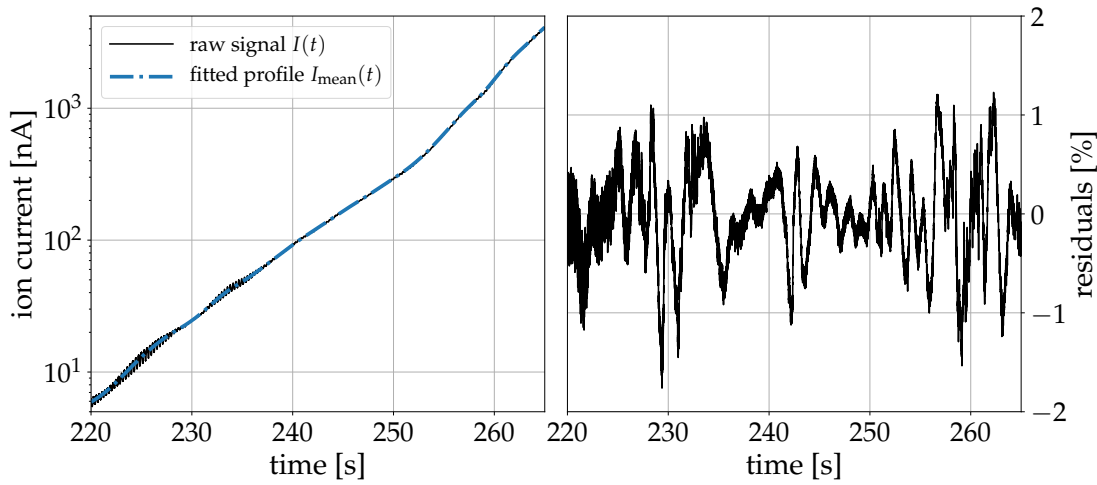


Figure 3.1. Left panel shows the measured ion current  $I(t)$  (black line) over the rocket flight time. Mean ion current  $I_{\text{mean}}(t)$  is shown as blue graph. The right panel exposes extracted residuals  $r(t)$  from the conversion given in Eq. 3.16

Residuals of current can be applied directly for spectral analysis. However, measurements typically contain signatures of the rocket spin. Since this spin frequency is stable (e.g.,  $\sim 3.5$  Hz) and well known from position measurements onboard rocket, it can be filtered by applying spectral filtering.

### Spectral transform

Two methods have been established for the spectral model analysis to derive time (space) resolved spectra from the residuals  $r(t|z)$ . The first is based on residual bins of  $\sim 1$  km resolution and subsequent Fast-Fourier-Transform (FFT) (Lübken, 1992). Another more recent approach uses a wavelet transform (WLT) to obtain high spatial resolution, resolving the intermittent spatial character of turbulence and its organization in thin patches in some cases (Strelnikov et al., 2003). Generally, a higher time (spatial) resolution is on the expense of frequency resolution and vice versa. Therefore, a 12<sup>th</sup> order Morlet wavelet function is chosen (Torrence and Compo, 1998, Grossmann and Morlet, 1984) as a pragmatic compromise of time (space)–frequency resolution. In each case the spectrum is



normalized, so that the variance of the time signal  $\sigma^2$  equals the area below frequency spectrum  $W(\omega)$ :

$$\sigma^2 = \int_{-\infty}^{\infty} W(\omega) d\omega \quad (3.17)$$

### 3.2.3 Derivation of turbulence dissipation rate $\varepsilon$

To obtain  $\varepsilon$ , one of the theoretical spectra, as described in the sections before, is fitted to the measured spectrum by applying a least-squares fitting procedure. One of the models of Heisenberg, Tatarski, and/or Driscoll&Kennedy is applied by using the inner scale  $l_0$  or corresponding wavenumber  $k_0$  and the variance dissipation rate  $\chi$  as free fitting parameters. From the inner scale  $l_0$ , the turbulence dissipation rate is derived using Eq. 3.8 or 3.12 to obtain the micro-scale  $\eta$  and Eq. 2.35 to ultimately calculate  $\varepsilon$ .

It was shown that results based on these models could reveal considerable discrepancies considering absolute values of  $\varepsilon$  but yield very similar vertical structures within the respective  $\varepsilon$ -profiles (Strelnikov et al., 2017, 2019, Staszak et al., 2021). In the following research all three models are applied, and discrepancies are interpreted as model uncertainties.

### 3.2.4 Variance dissipation rate $\chi$

In contrast to the energy spectrum of turbulence, i.e., derived from velocity fluctuations, the scalar spectrum, besides  $\varepsilon$ , further depends on the diffusive properties of the tracer, described by  $\chi$ , a quantity called ‘‘variance dissipation rate’’. Although this parameter is one of the free fitting parameters and thus is measured within density fluctuations, the direct use of this fitted parameter is questionable if absolute values are of interest. The main reasons for that are different techniques to obtain mean profiles to reveal the residuals  $r(t)$  and normalization of the spectrum. The latter is even more challenging with the use of WLT. If the atmospheric background, defined by  $N_N$ ,  $N_e$ ,  $\omega_B$  and ideally the horizontal wind profiles  $u$  and  $v$ , is measured simultaneously with turbulence,  $\chi$  can be calculated from these quantities. For stationary turbulence, the rates of destruction of turbulent structures by molecular diffusion and production of turbulent structures are equal. Under this consideration, a relationship for a tracer  $\theta$  can be derived (see L ubken, 1992, and references therein):

$$\chi_\theta = \frac{f_a \cdot B \cdot Ri \cdot \varepsilon}{Pr_\theta^{\text{turb}} \cdot \omega_B^2} M_\theta^2. \quad (3.18)$$

Where  $f_a=2$  is a normalization constant, chosen by L ubken (1992),  $\varepsilon$  is the turbulent dissipation rate,  $\omega_B$  is the buoyancy frequency, and the potential gradient of tracer  $\theta$  is denoted by  $M_\theta$ .  $M_\theta$  can be derived from measurements. Different potential gradients for tracers of neutrals and electrons are given by L ubken (1992), Hocking (1985) and Thrane and Grandal (1981), see also Eq. 2.44.

Further,  $B$  is the isotropy factor of turbulence:  $B=1$  for the stratified case and  $B=3$  for the isotropic case (Blix et al., 1990). The dimensionless Richardson number  $Ri$  connotes the

ratio of buoyancy forces to mechanical shear forces:

$$Ri = \frac{\omega_B^2}{\left(\frac{\delta u}{\delta z}\right)^2 + \left(\frac{\delta v}{\delta z}\right)^2}. \quad (3.19)$$

If  $Ri > 0$ , conditions are stable, whereas for  $Ri < 0$  the atmosphere is statically unstable, and turbulence is sustained by convection. Also, some observations suggest that there exists a critical limit  $Ri_{\text{crit}} = 0.25$  where strong dynamical forces can generate turbulence, even in statically stable regions (e.g., [Holton and Hakim, 2013](#)). The Prandtl number  $Pr_{\theta}^{\text{turb}}$  reveals the ratio of molecular and turbulent diffusion ( $K_{\text{mol}}$ ,  $K_{\theta}^{\text{turb}}$ , respectively) of the tracer ([Lübken, 1992](#)):

$$Pr_{\theta}^{\text{turb}} = \frac{K_{\text{mol}}}{K_{\theta}^{\text{turb}}}. \quad (3.20)$$

The determination of both characteristic numbers  $Ri$  and  $Pr_{\theta}^{\text{turb}}$  is challenging, and values were mostly taken from literature. For  $Ri$ , most values are in between 0.25 and 1, and  $Pr_{\theta}^{\text{turb}}$  values lie between 0.8 and 3 (e.g., [Hocking, 1985](#), [Blix et al., 1990](#), [Lübken, 1992](#), [Stebel et al., 2004](#), [Rapp et al., 2008](#)). However, the advantage of the spectral method described before is that the derivation of  $\varepsilon$  is independent of the absolute value of  $\chi$ , since the value of the inner scale  $l_0$  is used instead.

### 3.2.5 Derivation of the $Sc$ number

The  $Sc$  number can be derived from the comparison of spectra from neutrals and electrons. A vivid expression of this comparison is given by the relation of the smallest scales of both spectra, given by  $\eta_{\text{Kol}}$  for neutrals and  $\eta_{\text{Bat}}$  for electrons:

$$Sc^{-1/2} = \frac{\eta_{\text{Bat}}}{\eta_{\text{Kol}}}.$$

In practice, a standard technique to obtain the  $Sc$  number is the deduction of the energy dissipation rate with the model of, e.g., Heisenberg and to insert the resulting  $\varepsilon^{\text{H}}$  to the spectral model of Driscoll&Kennedy and to subsequently derive  $Sc$  ([Lübken et al., 1994a, 1998](#), [Strelnikov et al., 2009a](#), [Strelnikov and Rapp, 2011](#), [Asmus et al., 2017](#)). However, all spectral models mentioned before have their intrinsic uncertainties. To account for this and keep results comparable to investigations made before, [Staszak et al. \(2021\)](#) used two different models (Heisenberg, Tatarski) to derive  $\varepsilon^{\text{H,T}}$  as input for the model of Driscoll&Kennedy (see [Staszak et al., 2021](#)). However, a comparison between the Driscoll&Kennedy model with either Heisenberg or Tatarski model reveals discrepancies with both models (H and T), which subsequently affect the values of  $Sc$  (for fixed  $\varepsilon^{\text{H}}$  or  $\varepsilon^{\text{T}}$ ). This effect may be small, if large  $Sc$  affect the electron density spectrum, i.e., if charged ice particles of several nanometers are involved (e.g., [Lübken et al., 1998](#)). But it gains considerable significance, if charged particles in the sub-nanometer range can be expected. In Fig. 3.2, ratios of power spectra from H and T are compared with the D&K model. For this comparison,  $Sc$  was set to unity for the D&K model. The other parameters,  $\varepsilon$ ,  $\chi_{\theta}$ ,  $\omega_B$ , and  $\nu$ , are the same for all models. The relatively constant offset between

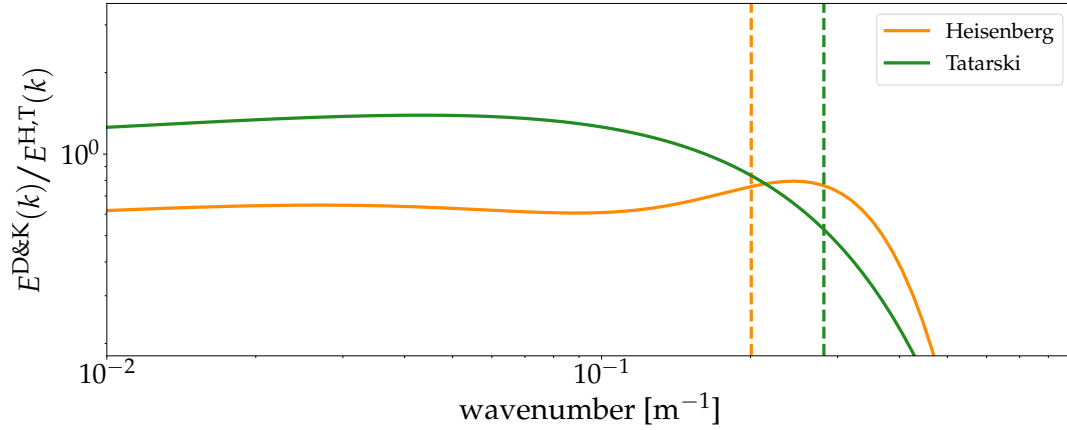


Figure 3.2. Comparison of D&K spectrum with spectral models for application on neutral density fluctuations. Solid lines indicate the ratio  $E^{\text{D\&K}}/E^{\text{H,T}}$ , where H,T denotes either model of Heisenberg or Tatarski. The inner scales  $l_0^{\text{H,T}}$  are given by vertical dashed lines. Model input parameters are:  $\varepsilon=10 \text{ mW kg}^{-1}$ ,  $\chi_\theta=6.7 \cdot 10^{-8} \text{ s}^{-1}$ ,  $\omega_B=0.02 \text{ s}^{-1}$ ,  $\nu=1 \text{ m}^2 \text{ s}^{-1}$ ,  $Sc=1$ .

the models of max.  $\pm 40\%$  in the inertial subrange shows that all models consistently have the same slope (i.e., of  $-5/3$ ). For wavenumbers larger than that corresponding to the inner scales  $l_0^{\text{H}}$  and  $l_0^{\text{T}}$ , discrepancies increase rapidly, reflecting our limited knowledge of the exact spectral shape in the viscous subrange. This problem can be avoided with the  $Sc$  derivation method utilized within this work. This is, applying the same D&K-model to the neutral density spectrum, with a fixed  $Sc=1$  and a subsequent fit to the same model with the formerly derived  $\varepsilon^{\text{D\&K}}$  to the electron density spectrum with  $\chi_\theta$  and  $Sc$  as free fitting parameters. This self-consistent method allows determining  $Sc$  without introducing ambiguities by intrinsic model uncertainties.

### 3.3 Ascertain aerosol radii from the $Sc$ number

The method to derive aerosol (e.g., MSP) radii from the  $Sc$  number is discussed by [Staszak et al. \(2021\)](#). The basic steps are summarized hereafter.

The  $Sc$  number generally describes the ratio of the kinematic viscosity  $\nu$  to the diffusivity of a tracer  $D_\theta$ . If the tracer is electron density fluctuation, the diffusivity of electrons  $D_e$  can be obtained, if the kinematic viscosity  $\nu$  is known (e.g., [Cho et al., 1992](#), [Lübken et al., 1998](#), [Asmus et al., 2017](#)). Since in the ionospheric plasma the diffusive properties of the electrons are coupled to all other plasma constituents, they are dominated by the most inertia (i.e., heaviest) charged components (e.g., [Chen, 2016](#), [Cho et al., 1992](#)). This ultimately enables the derivation of the properties of these heaviest charged species (i.e., MSP in the winter mesosphere) from  $Sc$  values, which are obtained by the spectral method described before.

[Cho et al.](#) investigated the diffusive properties of dusty ionospheric plasma and considered two different cases: Large and tiny aerosols. For large aerosols, a hard-sphere collision model can be applied, whereas a polarization model should be used for tiny particles. The limit below which the polarization must be used is given by a critical radius  $r_{\text{crit}}$  ([Cho](#)

et al., 1992):

$$r_{\text{crit}} = 4.55 \cdot 10^{-4} \left( \frac{2\alpha Z_a^2 e^2}{\epsilon_0 k_B T} \right)^{1/4} - r_n, \quad (3.21)$$

where  $k_B$  is the Boltzmann constant,  $T$  is the neutral temperature,  $\epsilon_0$  is the vacuum permittivity,  $Z_a$  is the aerosol charge number ( $Z_a=1$  for MSP),  $e$  is the elementary charge,  $\alpha=1.76 \cdot 10^{-18} \text{ m}^{-3}$  is the polarizability of  $\text{N}_2$  (the main neutral constituent), and the neutral molecule radius is  $r_n=1.8 \cdot 10^{-10} \text{ m}$ .

Lübken et al. (1998) related the aerosol radius  $r_a$  to measured  $Sc$  for large ice particles, relevant for PMSE, as  $r_a=\sqrt{Sc/6.5} \text{ nm}$ . A general algorithm to derive  $r_a$  from the measured  $Sc$  is given by Asmus et al. (2017), including tiny particles. Solving the expression  $Sc=v/D_a^{\text{H,P}}$  numerically, where  $D_a^{\text{H,P}}$  is the diffusion constant based either on the hard-sphere ( $D_a^{\text{H}}$ ) or the polarization model ( $D_a^{\text{P}}$ ), yields the aerosol radius. The diffusion constants for both cases are described by (Cho et al., 1992):

$$D_a^{\text{H}} = \frac{3}{8} \sqrt{\frac{k_B T}{2\pi\eta_{\text{an}}}} \frac{1}{N_n (r_a + r_n)^2} \quad r \geq r_{\text{crit}} \quad (3.22)$$

$$D_a^{\text{P}} = \frac{9.06 \cdot 10^5 k_B T}{N_n |Z_a| e} \sqrt{\frac{\epsilon_0}{\pi\alpha\eta_{\text{an}}}} \quad r \leq r_{\text{crit}} \quad (3.23)$$

where  $\eta_{\text{an}}=m_a m_n / (m_a + m_n)$  is the reduced mass,  $m_n=28.09 \text{ e-}3 \text{ kg mol}^{-1} / N_A$  is the mass of a single (neutral) molecule,  $N_A$  is the Avogadro number,  $N_n$  is the number density of neutrals, and  $m_a = 4/3\pi\rho \cdot r_a^3$  is the mass of the aerosol particle. In this study a typical MSP mass density of  $\rho=2 \text{ kg m}^{-3}$  is assumed (Hunten et al., 1980, Robertson et al., 2014, Plane et al., 2014). Inserting  $r=r_{\text{crit}}$  into Eq. 3.22 or 3.23 reveals the corresponding Schmidt number  $Sc_{\text{crit}}$ , whose exact value depends on the atmospheric background temperature and density.

### 3.4 Absolute neutral density and temperature

Neutral density is measured by the CONE sensor, an ionization gauge that yields electron and neutral density measurements with high spatial resolution. A schematic is shown in Fig. 3.3. A calibration against a reference is required before the instrument's launch to obtain the absolute number density. Due to the high payload velocity ( $\sim 1000 \text{ m s}^{-1}$ ) during the measurement phase, the atmosphere in the direct vicinity of the rocket gets compressed. In consequence, the measured density needs to be corrected to obtain absolute density from the undisturbed atmosphere. This correction is also essential to determine the temperature from the measured density profile. Due to different flow regimes, the correction values are a function of altitude. And since temperature derivation is especially sensitive to density gradients, the correction profile substantially influences its values. In the following sections, the laboratory calibration procedure will be explained, a method for aerodynamic corrections will be introduced, and the process to derive temperature from density profile will be described.

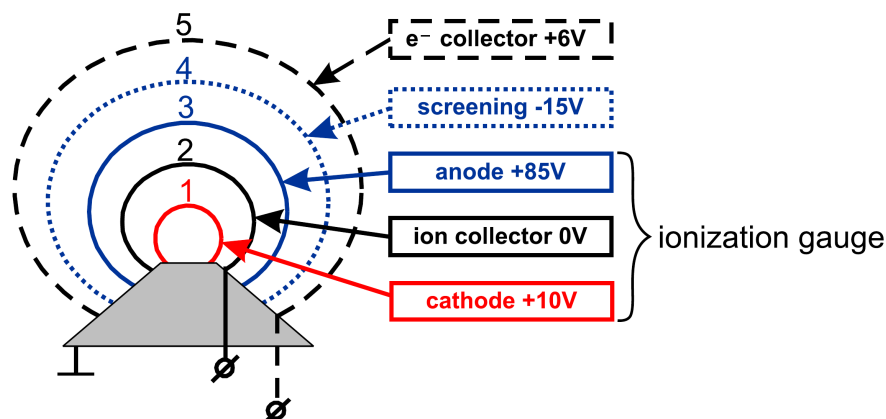


Figure 3.3. Schematic of the CONE sensor: The ambient plasma is shielded by grids 4 and 5, where the current of collected electrons is sampled on grid 5. Only the neutral gas enters the volume within grid 4, which is the ionization gauge. Electrons were emitted from the cathode (1) and accelerated towards the anode (3), thereby colliding with neutral molecules that get charged and subsequently measured by the ion collector (2). Reprinted with the permission of (Strelnikov, 2006)

### 3.4.1 Calibration

Laboratory calibration of the CONE ionization gauge is crucial to be able to retrieve absolute density from ionization gauge measurements. Since different generations of electronics, which may vary in some details, are used and the sensors themselves are hand-made, each sensor-electronic combination must be calibrated separately. Moreover, this should be done shortly before the measurement because chemical reactions of water, nitrogen, and oxygen gradually alter the cathode's filament and slightly change the ionization characteristics.

Calibrations are made in a laboratory vacuum chamber by use of an absolute calibrated<sup>1</sup> reference baratron pressure sensor. Simultaneous temperature measurements allow to convert pressure to number density, applying the ideal gas equation:

$$n = \frac{p}{k_B \cdot T}. \quad (3.24)$$

The resulting calibration curve is shown in Fig. 3.4, i.e., pressure/number density versus ion collector current. On the lower panel, the vacuumeter constant  $S$  is shown. This parameter indicates the sensitivity of the ionization gauge and is given by (Schulz and Phelps, 1957, Schulz, 1957):

$$p \cdot S = I_+ / I_- \leq 1 \quad (3.25)$$

where  $p$  denotes pressure,  $I_+$  and  $I_-$  positive ion and electron current measured on anode and cathode respectively. At high densities (pressure), the ionization gauge becomes saturated. The theoretical limit is  $I_+ / I_- = 1$ . That means all emitted electrons have ionized one neutral molecule. In practice, this value is smaller due to secondary electron emissions (Schulz and Phelps, 1957).

<sup>1</sup> according to DAkkS-R-6-2(6-2010), ISO 3567 (12-2011)

/home/so022/Repos/gpro/calibration/Calibration\_v1.py  
run on 2021-03-14 15:16 by Tristan Staszak

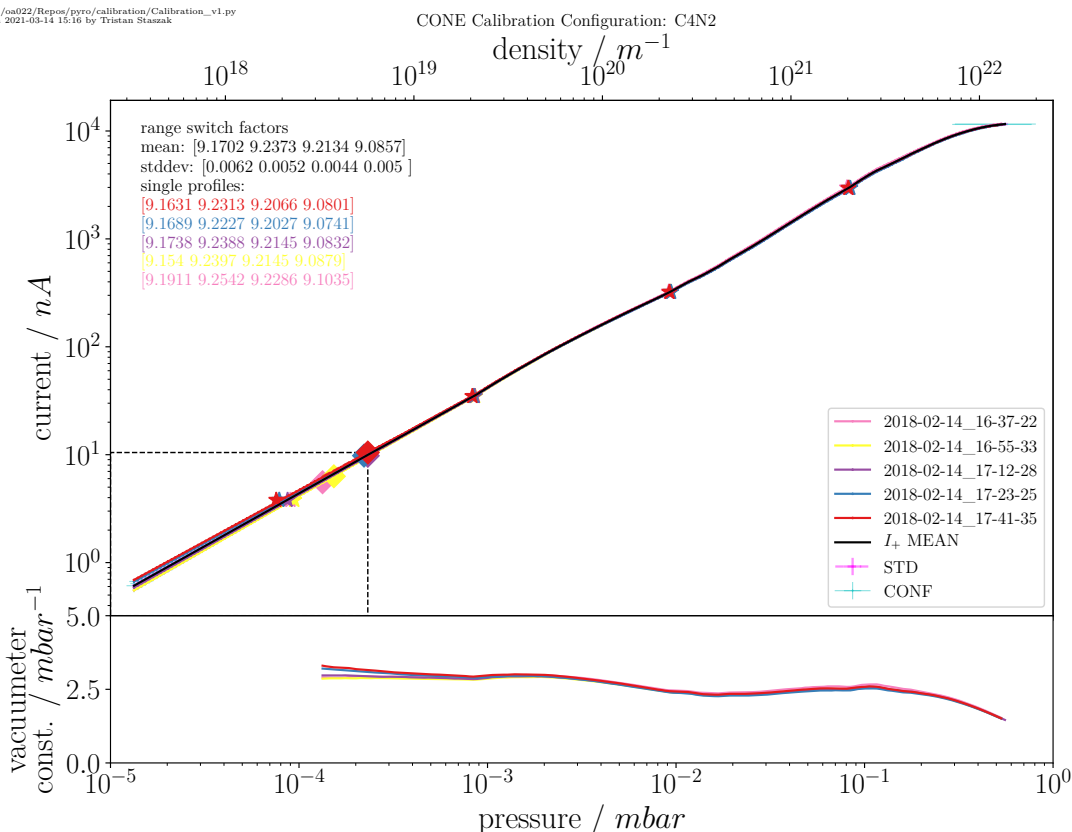


Figure 3.4. Calibration curve of the CONE sensor (C4N2) on flight PMWE1F. 5 different calibration runs were performed. The nearly identical single calibration runs demonstrate high reproducibility of the calibration process. The calibration curves are extended for  $p > 1.3e-4$  mbar (indicated by rhombus) by linear function, see text. Stars mark switches of the measurement range.

The absolute calibrated pressure range of the baratron reference is limited to  $p > 1.33e-4$  mbar. The measurement limit is  $p > 1.33e-5$  mbar. However, linearity between  $p$  and  $I_+$  holds also true for  $p > 1.33e-4$  mbar (Schulz and Phelps, 1957). Additional measurements also proved this linearity with a calibrated spinning rotor gauge (SRG). Thus, the low-pressure range is extended by a linear function that is fitted to the measurements at higher pressure where the baratron sensor is absolute-calibrated.

### 3.4.2 Aerodynamic correction

Sounding rockets typically move with speeds of several times the speed of sound, i.e.,  $Ma > 1$ . In these supersonic conditions, a shock front forms upstream of the payload. Subsequently, the flow quantities, in particular temperature and density, in the vicinity of the rocket are considerably different from those of the free atmosphere (see, e.g., Gumbel, 2001a). However, especially the state of the free atmosphere is of interest, and, therefore, aerodynamic correction must be applied. For the CONE instrument, the ratio of measured

neutral density and actual density of the atmosphere is given by:

$$\frac{N_{\text{meas}}}{N_{\text{atmo}}} = F, \tag{3.26}$$

where  $F$  is called ram factor and quantifies the aerodynamic influence of the measurements. However, the evaluation of  $F$  is challenging since atmospheric density during the measurement phase changes by several orders of magnitude. Therefore the flow gets increasingly rarefied with height. Thus, the molecular behavior of the flow becomes essential, and the continuum approach breaks. However, for a complete molecular description, density, and therefore the number of collisions, is too high and still not practical.

A computational fluid dynamic (CFD) method, Direct Simulation Monte Carlo (DSMC, Bird, 1994), has been established as a tool for simulations in the transition regime between continuum and molecular flow (Gumbel, 2001a, Rapp et al., 2001, Hedin et al., 2007, Staszak et al., 2015, 2017, Asmus et al., 2017).

Rapp et al. (2001) and Gumbel (2001a) derived a ram correction function for a sounding rocket flight (ECT02) with an apogee of 130 km. Wind tunnel measurements (SR3, Meudon, France) and independent in situ measurements of density by the Falling Sphere technique validated these results. Another ram correction profile for flight MMMI12 with an apogee of 105 km was obtained using the same DSMC code. A third-order polynomial (see Fig. 3.5)

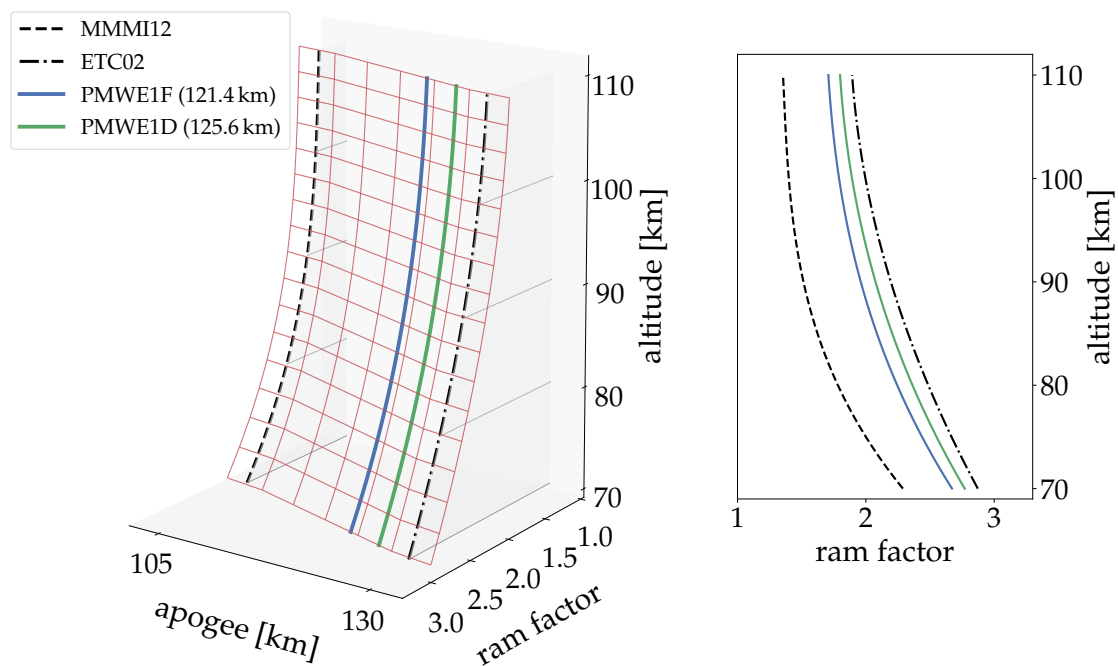


Figure 3.5. 2D interpolation of the established ram functions with apogee at 105 km (MMMI12, dashed black lines) and 130 km (ECT02, dashed-dotted black lines). The left panel visualizes the ram profile (as a function of altitude) vs. apogee. The ram functions for the flights PMWE1F and PMWE1D were obtained by interpolation of the apogee. The resulting ram profiles (ram factor–altitude plane) are shown on the right panel.

Based on these correction functions, a two-dimensional interpolation method was devel-

oped, taking the apogee as an additional interpolation variable. Note that the apogee is directly connected to the payload's velocity, and therefore this simple method accounts for various flow speeds. This method was validated by 3D DSMC (OpenFOAM, [Weller et al., 1998](#)) for the WADIS-1 flight ([Staszak et al., 2015](#)).

Another, new approach, further accounting for the actual state of the atmosphere including large-scale waves altering density and temperature, is discussed in Ap. D. This method utilizes interpolation based on a 4D data set of characteristic numbers (i.e.,  $Kn$ ,  $Re$ ,  $Ma$ ) and the corresponding ram factor. However, although this method promises to reveal highly accurate aerodynamic corrections for CONE measurements, further systematic DSMC simulations need to be done, and results should be validated with independent measurements.

### 3.4.3 Deriving temperature

By assuming a hydrostatic equilibrium, the measured density profile can be converted to a temperature profile via integration of the hydrostatic equation  $\delta p / \delta z - \rho g = 0$  and ideal gas law  $p = nk_B T$ , which yields:

$$T(z) = \frac{1}{N(z)} \left( N(z_0) \cdot T(z_0) - \frac{\bar{m}}{k_B} \int_{z_0}^z N(z') g(z') dz' \right) \quad (3.27)$$

where  $\bar{m}$  is the mean molecular mass,  $k_B$  is the Boltzmann's constant,  $g(z)$  is the acceleration by gravitation, and  $N(z_0)$  and  $T(z_0)$  are the start values of density and temperature at the altitude  $z_0$ . Note that the integration is made from  $z_0$ , denoting the high altitude limit, to  $z$ , representing an altitude below. Therefore, signs in Eq.,3.27 were changed.

## 3.5 Absolute Electron density

A method to derive absolute electron density in situ is the wave propagation experiment WPE (e.g., [Bennett et al., 1972](#), [Friedrich, 2016](#), and references therein). This experiment consists of two parts: ground-based transmitters and rocket-borne receiving antennas. The transmitters send linear polarized radio waves at frequencies of 1.300, 2.200, 3.883, and 7.835 MHz. Receiving antennas are mounted on the rocket's payload, which spins during the flight. Using two axis-symmetric antennas, positioned one from another at an angle of  $180^\circ$ , the polarization pattern of the radio waves is scanned twice per spin period, practically resulting in a vertical resolution of  $\sim 200$  m. Subsequently, the phase shift of a reference gyro signal from the rocket and the recorded polarization pattern are analyzed to obtain the Faraday rotation. Furthermore, the differential absorption (i.e., relating amplitudes of ordinary and extraordinary signal) and total reflection of each frequency provide information on the absolute electron density. Finally, a single electron density profile is obtained combining the measurements of the four different frequencies.



## 3.6 Calculated radar volume reflectivity

The relation of radar volume reflectivity  $\eta$  and the power spectrum of refractive index  $\Phi_n$  is given by Eq. 2.28, which reads:

$$\eta = \frac{\pi^2}{2} k^4 \Phi_n.$$

To compare in situ measurements with radar observations, it is necessary to relate them one to another. As discussed in Ch. 2, the spectral form of electron density and the refractive index is identical. The refractive index is the quantity measured by radar, and electron density can be measured in situ utilizing electrostatic probes onboard rocket.

Turbulent spectra of refractive index fluctuations and electron density measurements only differ due to different variance dissipation rates. More precisely, it is the different potential gradient  $M_\theta$  (cf. Eq. 3.18) that alters  $\chi_\theta$ . Consequently, to convert the 3D spectrum of absolute electron density  $\Phi_{N_e}$  to the spectrum of refractive index  $\Phi_n$ , a factor is added that is obtained by comparison of  $M_n$  and  $M_e$ :

$$\Phi_n = \left| \frac{\delta n}{\delta N_e} \right|^2 N_e^2 \cdot \Phi_{N_e}(k). \quad (3.28)$$

This factor is already given in Eq. 2.9 ( $=\delta n/\delta N_e$ ) for VHF. And Eq. 3.28 is identical with the expressions given by e.g., [Royrvik and Smith \(1984\)](#), [Lübken \(2014\)](#).

### 3.6.1 Derivation from turbulence spectral models

[Giebeler \(1995\)](#) derived a single expression for the volume reflectivity based on a 3D spectrum  $\Phi^{\text{D\&K}}(k)$  for scalar quantities, with  $Sc$  dependence ([Driscoll and Kennedy, 1985](#)), applying Eq. 3.28 and Eq. 2.28. After minor revisions by [Lübken et al. \(2006\)](#) and [Lübken \(2014\)](#) this expression reads:

$$\begin{aligned} \eta^{\text{D\&K}}(k) &= 8\pi^2 \cdot k^4 \cdot Q^{4/5} \cdot A \cdot \chi_n \varepsilon^{-1/3} \cdot \eta_{\text{Kol}}^{11/3} \cdot D(y) \\ D(y) &= (y^{-11/3} + y^{-3}) \cdot \exp \left\{ -A_{3\theta} \left( \frac{3}{2} y^{4/3} + y^2 \right) \right\} \\ \chi_n &= \frac{f_a \cdot B \cdot Ri \cdot \varepsilon}{Pr_\theta^{\text{turb}} \cdot \omega_B^2} M_n^2. \end{aligned} \quad (3.29)$$

with:

$$Q, A, A_{3\theta} \rightarrow \text{Eq. 3.13}$$

$$\eta_{\text{Kol}} \rightarrow \text{Eq. 2.35}$$

$$f_a, B, Ri, Pr_\theta^{\text{turb}} \rightarrow \text{Eq. 3.18}$$

$$M_n \rightarrow \text{Eq. 2.12}$$

Except the constants  $f_a$ ,  $B$ ,  $Pr_\theta^{\text{turb}}$ , and the  $Ri$  number, all other variables can be obtained from in situ measurements. Similar to the procedure for the derivation of Eq. 3.29, [Rapp et al. \(2008\)](#) derived an expression based on the 3D spectrum from [Batchelor et al. \(1959\)](#).

However, this model was developed for  $Sc \gg 1$ , and for this case it compares well with the expression above (see [Lübken, 2014](#)). But in the case of PMWE, only small MSPs are expected and, therefore, low  $Sc$  numbers, presumably in a range of  $\sim 1-10$ . The additional viscous-convective range (i.e., Batchelor range) does not span over a wide range of wavenumbers for this low  $Sc$ . At Bragg wavenumber  $k_{BC}$ , e.g., corresponding to a  $\sim 50$  MHz radar, a turbulent model spectrum must be able to reflect all subranges from inertial-convective over viscous-convective to viscous-diffusive, since it is not clear which subrange is met with  $k_{BC}$ . Eq. 3.29 satisfies this requirement.

### 3.6.2 Derivation from a measured power spectrum

To directly compare radar-measured volume reflectivity with measurements by electrostatic electron probes, [Royrvik and Smith \(1984\)](#) proposed a way to convert in situ electron density fluctuations to radar measurements. Similar to Sec. 3.6.1,  $\eta$  is basically derived by inserting Eq. 3.28 into Eq. 2.28. However, the in-situ-measured spectrum is 1D, while radars observe structures from the 3D spectrum. The transformation from 1D to 3D (i.e., from  $E(k)$  to  $\Phi(k)$ ) is possible if the spectral form ( $n$ ) at radar Bragg wavenumber of the 1D spectrum is known, [Royrvik and Smith \(1984\)](#):

$$\Phi_{Ne}(k) = -n \frac{1}{4\pi} k^{-2} \cdot E_{Ne}(k) \quad (3.30)$$

The value of  $n=n(k_{BC})$  can be estimated by the slope of the measured spectrum in the vicinity of the radar Bragg scale. As has been discussed by [Ottersten \(1969a\)](#), this conversion requires isotropic turbulence. Inserting Eq. 3.30 into Eq. 2.28 yields:

$$\eta(k) = -n \left(\frac{8}{\pi}\right) k^2 \left(\frac{\delta n}{\delta N_e}\right)^2 N_e^2 \cdot \frac{E_{Ne}(k)}{N_e^2}, \quad (3.31)$$

where  $E_{Ne}(k)$  is the power spectrum of absolute electron fluctuations. The electrostatic probe of CONE provides relative electron density fluctuations. Thus, the equation modifies to:

$$\eta(k) = -n \left(\frac{8}{\pi}\right) k^2 \left(\frac{\delta n}{\delta N_e}\right)^2 N_e^2 \cdot E_{\Delta Ne/Ne}(k). \quad (3.32)$$

This equation allows a direct measurement of volume reflectivity. And if structures on electron density fluctuations exist on radar Bragg scale (e.g.,  $\sim 3$  m) and the spectrum has formed the shape of a turbulent spectrum, this is the most direct proof for a turbulent mechanism creating PMWE.

## 4 | PMWE – Sounding rocket project

A sounding rocket project entitled PMWE was initiated to address the question of the creation mechanism of the radar phenomenon. Besides two instrumented rockets launched on each campaign from the north Norwegian Andøya Space Center (ASC, 69 °N, 16 °E), ground-based radars and lidar complement the measurements. Extensive statistical analysis of MAARSY observations reveals a maximum diurnal probability around noon and the best chances of PMWE observations during spring or autumn, i.e., approximately around the equinox. The first of two sounding rocket field campaign within the PMWE project was conducted in April 2018 and is short-named PMWE-1. An overview of the instrumental setup utilized in the first campaign is given in Fig 4.1. A multi-instrumental common-volume approach was set up, combining in situ measurements from sounding rockets, with unprecedented spatial resolution and/or precision, with ground-based measurements to monitor the evolution of atmospheric background and the radar echoes themselves. Ground-based instrumentation and payload instrumentation are discussed in detail in the following Sec. 4.1 and Sec. 4.2. A brief project description and an overview of the first field campaign can also be found in [Strelnikov et al. \(2021\)](#). The results of the analysis of measurements deduced during the first rocket launch have also been laid out in [Staszak et al. \(2021\)](#)

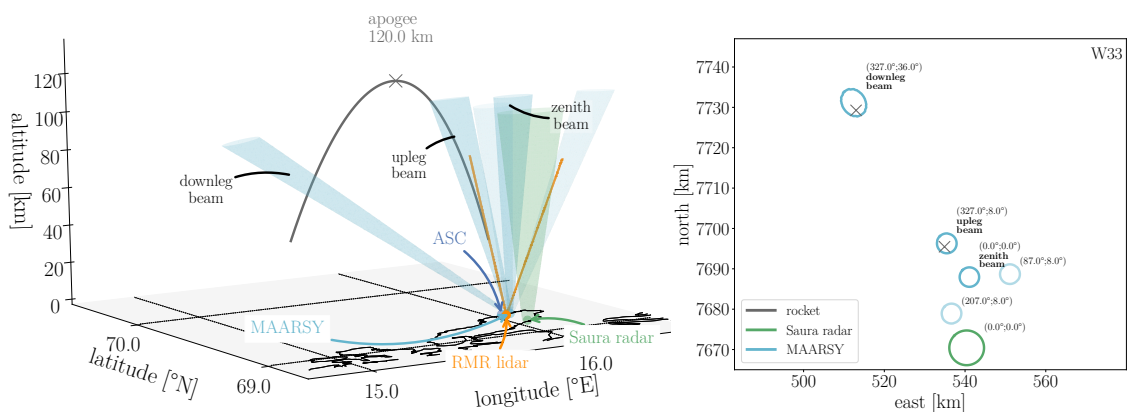


Figure 4.1. Left: Measurement setup with ground-based instrumentation: MAARSY with zenith, up-, and downleg beams (blue cones), Saura radar (green), and lidar (yellow), complementing the rocket measurements from ASC (dark blue) along the rocket trajectory (red). Right: Slice at 65 km altitude using UTM projection. Additionally, two more MAARSY beams for wind measurements are shown (transparent blue). As described in [Staszak et al. \(2021\)](#).

## 4.1 Ground-based instruments

Ground-based instruments supported rocket-borne experiments, providing continuous and time-resolved information, and thereby complemented in situ measurements. Moreover, most ground-based instruments were located very close to the rocket launch pad (ASC), allowing for simultaneous and practically common-volume measurements. Another, similar description of the ground-based instruments is also given by [Staszak et al. \(2021\)](#).

### 4.1.1 MAARSY

MAARSY, operated by IAP, is located close ( $<1$  km) to the rocket launch site and is continuously running throughout the year, observing both PMSE and PMWE which are used to study dynamics in the MLT region ([Latteck et al., 2021](#)). MAARSY runs on a frequency of 53.5 MHz, corresponding to a Bragg scale of  $\lambda_{BC}=2.8$  m and the wavenumber  $k_{BC}=2.24$  m<sup>-1</sup> (see [Latteck et al., 2010](#), for technical details).

During the PMWE-1 campaign, MAARSY was used to detect polar mesosphere winter echoes (PMWE) and defined the main launch criterion. Apart from detecting the echoes, these measurements further allow the deduction of geophysical parameters like winds and turbulence energy dissipation rates, if the returned signal is sufficiently strong (e.g., [Rapp et al., 2011a](#), [Latteck et al., 2012](#)). Absolute calibration of MAARSY ([Latteck and Bremer, 2013](#)) enables the measurement of absolute volume reflectivity in m<sup>-1</sup> ([Hocking and Röttger, 1997](#)).

During the campaign, MAARSY was operated in a five-beam configuration including a vertical beam, two beam positioned at  $8^\circ/327^\circ$  (i.e., zenith/azimuth) and  $36^\circ/327^\circ$  off-zenith, pointing towards the predicted rocket trajectory (see Fig. 4.1), and another two equally horizontally distributed beams at  $8^\circ/87^\circ$  and  $8^\circ/207^\circ$  off-zenith. The beams, pointing towards the predicted rocket trajectory covered an altitude range between 50.1 and 114.0 km with a range resolution of 300 m, allowed real common-volume measurements by radar and rocket during up- and downleg. This configuration is intended for local wind determination, to estimate the horizontal expansion of echoes, and to observe the horizontal drift of the PMWE.

The main parameters of the radar are summarized in Tab. 4.1, more technical specifics of MAARSY are given by [Latteck et al. \(2012\)](#) and a detailed description of its operation during the PMWE-1 rocket campaign is given by [Latteck et al. \(2019\)](#).

### 4.1.2 Saura radar

The Saura radar is also operated by IAP, is located only  $\sim 17$  km away from the rocket launch site and provides continuous measurements. This partial reflection radar operates at 3.17 MHz and yields long-term wind measurements, allowing for reliable analysis of long-period waves, e.g. tides (e.g., [Hoffmann et al., 2008, 2010](#)).

For the PMWE-1 campaign, Saura was operated in an operation mode that used the vertical and four oblique beam directions. This mode facilitates a homogeneous time series for wind and electron density estimates with a time resolutions of 4 min and a range resolution

of 1 km at best. A 4-bit complementary code was used to increase the average output power and to reduce noise and interference in order to maximize the signal-to-noise ratio.

Vertical and horizontal wind is derived by use of all five beam directions and both polarizations and considering the statistically corrected scattering positions (Renkowitz et al., 2018). Further, the applied operation mode enables measurements of electron density ( $N_e$ ) between 50 and 95 km, utilizing the vertical beam direction only (Singer et al., 2008). This is done by using the information of differential amplitudes and phases. Continuous  $N_e$  measurements are particularly important for the study of PMWE, as sufficiently strong absolute electron density fluctuations are a prerequisite for the observation of radar backscatter (Rapp et al., 2002).

Although MAARSY and Saura radar sounding volumes do not overlap, they are very close to each other at mesospheric heights (see right panel of Fig. 4.1).

### 4.1.3 EISCAT-VHF

The EISCAT-VHF radar is located ~130 km away from the launch site, near Trømsø (69° N, 19° E). It is an IS (incoherent scatter) radar, sensitive to (incoherent) scattering of free electrons. With a peak power of 1.6 MW and an antenna gain of 46.0 dBi, it is powerful and very sensitive, and has a very narrow beamwidth of only 0.8/1.2°, see Tab.4.1 for details. EISCAT-VHF operates at a frequency of 224 MHz, which corresponds to  $\lambda_{BC}=0.7$  m or  $k_{BC}=9.4$  m<sup>-1</sup>. During PMWE-1, EISCAT used the MANDA<sup>1</sup> operation mode to measure  $N_e$  between 60–150 km in zenith with a range resolution of 300 m, comparable with MAARSY. The radar was operated only for a few hours per day to observe the mesosphere since the availability of measurement time is limited.

Table 4.1. Radar system parameters: EISCAT parameters taken from Hocking and Röttger (1997), Belova et al. (2013), MAARSY details are given by Latteck et al. (2012), and Saura radar description to be found in e.g., Singer et al. (2008).

	EISCAT-VHF	MAARSY	Saura radar
Frequency (MHz)	224	53.5	3.17
Wavelength $\lambda_R$ (m)	1.34	5.6	94.57
Bragg wavelength $\lambda_R/2$ (m)	0.67	2.8	47.29
Bragg wavenumber $k = 4\pi/\lambda_R$ (m <sup>-1</sup> )	9.38	2.24	0.13
Minimal range resolution (m)	300 (mesosphere)	50	1000
Half-power full-beam width $\theta$ (°)	1.2 (north-south), 0.8 (east-west)	3.6	6.4
Transmitter peak power (MW)	1.6	0.8	0.116
Antenna gain (dBi)	46.0	33.5	19.5
Antenna geometry	4× parabolic	Yagi	2×1 km cross
Antenna area	each 1625 m <sup>2</sup>	~6300 m <sup>2</sup>	

<sup>1</sup> For EISCAT-experiments descriptions, see <https://www.eiscat.rl.ac.uk/experiments/mainland.html>

#### 4.1.4 RMR lidar

The RMR (Rayleigh/Mie/Raman) lidar at ALOMAR (Arctic Lidar Observatory for Middle Atmosphere Research) measures temperatures, winds, aerosols, and (during summer) NLCs, is placed only <2 km away from the launch area and is in operation since 1994. One strength of the lidar is the daytime measurement capability, realized by using narrow-band spectral filters with a width of about 5 pm (Von Zahn et al., 2000). Temperature profiles are obtained from the backscatter signals at the wavelengths of 532 nm and 355 nm, using a hydrostatic integration technique (Hauchecorne and Chanin, 1980). This RMR lidar is designed as a twin laser system with steerable telescopes, capable of performing common-volume operation together with sounding rocket experiments as well as horizontal wind measurements. Recent improvements enable day and nighttime measurements (e.g., Von Zahn et al., 2000, Schöch et al., 2008, Fiedler et al., 2011, Baumgarten et al., 2015). The RMR lidar was running continuously throughout the campaign period measuring temperature and horizontal wind in an altitude range from about 30 to ~90 km whenever weather permitted to characterize the atmospheric background properly. Relative densities obtained by the lidar are either normalized to a model or to more accurate in situ measurements, allowing for the reliable derivation of an instant absolute density profile.

## 4.2 Payloads instrumentation

Two different payloads were designed to be able to cover all relevant parameters that may play a role in PMWE formation. This includes the measurement of absolute values as well as fluctuations to be measured with high spatial resolution. A first payload, with the main emphasis on the study of ions, and a second one, mainly carrying instruments to measure charged dust particles, were named *FIONA* and *DUSTIN*.

In total, 24 different instruments were onboard the two payloads – unprecedented in IAP sounding rocket history. Furthermore, these instruments are operated by an international consortium of institutions. Collaborating partners are the Ludwig-Maximilian University Munich (LMU)/Institute for Atmospheric Physics (IPA), the Institute of Space Systems at University of Stuttgart (IRS), the Technical University Graz (TUG), and the Department of Meteorology at Stockholm University (MISU), the Royal Institute of Technology (KTH, Stockholm), for scientific instruments, as well as Andøya Space Center (ASC) and Mobile Rocket Base (MORABA) for operations.

Two new instruments were developed in the context of the PMWE project and this work. One is a new type of meteor smoke particle detector (MSPD), specially designed for measurements in challenging aerodynamic conditions of PMWE altitudes (Staszak et al., 2017, Giono et al., 2018). Secondly, a next-generation CONE (COMbined measurements of Neutrals and Electrons) instrument, named Turb3D, was prepared for a first-ever inflight validation.

Both payloads were prepared for salvo operation and flexible launch order, e.g., allowing to study the evolution of small-scale processes in PMWE, if promising PMWE conditions for such measurements are present. Thus, fully simultaneous ground support of both payloads was required.

### 4.2.1 PMWE1F–FIONA

Fig. 4.2 shows the Fiona payload configuration. The forward deck (FWD) is occupied by the cryogenic mass spectrometer ROMARA. This instrument is dedicated to measure both, species of charged ions and charged MSP with mass-to-charge ratios up to 2000  $m/z$ , using a mass-scan mode with an altitude resolution of  $\geq 1$  km (see [Stude et al., 2021](#), for technical details and first results).

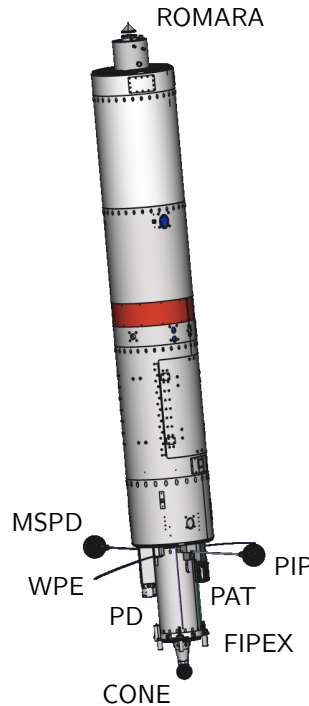


Figure 4.2. PMWE1F Fiona payload. Forward deck: cryogenic mass spectrometer ROMARA. Aft deck: Neutral and electron density measurements by CONE, absolute electron density measurements by WPE, MSP measurements by MSPD, PD and PAT, positive ion probe PIP, atomic oxygen flux by FIPEX.

The aft deck (AFT) is multi instrumented. The main instrument is CONE, able to measure absolute neutral density by means of laboratory calibration and fluctuations of both, neutrals and electrons, with high spatial resolution ([Giebeler et al., 1994](#), [Strelnikov et al., 2013](#)).

Furthermore, this deck is equipped with the meteor smoke particle detector (MSPD), the cup-like particle detector (PD), and another particle detector (PAT). All three measure a net current of negatively and positively charged MSP ( $MSP^{\pm}$ ) with high spatial resolution. The MSPD is a novel version of PD, with the Faraday-cup principle ([Havnes et al., 1996](#)) that has been transferred to spherical geometry carried on a boom in order to measure in the relatively low altitudes of PMWE (see [Staszak et al., 2017](#), for details). PD successfully measured MSP on previous sounding rocket campaigns (WADIS1&2), but also reveals limitations in detection due to the aerodynamics below  $\sim 80$  km ([Asmus et al., 2017](#)).

Another boom is placed at the rear deck to carry an electrostatic probe to measure positive

ions. Since absolute electron density measurement is crucial for PMWE investigation, the payload is further equipped with the Wave Propagation Experiment (WPE, [Bennett et al., 1972](#), [Friedrich, 2016](#)).

Except for WPE, all instruments measuring charged species of the plasma depend on the payload potential. WPE measures an electron density profile of a low altitude resolution of  $\sim 1$  km, but yields reliable measurements of absolute values whereas the electron probe of CONE only measures relative changes with a high spacial resolution of tenth of centimeters. Additionally, positive ions ( $\text{ion}^+$ ) and atomic oxygen density are measured with the electrostatic PIP (positive ion probe) and the FIPEX (flux probe experiment), respectively. A summary of instruments, measured parameters, location onboard the payload, and reference to literature, describing the technical specifications, is given in Tab. 4.2.

	Instrument	Institution	Parameter measured	Reference
FWD	ROMARA (ion mass spectrometer)	LMU/IPA	MSP $^{+/-}$ -, ion $^{+/-}$ - density	<a href="#">Stude et al. (2021)</a> , <a href="#">Arnold et al. (1977)</a>
	CONE-NP (ionization gauge)	IAP	absolute neutral density, $N_N$	<a href="#">Giebeler et al. (1994)</a> , <a href="#">Strelnikov et al. (2013)</a>
	CONE-EP	IAP	electron density, $N_e$	<a href="#">Skjelvan (1994)</a>
	MSPD(-3 V)	IAP	MSP $\pm$ -density	<a href="#">Staszak et al. (2017)</a> , <a href="#">Giono et al. (2018)</a>
AFT	MSPD(-3 V) negative grid	IAP	ion $^+$ -density	<a href="#">Staszak et al. (2017)</a>
	PD (Faraday cup)	IAP	MSP $^{\pm}$ -density	<a href="#">Asmus et al. (2013, 2017)</a>
	PD negative grid	IAP	ion $^+$ -density	<a href="#">Asmus et al. (2013, 2017)</a>
	WPE	TUG	absolute electron density, $N_e$	<a href="#">Bennett et al. (1972)</a> , <a href="#">Friedrich (2016)</a>
	PIP	IAP	ion $^+$ -density	<a href="#">Blix et al. (1994)</a>
	FIPEX	IRS	atomic oxygen density, $N_O$	<a href="#">Eberhart et al. (2015, 2019)</a>
	PaT	MISU	MSP $^{\pm}$ -density	<a href="#">Gumbel et al. (1997)</a>

Table 4.2. FIONA payload instrumentation, modified version of [Strelnikov et al. \(2021\)](#).

#### 4.2.2 PMWE1D–DUSTIN

The setup of the Dustin payload is shown in Fig. 4.3. On the forward deck (FWD), the meteor smoke particle detector MSPD and the electrostatic ion probe PIP are mounted on booms, which were designed to mitigate aerodynamic effects on the measurements.



The design has been chosen for being the best compromise between aerodynamic properties, determined by simulations, and mechanical requirements such as strength, reliability and available space inside the nosecone. On the front deck, the novel CONE-type sensor Turb3D is placed. It consists of an ionization gauge with improved sensitivity and a novel system for data distribution to the payload's service module and was mounted with an offset to the symmetry axis. Moreover, it is a simplified version of a multi-instrumental free-falling probe concept to measure three-dimensional structures in the MLT in future sounding rocket missions (Strelnikov et al., 2015).

Another instrument on the forward deck is the ECOMA (Existence and Charge state Of Meteor smoke particles in the middle Atmosphere) instrument, which is also placed offset the symmetry axis of the payload. This instrument is an advanced version of the Faraday-cup principle (Havnes et al., 1996), measuring a charged MSP net current ( $MSP^{\pm}$ ) and additionally measuring neutral MSP by active ionization via UV-flash lamp (Rapp and Strelnikova, 2009). Moreover, FIPEX sensors were mounted on a ring enclosing Turb3D and ECOMA to measure atomic oxygen densities.

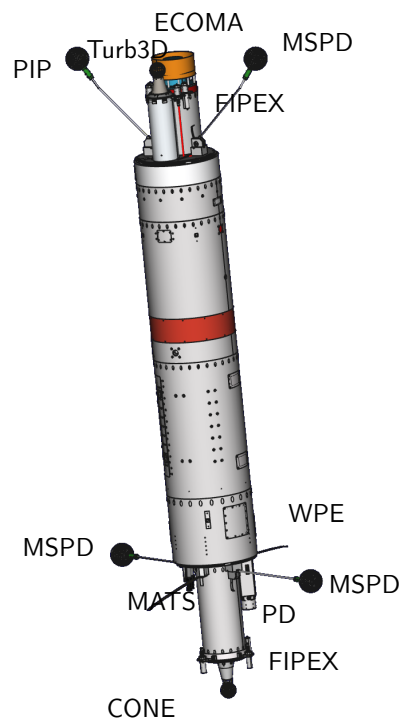


Figure 4.3. PMWE1D–Dustin payload. Forward deck: Neutral and electron density measurements by Turb3D, positive ion probe PIP, MSP measurements by ECOMA and MSPD, atomic oxygen sensor FIPEX. Aft deck: Neutral and electron density measurements by CONE, absolute electron density measurements by WPE, Mesospheric airglow sensor MATS, MSPD and PD, and FIPEX.

On the aft deck (AFT), two different versions of MSPD are carried by booms. These MSPD differ by their electrostatic sensor potential ( $-3\text{ V}/+12\text{ V}$ ) and therefore reveal a different charge and mass discrimination (see Staszak et al., 2017). The Faraday-cup PD and the MATS instruments are placed next to the CONE instrument, which is the main

instrument on the aft deck. MATS stands for Mesospheric Airglow/Aerosol Tomography and Spectroscopy, and aims to study gravity waves by means of O<sub>2</sub> atmospheric band dayglow, nightglow in near-infrared and scattered sunlight from NLC in the ultraviolet (Gumbel et al., 2020). The absolute electron density is measured by WPE also on this payload. FIPEX sensors are mounted on a ring around the CONE-cylinder. Information on numerous instruments on the PMWE1D (Dustin) payload is summarized in Tab. 4.3.

	Instrument	Institution	Parameter measured	Reference
FWD	ECOMA	LMU/IPA	MSP <sup>±/0</sup> -density	Rapp and Strelnikova (2009)
	Turb3D-NP (ionization gauge)	IAP	absolute neutral density, $N_N$	Strelnikov et al. (2015)
	Turb3D-EP	IAP	electron density, $N_e$	Strelnikov et al. (2015)
	MSPD(-3 V)	IAP	MSP <sup>±</sup> -density	Staszak et al. (2017), Giono et al. (2018)
	MSPD(-3 V) negative grid	IAP	ion <sup>+</sup> -density	Staszak et al. (2017)
	PIP	IAP	ion <sup>+</sup> -density	Blix et al. (1994)
	FIPEX	IRS	atomic oxygen density, $N_O$	Eberhart et al. (2015)
	CONE-NP (ionization gauge)	IAP	absolute neutral density, $N_N$	Giebeler et al. (1994), Strelnikov et al. (2013)
AFT	CONE-EP	IAP	electron density, $N_e$	Skjelvan (1994)
	PD (Faraday cup)	IAP	MSP <sup>±</sup> -density	Asmus et al. (2013, 2017)
	PD negative grid	IAP	ion <sup>+</sup> -density	Asmus et al. (2013, 2017)
	MSPD(12 V)	IAP	MSP <sup>±</sup> -density	Staszak et al. (2017), Giono et al. (2018)
	MSPD(12 V) negative grid	IAP	ion <sup>+</sup> -density	Staszak et al. (2017)
	WPE	TUG	absolute electron density, $N_e$	Bennett et al. (1972), Friedrich (2016)
	MATS	MISU	airglow emission	Gumbel et al. (2020)
	FIPEX	IRS	atomic oxygen density, $N_O$	Eberhart et al. (2015, 2019)

Table 4.3. DUSTIN payload instrumentation, modified version of Strelnikov et al. (2020).

## 5 | Results from the PMWE-1 sounding rocket campaign

A first sounding rocket campaign within the PMWE-Project was successfully conducted in April 2018. Within this campaign, two separate flights were conducted on the 13th and 18th of April, named PMWE1F and PMWE1D, where F stands for the FIONA and D for the DUSTIN payload. Additionally, ground-based measurements by radar (MAARSY, Saura radar, ESRAD MST, and EISCAT) and lidar were involved. The daily launch window between 6 am and 1 pm UTC opened the first time on the 9th of April. Between the 10th and 12th of April, relatively long-lasting PMWE were detected over a wide altitude range of 55–83 km during the launch window. However, flight safety conditions prohibited to launch. A full overview of the campaign can be found in [Strelnikov et al. \(2020\)](#). The campaign took place at the end of solar cycle 24 (~2008–2020) and under relatively low and stable ionization of the MLT. Recapitulating the conclusions drawn in Sec. 2.4, two prerequisites are crucial for PMWE formation: On the one hand, small-scale structures must be present in the refractive index (i.e., electron density). On the other hand, a certain ionization level of the background atmosphere must exceed a defined (radar-system-dependent) threshold. Ionization of the D-region during active sun is often accompanied by particle precipitation, ionizing the D-region sporadically. Thus, ionization is highly dynamic and happens on short time scales. Instead, a relatively stable ionization level entails the opportunity to study processes creating small-scale structures by minimizing the effects of rapidly changing background ionization.

### 5.1 Results from PMWE1F

For the first launch, the launch criterion was PMWE observation by MAARSY. Shortly after MAARSY observed PMWE in several radar beams along the predicted trajectory of the payload, the first sounding rocket (PMWE1F) was launched on the 13th of April at 09:44 UTC. Tab. 5.1 summarizes the instruments' status during the PMWE1F flight. The findings presented hereafter turned out to show a rather complex situation that requires a short description of the geophysical circumstances before discussing the measurements in detail: The in situ measurements of small-scale fluctuations were made on downleg, where turbulence was measured in coincidence or very close to PMWE observation altitudes. However, the PMWE observations were made in some spatial/temporal distance to the in situ ones. Analysis of radar data reveals that one PMWE instance, which has been observed in a common volume with in situ measurements, drifted from the downleg-

pointing beam to a south-westward direction where it was detected by the other radar beams. At the time of in situ measurements, the radar echo on downleg already disappeared and, consequently, only relics of turbulence were measured. By retrieving additional information on the spatial/temporal evolution of turbulence intensity from spectral width measurements, the intensity of turbulence during the time where PMWE was observed in the downleg-pointing beam has been reconstructed and shown to reveal very similar volume reflectivity values as has been observed by radar. Some of the following results are also discussed in [Staszak et al. \(2021\)](#).

Table 5.1. Instrument, measured physical parameters, and status for PMWE1F ([Staszak et al., 2021](#))

Instrument	Parameter	Success
ROMARA	negative ion density (resolved by mass)	✓
	positive ion density (resolved by mass)	✓
MSPD	MSP density	
PIP	positive ion density	
PD	MSP density	
CONE	neutral density (absolute)	✓
	neutral density (fluctuations)	✓
	electron density (relative)	
	electron density (fluctuations)	✓
FIPEX	atomic oxygen density	
PAT	MSP density	
WPE	electron density (absolute)	✓
Saura radar	electron density	✓
	winds	✓
MAARSY	volume reflectivity	✓
	spectral width	✓
RMR lidar	neutral density, temperature	✓

### 5.1.1 Launch conditions

Fig. 5.1 shows displays of  $\eta$  (MAARSY),  $N_e$  (Saura radar), and geomagnetic activity indices at the day of the PMWE1F launch. Three out of five MAARSY beams, pointing to the zenith, the upleg and the downleg of the rocket trajectory, are displayed in the first three panels. In all three beams PMWE was observed in three distinct layers, at  $\sim 65$ ,  $\sim 72$ , and  $\sim 78$  km, shortly before launch, which can be best inferred from the vertical beam observations. Limitations of the in situ measurements at altitudes below  $\sim 70$  km, due to supersonic aerodynamics accompanying the rocket-borne measurements, defined the primary launch criterion: MAARSY needs to observe at least some PMWE above 70 km. Below that altitude quantities like MSP and absolute neutral density are difficult to measure (e.g., [Gumbel, 2001a](#), [Rapp et al., 2001](#), [Hedin et al., 2007](#), [Strelnikova et al., 2009](#), [Staszak et al., 2017](#)).

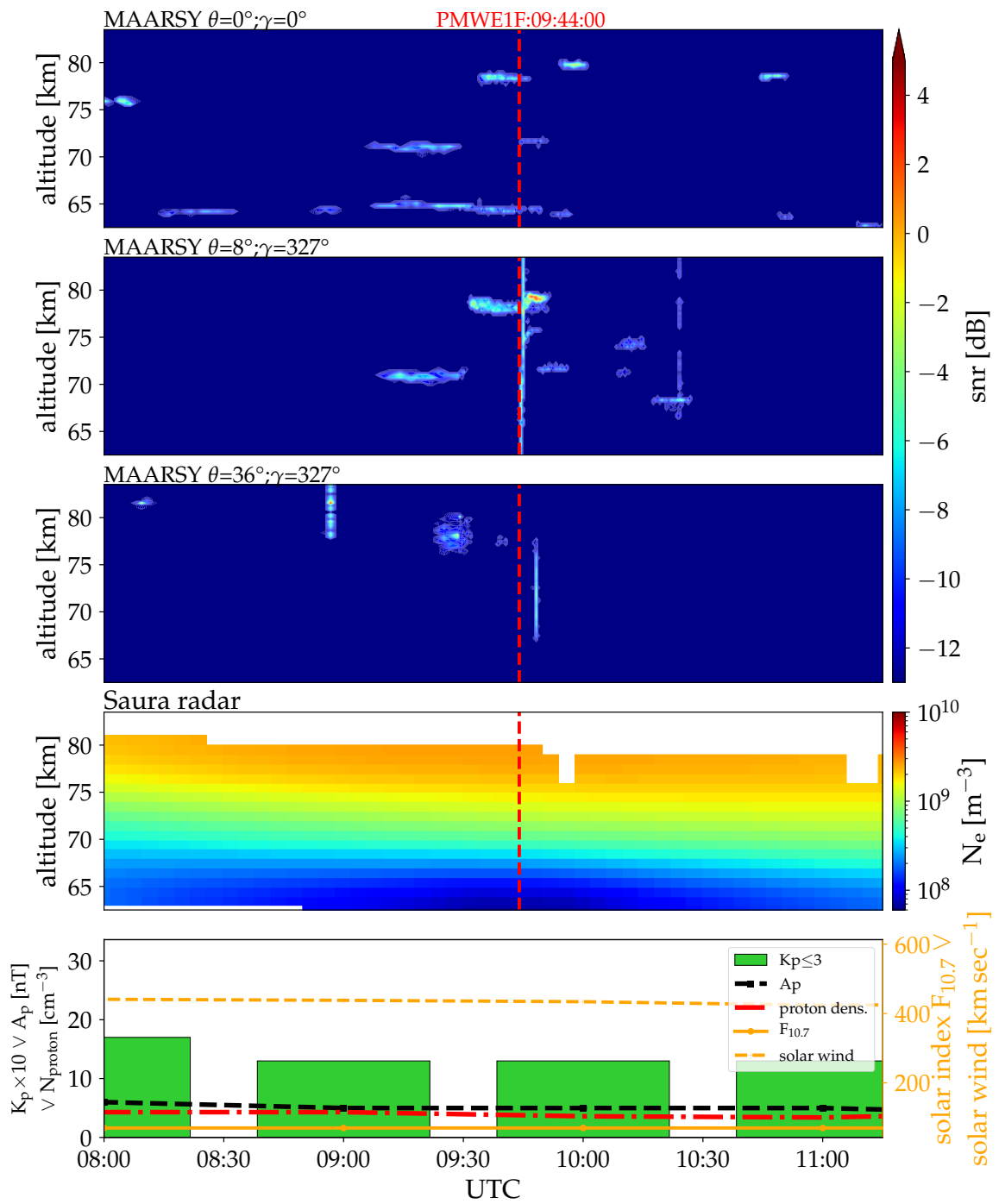


Figure 5.1. Conditions of the ionosphere's D-region around the PMWE1F flight. The first three panels from the top display MAARSY observations on zenith, upleg, and downleg beams, [Staszak et al. \(2021\)](#). The display below shows the electron density measurements by Saura radar, [Staszak et al. \(2021\)](#). Indices for solar and geomagnetic activity,  $K_p$ ,  $A_p$ ,  $F_{10.7}$ , and solar wind speed, that are given in the bottom panel, reveal low activities.

The electron density measurements by the Saura radar (see Fig. 5.1, third from top) reveal a low to medium and stable ionization of the D-region, with only slow changes in the electron density by a factor of  $\lesssim 5$  over several hours. In accordance to that, the solar flux  $F_{10.7}$ , the planetary magnetic  $A_p$ , and the geomagnetic  $K_p$  indices are low. These indices have been obtained from GSFC/SPDF OMNIWeb interface<sup>1</sup>. The solar wind speed revealed values of  $\sim 600 \text{ km s}^{-1}$  on the first days of the launch window (from the 10th of April), where safety conditions prohibited launching into PMWE. The solar wind speed revealed lower values of  $\lesssim 300 \text{ km s}^{-1}$  at the end of the launch window on 18th of April (not shown here). At the day of the PMWE1F launch, the solar wind speed was right in between, with values of  $\sim 430 \text{ km s}^{-1}$ . In anti-correlation to the solar wind, the proton density was low ( $\lesssim 5 \text{ cm}^{-3}$ ) at the beginning and high ( $\sim 15 \text{ cm}^{-3}$ ) shortly after the launch window was closed on 18th of April and PMWE appeared. Precipitation of solar protons can produce free electrons in the ionospheric D-region. For the PMWE1F period, a low proton density was measured ( $> 4 \text{ cm}^{-3}$ ).

Besides measurements of electron density, the Saura radar provides data of zonal ( $u$ ), meridional ( $v$ ), and vertical ( $w$ ) winds, shown in Fig. 5.2.

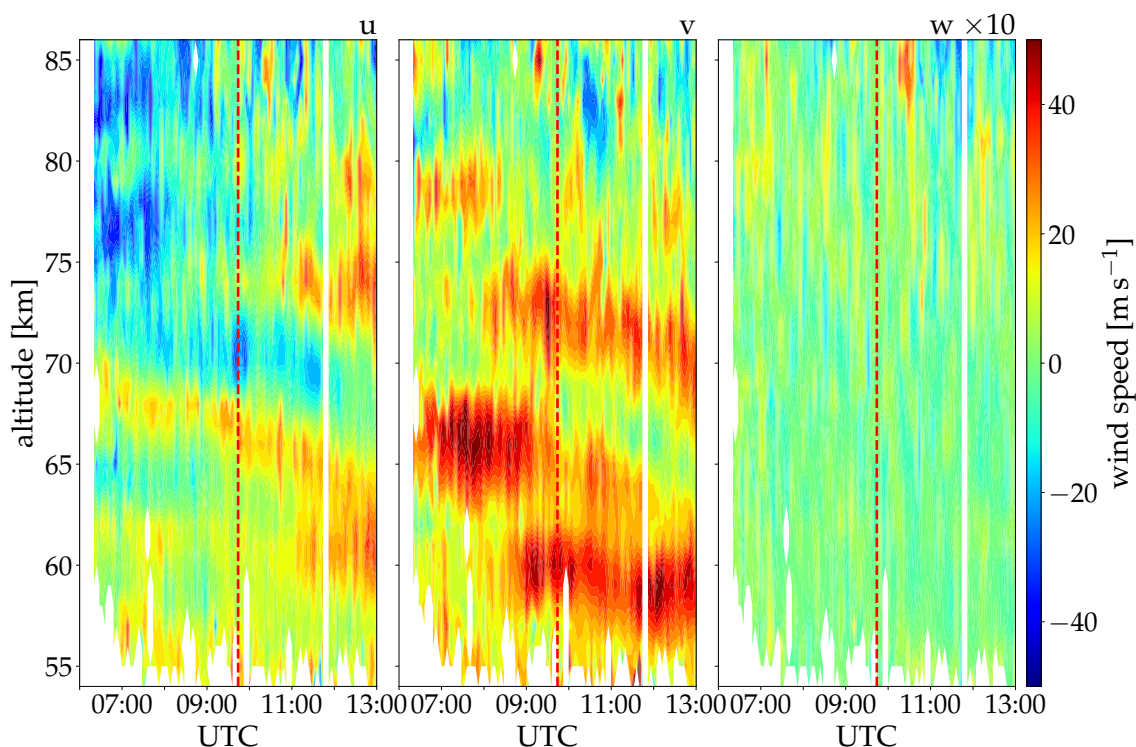


Figure 5.2. Saura radar wind measurements. Colorplots show time resolved wind observations of  $u$ ,  $v$ , and  $w$ , during the launch window on 13th of April. Red dashed vertical lines indicate the PMWE1F launch.

Wind measurements at the launch time (marked by vertical red lines in Fig. 5.2) are shown in Fig.5.3. The left panel displays the mean zonal (green dashed-dotted) and meridional

<sup>1</sup> <https://omniweb.gsfc.nasa.gov>

(red dashed-dotted) wind components, extracted by temporal and vertical filtering techniques (Strelnikova et al., 2020). The background zonal wind changes from  $\sim 12 \text{ m s}^{-1}$  in around 60 km to  $-12 \text{ m s}^{-1}$  at 83 km, and the meridional wind is  $\sim 16 \text{ m s}^{-1}$  around 60 km, turning to nearly zero in a range from 74–83 km. This means that the horizontal wind direction of the background wind changes from a north-eastward direction at lower altitudes ( $\sim 56$ –70 km) to straight northwards around 72–73 km and finally turns to westward directions above 73 km, as is visible from the hodograph in Fig. 5.3 (right panel).

Wind fluctuations (thin solid lines from left panel in Fig. 5.3) were derived by subtracting a mean profile from total winds and reveal structures of GWs throughout the altitude range of 55–85 km. Maximum amplitudes of  $\sim 30 \text{ m s}^{-1}$  in the horizontal wind (black) can be found at 71 km and 60 km. Another local maximum is located at 80 km, revealing  $\sim 20 \text{ m s}^{-1}$ . Between 75–80 km and  $\sim 62$ –69 km, the values are around  $10 \text{ m s}^{-1}$ . Vertical

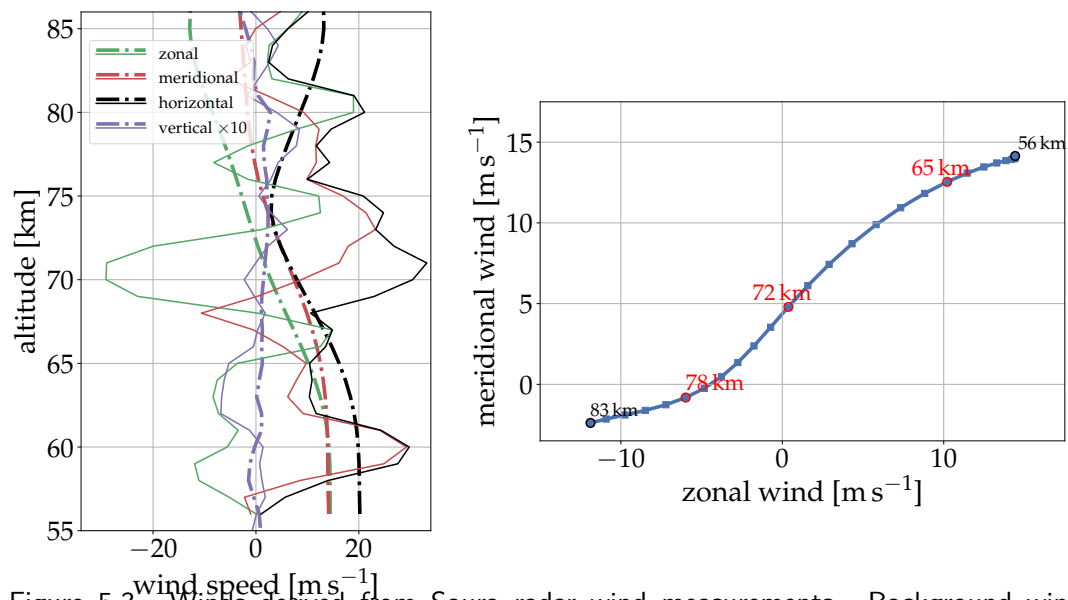


Figure 5.3. Winds derived from Saura radar wind measurements. Background winds ( $\bar{u}$ , thick lines) are derived by temporal and vertical filtering techniques (Strelnikova et al., 2020). Fluctuations (thin lines) are obtained by  $u' = u(t) - \bar{u}$ . The left panel shows zonal and meridional background wind components vs. altitude. A hodograph from the altitude range of 56–83 km is given on the right panel. Red annotations mark the altitudes where PMWE is observed. Courtesy of Irina Strelnikova.

For further description of the measurements and discussion, MAARSY observations close to PMWE1F rocket sounding are shown in more detail in Fig. 5.4. Individual instances of PMWE are labeled with letters and numbers, indicating where the echo is observed (Z, U, D, for zenith, upleg, and downleg radar beam) and giving the order of detection (#1, #2, etc.). Identical numbers indicate the same PMWE drifting through multiple beams.

As can be seen from Fig. 5.4, a very thin PMWE (instance Z0) was observed throughout the morning at an altitude of 63 km, with a vertical extent of only 1–2 range gates, i.e., 300–600 m. The first echo with index #1 (Z1 and U1) that was suitable for in situ soundings (i.e., above 70 km), was observed at 09:20 UT in both zenith and upleg radar beams.

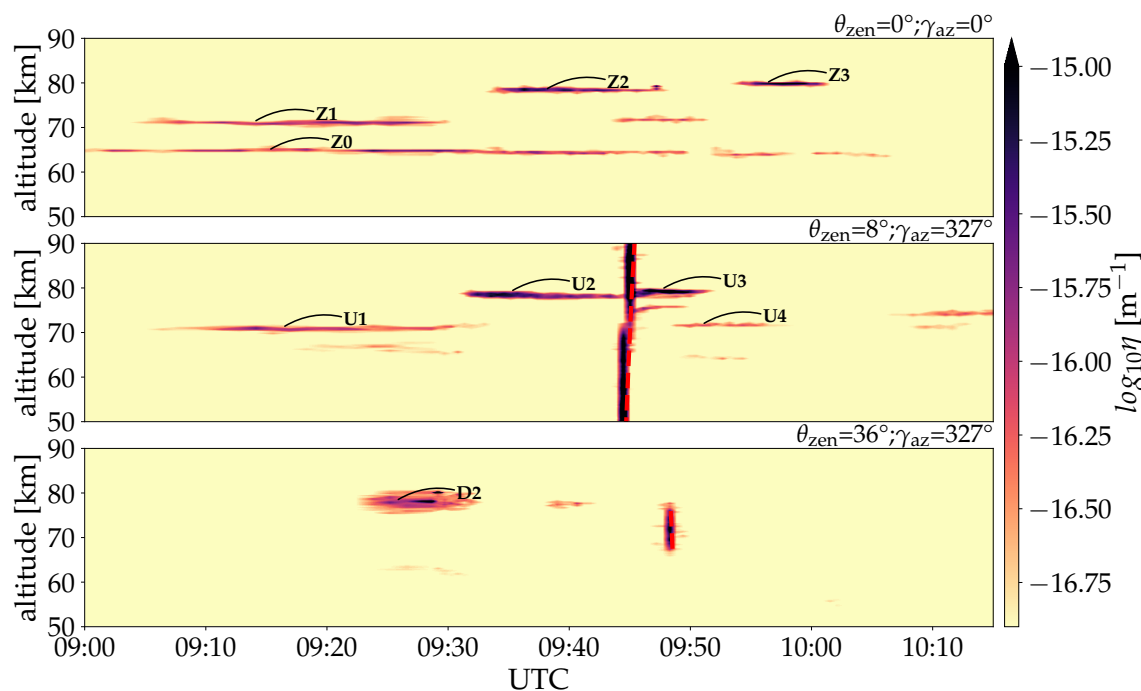


Figure 5.4. Details of the PMWE event around PMWE1F launch. Panels reveal the volume reflectivity  $\eta$  from zenith, upleg, and downleg beams of MAARSY, from top to bottom, respectively. Echoes around the launch are labeled: Z, U, D, denote zenith, upleg and downleg observations, and corresponding numbers indicate a single PMWE drifting through multiple beams. Red dashed lines show rocket traversal. After Staszak et al. (2021)

Some minutes later, another PMWE was observed in the downleg-pointing beam (D2), and the decision was made to launch. Subsequently, D2 disappeared before launch. The echo U2 gradually became weaker during the period from lift-off until the rocket reached the PMWE altitude at  $\sim 78$  km. The quasi-vertical lines of strong radar reflection (highlighted by dashed red lines in panels for upleg and downleg observation) show signals that were induced by the payload itself.

After the rocket's passage, two new artificially produced echoes appeared at  $\sim 75$  km (not labeled) and 79 km (U3). The latter was also seen in the zenith beam with a comparable lifetime of  $\sim 360$  s.

### 5.1.2 In situ measured atmospheric background

The mesosphere's background is precisely determined by rocket-borne in situ measurements. Most important to mention is CONE, yielding absolute neutral density and fluctuations with high spatial resolution and electron density measurements and fluctuations relative to the payload potential. The best quality data is obtained during the payload's descent in ram flow conditions, whereas absolute electron densities obtained by WPE are measured during the ascent flight phase. A schematic of the measurement geometry is given in Fig. 5.5. The payload's trajectory is directed north-westwards with an apogee of 121.4 km and an impact at the Norwegian arctic sea,  $\sim 60$  km away from the launchpad. Subsequently, the payload was recovered by a ship. Around an altitude of 70 km, upleg



and downleg measurements are separated by  $\sim 40$  km. The distance between the zenith radar beam and the upleg measurements is  $\sim 10$  km at the same altitude.

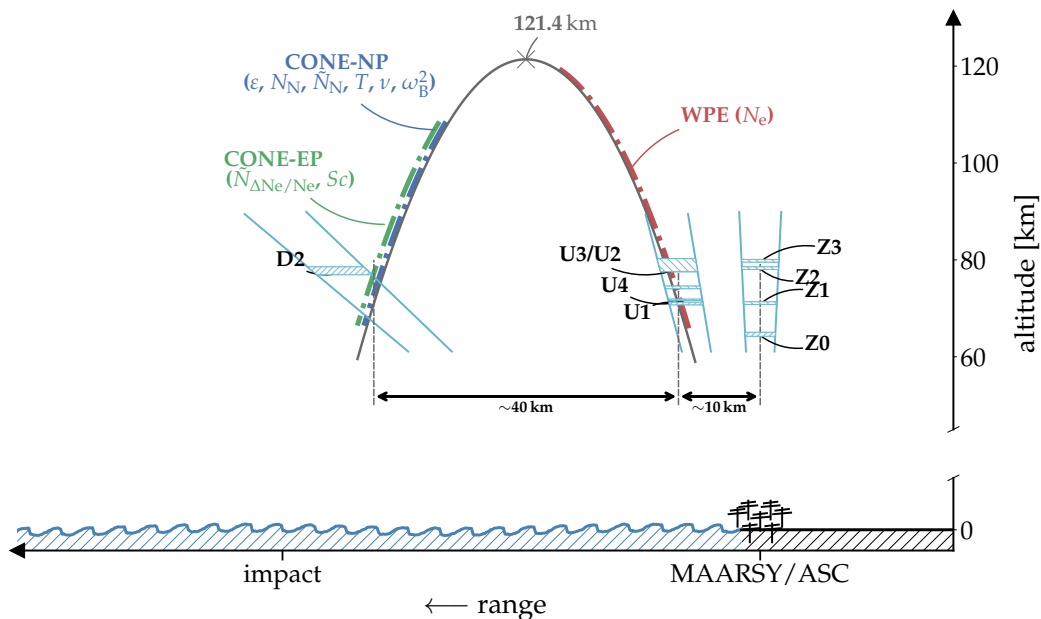


Figure 5.5. Schematic of the measurement geometry: In situ data by CONE was obtained from downleg, i.e., parameters of neutrals were measured by CONE-NP (blue section). CONE-EP deduced relative electron density and fluctuations (green section). Absolute electron density during upleg (red) was measured by WPE. The payload's apogee was at 121.4 km, with a trajectory towards the northeast ( $EL=83.5^\circ$ ,  $AZ=339.2^\circ$ ). Three MAARSY beams (zenith, upleg, downleg) and labels of PMWE observations from Fig. 5.4 are plotted with light blue colors.

Fig. 5.6 displays combined profiles of the rocket-borne CONE-NP and the ground-based RMR lidar. Note that the lidar density measurements are normalized to CONE-NP measurements at 70 km altitude, marked by a black cross. Error bars of both temperature measurements are largest at the seeding altitudes and decrease rapidly within one scale-height. A rigorous discussion on absolute density and temperature uncertainties by CONE-NP measurements can be found in Ap. C. The seeding temperature for density integration of in situ measurements was taken from the NRLMSISE-00 model (Picone et al., 2002) at 110 km, whereas the seeding of lidar measurements at 70 km was done using CONE-NP temperature.

The temperature profile exposes both large-scale oscillations with amplitudes of several K and small-scale signatures caused by GWs (cf. Strelnikov et al., 2019). The temperature gradient at altitudes of PMWE and slightly below shows an adiabatic lapse rate  $\Gamma$ . Between two such  $\Gamma$ -layers ( $\sim 76$ – $79$  km) PMWE with labels #1, #2 and #3 were observed in different radar beams. The temperature gradient in this region is  $\sim 5$  K  $\text{km}^{-1}$ . A similar behavior can be observed between two adiabatic layers around 71 and 72 km, where the temperature gradient reveals less steep values, but remains negative. Note that the period of 14 minutes between the temperature measurement and the echo #1 is relatively large.

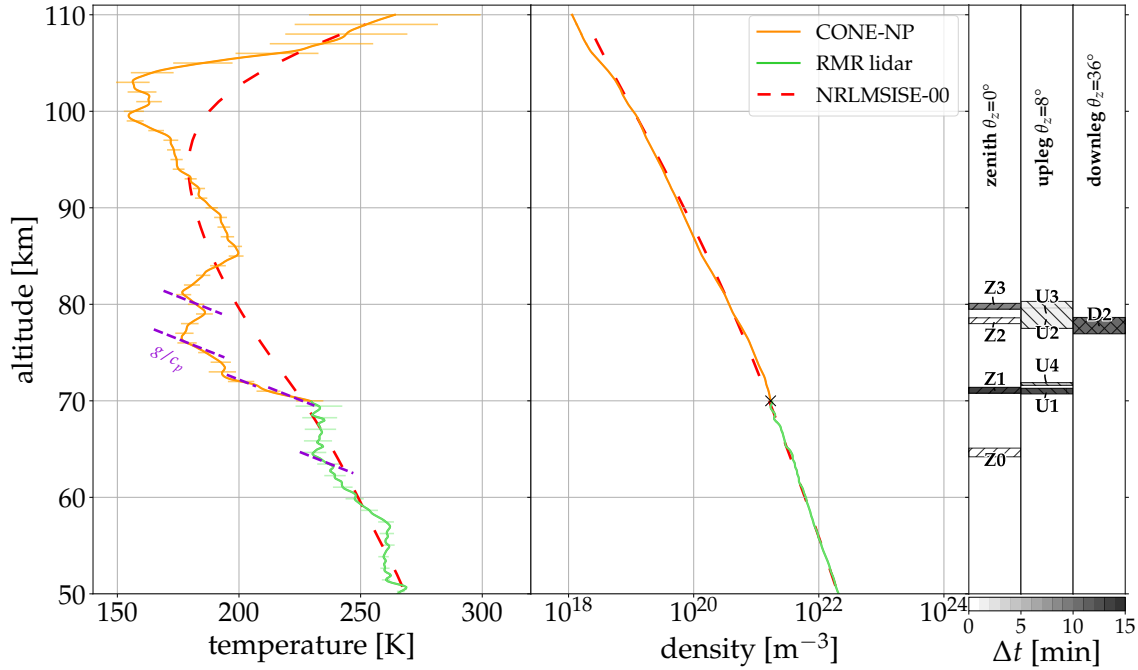


Figure 5.6. Combined temperatures (left panel) and densities (mid panel) (after [Staszak et al., 2021](#)), measured by CONE-NP on downleg (orange) and lidar (green), compared with NRLMSISE-00 (red dashed [Picone et al., 2002](#)). The black cross shows the normalization height of lidar density to CONE-NP measurements. The adiabatic temperature gradient  $\Gamma=g/c_p$ , is indicated by violet dashed lines. Error bars indicate measurement uncertainties. The rightmost panel indicates PMWE detections on zenith, upleg, and downleg beam around the PMWE1F flight (label notation introduced in Fig. 5.4). Patches' face colors (gray-value) reveal the past time between PMWE and liftoff at 09:44 UT (i.e., from ending PMWE before and beginning PMWE after launch).

Measurements of absolute electron density are shown in Fig. 5.7, deduced from in situ measurements by WPE and from remote sensing by Saura-radar. For reference, the dashed red line shows a modeled profile derived from Ionospheric Model for the Auroral Zone (IMAZ) ([McKinnell and Friedrich, 2007](#)). Model inputs are  $F_{10.7}$  solar flux index 70.1 Jy, planetary magnetic  $A_p$  index 5, and riometer absorption 0.2533 dB at 27.6 MHz. The riometer absorption was estimated from electron density measurements by WPE according to [Friedrich and Torkar \(1983\)](#).

Measurements and model both indicate a relatively low ionization level of the ionosphere. The WPE measurements at the E-region peak reveal electron densities of  $7.6 \cdot 10^{10} \text{ m}^{-3}$ . Comparisons with other high latitude WPE measurements show that this value often exceeds  $3 \cdot 10^{11} \text{ m}^{-3}$ , and can reach values of  $\sim 1 \cdot 10^{12} \text{ m}^{-3}$  ([Friedrich, 2016](#)). The comparison of radar and in situ measurements reveals a good overall agreement, in particular regarding vertical gradients. This strengthens the picture that the vertical structure of the ionosphere only slightly changes with horizontal distances in the order of  $\sim 40 \text{ km}$ , e.g., between upleg and downleg measurements. As has been discussed by [Staszak et al. \(2021\)](#), echoes #2 and #3 were detected at an altitude (76–80 km), where the overall WPE electron density gradient is relatively weak compared to gradients above (80–83 km) and below (68–76 km).

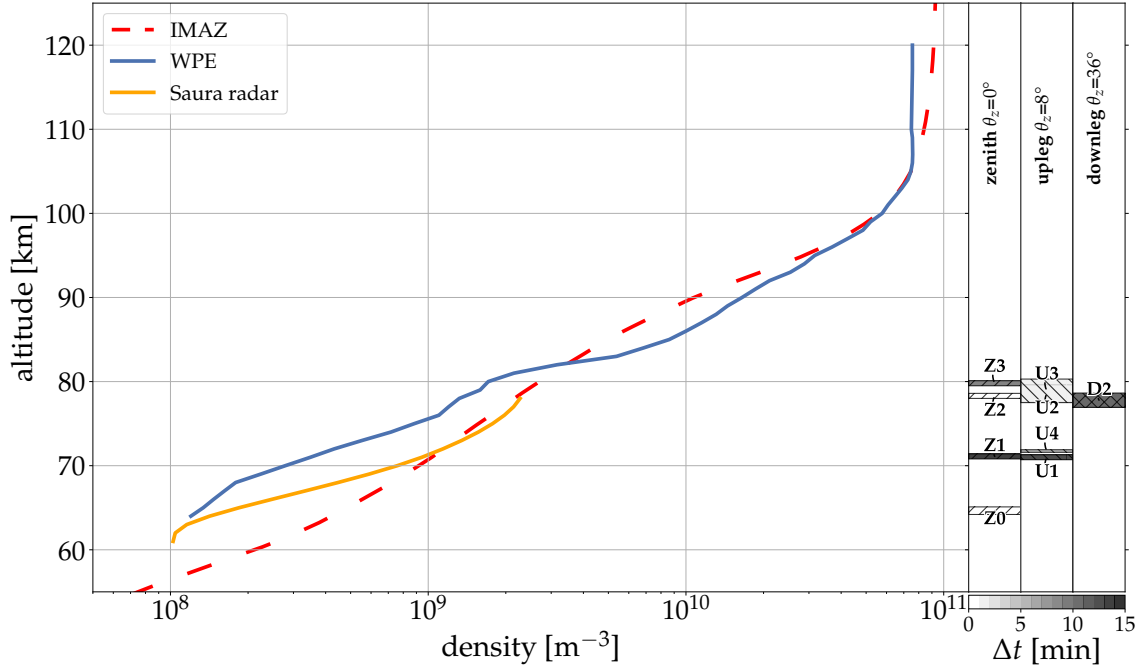


Figure 5.7. Absolute electron density profiles, revealed in situ by WPE (solid blue), remotely by Saura-radar (orange), and compared to IMAZ model (dashed red) after [Staszak et al. \(2021\)](#). See text for more details. The left panel indicates radar echo detections by MAARSY, analog to Fig. 5.6.

Fig. 5.8 reveals other atmospheric background parameters like the kinematic viscosity  $\nu$ , the scale heights of neutrals  $H_N$  and electrons  $H_e$ , the buoyancy frequency squared  $\omega_B^2$ , and the potential electron density gradient  $M_e$  (see Eq. 2.10). Since the potential electron density gradient is closely related to the potential refractive index gradient  $M_n$ , an atmospheric background yielding high  $M_e$  values is favorable for radar echoes.  $M_e$  reveals a local maximum at the same altitude where U4 is observed ( $\sim 71.5$  km) during the time of the in situ measurements on downleg. At that altitude,  $|H_e|$  is relatively small ( $< 5$  km) and remarkably stable in the altitude range of  $\sim 71$ – $75$  km. Thus, the variation of  $M_e$  is mainly defined by neutral density and temperature gradients, expressed by the quantities  $H_N$  and  $\omega_B^2$ . At altitudes between 75 and  $\sim 80$  km,  $M_e$  is locally enhanced with the highest values at  $\sim 77$  and  $\sim 79$  km. In contrast to the vertically thin PMWE and  $M_e$  peaks at lower altitudes (i.e., at 71.5 km), this locally enhanced  $M_e$  extends vertically over several kilometers, similar to the PMWE observations. However, the highest values of  $M_e$  are observed above 82 km, where the neutral density gradient reveals relatively constant values of  $H_N \sim 5$  km. In this height, the temperature gradient is positive (see also Fig. 5.6),  $\omega_B^2$  reveals relative high values of  $\sim 8 \cdot 10^{-4} \text{ s}^{-2}$  and slowly increases with height. Although the value of  $M_e \sim 2$ – $3 \cdot 10^6 \text{ m}^{-4}$  reveals preferable conditions for radar echoes, no PMWE were detected at these altitudes. The overall structure of  $M_e$  is determined by the absolute electron density profile (Fig. 5.7) whereas the structure on kilometer scales is dominated by  $\omega_B^2$  and  $H_N$ , and therefore by the vertical structure of atmospheric temperature and neutral density.

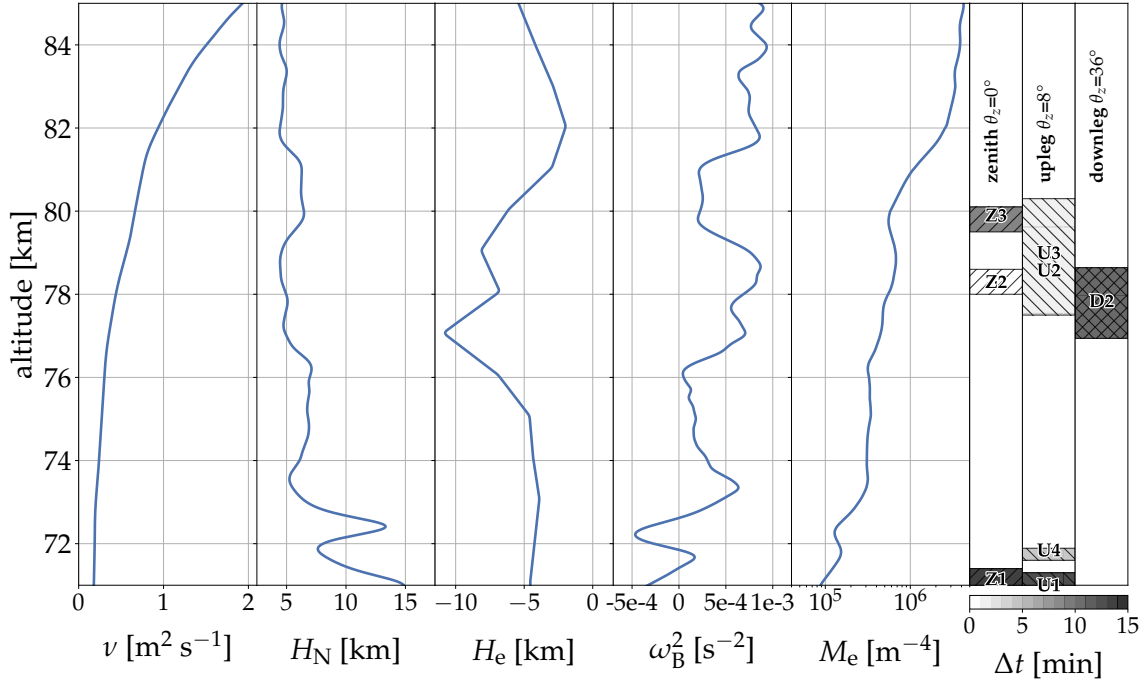


Figure 5.8. Profiles of kinematic viscosity  $\nu$ , neutral, and electron scale height  $H_N$ ,  $H_e$ , squared buoyancy frequency  $\omega_B^2$ , and potential electron density gradient  $M_e$ . The right panel shows radar echo detections by MAARSY, analogous to Fig. 5.6. Updated version after [Staszak et al. \(2021\)](#)

### 5.1.3 Small scale fluctuations

Small-scale fluctuations obtained from CONE were analyzed according to Sec.3.2.2. As the best quality data is obtained in aerodynamic ram conditions and CONE is placed on the aft deck, downleg data is used for further analysis. Figs. 5.9 and 5.11 show residuals (fluctuations), color-coded wavelet spectrum, and radar echo detections (on zenith, upleg and downleg) for neutrals and electrons, respectively, as a function of altitude and frequency. The frequency  $f$  is converted to scales  $s$  by knowledge of the payload velocity  $v$  (i.e.,  $s=v/f$ ).

The wavelet spectrum of neutrals (Fig. 5.9) exposes several layers of enhanced PSD (power spectral density) at scales from several hundred meters down to much smaller ones (e.g., to meter-scales). The most pronounced layers are visible as at  $\sim 67, 70.5, 78, 86, 93.5,$  and  $102$  km. An advanced turbulence analysis technique is used in this work, extending the one applied by [Staszak et al. \(2021\)](#), with increased vertical resolution and adopting an additional theoretical model for the neutral density fluctuations. Furthermore, a careful analysis in noisy parts and in sections where absolute values are ambiguous has been carried out and discussed in the following.

To fit theoretical spectra (see. Sec. 3.2) to the measured spectrum, the global wavelet spectra were calculated for 100 m sized altitude bins. In the subsequent analysis of these bins, it turned out that the very strong signatures at 68 and 70.5 km are correlated with the cathode current (i.e., with the ionization source). For reliable turbulence measurements by

CONE, the cathode current must be constant to assure that atmospheric density perturbations only cause the measured fluctuations. Therefore these regions were excluded from further analysis (marked by gray patches in Fig. 5.10). For turbulent spectra, theoretical models of Heisenberg H, Tatarski T, and Driscoll and Kennedy D&K were fitted by least-squares method, revealing a profile of energy dissipation rates  $\epsilon$  (see Fig. 5.10).

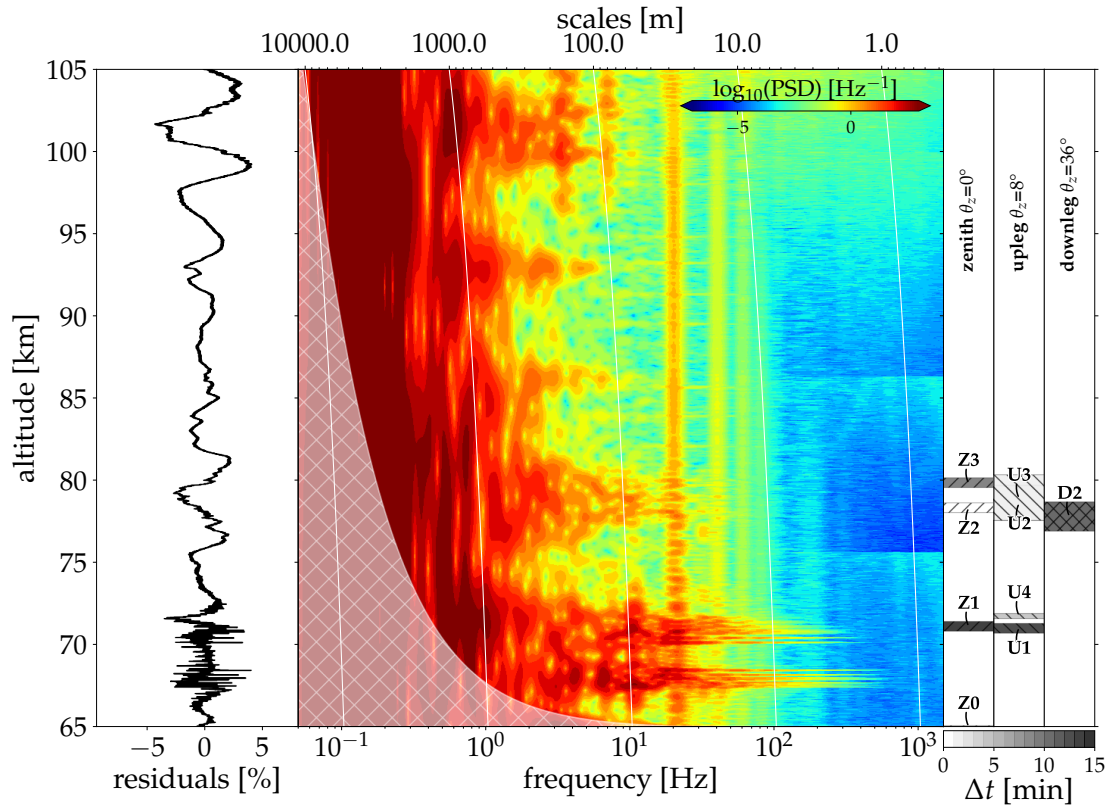


Figure 5.9. Neutral density fluctuations: Left panel shows residuals (%). PSD from wavelet transform (12th order Morlet) is shown as a color-plot over frequency/scale (abscissa) and altitude (ordinate). Note that scales are a function of altitude as indicated by white lines. Color indicates  $\log_{10}(\text{PSD})$  with the colorbar in the upper-right. On right panel labeled radar echoes with gray-coded  $\Delta t$  are shown.

Energy dissipation rate values for the Heisenberg and the Tatarski models are essentially the same as reported by Staszak et al. (2021), but with higher vertical resolution. Compared to Staszak et al. (2021), an additional patch at  $\sim 69$  km is shown here, thanks to the higher resolution. However, the inner scale of turbulent spectra ( $l_0$ ) in this layer falls in the range of spin modulations, which introduces some uncertainty in absolute value of  $\epsilon$ . In addition to H and T models, the DK model was applied for a model-consistent comparison of electron density spectra in this thesis. All  $\epsilon$  derived from different models reveal the same relative profiles. Staszak et al. (2021) noted that the differences in absolute values should be interpreted as model uncertainties. Additionally, also the majority of absolute values  $\epsilon^{\text{D\&K}}$  are in-between  $\epsilon^{\text{H}}$  and  $\epsilon^{\text{T}}$ . Only a few  $\epsilon^{\text{D\&K}}$  values exceed values of  $\epsilon^{\text{T}}$ , while  $\epsilon^{\text{H}}$  marks the lower end values. For reference, typical mean  $\epsilon$  values for summer

and winter seasons (Lübken, 1997, Lübken et al., 2002) are shown in Fig. 5.10. From simultaneous absolute density and temperature measurements, minimal values of turbulent energy dissipation rate are estimated by  $\epsilon_{min} = \nu \omega_B^2$  (see, e.g., Lübken, 1992, for details). The measured  $\epsilon$  profile is highly intermittent, revealing rather isolated patches of turbulence than a continuous profile with maximum values of  $\sim 20\text{--}150 \text{ mW kg}^{-1}$  between 76 and 80 km. These values are comparable with summer mean values from  $\sim 83 \text{ km}$  and above. Turbulence layers below 75 km reveal  $\epsilon$  very similar to winter mean values (while

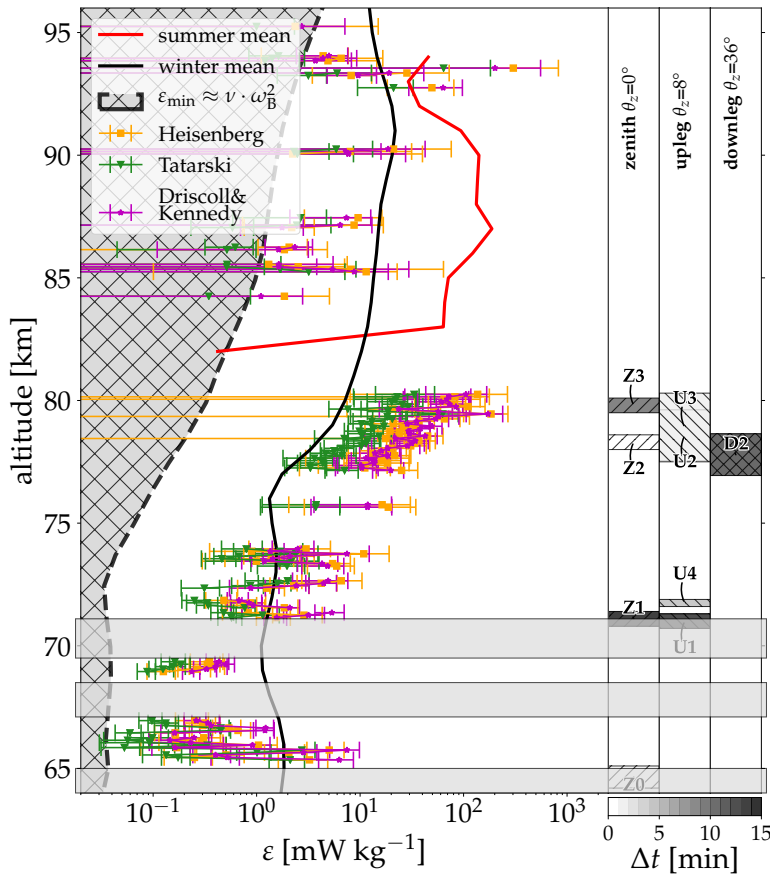


Figure 5.10. Energy dissipation rates  $\epsilon$  deduced from CONE measurements on PMWE1F, as revealed from the Heisenberg (yellow), the Tatarski (green), and the Driscoll&Kennedy model (magenta). Error bars indicate the measurement uncertainty (see Ap. C). The single spectral fits are given in Ap. F.1. The dashed line marks the lower theoretical energy dissipation rate limit  $\epsilon_{min}$ . Solid red and black lines show mean values for summer and winter, respectively (Lübken, 1997, Lübken et al., 2002). The measurement range that is excluded from the analysis is marked by gray rectangular patches (see text for more details). Again, the right panel exposes PMWE detections with gray-coded  $\Delta t$  from launch time.

ones below 70 km show  $\epsilon < \epsilon_{mean}$ ). Layers above 80 km are even more isolated and reveal  $\epsilon$  similar to the winter mean between  $\sim 88\text{--}95 \text{ km}$  and even lower values ( $\epsilon < \epsilon_{mean}$ ) in the range of 80 to 88 km.

Altitudes where the temperature profile reveals an adiabatic lapse rate must be treated with caution: The amplitude of measured density fluctuations is given by the difference of the

actual to the adiabatic lapse. Since turbulence vertically mixes air adiabatically, finally causing an adiabatic lapse, CONE-NP is less sensitive in regions where the background atmosphere reveals a near-adiabatic lapse rate. It is also worth pointing out that the spectral method remains still valid in regions of near-adiabatic lapse since the method depends on scales rather than on the amplitude of the spectrum. A comparison of the  $\varepsilon$  profile and PMWE detections (right panel of Fig. 5.10) shows that turbulence was measured in all altitudes where PMWE was detected (note that no measurements were made below 65 km, i.e., where Z0 is observed). However, this connection is not unambiguous, and turbulence was also measured at altitudes where no PMWE appeared, for example at around 66, 69 and between 73 to 76 km, but also above 81 km. Interestingly, no turbulence was measured between 74–75.6 km, where the lower artificial radar echo is observed (cf. upleg panel of Fig. 5.4). Due to the higher vertical resolution (compared to Staszak et al., 2021) a very thin layer of  $\sim 200$  m was measured at the upper end of this echo with centers at 75.65 and 75.75 km.

In Fig. 5.11, the residuals of relative electron density fluctuations measured in the same volume as neutrals (left panel) and the corresponding wavelet plot are shown. For comparison, PMWE detections are plotted on the right panel.

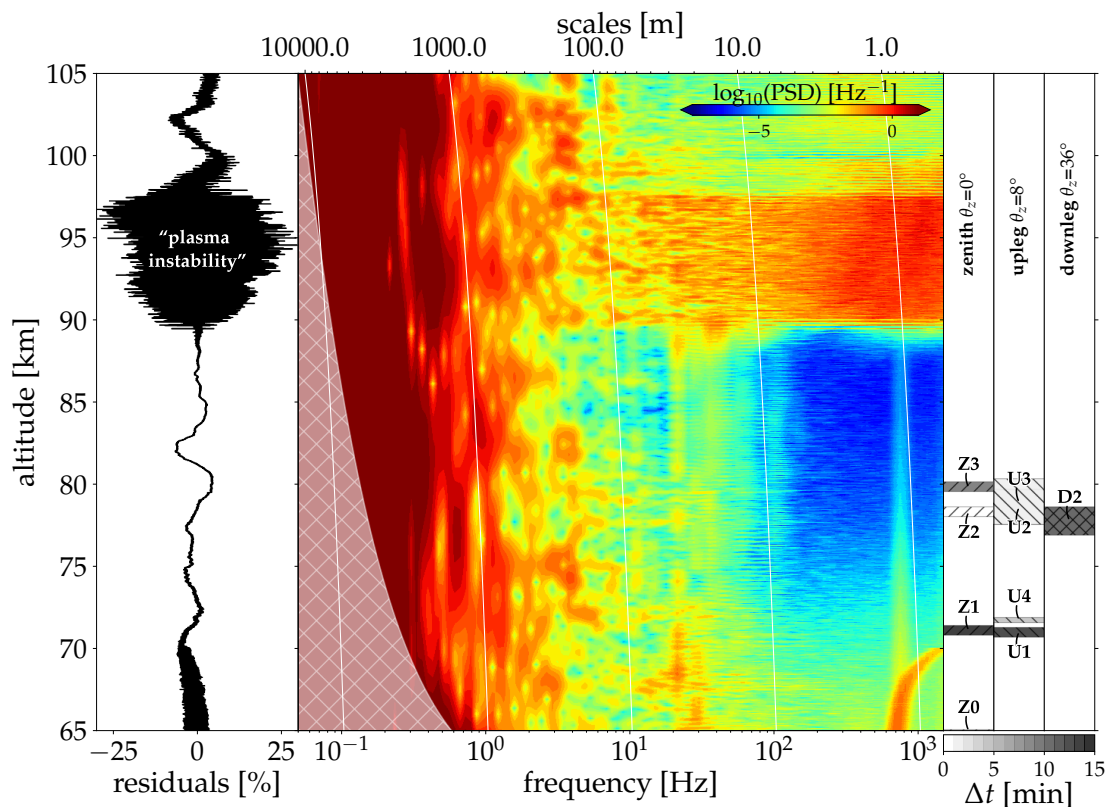


Figure 5.11. Relative electron density fluctuations: Left panel shows residuals (%). PSD from wavelet transform (12th order Morlet) is shown as color plot over frequency/scale (abscissa) and altitude (ordinate). Scales are a function of altitude. White solid lines indicate decades of scales. Color shows  $\log_{10}(\text{PSD})$  (corresponding colorbar in the upper-right). On right panel, labeled radar echoes, with gray-coded  $\Delta t$  (relative to liftoff) is shown.

Similar to the neutral density fluctuations, relative electron density data reveal signatures of atmospheric gravity waves almost in the entire altitude range (see also [Strelnikov et al., 2019](#), where this was shown based on similar measurements.). Between 90–100 km, very strong fluctuations with amplitudes up to  $\sim 30\%$  were measured. These fluctuations contain energy at high frequencies (small scales) which are not coupled to the neutral density fluctuations at those altitudes (see Fig. 5.9). Such strong electron density fluctuations were most likely caused by plasma instabilities, often observed at polar latitudes with various instruments (e.g., [Blix et al., 1994](#), [Sahr and Fejer, 1996](#), [Strelnikov et al., 2009b](#)). Notably, although these fluctuations are ambient at the radar Bragg scale of  $\sim 3$  m, MAARSY did not received echoes from these heights.

Below 90 km, structures of enhanced PSD, cascading from scales of hundreds of meters down to meters, are observed (similar to neutral density fluctuations data). Note, that structures of enhanced PSD with small bandwidths at around  $\sim 700$  Hz (partly drifting to higher frequencies) in the altitude range from 65–82 km (at the lower-right in the color plot of Fig. 5.11) are of instrumental (i.e. electronic) origin. However, they do not affect the turbulence analysis because they only appear at very small scales (high frequency). Similar to spectral analyses of neutral density fluctuations, global wavelet spectra were derived for the same altitude bins of 100 m.

From the comparison of both spectra,  $Sc$  numbers were fitted subsequently. An example of spectra from measured density fluctuations and fitted models is shown in Fig. 5.12 for an altitude of 79.05 km.

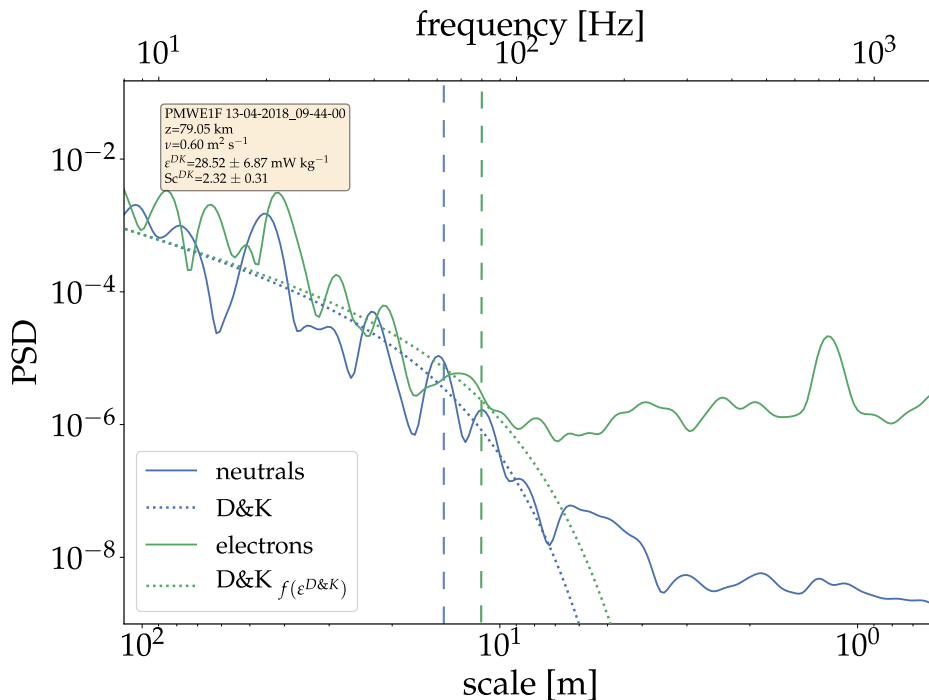


Figure 5.12. Global wavelet power spectra of neutrals (blue) and electrons (green) for a 100 m altitude bin centered at 79.05 km. Dotted lines show fits of the spectral D&K-model for neutral density fluctuations (blue,  $Sc=1$ ) and relative electron fluctuations (green) with  $\epsilon^{D\&K}$  from neutral model fit and  $Sc$  as free parameter. Vertical lines indicate inner scales  $l_0$ .



This spectrum is linked to PMWE #2. For both tracers (i.e., electron and neutral density fluctuations), the D&K-model was applied. For neutral density ( $Sc$  equals unity), the model fit reveals  $\epsilon^{D\&K} \sim 30 \text{ mW kg}^{-1}$ . For a fit of the same D&K-model to electron density fluctuations, this  $\epsilon^{D\&K}$  is used as a fixed parameter, while  $Sc$  is variable. A fit yields  $Sc=2.3$ . Thus, the electron density spectrum is only slightly extended to small scales, compared to the spectrum of neutrals. This extension is caused by the effect of  $Sc > 1$ . Note that the Batchelor  $k^{-1}$  sub-range in the D&K-model was derived as an asymptotic behavior and is pronounced for large  $Sc$  numbers only (i.e.,  $Sc \geq 1000$ ).

As can be seen from Fig. 5.12, the scale where the turbulent spectrum exceeds the instrumental noise level of the electron spectrum is only at slightly lower values compared to the inner scale  $l_0$  (dashed green vertical line), where the transition to the viscous-diffusive subrange takes place. Thus, only a small part of the viscous subrange is resolved. A calculation of the smallest scale of turbulence yields  $\eta_{\text{Bat}} \sim 1 \text{ m}$ . Therefore, scales of turbulence on Bragg scale (i.e.,  $\lambda_{\text{BC}} = 3 \text{ m}$ ) exist, but are not resolved by the sensor. However, the Bragg scale is far within the viscous subrange and, due to the rapid power decrease in this range, did not produce a detectable radar echo in the downleg-pointing beam simultaneously to the in situ measurements. This issue is further discussed in the analysis and in context with other instruments below. Following the procedure described in Sec. 3.2.5, a full profile of Schmidt numbers was derived. Results are shown in Fig. 5.13.

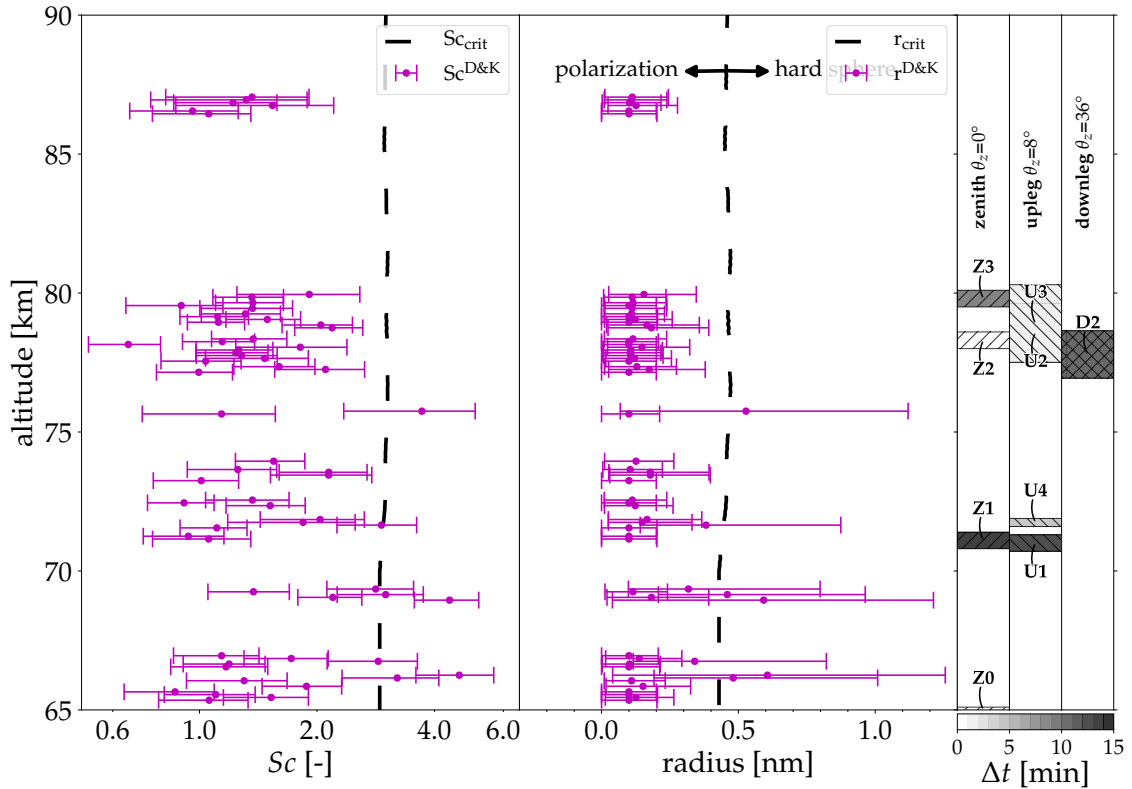


Figure 5.13. Left panel: Profiles of Schmidt numbers derived by using  $\epsilon^{D\&K}$  from Driscoll & Kennedy model results. The middle panel shows the corresponding particle radii. Dashed black lines indicate the transition from the polarization ( $r < r_{\text{crit}}$ ) to the hard sphere diffusion model ( $r \geq r_{\text{crit}}$ ), see also Sec. 3.3. Right panel: Labeled radar echoes with gray-coded  $\Delta t$ .

Vertical black dashed lines indicate the critical  $Sc_{\text{crit}}$  and the corresponding critical radius  $r_{\text{crit}}$ . Below these critical values, radii were calculated using a polarization diffusion scheme. For  $r \geq r_{\text{crit}}$ , a hard-sphere model was used instead. While the discussion on  $Sc$  numbers in Staszak et al. (2021) focuses on the altitude range of upper PMWE events (i.e., 77–80 km), additionally results of the  $Sc$  analysis below 74 km are presented here. From the range of 80–77 km, mean values of  $Sc \sim 1.55$  and  $r \sim 0.15$  nm were obtained, comparable to investigations made before which yields  $Sc \sim 1.5\text{--}2.3$ , and  $r \sim 0.15\text{--}0.3$  nm using a method combining two different turbulence models (see Staszak et al., 2021).

At altitudes below 77 km, derived  $Sc$  values comprise a broader range, i.e.,  $\lesssim 1$  to  $\sim 3$  in a range of 70–75 km, corresponding to equivalent radii of up to  $\sim 0.5$  nm. Below 70 km,  $Sc$  values are even more widespread, reaching  $Sc \sim 5$  and  $\sim 0.6$  nm. Interestingly, Schmidt number values are not randomly distributed everywhere but rather reveal a continuous change from low  $Sc$  to local maxima. This is most clearly visible for the maximum at 66.25 km and 71.25, but also 73.55 km. Values of  $Sc$  in the range of  $\sim 77\text{--}80$  km (where PMWE #2 and #3 were detected) show three distinct local maxima: A narrow layer around 77.25 km, a broader one extending over almost 1 km with center at  $\sim 78.8$  km, and a single peak at 79.95 km.

#### 5.1.4 Comparison of volume reflectivity from radar and in situ soundings

Since the volume reflectivity  $\eta$  in the MLT ultimately results from electron density structures at Bragg scale, a direct proof of whether turbulence works as a structuring mechanism for electrons can be made, by analyzing electron density fluctuation at the Bragg scale, subsequent comparison with the radar signal, and by analysis of the form of the spectrum (i.e. if the measured spectrum equals the spectrum of turbulence or not). The relative electron density fluctuations  $\Delta N_e/N_e$  at  $\lambda_{\text{BC}}^{\text{MAARSY}}$  were derived as a slice of the wavelet power spectrum, shown in Fig. 5.11, and subsequent conversion to  $\eta(\lambda_{\text{BC}})$ , applying Eq. 3.32. Additionally, the absolute electron density, derived by WPE, is used for converting PSD to  $\eta$ . The results are shown in Fig. 5.14.

The in situ measured  $\eta(\lambda_{\text{BC}})$  is shown as solid red line. As discussed before, the increased power on the 2.8 m scale below  $\sim 77$  km is not a geophysical signature and originates from the electronics's noise and, therefore, is plotted as transparent red line. MAARSY observations in the same volume around the time of the descending rocket is shown as a solid blue line. Both instruments do not yield any enhancement, but just show the instruments' noise levels. This is consistent with the results from analysis of individual spectra discussed before (e.g., Fig. 5.12). On its downleg the rocket passed through layers of turbulence, but not through PMWE. In the analysis carried out before, however, small-scale fluctuations of turbulence in both neutrals and electrons were observed in situ, at the same altitudes PMWE was detected  $\sim 13$  min earlier on downleg (PMWE D2) and also south-eastwards, in the zenith and upleg-pointing beams (e.g., Z2 and U2), around the time of measurement. At the same height of PMWE U4 ( $\sim 72$  km), which was observed  $\sim 5$  min after launch, structures of turbulence were measured. This strongly suggests that the in situ measurements detected remaining structures of turbulence, acting on smaller scales ( $\lesssim 2.8$  m), shortly before the rocket launch.

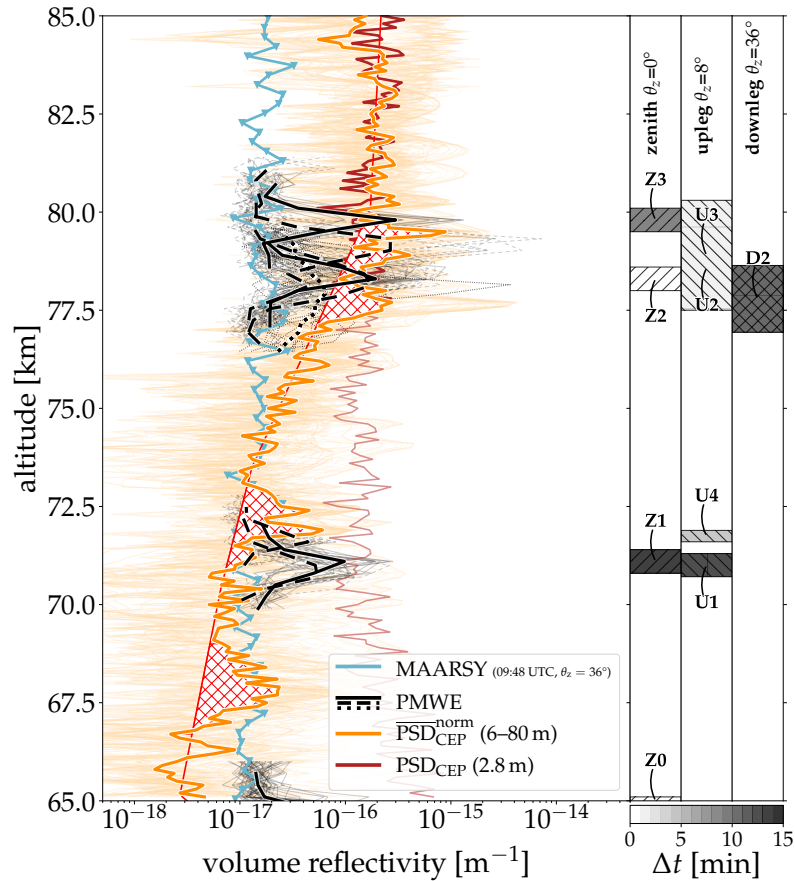


Figure 5.14. Volume reflectivity profiles  $\eta$ , derived by Eq. 3.32, converted from slices at different scales of in situ measured PSD (red and orange lines), and  $\eta$  by radar observations during the time of measurement in the same volume (blue line). Black lines indicate PMWE observations (solid (zenith), dashed (upleg), and dotted (downleg)). The red line shows in situ PSD at  $\lambda_{BC}=2.8$  m. In agreement with simultaneous radar measurement (blue), the PSD at Bragg-scale does not reveal PMWE structures above the noise-level. In orange, the normalized PSD at scales between 6–80 m reveals patches of enhanced values (red-hatched patches). See text for further explanation and discussion.

To validate this interpretation,  $\eta$  is calculated from various scales of the wavelet power spectrum of  $\Delta N_e/N_e$  between 6–80 m (i.e., predominantly within the inertial sub-range). This corresponds to signatures that would be observed by radars operating at  $\sim 1.8$ –25 MHz. The outcome of this analysis is shown as solid orange lines in Fig. 5.14. Thin lines represent individual profiles and the heavy line indicates the mean profile, normalized to the noise level between 77–90 km. This analysis reveals signal enhancements at  $\sim 67$ –69, 71–73, and 77–80 km, illustrated as red-hatched areas between the enhanced signal and the approximated mean noise-level.

The radar observations of PMWE are shown by black solid, dashed and dotted lines for zenith, upleg, and downleg. Thin lines indicate the individual profiles (i.e., with time resolution of the radar) and bold lines show the mean of each PMWE instance.

On the right panel, these PMWE instances are shown as patches revealing information on

altitude and the time difference to lift-off, similar to the figures presented before.

The enhancement between 77–80 km coincides with the PMWE instances #2 and #3, observed by radar (see also [Staszak et al., 2021](#)). Furthermore, the enhancement between 71–73 km overlaps with the lower PMWE instance #1. It is worth noting that the peak of this signal enhancement is at a similar altitude where PMWE #4 was observed ~5 min after liftoff on the upleg-pointing beam, located in south-east direction of the in situ measurements.

The lowest patch of the enhanced in situ signal (67–69 km) is not accompanied by PMWE. At this altitude the ionization is too low ( $N_e \lesssim 2 \cdot 10^8 \text{ m}^{-3}$ , cf. Fig. 5.7) to create significant radar backscatter.

Analyzing the drift of the PMWE instances through MAARSY's field of view yields that PMWE D2 (see Fig. 5.4) appeared in the downleg-pointing beam shortly before the rocket's launch, drifted towards the south-east and, subsequently, appeared in the upleg beam (U2) as well as in the zenith beam (Z2). Since this PMWE was observed simultaneously in the upleg and zenith radar beams, the horizontal extent of the structure was  $\geq 15$  km, i.e., the distance between the two radar beams at the PMWE #2 altitude.

On the other hand, this implies that the horizontal extent at the time of the in situ measurements was  $< 30$  km, which is the distance between downleg and upleg-pointing radar beams.

### 5.1.5 Radar measurements of turbulence

The radar observation of the PMWE instance #2 reveals a good signal-to-noise ratio and therefore allows for detailed analysis of MAARSY data for the derivation of turbulence parameters (see Sec. 3.1). Zenith beam data of HPHW (Half-power half-width,  $\sigma/2$ ), derived from spectral analysis, are shown as black squared markers, measurements of the received power as orange circles in Fig. 5.15. Both quantities were obtained by a vertical average over the vertical extension of the echo, i.e., 77.5–79 km. The dashed-dotted line shows a linear regression to  $(\sigma/2)^2$  in log-space in between the bounds that are marked by vertical red lines.

As discussed in Sec. 3.1, both power and spectral width are related to the turbulent energy dissipation rate  $\epsilon$ . Consequently, if PMWE were created by turbulence creating structures on radar Bragg scale, it would be possible to see changes of PMWE also as changes in spectral width and power. As is apparent from Fig. 5.15, the decrease in power and spectral width are indeed consistent with the interpretation of a decaying PMWE signature.

At the start of PMWE Z2 (i.e., 09:36) both values of spectral width and power are ~10 times larger compared to values at the end of this PMWE at 09:47.

### 5.1.6 Evolution of the PMWE layer

The results discussed before show that the PMWE1F-payload did not directly passed through a PMWE on downleg. However, measurements of residual structures in both electrons and neutrals, in an altitude range where MAARSY detected PMWE before and after launch, are found in the in situ data on downleg. Additionally, MAARSY observations from the zenith beam reveal that the intensity of velocity fluctuations decreased by one

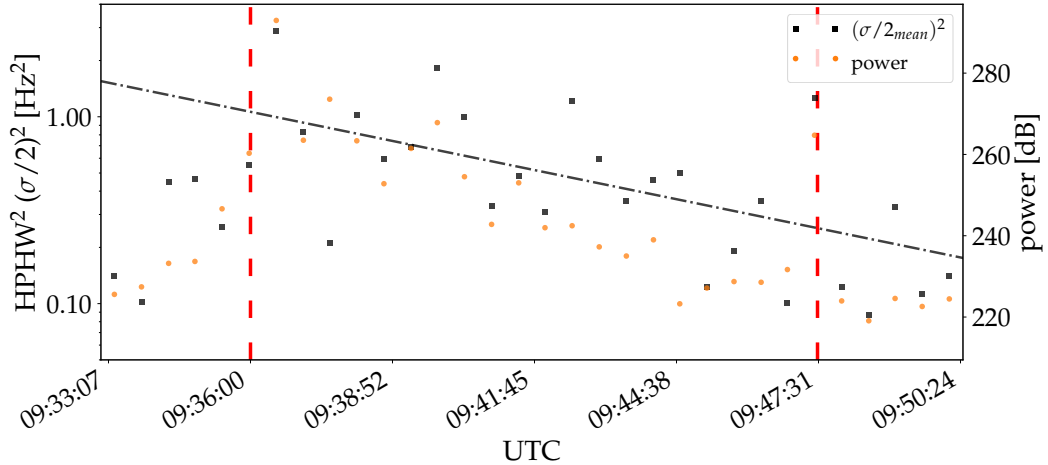


Figure 5.15. Half-power half-width (HPHW, black) and power (orange) derived from the zenith pointing beam of MAARSY at the period of PMWE instance #2. Markers indicate mean values over the vertical extent of the PMWE layer (i.e., 77.5–79 km).

order of magnitude. This strongly indicates an active role of turbulence in the creation of small-scale structures on radar Bragg scale (i.e., 2.8 m), consequently, forming PMWE #2.

To prove if the behavior of this PMWE-layer is in accordance with either hypothesis H1.1 or H1.2, namely that small-scale structures are created by turbulence (with or without MSP),  $\eta$  is calculated on basis of the in situ measurements (see Sec. 3.6.1).

It is proceed as follows: since Saura radar’s time-resolved electron density measurements show almost no variation during PMWE observation,  $N_e$  is assumed to be constant. Spectral width and power (measured by MAARSY) in contrast show that the turbulence intensity (and consequently  $\varepsilon$ ) of PMWE #2 has decreased by one order of magnitude from the maximum (reached shortly after the beginning of detection) to the end of this PMWE instance. Consequently, to reconstruct radar echo’s volume reflectivity  $\eta$ , in situ measured  $\varepsilon$  must be scaled by the same factor  $s \sim 10$ . Fig. 5.16 shows the measured (solid lines) and scaled spectra (dashed-dotted lines) converted to volume reflectivity. This is done for two cases: first, for the “pure” turbulence approach (black lines) and for the “dusty” turbulence case (magenta/cyan, i.e., the case where MSP are involved).

Measured values of  $\varepsilon_0 \sim 40 \text{ mW kg}^{-1}$  and  $Sc \sim 1.5$  represent the mean values between 77–80 km (i.e., the altitude range of upper PMWE instances).  $N_e$ ,  $\omega_B^2$ ,  $\nu$ ,  $H_e$ , and  $H_N$  were taken from the same altitude range and kept constant. Intersections of spectra with vertical lines indicating the Bragg scale (wavenumber) at 53.5 MHz for MAARSY and 224 MHz for EISCAT shows the calculated volume reflectivities which each radar would detect.

Apparent from the results shown in Fig. 5.16, the dissipation rate  $\varepsilon_0$  produces a volume reflectivity  $\eta \sim 10^{-23} \text{ m}^{-2}$  at the MAARSY Bragg scale (black and magenta circles), which is far below the detection limit of MAARSY.

Even in presence of tiny MSPs, resulting in a  $Sc$  number of  $\sim 1.5$ , turbulence creates structures that yield  $\eta \sim 10^{-20} \text{ m}^{-1}$ , –still much to small for radar detection. However, taking into account the decreasing turbulence intensity, and therefore scaling the energy dissipation rates to values which were measured before by MAARSY ( $\varepsilon_1 = \varepsilon_0 \cdot 10$ ), the calculated

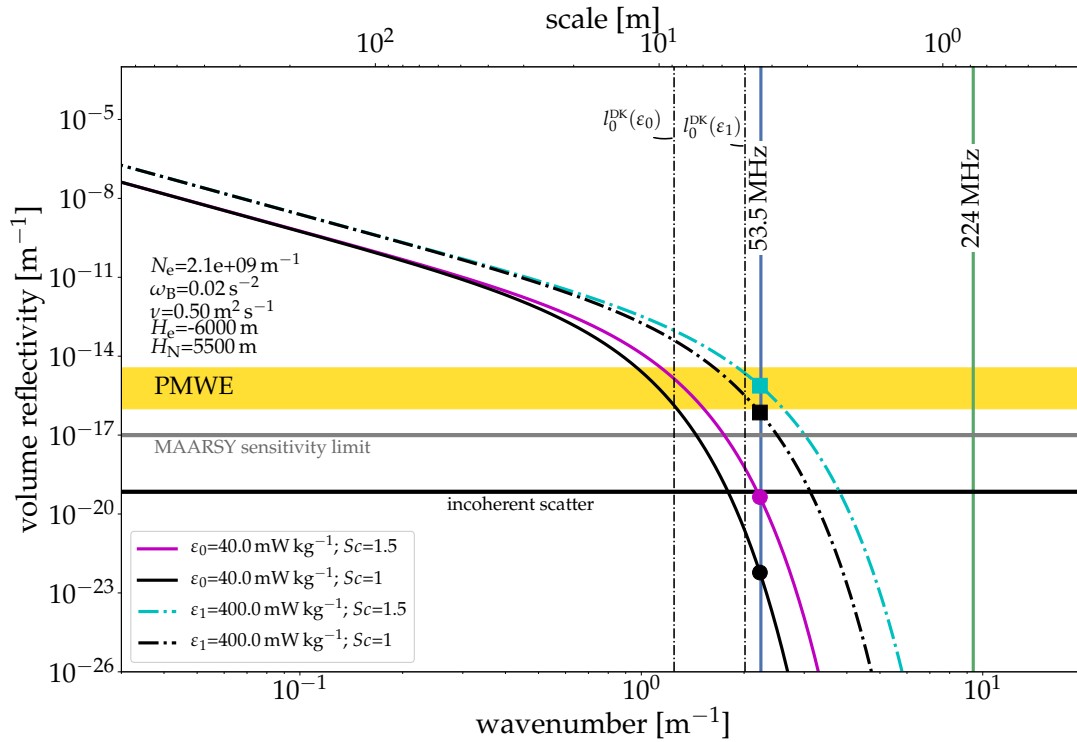


Figure 5.16. Volume reflectivity, derived from power spectra of neutrals (black) and electrons (magenta & cyan). Solid lines give actual CONE measurements. Dashed-dotted lines show spectra from combination of in situ and radar observations. Vertical lines indicate the Bragg scale (wavenumber) for 53.5 MHz (i.e., MAARSY, blue) and 224 MHz (i.e., EISCAT, green). The yellow patch shows the peak values observed by MAARSY in the range of 76–81 km, i.e.,  $\eta$  from  $\sim 1 \cdot 10^{-16}$  to  $3.6 \cdot 10^{-15} \text{ m}^{-1}$ . The gray and black horizontal lines denote detection limits of MAARSY and EISCAT, respectively.

$\eta$  reproduces MAARSY’s observations of  $\eta$ . In this case,  $\eta$  at the Bragg scale of  $\sim 3 \text{ m}$  lies inside the peak values observed by radar between 77–80 km, accounting for  $Sc=1.5$  (cyan square) and at the lower edge of observed values for  $Sc=1$  (i.e., no influence of MSPs). The combined spectra from in situ and radar measurements provide intersections with  $k_{BC}=2.24 \text{ m}^{-1}$  in the transition regime of the inertial-convective ( $Sc=1$ ) or viscous-convective ( $Sc>1$ ) to the viscous-diffusive subrange. Not surprisingly, even the combined (i.e., reconstructed) spectra do not provide structures at scales that can be observed by EISCAT (i.e., at 224 MHz).

In Figs. 5.17 and 5.18, dependencies of  $\eta$  on  $Sc$ ,  $\epsilon$ , and the potential refractive index  $M_n$  are shown to elucidate the entire range of parameters taking part in the creation of PMWE. For these calculations, the same background values that were used in Fig. 5.16 were taken. Individually measured values are indicated by dots, mean values by squares. Error bars, in this case, represent mean uncertainties (details on error estimations can be found in Ap. C).

It can be concluded from Figs. 5.17 and 5.18 that the combined values reveal the echo strengths (i.e., volume reflectivities) that are within the limits of observed  $\eta$  at the range

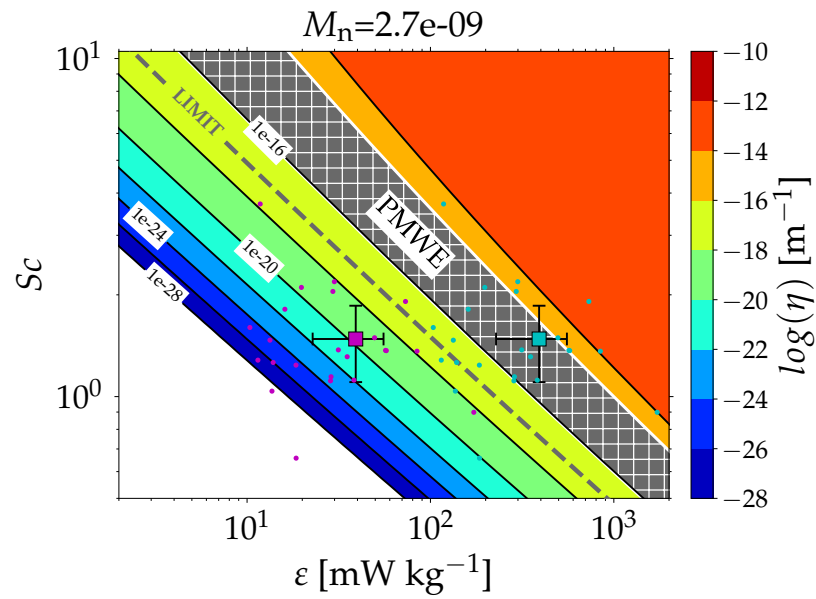


Figure 5.17. Volume reflectivity (color-coded) as a function of  $\varepsilon$  and  $Sc$  derived by Eq. 3.29 using measured background values of  $N_e$ ,  $\omega_B^2$ ,  $\nu$ ,  $H_e$ , and  $H_N$  from the range of 77–80 km. The gray hatched area gives the span of peak values observed by MAARSY in the range of 76–81 km (i.e.,  $\eta$  from  $\sim 1 \cdot 10^{-16}$  to  $3.6 \cdot 10^{-15}$   $\text{m}^{-1}$ ). Individual values are marked with dots, mean values as squares. Corresponding error bars show the mean error of individual measurements. Actual CONE measurements are colored magenta, while reconstructed (i.e., combined in situ and radar observations) ones are colored cyan.

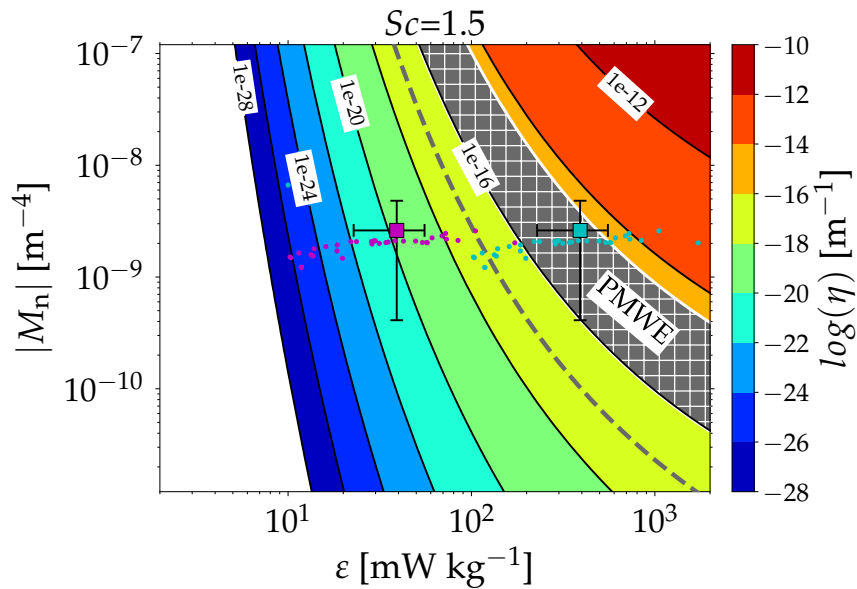


Figure 5.18. Same as Fig. 5.17, but for  $\varepsilon$  and  $M_n$ .  $M_n$  is derived from in situ measurements of the background, according to Eq. 2.12.

of 76–81 km (i.e.,  $\sim 1 \cdot 10^{-16} - 3.6 \cdot 10^{-15} \text{ m}^{-1}$ ).

On the other hand, the in situ measured values (i.e., no scaling applied) are consistent with actual observations of MAARSY during the time of flight.

### 5.1.7 Discussion and Conclusions

Even though some advanced methods were applied and results are presented in more detail in the text above, the discussion and conclusion of the PMWE1F flight have not changed substantially from those presented in [Staszak et al. \(2021\)](#).

The best quality in situ measurements by CONE were conducted in ram conditions, i.e., on the descending part of the PMWE1F rocket trajectory (see Fig. 5.5). However, the PMWE layer D2, observed in the volume of the payloads' descent (i.e., beam tilted  $36^\circ$ ), disappeared shortly before the PMWE1F launch.

MAARSY observations on zenith and upleg-pointing beams revealed PMWE detections simultaneously to the in situ measurements, but not in the same volume. In situ measurements of energy dissipation rates showed that layers of turbulence accompany layers of PMWE (65–81 km, #1, 2, 3 and 4). On the other hand, turbulence was also measured where no PMWE was observed.

A model-consistent comparison of spectra from electrons and neutrals, revealing in situ measured  $Sc$  numbers, yields a mean  $Sc \sim 1.5$ . Higher numbers, up to  $Sc \sim 5$ , were measured in the turbulent layers between 65–70 km. The observed  $Sc$  numbers correspond to (MSP) radii of  $0.1 \text{ nm} < r \leq 1 \text{ nm}$ .

PMWE #1 and #4 appeared as weak signatures in both radar and in situ measurements of turbulence parameters (i.e.,  $(\sigma/2)^2$ ,  $\epsilon$ ). Therefore, the subsequent analysis was focused on the upper PMWE #2 with the strongest SNR and highest values of  $\epsilon$ .

MAARSY observations on the zenith beam reveal that the intensity of PMWE Z2 (Fig. 5.4) gradually decreased from the time of the decision to launch until the payload reached PMWE altitude. Further analysis of power and spectral width confirms that turbulence intensity decreased by one order of magnitude during that period. The correlation between power and spectral width suggests that turbulence was responsible for PMWE formation. Although electron density fluctuations did not resolve fluctuations at MAARSY Bragg scale higher than the instrumental noise level, wavelet spectra of both neutrals and electrons show distinct layers of turbulence in the altitude range of PMWE Z2. These signatures appear at scales  $\geq 6 \text{ m}$  (cf. Fig. 5.14) where they exceed the instrumental noise level (see, e.g., Fig. 5.12). This suggests that a more sensitive instrument could have detect structures at the MAARSY Bragg scale.

The fact that MAARSY did not observe any PMWE on downleg during the rocket passage through the sounding volume can either be explained with high viscous dampening of structures far within the viscous subrange or by an insensitivity of the tilted beam ( $36^\circ$ ) to these structures. On the one hand, oblique-looking radar beams are prone to signal weakening effects due to beam filling issues (e.g., [Sommer et al., 2016](#)) and because of their observational geometry, (e.g., [Hocking, 1989](#)). On the other hand, observations of PMWE #2 drifting through MAARSY's field of view as discussed in Sec. 5.1.4 suggest that the structure forming PMWE was spatially localized and drifted south-eastwards.



A precise analysis reveals:

- The echo drifted in south-eastward direction, i.e., towards  $\sim 150^\circ$  from the north with a velocity of  $\sim 68 \text{ m s}^{-1}$
- Echoes were observed in the zenith and upleg pointing beam for 11–14 min
- This corresponds to a horizontal extent of PMWE #2 of 45–57 km along the drift direction

This estimate of the horizontal extent of PMWE #2 exceeds the distance between the upleg and downleg directed beams of  $\sim 35$  km. Therefore, this strongly suggests that the downleg pointed beam might indeed have only observed the most intense part of PMWE #2 due to the decreased sensitivity of the oblique observational geometry. This part of the structure was most probably created by active turbulence during the 8 min time period where D2 was observed. Interestingly, the PMWE reflectivity increased rapidly, in less than 2 min, at the beginning of the event, whereas its decay took more than 5 min. Accounting for the drift velocity of  $68 \text{ m s}^{-1}$  and a beam cone diameter of  $\sim 5$ – $10$  km at about 80 km, this yields a time interval to fill the entire structure of  $\sim 75$ – $150$  s. This is consistent with the observed behavior in its initial state. Since the decay of this PMWE took much longer, this cannot be solely explained by the beam filling effect. However, such a characteristic with rapid and intense start and slow fade would be expected when the structure was created locally by turbulence (e.g., by GW breaking) and subsequently drifted through MAARSY's field of view.

Since in situ measurements only captured the end of the decaying PMWE #2, the PMWE echo strength was reconstructed to its stage where it was observed in the downleg pointing beam, by combining precise in situ measurements with time-resolved observations by MAARSY. The resulting reconstructed volume reflectivity agrees with those observed by MAARSY, again supporting the interpretation of a decaying turbulent structure.

The reconstruction was made by assuming that the absolute electron density  $N_e$  remained constant during the entire event (Z2). However, the  $N_e$  measured by the Saura radar in an altitude range of 77–79 km (see Fig. 5.1) reveals that in the period from 09:20 to 09:45 UTC, slightly decreases from  $2.1 \cdot 10^9$  to  $1.7 \cdot 10^9 \text{ m}^{-3}$ . Since  $\eta \propto N_e^2$ , a drop in  $N_e$  results in a decrease of  $\eta$ , keeping other parameters constant. Nevertheless, the measured  $N_e$  decreases only slightly and resulting  $\eta$  changes by only  $\lesssim 10^{-18} \text{ m}^{-1}$ , which is even below the sensitivity limit of MAARSY.

Another uncertainty in the reconstruction is the relatively broad distribution of  $\varepsilon$  values over  $\sim 1$  decade within the vertical extension of the upper PMWE of 3 km. This scatter of turbulence energy dissipation rates within a limited altitude range is a well-known property of turbulence, called intermittency (e.g., [Strelnikov et al., 2003](#), [Fritts et al., 2017](#)). Rocket-borne in situ measurements yield instant point measurements, whereas MST radar observations represent an average over the observation volume and integration time. However, if a proper averaging is applied to both data sets, the in situ measurements are well comparable with the radar observations ([Strelnikov et al., 2017](#)). For the PMWE observations, this implies that averaging over the vertical extent of the layer must be applied.

This approach makes the apparently large uncertainty significantly smaller and allows to use the mean values.

Another input for the reconstruction of  $\eta$  is given by the  $Sc$  number, which accounts for the influence of MSPs. The  $Sc$  numbers were derived from spectral analyses of electron and neutral density fluctuations and revealed that only tiny charged particles were abundant in the altitude range of PMWE observation. It is important to notice that  $Sc$  (and therefore MSP radii) estimations are rather an estimate of the lower limit, since the electron probe only resolved a small part of the viscous(-convective) subrange.

However, it is also evident that an improved sensitivity could give only slightly enhance values, i.e.,  $Sc < 10$  or  $r < 1$  nm. Measurements in the upper altitude range of PMWE (i.e., 77–80 km) only reveal  $Sc < 3$ , and correspondingly,  $r < 0.4$  nm, including error bars. At lower altitudes, layers of higher values up to  $Sc \lesssim 5$  ( $r \lesssim 1.0$  nm) were measured.

However, the effect of these low  $Sc$  numbers is difficult to quantify. As apparent from Fig. 5.15, both (reconstructed) spectra for neutrals ( $Sc=1$ ) and electrons ( $Sc=1.5$ ) quantitatively explain the observations by MAARSY, although the neutral case reveals values representing lower  $\eta$  observations. Therefore, the comparison of MAARSY and in situ measurements can neither confirm nor rule out the necessity of the presence of MSP for the PMWE formation.

Anyway, numerous in situ measurements show that MSPs are always present in the MLT (see [Baumann et al., 2013](#), for a recent review). Hence, MSPs unavoidably constitute a background for PMWE formation and their influence is not negligible.

An analysis of wind measurements by Saura radar between 77–80 km around launch time shows that the meridional wind component is stably directed towards the north, whereas the zonal component fluctuates around zero. Both values do not exceed  $20 \text{ m s}^{-1}$  (see [Latteck et al., 2019](#)). The vertical wind, slightly varying around zero, is  $\lesssim 0.6 \text{ m s}^{-1}$  throughout the profile (i.e., 55–85 km). Background winds, derived by the filtering techniques of [Strelnikova et al. \(2020\)](#) reveal that the horizontal wind in the altitude range of PMWE #2 was directed westward, opposed to the drift of PMWE. A very similar behavior of a PMWE is also described by [Rapp et al. \(2011a\)](#). It is known from direct numerical simulations ([Fritts, 2003](#)) and observations (e.g., [Strelnikova et al., 2020](#)) that GW often propagate against the background wind. If such a GW breaks, the generated turbulence moves with the phase of the waves ([Fritts and Alexander, 2003](#)). This behavior is consistent with the picture that PMWE #2, which partly drifts against background wind, originates from turbulence, created by a dissipating gravity wave.

## 5.2 Results from PMWE1D

After the first payload (PMWE1F) was successfully launched, no favorable conditions for in situ measurements inside PMWE were met. Although some PMWE appeared, they were very weak, short-lived, and at relatively low heights. Thus, launching into PMWE was impossible due to geophysical conditions, operational restrictions (i.e., end of funded launch window), and aerodynamic limitations for low-altitude measurements. However, the PMWE1D payload was instrumented with novel instruments and a new generation of the service module that should be at least tested in the frame of the first rocket cam-

paign. Therefore, the rocket was launched during the last minute of the campaign’s launch window on 18th of April at 13:00 UTC. For a brief description of the PMWE1D measurements, see also [Strelnikov et al. \(2021\)](#).

### 5.2.1 Launch conditions

MAARSY was operated in the same mode as for the PMWE1F launch (see Sec. 4.1.1) and did not observe any PMWE suitable for in situ investigation until launch at 13:00 UTC. Remarkably, a strong echo appeared in connection with the rocket traversal through the upleg beam of MAARSY (see mid-panel of Fig. 5.4). The same behavior was already

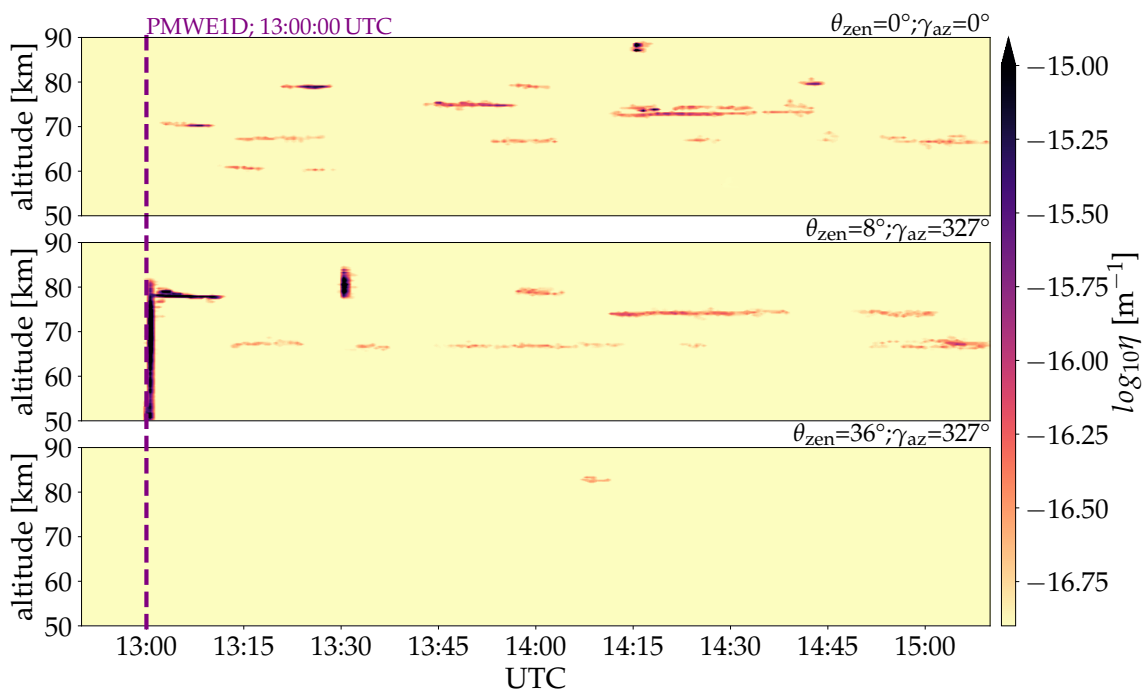


Figure 5.19. MAARSY observations around the PMWE1D launch at 13:00:00 UTC. Zenith, upleg, and downleg pointing radar beams are shown on the top, mid, and bottom panels. The first patches of PMWE appear a few minutes after the launch. Note that another echo ( $\sim 78.5$  km, see mid panel) was induced by the rocket, similar to the observations during the PMWE1F flight. As described in [Strelnikov et al. \(2021\)](#).

observed during the PMWE1F launch. However, it is more apparent here since this echo is isolated from any “natural” echo. This “artificial” echo reveals a strong, thin, and very stable layer at 78 km altitude with a vertical extent of one range gate (i.e.  $\sim 300$  m). Another layer of similar vertical extent appeared  $\sim 1$  min apart. This signature slightly descends from 79.5 km and merges with the echo described before. The total lifetime of this echo was about 11 min.

The strong vertical signature in the upleg pointing beam (i.e., middle panel of Fig. 5.19) shows the rocket traversal through that beam. The vertical dashed line in Fig. 5.19 marks the time of the PMWE1D launch. Shortly after the launch, some PMWE were observed;

the first in the zenith, followed by observations in the upleg-pointing beam. These layers were very thin, often only observed within one range gate, faint, and surprisingly stable in altitude. No remarkable detections were made in the downleg pointing beam.

The PMWE observations correlate well with the  $N_e$  measurements by the Saura-radar, which reveal very low electron densities (i.e.,  $<10^8 \text{ m}^{-3}$  at 70 km) until approximately fifteen minutes before launch, where the electron density started to increase. When the

n

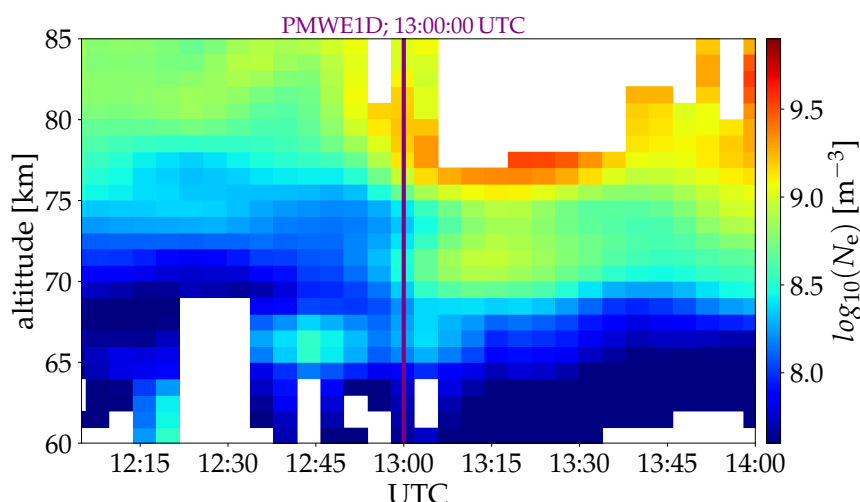


Figure 5.20. Electron density measured by the Saura radar. The vertical line indicates the PMWE1D launch time. As described in [Strelnikov et al. \(2021\)](#).

A similar picture is obtained from the  $N_e$  measurements by the EISCAT-VHF, which is sensitive to higher electron densities at higher altitudes (see Fig. 5.21). No PMWE were

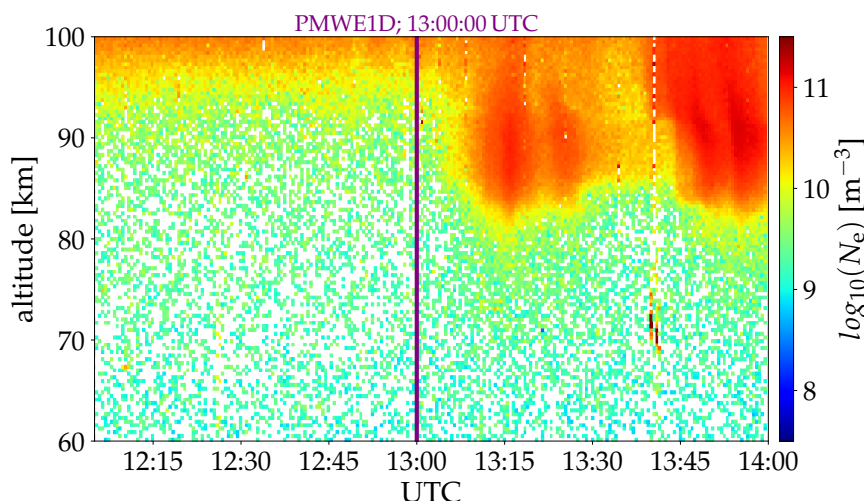


Figure 5.21. Electron density measured by EISCAT in Tromsø. The vertical line shows PMWE1D launch time. According to [Strelnikov et al. \(2021\)](#).

## 5.2.2 Neutral background

The combined results from temperature and density measurements, obtained in situ by the new generation CONE instrument (called Turb3D) and remotely by RMR lidar, are shown in Fig. 5.22. The temperature profile reveals signatures of GWs throughout the entire altitude range. However, the amplitudes in the range from  $\sim 75$ – $82$  km are much smaller compared to the first flight. Moreover, the temperature profile shows distinct layers of near to super-adiabatic lapse rates around 64, 67.5, and 71.5 km.

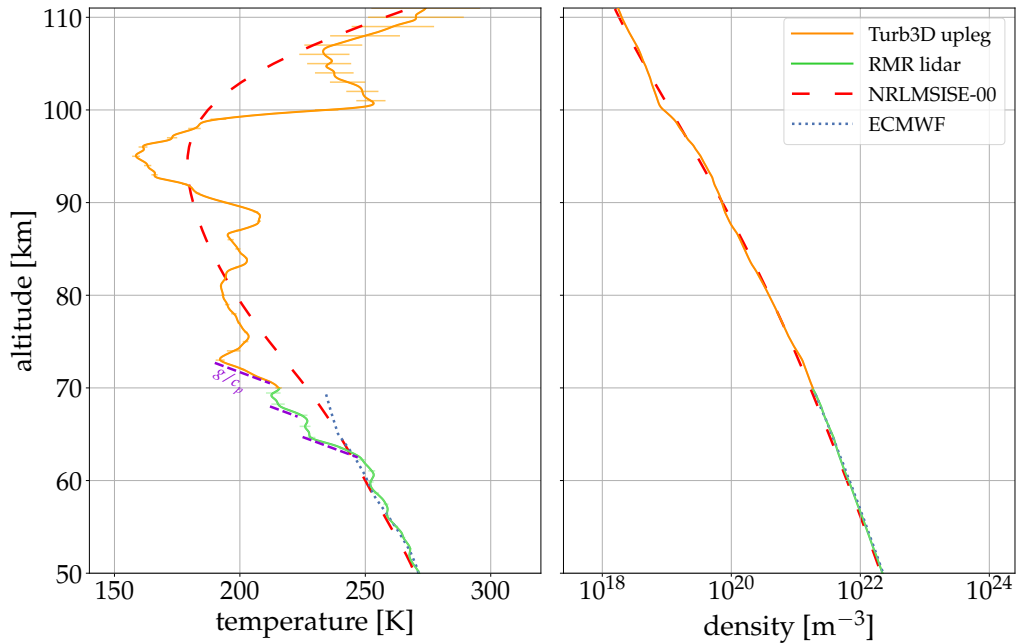


Figure 5.22. Combined measurements by Turb3D (orange) and RMR lidar (green). The left panel shows the temperature profile. Violet lines indicate the adiabatic lapse rate. Neutral density is shown on the right panel. The dashed red and dotted blue lines give reference profiles from NRL-MISE00 and ECMWF (European Centre for Medium-Range Weather Forecasts). As reported by [Strelnikov et al. \(2021\)](#).

From measurements of neutral density and temperature,  $\nu$ ,  $H_N$ , and  $\omega_B^2$  were derived (shown in Fig. 5.23). The profile of kinematic viscosity is similar to the one measured during the first flight and reveals typical values for springtime (e.g.,  $\sim 0.5 \text{ m}^2 \text{ s}^{-1}$  at 80 km). The neutral density scale height and buoyancy frequency are relatively smooth and stable below  $\sim 70$  km and are positive over the entire altitude range.  $H_N$  values decrease above 70 km altitude, from values around 7.5 km to 6 km, where  $\omega_B^2$  slightly increases (i.e., mean and amplitudes).

The rocket-borne measurements of turbulence dissipation rates are shown in Fig. 5.24. The yellow and green symbols with error bars show results of the spectral fits to the model of Heisenberg and Tatarski, respectively. They only reveal three patches of low  $\varepsilon$  near the theoretical limit of  $\varepsilon_{\min} = \nu \omega_B^2$ .

Fig. 5.25 shows measurements of neutral MSPs from the ECOMA instrument. Three profiles of photo currents are revealed by three different flash lamps on downleg of the flight. The currents are produced by photo-electron emissions of MSPs on three different wave-

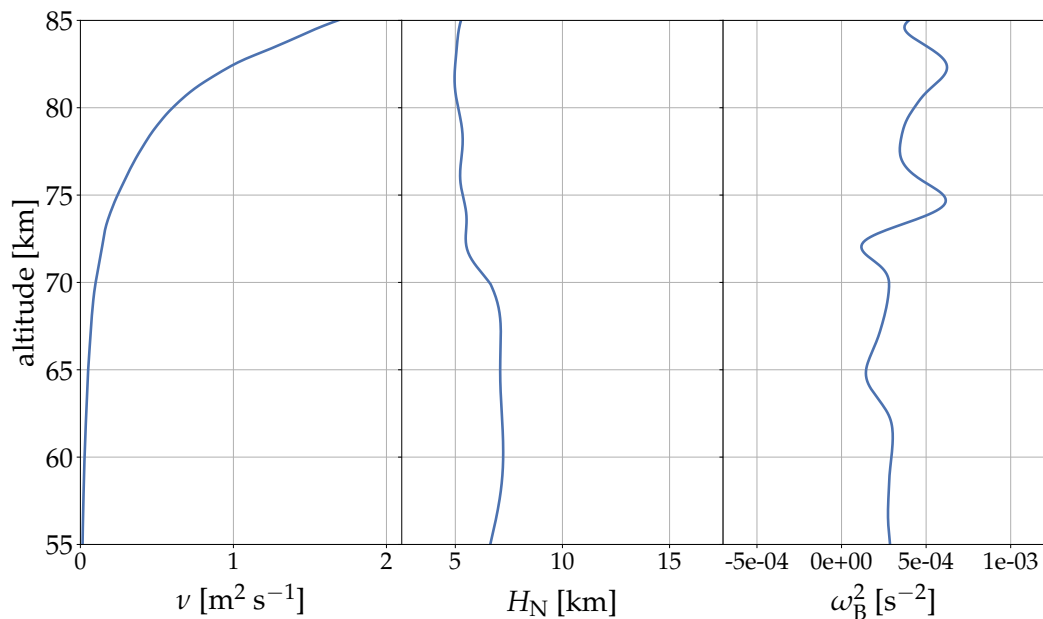


Figure 5.23. Kinematic viscosity  $\nu$ , neutral scale height  $H_N$ , and squared buoyancy frequency  $\omega_B^2$ , deduced from a combination of Turb3D ionization gauge and RMR lidar measurements.

lengths of 110, 190, and 225 nm (see [Rapp and Strelnikova, 2009](#), for a description of the measurement principle). The strongest signal is revealed from the flash lamp with wavelength  $\lambda > 110$  nm, corresponding to a photon energy of  $\sim 11$  eV. This profile reveals that MSPs are present in heights below  $\sim 100$  km. The peak currents are measured at  $\sim 77$ – $80$  km altitude. However, it should be noted that the influence of aerodynamics increases below  $\sim 80$  km. That means, because these measurements were made in wake conditions, the MSP number density in the free atmosphere (and therefore the photo-current) is expected to be larger than that in direct vicinity of the payload.

As has been noted by [Strelnikov et al. \(2021\)](#), the photo-currents can be converted to number density by knowledge (or assumption) of the chemical composition of the MSP to derive the corresponding work function of the material. A conversion to MSP densities can introduce large uncertainties and needs careful treatment of many aspects which is not the scope of the analysis below.

However, the revealed profiles are in agreement with earlier measurements ([Rapp et al., 2011b](#)) and show typical currents corresponding to volume density values in a range of  $\sim 10^{-16}$ – $10^{-15}$  cm<sup>3</sup>/cm<sup>3</sup> of MSP (e.g. for Fe<sub>2</sub>O<sub>3</sub>) for winter conditions ([Rapp et al., 2010, 2011b](#)).

### 5.2.3 Estimation of necessary turbulence dissipation rates $\varepsilon$ for the onset of PMWE

The atmospheric background conditions during the first PMWE events that appeared some minutes after the in situ measurements, and were observed in the zenith and the upleg pointing MAARSY beams, will be discussed in more detail. Fig. 5.26 shows three electron

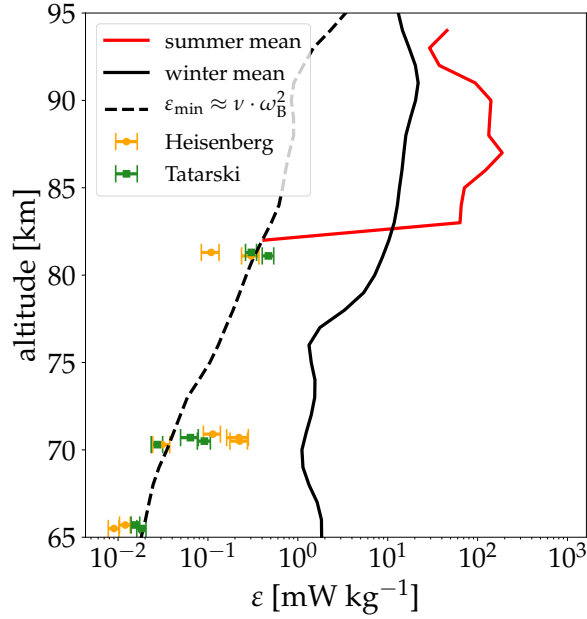


Figure 5.24. Energy dissipation rates  $\epsilon$  deduced from Turb3D measurements for the Heisenberg (yellow) and the Tatarski model (green). The error bars indicate measurement uncertainties (see Ap. C). The single spectral fits can be found in Ap. F.2. The solid red and black lines show summer and winter mean values (Lübken, 1997, Lübken et al., 2002). According to Strelnikov et al. (2021).

density profiles measured by the Saura radar during the flight, at 13:00, at the onset of PMWE at 13:15, and the end of this PMWE event at 13.31. All three profiles reveal electron densities within the same order of magnitude. At the onset and end of the PMWE, gradients at  $\sim 67$  and  $75$  km altitude are much steeper than those measured during flight. The corresponding scale height for the steep gradients is  $\sim 2\text{--}4$  km. The altitudes of these steep gradients correlate with layers of PMWE (see right panel of Fig. 5.26).

No turbulence was measured around  $75$  km, whereas, at  $67$  km, a weak turbulence layer was measured in situ. At the altitude of  $67$  km, all measurements are available to model the volume reflectivity (see Sec.3.6.1) based on turbulence theory. In contrast to the investigations made from the PMWE1F measurements, where the analysis benefits from stable ionization, the situation around the PMWE1D flight was quite dynamic. Therefore, the different vertical structure of electron density is supposed to play the dominant role to the potential refractive index gradient  $M_n$ . Since  $M_n$  and the potential electron density gradient  $M_e$  are proportional to each other (i.e., only connected via a constant for a single radar frequency), the dependencies of volume reflectivity  $\eta$  on  $M_e$  are studied. The other dynamic quantity is turbulence dissipation rate  $\epsilon$ . Other parameters like  $\nu=0.07 \text{ m}^2 \text{ s}$  and  $H_N$  were taken from lidar measurements and are kept constant.

In Fig. 5.27, results of this analysis are shown for two different situations: first assuming “pure” turbulence (i.e., no dust is involved,  $Sc=1$ ), and secondly, taking our findings from MSP measurements from PMWE1F at the same height into account, i.e.,  $Sc\sim 4$  and assuming a “dusty” turbulence process. Notice, that the in situ ECOMA measurements onboard the PMWE1D payload showed the existence of MSPs in the entire height range

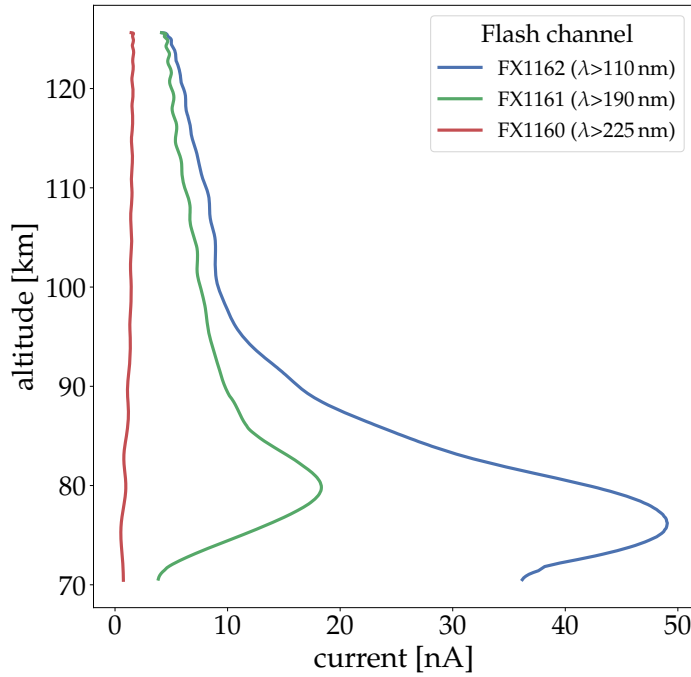


Figure 5.25. MSP measurements by the flash channels of the ECOMA instrument, adopted from [Strelnikov et al. \(2021\)](#).

below  $\sim 100$  km.

The magenta-colored bar in both panels of Fig. 5.27 marks the range of in situ measured energy dissipation rates. The horizontal red and green lines indicate  $M_e$  deduced at onset of PMWE (13:15), and the end of PMWE (13:30). The dashed lines mark the lower value cases, i.e., low  $N_e$  and high  $H_e=4$  km, whereas solid lines indicate the largest values (high  $N_e$  and  $H_e=2$  km). See Fig. 5.26 for values of  $N_e$ .

As shown in Fig. 5.27, the very low dissipation rates measured by Turb3D and the  $M_e$  values obtained from Saura measurements do not reveal  $\eta$  values above the detection limit of MAARSY (neither for  $Sc=1$  nor for  $Sc=4$ ). However, by combining the range of measured  $M_e$  with volume reflectivities measured by MAARSY (gray patch with white hatches), it is possible to obtain a range of  $\varepsilon$  that is needed to produce the corresponding echo strength. This is done twice: for  $M_e$  at the onset of PMWE (green lines), where MAARSY measured  $\eta$  from  $10^{-16}$  to  $10^{-16.5} \text{ m}^{-1}$ , and for values at the end of the PMWE (red lines), where this PMWE has just vanished and, therefore,  $\eta \sim 10^{-17}$  (i.e., MAARSY detection limit). Both scenarios reveal very similar results for  $\varepsilon$ . For the “pure” turbulent model, the range of  $\varepsilon$  is from  $2\text{--}6 \text{ mW kg}^{-1}$ . For the case of “dusty” turbulence, much lower values from  $0.15\text{--}0.6 \text{ mW kg}^{-1}$  were obtained.

## 5.2.4 Discussion and Conclusions

The PMWE1D rocket was launched when MAARSY observed no PMWE. The electron density measurements by Saura radar reveal a low ionization of the mesosphere during



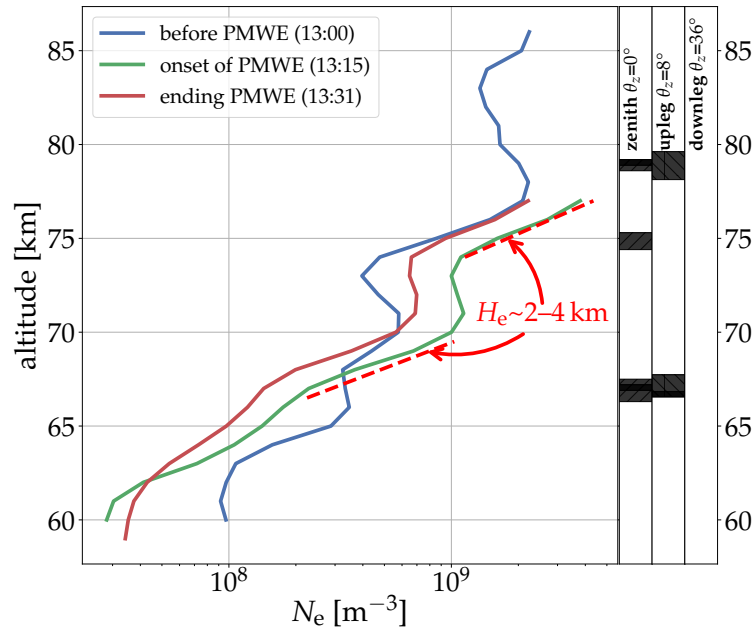


Figure 5.26. Electron density profiles measured by the Saura radar. The profiles show  $N_e$  measurements at the time of launch (13:00, blue profile), the onset of the PMWE event at  $\sim 67$  km (13:15, green profile), and at the end of the PMWE (13:31, red profile). For comparison, PMWE events and their corresponding altitude are indicated on the right hand side.

the morning of the launch that slightly increased shortly before launch.  $N_e$  reached higher values some minutes after launch, when also PMWE were observed by MAARSY at the same time. The EISCAT-VHF makes the same observations. However, the onset of ionization is delayed by about 10 min. The in situ measurements of turbulence reveal several patches of faint turbulence at altitudes where PMWE was observed later on, when the electron density had sufficiently increased. Furthermore, the electron density profiles showed strong gradients with scale heights of only 2–4 km at the altitudes of PMWE.

An analysis of the expected volume reflectivity from in situ measured neutral background and the electron density from Saura reveals that the very low dissipation rates, measured by the new Turb3D instrument, are consistent with the no-PMWE observations by MAARSY. The no-PMWE conditions persist even for the enhanced electron density around 13:10 UTC. This suggests that the electron density increased, but the turbulence intensity must have increased too, for producing the echo that appeared shortly later.

Based on the measured neutral background and the  $N_e$  profiles that were obtained by Saura, it was possible to calculate the turbulence intensity that is needed to produce the volume reflectivity observed by MAARSY at the same time. Two cases were considered: One accounts for a “pure” turbulence, the other accounts for a “dusty” turbulence explanation. The obtained turbulence dissipation rate for “pure” turbulence process (i.e.,  $Sc=1$ ) reveals a range of  $\epsilon$  from 2–6  $\text{mW kg}^{-1}$ , comparable to in situ measured winter mean values by Lübken (1997).

Measurements of MSPs by various different instruments like CONE, ECOMA, and the

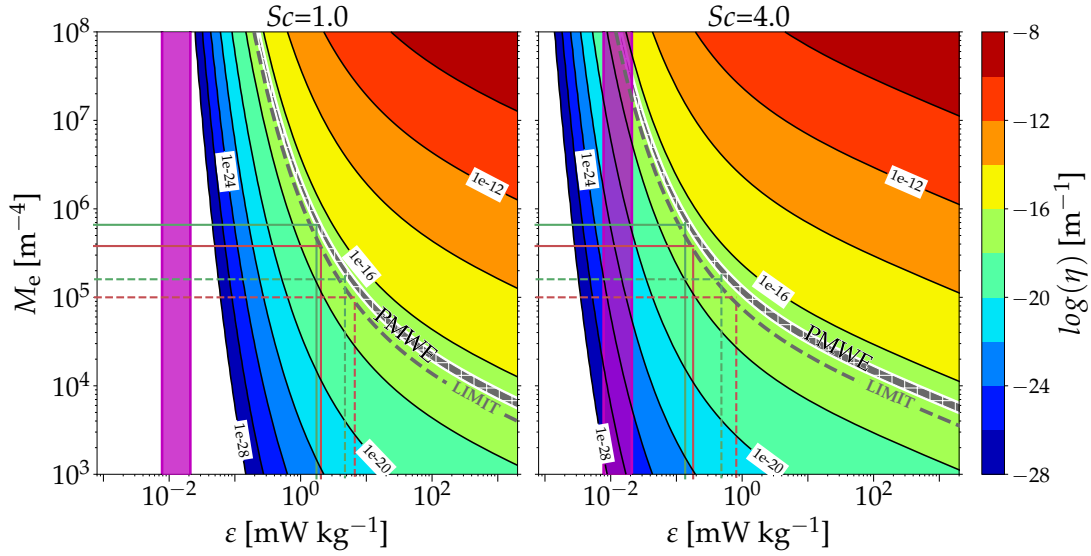


Figure 5.27. Volume reflectivity (color-coded) as a function of  $\varepsilon$  and  $M_e$ , derived by Eq. 3.29, using the measured background values of  $\omega_B^2=2\cdot 10^{-4} \text{ s}^{-2}$ ,  $\nu=0.07 \text{ m}^2 \text{ s}$ , and  $H_N=7.5 \text{ km}$ , for  $Sc=1$  (left panel) and  $Sc=4$  (right panel). The dashed gray line marks the sensitivity limit of MAARSY. The gray hatched area reveals  $\eta$ -values observed within the PMWE layer. Horizontal lines indicate  $M_e$  values derived for varying  $N_e$  profiles, measured by the Saura radar (colors correspond to colors in Fig.5.26, i.e., green for onset, red for end of PMWE). The vertical lines mark the value of  $\varepsilon$  that are necessary to produce the observed echo strength.

ROMARA mass-spectrometer (see [Stude et al., 2021](#)), show that MSPs are present in the entire altitude range of the PMWE observations. Therefore, the “dusty” turbulence theory is applied using the  $Sc$  number that was derived by in situ measurements on PMWE1F, i.e.,  $Sc=4$  around 67 km. The values of the resulting  $\varepsilon$  are approximately one order of magnitude lower, i.e.,  $0.15\text{--}0.6 \text{ mW kg}^{-1}$ , compared to those derived from “pure” turbulence theory. However, the in situ measurements of  $\varepsilon$  were made about 10 min before the onset of PMWE and revealed values of  $7.8\cdot 10^{-3}\text{--}2.1\cdot 10^{-2} \text{ mW kg}^{-1}$ . These values are very low and near the theoretical minimum. The period of 10 minutes is similar to the period discussed for the first flight, when a weakening by about an order of magnitude in the spectral width was observed by MAARSY, shortly before the PMWE1F launch (see Fig.5.15). This difference of measured faint  $\varepsilon$  and expected ones (for  $Sc=4$ ) is consistent with the turbulence intensity rate observed shortly before the first (PMWE1F) flight.

Moreover, this behavior agrees with results from DNS simulations of GW breaking by [Fritts et al. \(2017\)](#). There, it is shown that the time between the onset of turbulence and intense dissipation is about two buoyancy periods (i.e.,  $2\cdot T_B\sim 10 \text{ min}$ ). The same simulations reveal that a mean turbulence intensity develops approximately symmetrically around a dissipation maximum. In other words, the rate of increase and decay of the mean turbulence intensity is the same around its maximum. Nonetheless, drifting PMWE was observed during PMWE1F, showing that turbulence structures (and therefore intensity) can be advected horizontally.

The intensity of turbulence dissipation rates can vary by  $\sim 2\text{--}3$  orders of magnitude ([Strelnikov et al., 2017](#)). Although, the same measurements show that these variations are rather

expected on timescales of hours than of several  $T_B$ . Thereby, it is not clear if an intensification of turbulence of two orders of magnitude within two buoyancy periods, that is needed to explain the turbulence dissipation rates for a “pure” turbulent process, is a realistic scenario.

### 5.3 Verification of the viscous waves theory

The data obtained from both flights were carefully analyzed to find indications that support the theory that an ion acoustic wave–viscous wave mechanism could have created partial reflection visible in the radar. As discussed before, the spectral analyses of the in situ measured neutral and electron density fluctuations did not show sufficiently strong fluctuations on the 3 m Bragg scale.

Moreover, it is not known which form a spectrum, originating by such a mechanism should have. Otherwise, it was shown that turbulent patches occupied the altitudes at which PMWE were observed. This alone contradicts the necessary requirement of a laminar flow region, that is required to, theoretically, allow a once generated viscosity wave to propagate by up to one wave-period (Hocking, 2003). This is because turbulence acts as an additional viscosity that would instantly diffuse such a viscosity wave. Since it is arguable if a wave of such a short extent could be clearly seen in the data (Nyquist resolution of, e.g., the electrostatic CONE probe is 2 kHz, thus  $\sim 0.5$  m), the background was also carefully analyzed.

In the theory, it is expected that steep gradients, e.g., inversions in the vertical temperature profile of 10–100 m, provide surfaces for transfer from ion-acoustic infrasound waves to viscous waves, Hocking (2003). No such steep gradients or steps were found in our high-resolution data (i.e., not smoothed, binned, etc.). Furthermore, no other parameter influencing the radar refractive index showed such steps of high amplitude and short vertical extent.

The wind measurements by the Saura radar also did not observe the extremely high horizontal velocities that have been proposed as a distinct feature of the viscosity waves, (Kirkwood et al., 2006). Moreover, such a mechanism is associated with enhanced vertical winds (dependent on the tilt of the wave, see Fig. A.4). However, the measured vertical velocity was much lower ( $< 0.6 \text{ m s}^{-1}$ ) than necessary for the explanation by viscous waves.

A mechanism of viscous waves which extends only in the order of one Bragg scale (i.e.,  $\sim 3$  m) would create either echoes with a very limited vertical extend (e.g., with the contribution of only one or a few layers of viscous waves in one range gate), or powerful reflection (i.e., many partial reflections of one or more range gates). However, the observations made by MAARSY instead showed moderate values of  $\eta < 10\text{--}14 \text{ m}^{-1}$  and structures that often extend over more than a kilometer, with the most substantial reflection from the cores of these echoes.

## 5.4 Artificially induced radar echoes

Another feature that was observed on both flights (PMWE1F and PMWE1D) was the creation of an “artificial” radar echo. At the first flight, two layers in connection with the rocket traversal through the upleg-pointing beam were observed at 74.7 and 78.7 km. These echoes reveal a slight upward drift of 800–900 m (1 min after the rocket traversal) and disappeared after 4 and 6 min, respectively. Moreover, the upper artificial echo seemed to reinforce the out-fading structure that was observed before and has been discussed in detail. At the second flight, one single “artificial” layer at 78.1 km was induced during the rocket traversal and disappeared 11 min after its onset. In this case, the “artificial” character is even more clear, since no other natural echo was observed in connection to this event. All these echoes extended vertically over ~1 km.

The reasons for these echoes are not clear. However, with our knowledge of coherent radar scattering, it can be proposed that, similar to their natural counterpart, they are created by Bragg scale structures.

Although, the payload and the motor are effective reflectors (i.e. comparable to radar Bragg scale in length) for radar waves (see e.g., [Renkowitz et al., 2015](#), where scattering from the rocket was used to validate the radiation pattern of MAARSY) as is visible as vertical signal enhancements in Fig. 5.4 and Fig. 5.19, it is worth pointing out that the artificial echoes are organized horizontally and could not be reflections from the sounding rocket itself.

Instead, a source of such radar signals could be the complicated aerodynamics of the supersonic flow around the payload, with  $Ma \gg 1$  and  $Re \sim 6 \cdot 10^3$ , that produces such small scales. The critical Reynolds numbers are usually given in a range of  $2 \cdot 10^3$  (pipe flows) to  $10^5$  (flows along a flat plate) and also depend on the intensity of perturbations in the upstream flow (e.g., [Schlichting, 2005](#)). In supersonic flows, besides bow shock, compression shock, and expansion waves, a turbulent Kármán wake may envelop, with expanding structures in the lee of the rocket (e.g., [Friedrichs, 1963](#)). Another explanation is that the rocket’s motor has transported smoke particles in layers of turbulence and, subsequently, altered the diffusive properties of the electrons (i.e.,  $Sc \gg 1$ ). This would allow turbulent structures to extend to smaller scales, according to the “dusty” turbulence theory. Another mechanism including (infra-) soundwaves induced in situ by the rocket’s shock waves, however, is not a promising candidate, since it would only allow for echoes with a maximum lifetime of 4–4.5 min at 80 km. This is the approximate time a sound wave, generated near the ground, needs to propagate to an altitude of 80 km. The lifetime of the artificial echo on the PMWE1D flight, however, was 11 min. Furthermore, such a mechanism should produce a radar echo at least in the co-located beams, i.e., it should be visible in zenith beam at about the same time as it is observed in upleg-pointing beam.

## 6 | Summary and Outlook

In the frame of this work, data from the first sounding rocket campaign dedicated to the investigation of Polar Mesosphere Winter Echoes (PMWE) was analyzed and discussed. This rocket campaign took place at the Andøya Space Center (ASC) at the Norwegian island of Andøya (69°N, 16°E) in April 2018. It involved the launch of two sounding rockets, equipped with numerous instruments to precisely measure small-scale fluctuations in all constituents of dusty plasma and neutrals. The atmospheric background was characterized simultaneously and in the same volume by rocket-borne measurements and ground-based facilities; lidar and radars. Such common-volume investigations are only possible due to the steering capabilities of these instruments. The supporting ground-based instruments further provided time resolved information. This thesis aimed to shed light on the yet unknown creation mechanism of PMWE. After an extensive review of the theory of coherent radar scattering and careful study of the dynamical processes, which can create small-scale fluctuations, and the relevant background parameters needed to generate the radar echoes, three hypotheses were formulated to be proven in this work. Briefly, the main findings of this thesis are:

- The analysis of both rocket flights showed that all measurements support a turbulent mechanism as an explanation for PMWE.
- Moreover, the existence of charged MSPs, measured by three independent in situ instruments in altitudes of PMWE, is evident.
- Detailed quantitative studies of both flights showed that turbulence in interaction with tiny MSPs can consistently explain all measurements, both, rocket-borne in situ measurements and ground-based observations by radar.
- Within the investigations of this thesis, no indications supporting the hypothesis of viscosity waves were found. Instead, only arguments that are not in agreement with this theory, like measurements of turbulence in the altitude of PMWE, no steps in temperature and densities, no observations of extremely high horizontal velocities, and a too short lifetime for explaining an “artificial” echo, were found.

In summary, the measurements of the PMWE-1 campaign clearly show that turbulence in combination with MSPs has created the observed PMWE, thus confirming the hypothesis H1.2.

Although the hypothesis of “pure” turbulence (H.1.1), which does not take MSPs into consideration, does not precisely reflect the geophysical findings, it applies for cases where

$Sc$  does not differ much from unity. This is because low  $Sc$  numbers only slightly extend the turbulence spectrum to smaller scales. Also, a careful search within the PMWE-1 data for evidence hinting towards the alternative explanation of a mechanism including viscous waves (H.2) did not support this theory.

Even though the atmospheric conditions during the flights analyzed in this thesis were very different, they conclusively support the “dusty” turbulence hypothesis H1.2.

The analysis from the PMWE1F flight on the 13th of April at 09:44:00 benefits from ionospheric conditions that were remarkably stable and revealed a relatively low and smooth ionization. Around the time of launch, PMWE were observed. The main findings of this flight are summarized as follows:

- During the time of in situ measurements, remains of intense turbulence were measured. Structures on Bragg scale were below the sensitivity of the CONE-EP, far within the viscous subrange, and therefore too weak to create a detectable radar echo. This is consistent with the no-PMWE observations at the downleg-pointing beam of MAARSY.
- $Sc$  number measurements yielded only small numbers, most of them between 1–2 in the range of 75–80 km, and larger numbers of up to 5–6 at lower altitudes. This corresponds to tiny MSPs (0.1–0.2 nm) in the upper part and maximum radii of  $\lesssim 1$  nm between 65–70 km.
- The combination of precise in situ measurements of turbulence, the atmospheric background, and observation of the evolution of the spectral width measured by MAARSY show that a turbulent process involving tiny charged MSPs explains the echo strengths observed by MAARSY shortly before launch.
- The winds obtained by Saura showed no unusually high velocities. An analysis of the background winds and the drift velocities rather draws a dynamical situation that is likely to invoke GW breaking and subsequent production of small scales.

In contrast to the first flight, the initially low ionization of the D-region during the time of the PMWE1D flight changed towards enhanced ionization conditions with high electron densities and scale heights of partially less than 2 km some minutes later. The second instrumented sounding rocket, PMWE1D, was launched into conditions where no PMWE were observed. The echoes appeared only when the ionization reached an enhanced state. The results of the second flight are summarized as follows:

- In situ measured turbulence was very faint, revealing fluctuations with the smallest scales similar to the Bragg scale of three meters. However, patches of turbulence were measured at altitudes that coincides with heights where PMWE appeared some minutes after the in situ soundings.
- Those fluctuations, in combination with relatively low electron densities and large scale heights, could not produce any PMWE.
- A detailed study for a PMWE layer at 67 km revealed that turbulence must have been more intense than what has been measured in situ 10 min before the echo appeared.

- A scenario of a turbulent creation mechanism, involving MSPs, reveals that the turbulence intensity must have been at least one order of magnitude higher than the measured values. Higher values of  $\varepsilon$  would be necessary to explain the measured volume reflectivities by a “pure” turbulence approach. Those values match the winter mean values. However, these  $\varepsilon$  are two orders of magnitude higher than those measured in situ only about ten minutes before.
- By assuming a “dusty” turbulent mechanism, the absolute intensification rate of turbulence is comparable to the rate observed and discussed during the first flight. Furthermore, it is in accordance with DNS simulations and recent studies of temporal variability of turbulence in the MLT.

Both flights revealed “artificial” echoes in the upleg-pointing radar beam, which were induced in connection to the rocket traversal. It is expected that a similar mechanism as the one discussed for its natural counterpart (PMWE) caused these “artificial” echoes. A theory that includes an infrasound-viscous wave interaction does not provide an auspicious solution since the maximum lifetime of such an echo would be much shorter than the one observed at the second flight. Another explanation is the formation of structures at the radar Bragg scale by aerodynamic effects in the vicinity of the rocket. The corresponding  $Re$  number of  $\sim 6 \cdot 10^3$  may be sufficient to create an unsteady flow, including scales of  $\sim 3$  m in the downstream flow of the payload. A third explanation involves smoke particles originating from the rocket’s motor. According to the “dusty” turbulence theory, the spectrum of turbulence gets extended to smaller scales, by injecting smoke particles either into an existing layer of atmospheric turbulence or into a turbulent wake of the motor. In both cases, it is not obvious why these echoes only appear in very thin layers at certain altitudes. Both mechanisms should be studied in more detail regarding aerodynamic effects and boundary-layer stability as well as regarding the role of smoke particles from the rocket’s motor.

A second PMWE field campaign is planned to take place in autumn 2021. Within this campaign, two similar payloads will be launched with many improved instruments. The results shown in this thesis imply that turbulence intensity can vary substantially (i.e., at least one order of magnitude) within short time periods (i.e., of two buoyancy periods) and also in its horizontal distribution. The evolution of turbulence intensity, the role of (large) particles inside a PMWE layer and the artificially induced echoes could be precisely measured in situ by salvo measurements, i.e., a launch of both rockets in a short time period within a few minutes. The question of the horizontal structure of turbulence could be answered by 3D in situ soundings, using a further developed multi-satellite Turb3D experiment. This concept provides simultaneous measurements of three CONE instruments, ejected from a sounding rocket. To finally exclude viscous waves as a mechanism for PMWE formation, high-resolution wind measurements using the Chaff-technique (i.e., by exposing snippets of radar reflective foil and tracking them by radar) will be performed in the frame of the next campaign since it was speculated that wind measurements by the Saura radar might not have sufficient range resolution to observe the very high velocities associated with such a mechanism. Finally, direct measurements inside an active PMWE would provide even better quantitative results, although the first campaign showed that this is the most challenging part of the experiment.





# A | Viscous wave theory for the D-region case

A theory of gravity wave (GW)/infrasound–viscous wave interaction was proposed to explain strong radar returns from stratosphere and mesosphere (Hocking et al., 1991). In this picture, it is supposed that GW or infrasound waves originate from lower altitudes, interact on critical layers and generate viscous waves on radar Bragg scale, evanescent within  $\lesssim 1/2$  radar wavelength and generate strong partial reflection.

## A.1 Potential refractive index gradient at 2, 53.5, and 224 MHz

Hocking et al. derived an expression for the effective reflection coefficient  $R$ , given by (their Eq. 40):

$$R = 0.4 \left( \frac{k}{|m|} \right) \frac{1}{\omega} M_n u' \quad (\text{A.1})$$

with ratios of horizontal and vertical wavelength  $k/m$ , viscosity wave frequency  $\omega$ , potential (or effective) refractive index gradient  $M_n$  and horizontal wind fluctuation  $u'$ .

In a subsequent article, (Hocking, 2003) stated that there is an error on one input variable. However, a corrected formula (Eq. 8 in Hocking, 2003) does not allow to directly locate this error because some parameters from Eq. A.1 were combined to a single factor. Therefore,  $M_n$  and  $R$  are recalculated using the same sources that were given by Hocking et al. (1991) as follows:  $M_e$ , see Eq. 2.12 is derived by knowledge of background density and temperature profiles. At this place, typical values were used for the neutral terms. Thus,  $H_e^{-1} = 1.4 \cdot 10^{-4} \text{ m}^{-1}$ ,  $\omega_B = 0.021 \text{ s}^{-1}$ , acceleration by gravity  $g = 9.81$ , are constant, while  $N_e (H_e)$  is taken from Mechtly et al. (1972) as it was done by Hocking et al. (1991).

Original  $N_e$  profiles are shown in Fig. A.1.

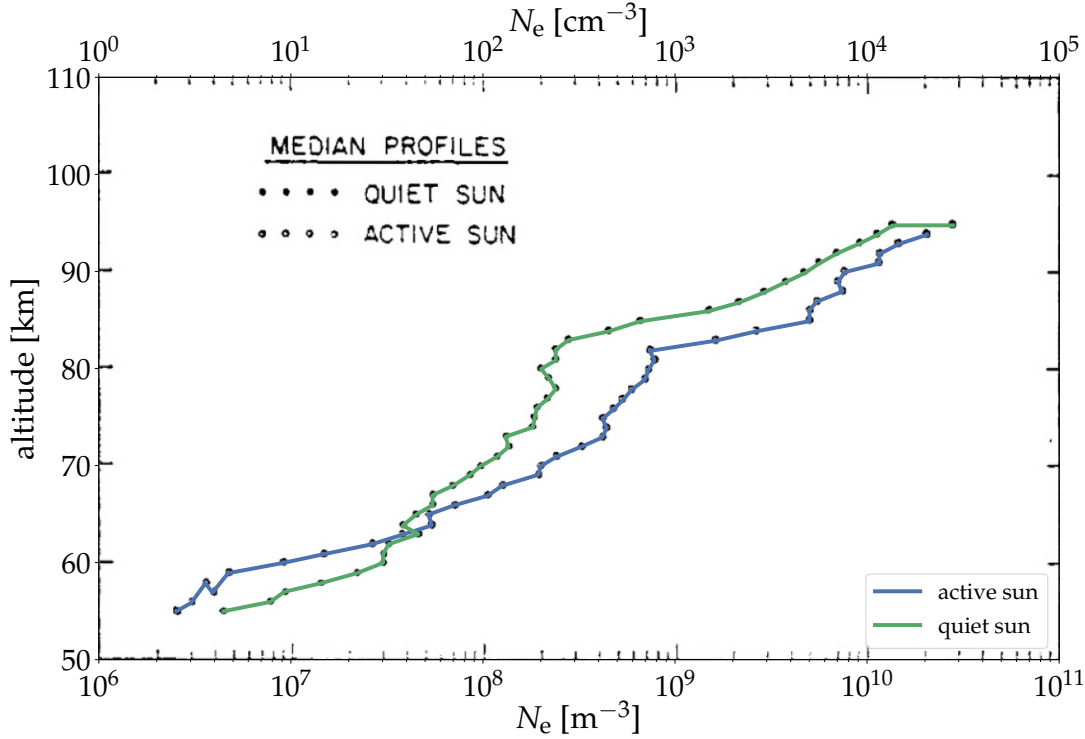


Figure A.1. Median electron density profiles adopted from Mechtly et al. (1972) for quiet and active sun conditions (deduced from five profiles each).

The converted  $M_e$  profiles are shown in Fig.A.2. Note, that terms of neutrals are kept constant for the whole profile.

The potential refractive index gradient  $M_n$ , is calculated according to Eq.2.12 for 2 MHz, 53.5 MHz, and 224 MHz, for active and quiet sun conditions and are shown in Fig. A.3. The value of  $M_n$  at 70 km reported by Hocking et al. (1991) is  $\sim 1$  order of magnitude higher than those calculated here.

For recalculation of  $R$ , same values of  $k/|m|=0.02$ . (corresponding to  $1^\circ$  tilt of phase fronts to horizontal), kinematic viscosity  $\nu=0.1 \text{ m s}^{-1}$  as given in Hocking et al. (1991) are used for  $\lambda_\nu=\lambda_{BC}(2 \text{ MHz})=75 \text{ m}$ . The relation between the viscous wave wavelength  $\lambda_\nu$ ,  $\nu$  and period  $T$  is given by (Hocking et al., 1991):

$$\lambda_\nu = 2(\pi \cdot Sc \cdot \nu \cdot T)^{0.5}, \quad (\text{A.2})$$

where  $Sc=1$  for viscous case, and  $Sc<1$  for diffusive case. For  $\lambda_{BC}(2 \text{ MHz})=75 \text{ m}$ , Eq. A.2 yields a cyclic frequency of  $\omega=1.4 \cdot 10^{-4} \text{ s}$ . Additionally inserting  $u'=2 \text{ m s}^{-1}$  into Eq. A.1 yields  $R$  values of  $6 \cdot 10^{-7}$  and  $1.5 \cdot 10^{-6}$  for quiet sun and active sun, respectively. Not surprisingly (due to erroneous  $M_n$ ), these values are  $\geq 1$  order of magnitude lower than  $R \sim 10^{-5}$ , given by Hocking et al. (1991).  $R$  values at 70 km are typically between  $\sim 10^{-6} - 10^{-4}$  (cf. Hocking et al., 1991, and references therein).

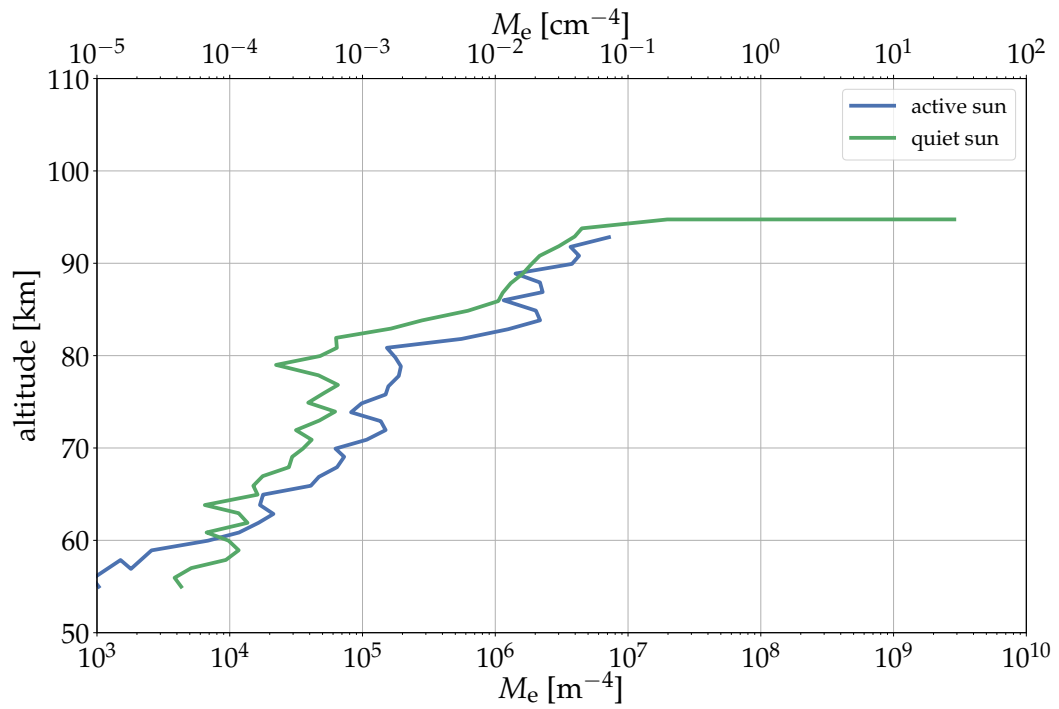


Figure A.2.  $M_e$  for constant values of  $H_e^{-1}=1.4 \cdot 10^{-4} \text{ m}^{-1}$ ,  $\omega_B=0.021 \text{ s}^{-1}$ ,  $g=9.81$ .

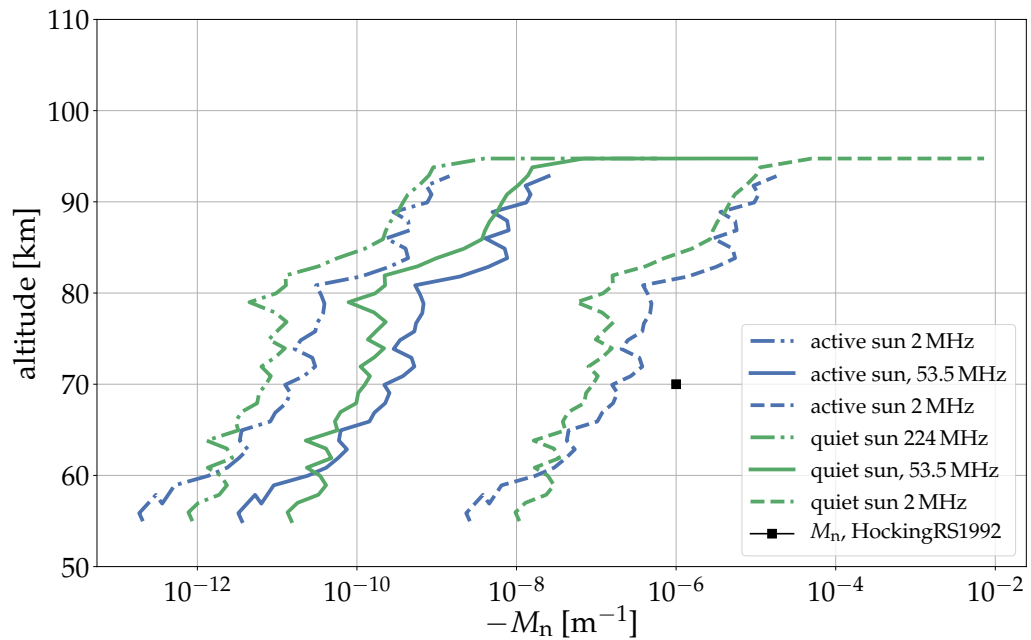


Figure A.3.  $M_n$  for constant values of  $H_e^{-1}=1.4 \cdot 10^{-4} \text{ m}^{-1}$ ,  $\omega_B=0.021 \text{ s}^{-1}$ ,  $g=9.81$ , for Bragg scales of  $\lambda_{BC}=2.8 \text{ m}$  (53.5 MHz), and  $75 \text{ m}$  (2 MHz).

## A.2 Parameters for infrasound for ~50 and 224 MHz

D-region calculations were only for 2 MHz radars in the paper discussed above. However, [Hocking \(2003\)](#) speculated that the same mechanism could be used for radars at higher frequencies (i.e., 50 and 224 MHz) to explain mesospheric echoes as well. Proposing infrasound wave interaction on critical layers on temperature steps of hundred meters vertical extend, creating viscous waves at radar Bragg scale (i.e., 3 and 0.7 m). [Kirkwood et al.](#) connected these proposals to observations of PMWE and also considered the case (which was also discussed in [Hocking, 2003](#)) of diffusive waves, that is  $D_e > \nu$ , and consequently,  $Sc < 1$ . Since in situ measurements of  $Sc$  (e.g., [Asmus et al., 2017](#)) in the winter mesosphere show that  $Sc$  can be substantially greater than unity. This case is included in Fig. A.4. Fig. A.4 shows the relevant parameters for partial reflection scattering for D-region conditions for radars at 53.5 and 224 MHz, similar to that one be found in [Kirkwood et al. \(2006\)](#). Data for density and temperature to derive  $c$  (speed of sound) and  $\nu$ , are taken from NRLMSISE-00 ([Picone et al., 2002](#)). Solid, dashed, and dotted lines in Fig. A.4 show cases of  $Sc=1$ ,  $Sc<1$ , and  $Sc>1$ , respectively. The blue and green graphs in Fig. A.4b, c, and d represent cases of  $\lambda_{BC}=2.8$  m, for 53.5 MHz and  $\lambda_{BC}=0.7$  m for 224 MHz observations. The periods of viscous waves  $T_\nu$  in Fig. A.4b) are derived by Eq. A.2, the tilt  $\theta$  (from horizontal) by

$$\theta = \sin^{-1} \left( \frac{\lambda_{BC}}{T_\nu \cdot c} \right). \quad (\text{A.3})$$

Vertical velocity is defined by

$$v_z = \lambda_{BC}/T_\nu. \quad (\text{A.4})$$

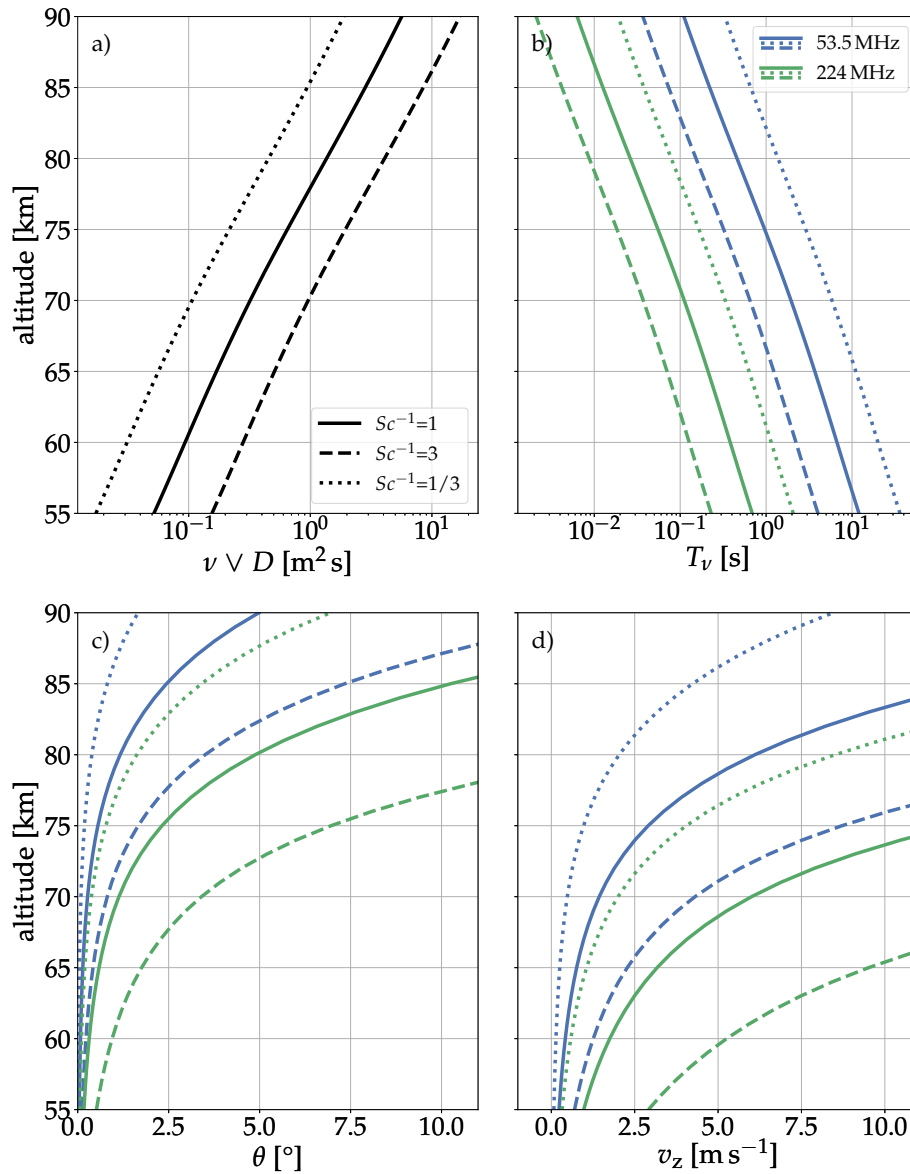


Figure A.4. Parameters able to produce viscous waves at radar Bragg scale  $\lambda_{BC}$  for 53.5 MHz (blue) and 224 MHz (green) radars. Values of temperature and density were taken from NRLMSISE-00 (Picone et al., 2002), to derive viscosity  $\nu$  and the speed of sound  $c$ . The cases of  $Sc=1$ ,  $Sc<1$ , and  $Sc>1$  are indicated by solid, dashed and dotted lines respectively.

## B | CONE Calibration curves

Different sensor-electronic combinations were calibrated in the laboratory with use of an absolute calibrated baratron sensor (according to DAkkS-R-6-2(6-2010), ISO 3567 (12-2011) standard). This allows the assignment of currents measured by the ionization gauge to values of pressure.

The final flight configuration was: C4N2 (C4 identifies sensor, N2 indicates the electronic) mounted on the aft deck of the PMWE1F (Fiona) payload, C2T1 (i.e., Sensor#2 on Turb3D electronic#1) on the forward deck of the PMWE1D (Dustin) payload, and C7N1 on PMWE1D's aft deck.

The calibration curves are shown below. On the top panel, the calibration curve is shown for different calibration runs. The lower panel reveals sensitivity, i.e., vacuumeter constant (see Sec. 3.4.1 for details).

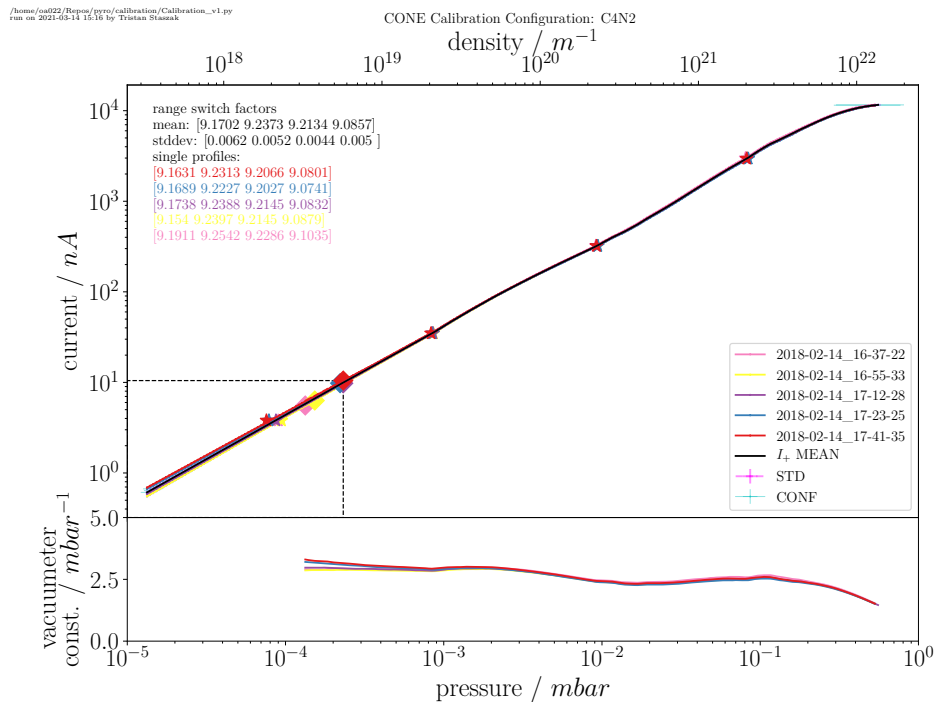


Figure B.1. Calibration curve for CONE sensor-electronic combination C4N2. Top panel: calibration curve. Lower panel: sensitivity.

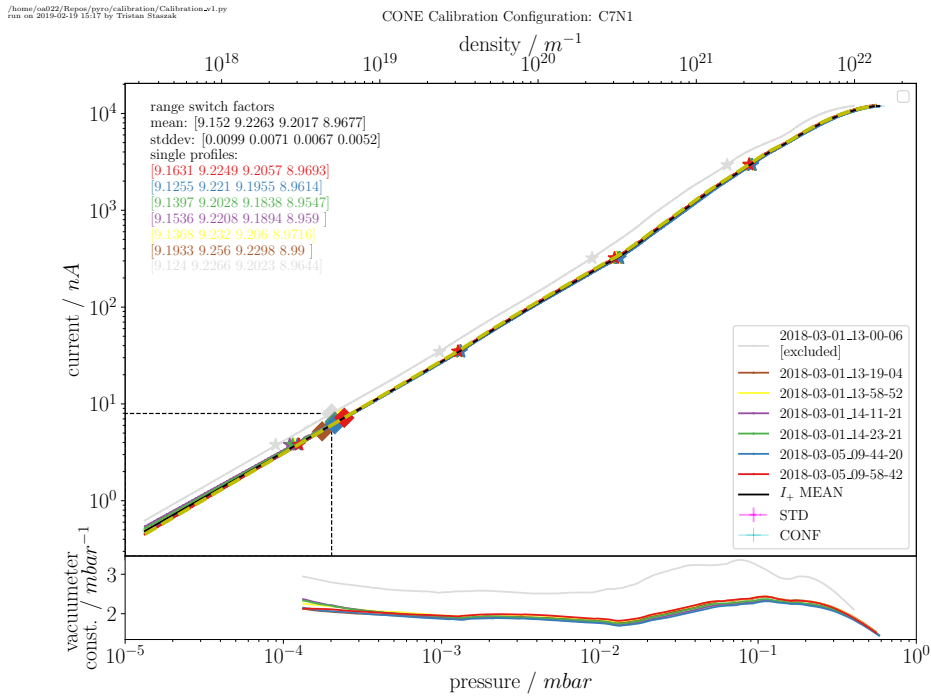


Figure B.2. Calibration curve for CONE sensor-electronic combination C7N1. Top panel: calibration curve. Lower panel: sensitivity.

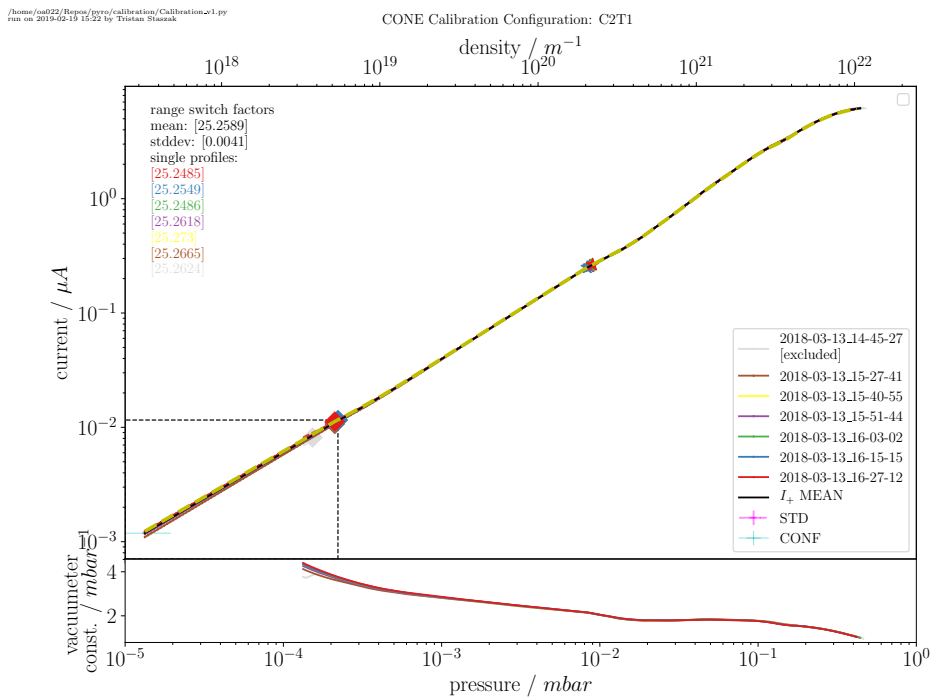


Figure B.3. Calibration for Turb3D sensor-electronic combination C2T1. Top panel: calibration curve. Lower panel: sensitivity.

# C | Uncertainties

## C.1 Error estimations of background parameters

### C.1.1 Density

Absolute densities are obtained from CONE ionization gauge measurements. These instruments (i.e., individual combination of Sensors and Electronics) are calibrated shortly before a sounding rocket campaign (~4 weeks) and the use after calibration is reduced to a necessary minimum (and low pressure only), since chemical reactions alter the filament composition and therefore sensitivity (Schulz, 1957, Schulz and Phelps, 1957). A set of calibration curves are produced by a controlled flow of dry air into the vacuum chamber, simulating the pressure conditions during a flight. The reference pressure sensor used, measures in a range of  $\sim 10^{-5}$ –1 mbar, e.g., baratron type. For conversion from pressure to density, temperature is measured for each calibration run. From this set of calibration lines, a mean calibration line and the standard deviation is obtained, including all relevant calibration errors (filament- and electrometer current, reference pressure, and temperature measurement). The resulting standard deviation in a range of  $1.3e^{-4}$ – $1.3e^{-1}$  mbar, correspond to an altitude range of approximately ~70–105 km and is  $< 2\%$ . For higher altitudes, i.e., lower pressures, the calibration error rises due to the limited sensitivity of the pressure sensor. Therefore, the calibration lines are extrapolated by linear functions for  $< 1.3e^{-4}$  (using  $\log(p)$ ). That method was validated by additional low pressure measurements (Spinning rotor gauge) but introduces larger standard deviations. However, for subsequent temperature analysis, the seeding temperature error dominates. Further, the atmospheric composition starts to change drastically in high altitudes due to atomic oxygen that alters the gauges ionization efficiency and therefore the measured density above ~110 km.

However, due to the supersonic speed of the payload, shock effects influence the density measurements (e.g., Gumbel, 2001a, Staszak et al., 2015). Upstream the payload the atmospheric air is compressed and therefore the measured density values  $N_{\text{meas}}$  in vicinity of the rocket is enhanced by a factor  $f_{\text{ram}}$  compared to undisturbed atmospheric density  $N_{\text{atmo}}$ :

$$N_{\text{atmo}} = N_{\text{meas}}/f_{\text{ram}}, \quad (\text{C.1})$$

where both  $N_{\text{meas}}$  and  $f_{\text{ram}}$  are afflicted with errors.  $N_{\text{meas}}$  contains all calibration uncertainties discussed before,  $f_{\text{ram}}$  contains the error of the aerodynamic ram correction.



Linear error propagation delivers an estimate total density error:

$$\Delta N = \Delta N_{\text{atmo}} = \left| 1/f_{\text{ram}} \right| \cdot \Delta N_{\text{meas}} + \left| N_{\text{meas}}/f_{\text{ram}}^2 \right| \cdot \Delta f_{\text{ram}}. \quad (\text{C.2})$$

The first term is small compared to the second since 2 % is an upper limit of  $\Delta N_{\text{meas}}/N_{\text{meas}}$ . The error of the ram correction depends on the underlying method. Direct numerical simulation of molecule interaction using the DSMC method (Bird, 2003) has become an important tool for efficiently simulating gas dynamics in the transition regime from continuum flow to free molecular flow. Investigations comparing wind channel measurements with DSMC simulations reveal an uncertainty of  $\sim 10\%$  (Gumbel, 2001b, Rapp et al., 2001). However, by use of more advanced 3D DSMC solvers, i.e., *dsmcFoam* (and customizations) from the OpenFOAM toolbox this error could be sufficiently reduced. In Fig. C.1 a comparison of wind tunnel experiments, 2d DSMC- simulations (Gumbel, 2001a) and a novel, preliminary full 3D DSMC simulation are shown. The largest discrepancies from

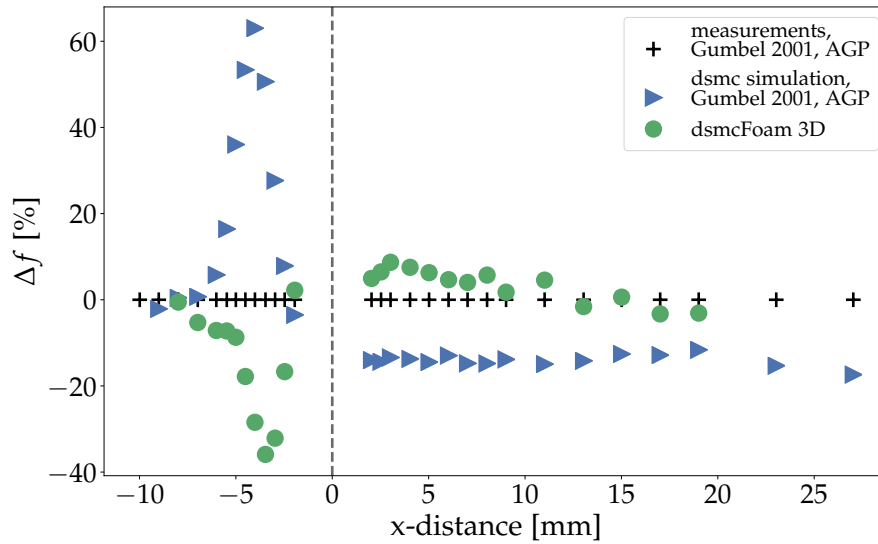


Figure C.1. Difference of DSMC simulation results to wind channel measurements at *Laboratoire d'Aerothermique du Meudon* (Allerge, 1992). The test geometry is a metal ring carrying a mesh of 76 % transparency. 2D simulation uses a mesh parametrization, see Gumbel (2001a). A full 3D simulation on basis of *dsmcFoam* is performed with full mesh resolution (i.e.,  $\Delta x < 0.05$  mm) for benchmarking the algorithm. The gray vertical line indicates the mesh structure, where negative abscissa value range denotes upstream, positive ones the downstream path relative to the center of the mesh ring.

simulations to measurements appear inside the shock wave, where density gradients are the steepest. Behind the mesh, where gradients are smoother, the agreement of simulations and measurement is much better. Since density measurement by CONE is downstream, after the three grid structures of Cone's ionization gauge, at least similarly smooth gradients are expected. Meaning that the path downstream the grid structure (gray vertical line), is of major interest. In this area the novel simulations with *dsmcFoam* reveal an error of  $\sim 5\%$  only, whereas 2d dsmc results differ by more than 10 %.

### C.1.2 Temperature

The temperature is derived from the measured absolute density profile by the assumption of hydrostatic equilibrium and integration over altitude, see Eq. 3.27. Since absolute neutral density  $N$  and seeding temperature are erroneous also the resulting temperature is prone to errors. By assumption of  $\Delta T/T \ll 1$ , a series expansion for error propagation is applied:

$$\Delta T = \left| \frac{dT}{dN_0} \right| \Delta N_0 + \left| \frac{dT}{dN} \right| \Delta N + \left| \frac{dT}{dT_0} \right| \Delta T_0, \quad (\text{C.3})$$

where  $T_0$  is the seeding temperature and  $\Delta T_0$  is the corresponding error,  $N_0 = N(z=z_0)$ ,  $\Delta N_0$ , denote density at seeding error,  $N$  is the absolute density with error  $\Delta N$ . The error of  $g$  is neglected. Then, the partial errors are given by:

$$\begin{aligned} \frac{dT}{dN_0} &= T_0/N(z) \\ \frac{dT}{dN} &= \frac{\bar{m}}{k_B \cdot N(z)} \cdot \left\{ \frac{1}{N(z)} \int_{z_0}^z N(z) \cdot g(z) dz - \frac{\delta}{\delta N(z)} \left( \int_{z_0}^z N(z) \cdot g(z) dz \right) \right\} \\ \frac{dT}{dT_0} &= N_0/N(z), \end{aligned} \quad (\text{C.4})$$

where  $\bar{m}$  is the molecular mass,  $k_B$ , the Boltzmann's constant, and  $g$  is the acceleration by gravitation. This equation is solved numerically. Results are shown in Fig. C.2. As is apparent from Fig. C.2 the seeding error dominates the overall error in the upper part of the temperature profile and becomes negligible in the lower part, where density error dominates. By neglecting the errors introduced by ram correction, the resulting overall temperature error does not exceed  $\sim \pm 5$  K two scale heights below seeding altitude, corresponding to a relative error of less than 3%. However, as discussed before the ram correction does introduce an extra error. For the standard DSMC simulations for CONE with an error of  $\sim 10\%$  (Rapp et al., 2001), the temperature error reaches  $\pm 15$  K at 70 km altitude. If the ram correction error could be reduced to  $\leq 5\%$ , resulting temperature uncertainty would be less  $\pm 10$  K at the same height.

### C.1.3 Viscosity

The dynamic viscosity is deduced by use of Sutherland's formula (Sutherland, 1893):

$$\mu = \frac{\beta \cdot T^{3/2}}{T + S}, \quad (\text{C.5})$$

with constant  $\beta = 1.458 \cdot 10^{-6} \text{ kg m}^{-1} \text{ s}^{-1} \text{ K}^{-0.5}$ , and Sutherland's constant  $S = 110.4 \text{ K}$ . In most cases, e.g., to derive energy dissipation rate  $\varepsilon$  from spectral method, kinematic viscosity is needed and obtained by:

$$\nu = \mu/\rho, \quad (\text{C.6})$$

where mass density  $\rho$  can be calculated by number density  $N$  by knowledge of molecular mass  $\bar{m}$ :

$$\rho = N \cdot \bar{m}. \quad (\text{C.7})$$

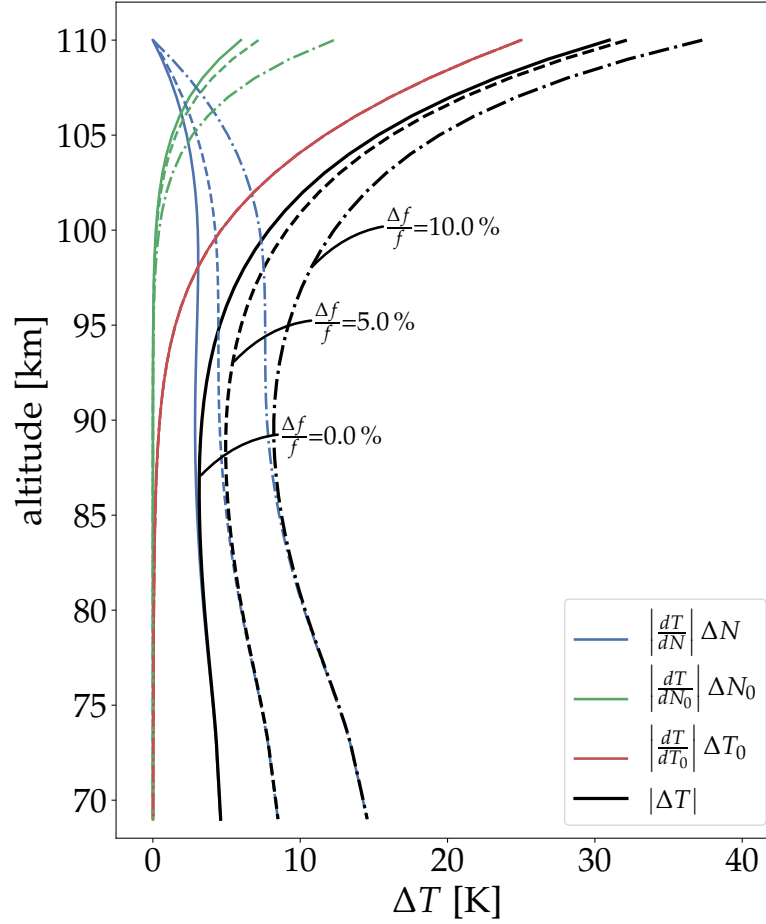


Figure C.2. Partial errors for temperature integration. Seeding temperature error  $\Delta T_0$  is assumed to be 25 K. Example for density data taken from NRLMSISE-00 (Picone et al., 2002), a constant density error  $\Delta N_{\text{meas}}$  of 2% is assumed. This is the upper error limit revealed from calibration. Profiles with additional ram correction error  $\Delta f$  altering overall  $\Delta N$  are given by dashed, and dashed-dotted lines.

For an erroneous  $T$ , the error of dynamic viscosity is given by:

$$\Delta\mu = \left| \frac{\beta \cdot T^{1/2} (3S + T)}{2(S + T)^2} \right| \cdot \Delta T. \quad (\text{C.8})$$

Finally, for kinematic viscosity  $\nu$ , with erroneous  $T$  and  $\Delta N$ :

$$\Delta\nu = \underbrace{\left| \frac{1}{\bar{m} \cdot N} \right| \cdot \Delta\mu}_{\approx 0} + \left| -\frac{\mu}{\bar{m} \cdot N^2} \right| \cdot \Delta N. \quad (\text{C.9})$$

First term depends on the error of dynamic viscosity and is  $\sim 3$  orders of magnitude smaller compared to the second and therefore negligible. Thus,  $\Delta\nu$  is dominated by absolute density error  $\Delta N$ . Regarding 2% calibration error and 10% from ram correction influencing  $\Delta N$ , the resulting error of kinematic viscosity is 4–6% and is lower at higher altitudes.

### C.1.4 Buoyancy frequency

The buoyancy frequency  $\omega_B^2$  is given by following equation:

$$\omega_B^2 = \frac{g}{T} \cdot \frac{dT}{dz} + \frac{g}{T} \cdot \frac{g}{c_p}. \quad (\text{C.10})$$

Propagation of  $\Delta T$  to  $\Delta\omega_B^2$  yields:

$$\Delta\omega_B^2 = \frac{g^2}{T^2} \left( \frac{1}{c_p} - \frac{1}{T} \cdot \frac{d^2T}{dz^2} \right) \cdot \Delta T \quad (\text{C.11})$$

Again taking 2 % calibration error and 10 % ram correction uncertainty reveals  $\Delta\omega_B^2/\omega_B^2$  of 2–5 % near a local temperature minimum (i.e., Mesopause), and 10–20 % if  $\frac{d^2T}{dz^2} \lesssim 0$ .

## C.2 Uncertainty of $\varepsilon$ and $Sc$ derived from the spectral model technique

Turbulence energy dissipation rate  $\varepsilon$  is derived by fit of a theoretical model to a measured spectrum of neutral density fluctuations. The Levenberg-Marquardt least-square technique is utilized for this purpose. The error of  $\varepsilon$  determination is discussed by [Szewczyk \(2015\)](#) in some details. The main error source in the fitting procedure is induced by the least square technique and given by the 1- $\sigma$  error, scaled by the measured  $\chi^2$ -value (see [Szewczyk, 2015](#)):

$$\Delta_\varepsilon = \sqrt{C_{kk}^{-1} \frac{\chi^2}{n-p}}, \quad (\text{C.12})$$

where  $C_{kk}^{-1}$  denotes the 1- $\sigma$  error of each fitted parameter,  $\chi^2$  is the weighted chi-square value,  $n$  is the number of data points and  $p$  the number of free fitting parameters.

As has been noted in the text, a main uncertainty of the spectral technique is inherent in the underlying theoretical models, all revealing similar relative profiles but different absolute values, often differing by a factor of  $\sim 2$ – $3$ .

The Schmidt number is derived by comparison from the spectrum of neutral density fluctuations and electron density fluctuations. Practically, one uses the turbulence dissipation rate  $\varepsilon$  that is derived by a model fit for neutrals as a fixed parameter and the  $Sc$  number as well as  $N_\theta$  as free fitting parameters for a model to be fitted to the spectrum of electron density fluctuations. It was shown in this work, that using a single theoretical spectrum that is capable for the use on both tracers (i.e., neutrals and electrons) prevents from inducing errors that are related to the difference within the models (i.e., induced by difference in absolute values of  $\varepsilon$ ). For estimating the error in  $Sc$  number of a consistent-model procedure, a simple approach is made by defining that the uncertainty is constituted by the error of the least-square fitting (Eq. C.12) and the uncertainty of  $\varepsilon$ , derived from neutral spectrum. Pragmatically, the theoretical model is fitted three times, using  $\varepsilon - \Delta\varepsilon$ ,  $\varepsilon + \Delta\varepsilon$  and

$\varepsilon$ . Subsequently fitting  $Sc$  reveals an upper and lower limit for  $Sc$  number, for  $\Delta Sc_{\varepsilon+0.5\Delta\varepsilon}$ , and  $\Delta Sc_{\varepsilon-0.5\Delta\varepsilon}$ , respectively. The total estimate is given by:

$$\Delta Sc = \sqrt{\Delta Sc_{\text{fit}}^2 + \Delta Sc_{\varepsilon}^2}, \quad (\text{C.13})$$

where  $\Delta Sc_{\text{fit}}$  denotes the error by fitting and  $\Delta Sc_{\varepsilon}$  is related to error propagation of  $\varepsilon$  estimated by the approach described before.

### C.3 Potential electron density/ refractive index gradient

Potential electron density gradient  $M_e$  is defined by

$$M_e = N_e \left( \frac{\omega_B^2}{g} - \frac{1}{H_e} + \frac{1}{H_N} \right), \quad (\text{C.14})$$

where  $\omega_B^2$  denotes buoyancy frequency squared,  $g$  gravitational acceleration and scale heights of electrons  $H_e$  and neutrals  $H_N$  are given by

$$\begin{aligned} \frac{1}{\rho} \frac{d\rho}{dz} &= \frac{1}{N} \frac{dN}{dz} = -\frac{1}{H_N} \\ \frac{dN_e}{dz} &= -N_e \cdot \frac{1}{H_e}. \end{aligned} \quad (\text{C.15})$$

The variable  $z$  denotes altitude,  $\rho$  is mass density and  $N$  is number density. Note that  $1/H_N$  is positive and  $1/H_e$  usually is negative, due to decreasing neutral, and increasing electron density with increasing altitude. To derive the error  $\Delta M_e$ , first the absolute errors of scale heights  $\Delta 1/H_N$  and  $\Delta 1/H_e$  are obtained by linear error propagation ( $\Delta \omega_B^2$  is already defined in Eq. C.11):

$$\begin{aligned} \Delta \frac{1}{H_e} &= -\frac{1}{N_e} \left( \frac{1}{dz} - \frac{1}{N_e} \frac{dN_e}{dz} \right) \Delta N_e \\ \Delta \frac{1}{H_N} &= -\frac{1}{N_N} \left( \frac{1}{dz} - \frac{1}{N_N} \frac{dN_N}{dz} \right) \Delta N_N. \end{aligned} \quad (\text{C.16})$$

Total error of  $M_e$  is given by:

$$\Delta M_e = \left( \frac{\omega_B^2}{g} - \frac{1}{H_e} + \frac{1}{H_N} \right) \Delta N_e + \frac{N_e}{g} \Delta \omega_B^2 - N_e \Delta \frac{1}{H_e} + N_e \Delta \frac{1}{H_N}. \quad (\text{C.17})$$

Since the error of absolute electron density  $\Delta N_e$  (derived by WPE) was not evaluated for PMWE measurements, this error is estimated from the analysis of the same measurement method on a different flight. [Bennett et al.](#) evaluated the WPE measurements of  $N_e$  derived by (differential) absorption and faraday rotation, and subsequently, derived errors using the spread of  $N_e$  and weighting of different methods. Maximal errors of ~15 % were obtained in an altitude range of 80–90 km. Between 70–80 km the maximal error is ~6 %

and slightly higher below 70 km (see [Bennett et al., 1972](#), Fig. 7). Furthermore, a comparison with independent measurements (Ionosonde and Langmuir-probe) showed that the systematic errors are negligible.

Since the potential refractive index is closely connected (via constant for the MLT and for a single radar frequency), one can apply the same error for potential electron density gradient  $M_e$  and potential refractive index gradient  $M_n$ .

$$\Delta M_e = \Delta M_n \quad (\text{C.18})$$

## D | A new aerodynamic correction approach for axis symmetric payloads

A new approach to derive aerodynamic correction is made hereafter, introducing a method that finally obtains a correction function considering the actual flow characteristic during measurements, defined by a set of dimensionless characteristic numbers and the ram factor (i.e., ratio of measured density and atmosphere's density):

$$\frac{N_{\text{meas}}}{N_{\text{atmo}}} = F. \quad (\text{D.1})$$

The final ram profile (i.e., ram factors  $F$  over altitude), can be derived by iteration, through feedback of characteristic numbers yield from (corrected) measurements. For flow description, Mach, Reynolds, and Knudsen number, were used. Recall that Mach number  $Ma$  is given by:

$$Ma = \frac{u}{c}; \quad c = \sqrt{\kappa \frac{R}{M} T}. \quad (\text{D.2})$$

Where  $u$  is the flow velocity upstream of the payload, and  $c$  is the speed of sound. Note that  $c$  is defined by constants, i.e.,  $\kappa$ , denoting isentropic expansion factor, molar gas constant  $R$ , molar mass  $M$  and by temperature  $T$ . Where  $T$  differs drastically from annual seasons and realistically also includes signatures of e.g., GWs. Reynolds number  $Re$  was already introduced in Sec. 2.31:

$$Re = \frac{L \cdot u}{\nu},$$

with kinematic viscosity  $\nu$  and characteristic length  $L$ . The kinematic viscosity is derived by Eq. 2.45 and therefore  $\nu \propto T^{-1/4}$  and  $\propto N^{-1}$  (density). The characteristic length scale  $L$  is a typical scale of the instruments and is set to 0.05 m (according to [Rapp et al., 2001](#)). Another dimensionless number is  $Kn$ , defined by:

$$Kn = \frac{\lambda}{L}, \quad (\text{D.3})$$

with the free mean path  $\lambda$ , standing for the mean distance between two subsequent collisions of a particle (i.e., molecule).  $Kn$  quantifies the ‘‘rarefiedness’’ of a flow. If  $Kn \ll 1$ , the flow can be described by continuum approach. For  $Kn \gg 1$ , a molecular flow is suitable, (e.g., [Bird, 1994](#)). Depending on the underlying collision model  $\lambda$  is  $\propto N^{-1}$  (Hard Sphere), or  $\propto N^{-1}$  and  $T^{-1/2}$  (Variable Hard Sphere).

For MLT conditions  $Kn$  spans over almost 4 decades in a range of  $0.01 > Kn > 100$ . Approximately below a value of 0.01, the continuum approach holds and for  $Kn \gtrsim 10$ , a molecular

dynamic approach is suitable. Since most of the measurements are in the transition regime, a computational method establishes that simulates collisions of representative particles (each standing for a multiple of real molecules), using a statistic-random kernel and subsequently, translates the molecular quantities to macroscopic ones (i.e., density, pressure, macroscopic velocity, and temperature). This method is called Direct Simulation Monte Carlo (DSMC) and was developed on basis of the theory by Bird. This method was successfully applied to sounding rocket measurements (Gumbel, 2001a, Rapp et al., 2001, Hedin et al., 2007, Staszak et al., 2015, 2017, Asmus et al., 2017).

On the basis of DSMC simulations, the ram factor  $F$  is calculated using boundary conditions from model or climatology (i.e., for temperature and density) and the velocity information from the trajectory. The drawback of this method is the huge computational effort (as well as pre and post processing) for every single rocket flight. This has been overcome with use of the interpolation method presented in Sec. 3.4.2. However, all these methods do not account for the real and actual atmospheric conditions the payload is exposed to, consequently altering the flow conditions in vicinity of the rocket. A solution to this is the use of an iterative method. Using boundary conditions from model only initially and subsequently using values obtained from the previous simulation. However, this drastically increases the computational effort and is not convenient for the use as a standard tool for CONE density analysis.

Therefore, another solution is proposed here, also on basis of an iterative process, but drastically increasing computational and human effort costs by developing an interpolation formula on basis of DSMC simulations that have to be made only once since universal dimensionless flow parameters are used instead of absolute values.

The flow conditions are described by  $Ma$ ,  $Kn$ ,  $Re$ , and  $F$  resulting in a four dimensional set of data, see Fig.D.1. As a first test of the method, a tri-variant 2nd-order polynomial is fit-

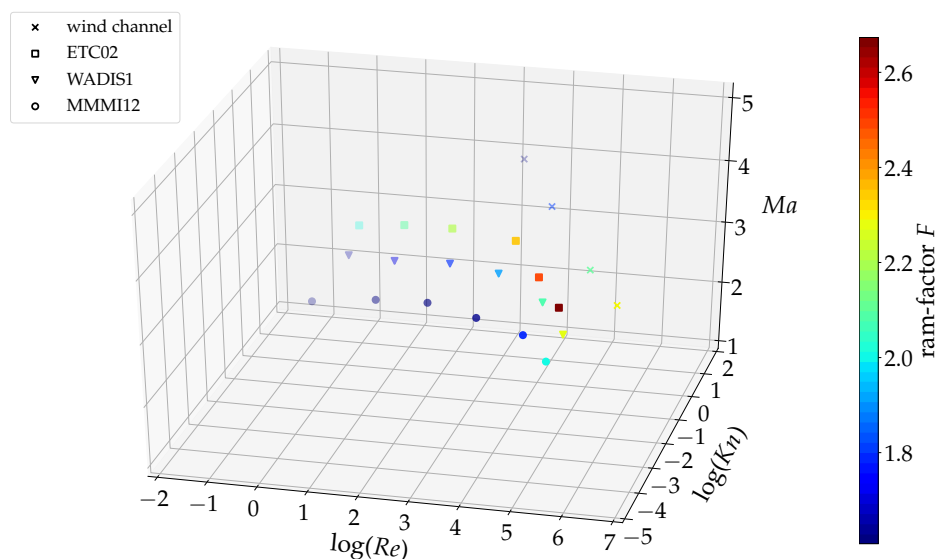


Figure D.1.  $Kn$ ,  $Re$ ,  $Ma$ ,  $F$  dataset, derived from established ram correction functions for 105 km and 130 km apogee for sounding rocket flights MMMI12 and ETC02, respectively (Rapp et al., 2001). SR3 wind channel measurements slightly offsets  $Kn$ ,  $Re$  and  $Ma$ , while ram factors are moderate. This is explained by much lower temperature of wind channel (i.e., only  $\sim 70$ - $90$  K, compared to MLT temperatures of  $\geq 140$  K) (see also Rapp et al., 2001).



ted to the dataset, revealed from corrections on basis of previous simulations (i.e., ECT02, MMMI12, WADIS1 Rapp et al., 2001, Staszak et al., 2015).  $Ma$ ,  $Kn$  and  $Re$  have been calculated on basis of the corresponding in situ measurements. This tri-variant polynomial has the form:

$$\begin{aligned}
 F(Re, Kn, Ma) = & c_{0,0,0} + c_{1,0,0} \cdot Re + c_{0,1,0} \cdot Kn + c_{0,0,1} \cdot Ma \\
 & + c_{2,0,0} \cdot Re^2 + c_{0,2,0} \cdot Kn^2 + c_{0,0,2} \cdot Ma^2 \\
 & + c_{1,1,0} \cdot Re \cdot Kn + c_{1,0,1} \cdot Re \cdot Ma + c_{0,1,1} \cdot Kn \cdot Ma,
 \end{aligned}
 \tag{D.4}$$

where  $c$  denotes the polynomial coefficients.

Results for  $n=11$  iterations are shown in Fig. D.2. The ram factor  $F$  is only obtained for  $Re$ ,  $Ma$ ,  $Kn$  number combinations in the boundaries that were given by minimum and maximum values of the original dataset, shown in Fig. D.1. The final ram correction profile (left panel) clearly shows modulations from actual structures of the real atmosphere that significantly differs from the model data (i.e., density and temperature of NRLMSISE-00), which is used for the standard ram correction. Thus, errors prone to ram correction discussed in Ap. C are not only slightly shifting the whole temperature profile, but indeed influence the gradients. For example, this is visible from comparing the temperature pro-

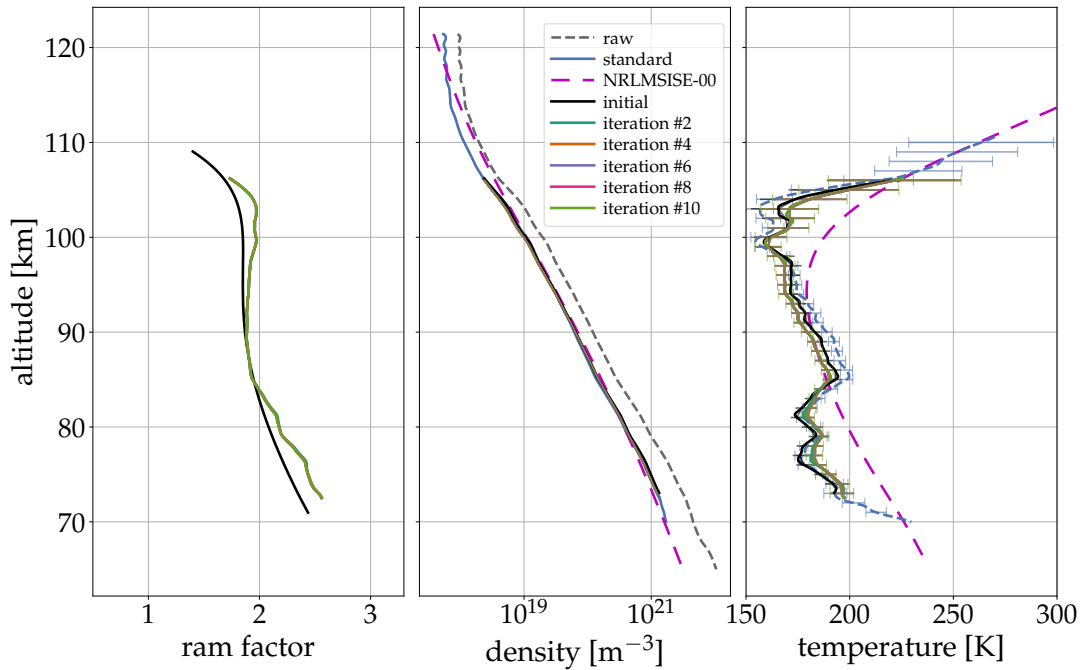


Figure D.2. Results of new aerodynamic correction approach: Ram factor  $F$  is shown on left panel, derived number density on mid-panel, and temperature on right panel.

file derived from standard method (blue line) with the new method's results (light green line, iteration #10) in range of  $\sim 75$ – $80$  km. However, it should be noted that most of the errorbars (indicating error prone to calibration and seeding) overlap. Note that the altitude of the temperature seeding has been changed from 110.6 km (standard method), to 106.2 km, since  $Re$ -,  $Ma$ -,  $Kn$ -number combinations exceed the limits of the underlying

data set and consequently no value for  $F$  was derived. Keep in mind that all methods, standard method, and using apogee as interpolation variable (see. Sec. 3.4.2) and this new method, are practically based on the same dataset and are used for demonstration purpose only. For final use of this approach systematic simulations covering the whole ranges of  $Re$ ,  $Kn$ , and  $Ma$  that are met within our in situ soundings, have to be carried out. Also the implementation of results from wind tunnel data is possible, if the influence of different temperature in the wind channel and the atmosphere can be appropriately corrected.

# E | PMWE-1 launch informations

## E.1 Vehicle and flight informations

The main vehicle characteristics and flight informations are given for both flights (i.e., PMWE1F and PMWE1D) in tables below.

Table E.1. PMWE1F (Fiona) vehicle information

payload	diameter	356 mm
	length	4235 mm
	mass	236.1 kg
motor	type	Improved Malemute (IM)
	diameter	410 mm
	length	3330 mm
	mass	602.0 kg
fin assembly	mass	40.3 kg

Table E.2. Flight informations and events of PMWE1F (Fiona) flight. Actual values in ().

Launch time	13-04-2018 09:44:00 UTC
Launcher settings	83.5°/339.2°
Nosecone separation	44.0(44.317) s; 53.0 km
Motor separation	51.0(51.322) s; 61.0 km
Apogee	166.0(164.569) s; 125(121.42) km

Table E.3. PMWE1D (Dustin) vehicle information

payload	diameter	356 mm
	length	3893 mm
	mass	234.0 kg
motor	type	Improved Malemute (IM)
	diameter	410 mm
	length	3330 mm
	mass	602.0 kg
fin assembly	mass	40.3 kg

Table E.4. Flight informations and events of PMWE1D (Dustin) flight. Actual values in ().

Launch time	18-04-2018 13:00:00 UTC
Launcher settings	82.8°/325.7°
Nosecone separation	44.0(44.384) s; 53.5 km
Motor separation	51.0(51.391) s; 61.5 km
Apogee	168.0(167.936) s; 126.6(125.63) km

## E.2 Trajectory

The trajectory of a sounding rocket is described by latitude, longitude, altitude, and flight time. This information is provided by GPS, radar track, and the onboard platform DMARS, providing different time resolution. To assign a precise position to each time defined by the sampling rate of each instrument, the trajectory is described by a fourth order polynomial, given by:

$$y(t) = \sum_{i=0}^n c_i (t - t_{\text{ref}})^i, \quad (\text{E.1})$$

where  $y(t)$  is either altitude  $z$ , latitude  $lon$  or longitude  $lon$ . Variable  $i$  is  $1 \dots 4$ ,  $t_{\text{ref}}$ ,  $t$  denotes the actual time variable and  $t_{\text{ref}}$  is a reference time. In this case  $t_{\text{ref}}=0$ . The polynomial coefficients are given by  $c_i$ , for either latitude, longitude or altitude, and are given below.

Table E.5. Polynomial coefficients for PMWE1F

	altitude [m]	latitude [°]	longitude [°]
$c_0$	$-7.84582155 \cdot 10^3$	$6.92863669 \cdot 10^1$	$1.60320844 \cdot 10^1$
$c_1$	$1.57944987 \cdot 10^3$	$1.62809663 \cdot 10^{-3}$	$-2.43104802 \cdot 10^{-3}$
$c_2$	$-4.91884983 \cdot 10^0$	$-3.41818746 \cdot 10^{-7}$	$-2.59355873 \cdot 10^{-7}$
$c_3$	$7.64093596 \cdot 10^{-4}$	$-3.41818746 \cdot 10^{-10}$	$6.97765108 \cdot 10^{-10}$
$c_4$	$-1.16021593 \cdot 10^{-6}$	$-1.30533485 \cdot 10^{-14}$	$2.324216 \cdot 10^{-13}$

Table E.6. Polynomial coefficients for PMWE1D

	altitude [m]	latitude [°]	longitude [°]
$c_0$	$-8.35515336 \cdot 10^3$	$6.92848758 \cdot 10^1$	$1.60324105 \cdot 10^1$
$c_1$	$1.607401 \cdot 10^3$	$1.78951203 \cdot 10^{-3}$	$-2.48320161 \cdot 10^{-3}$
$c_2$	$-4.91751875 \cdot 10^0$	$-3.79603845 \cdot 10^{-7}$	$-2.72589431 \cdot 10^{-7}$
$c_3$	$7.68922832 \cdot 10^{-4}$	$8.21305127 \cdot 10^{-10}$	$7.83630004 \cdot 10^{-10}$
$c_4$	$1.14355663 \cdot 10^{-6}$	$3.03070658 \cdot 10^{-14}$	$6.47110138 \cdot 10^{-14}$

# F | PMWE-1 Spectra

## F.1 PMWE1F spectra for neutral- and electron density fluctuations (CONE)

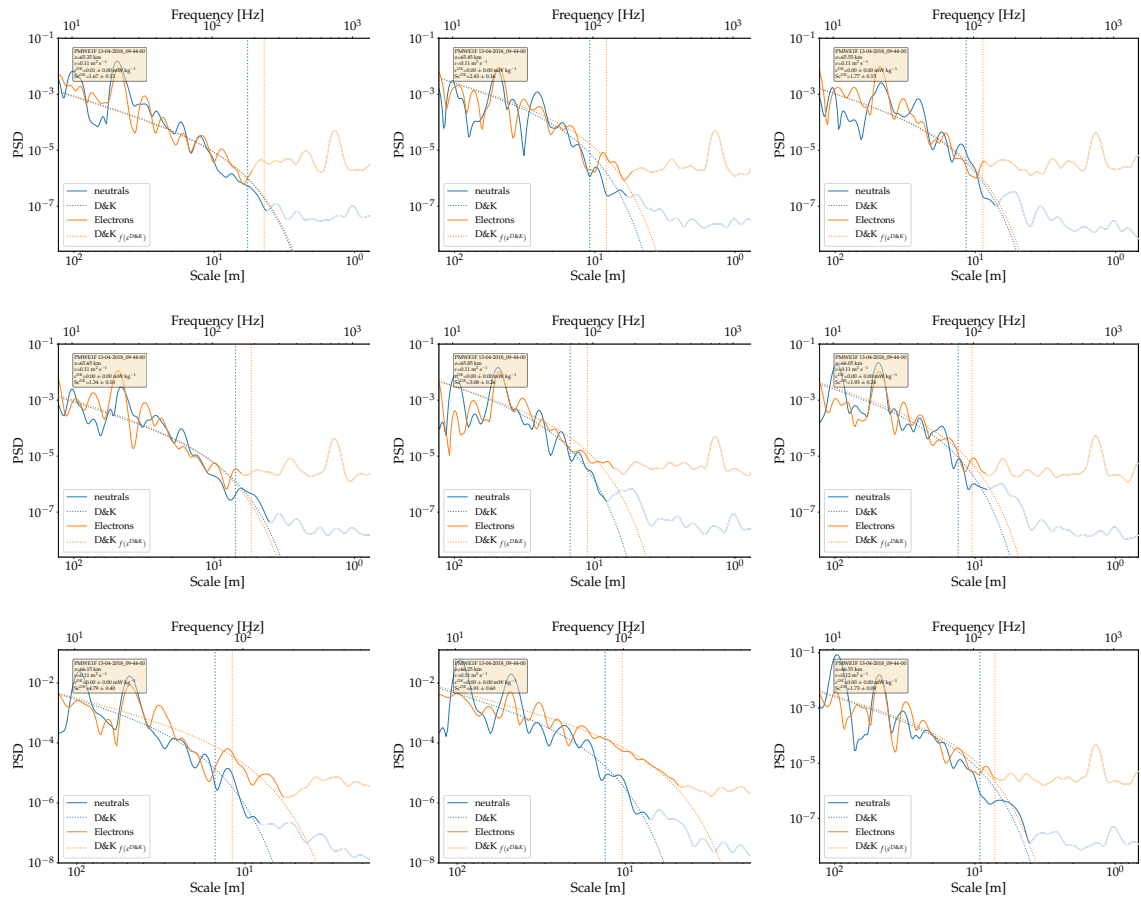


Figure F.1. Measured PSD from electron- and neutral density fluctuations (blue and orange graphs) for 100 m altitude resolution. Dotted lines show model fit (D&K) for  $Sc=1$  (neutrals) and fitted  $Sc$  for electron density spectra. Vertical lines indicate inner scale  $I_0$ . Results from CONE measurements onboard PMWE1F 65.35–73.25 km.

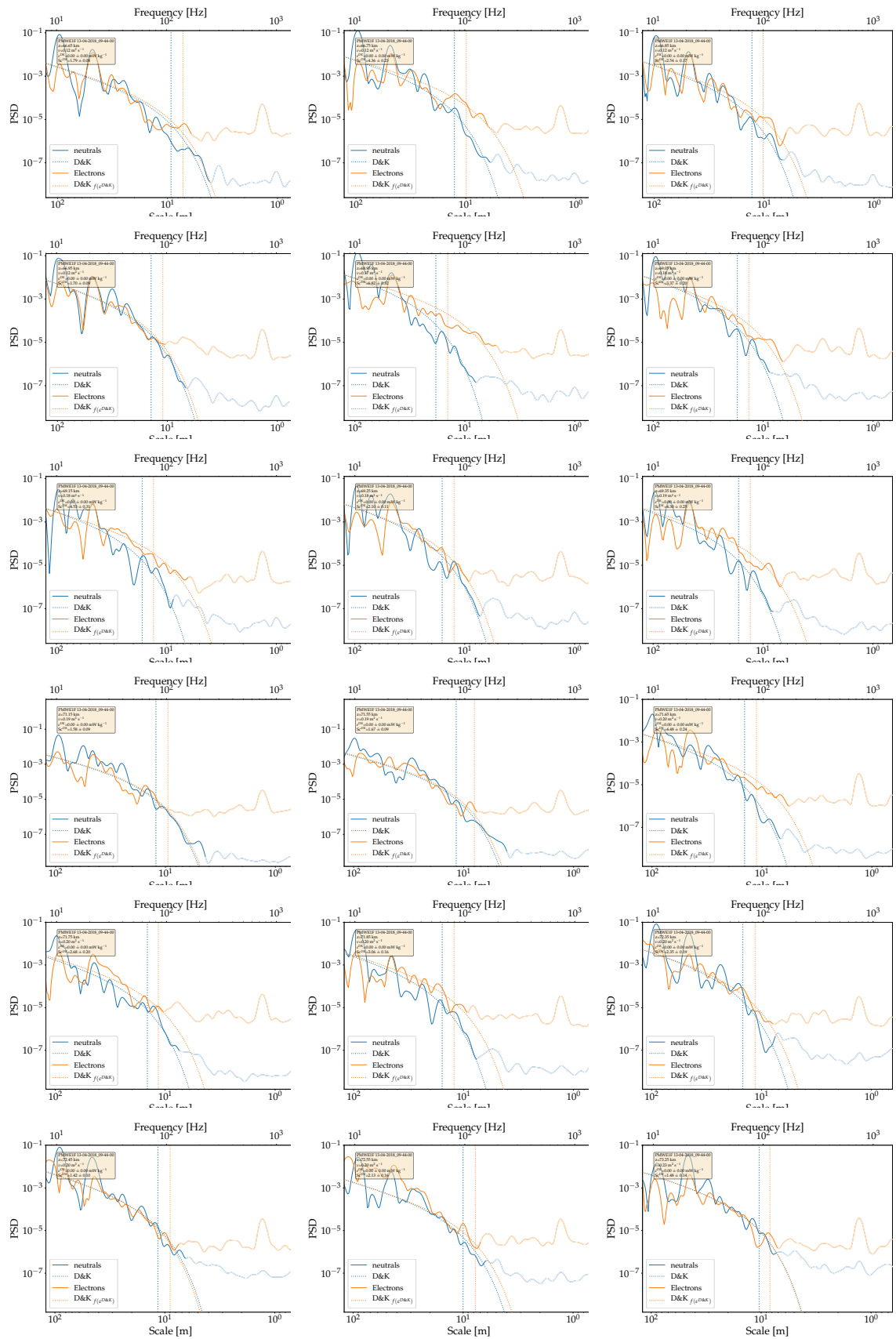


Figure F.2. Same as Fig. F.2 but for altitude range from 66.65 to 73.25 km.

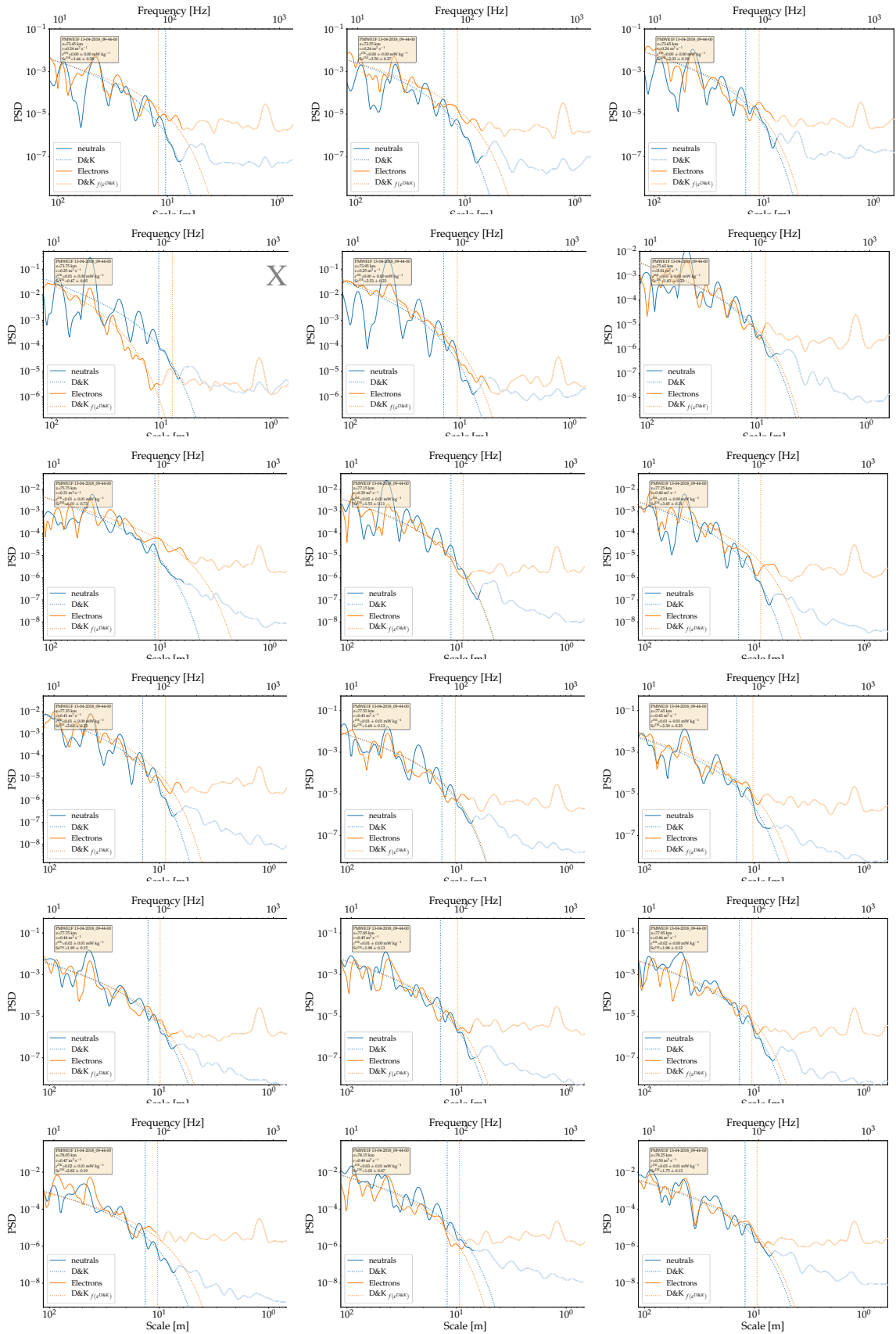


Figure F.3. Same as Fig. F.1 and F.1, but for 73.95–78.25 km.

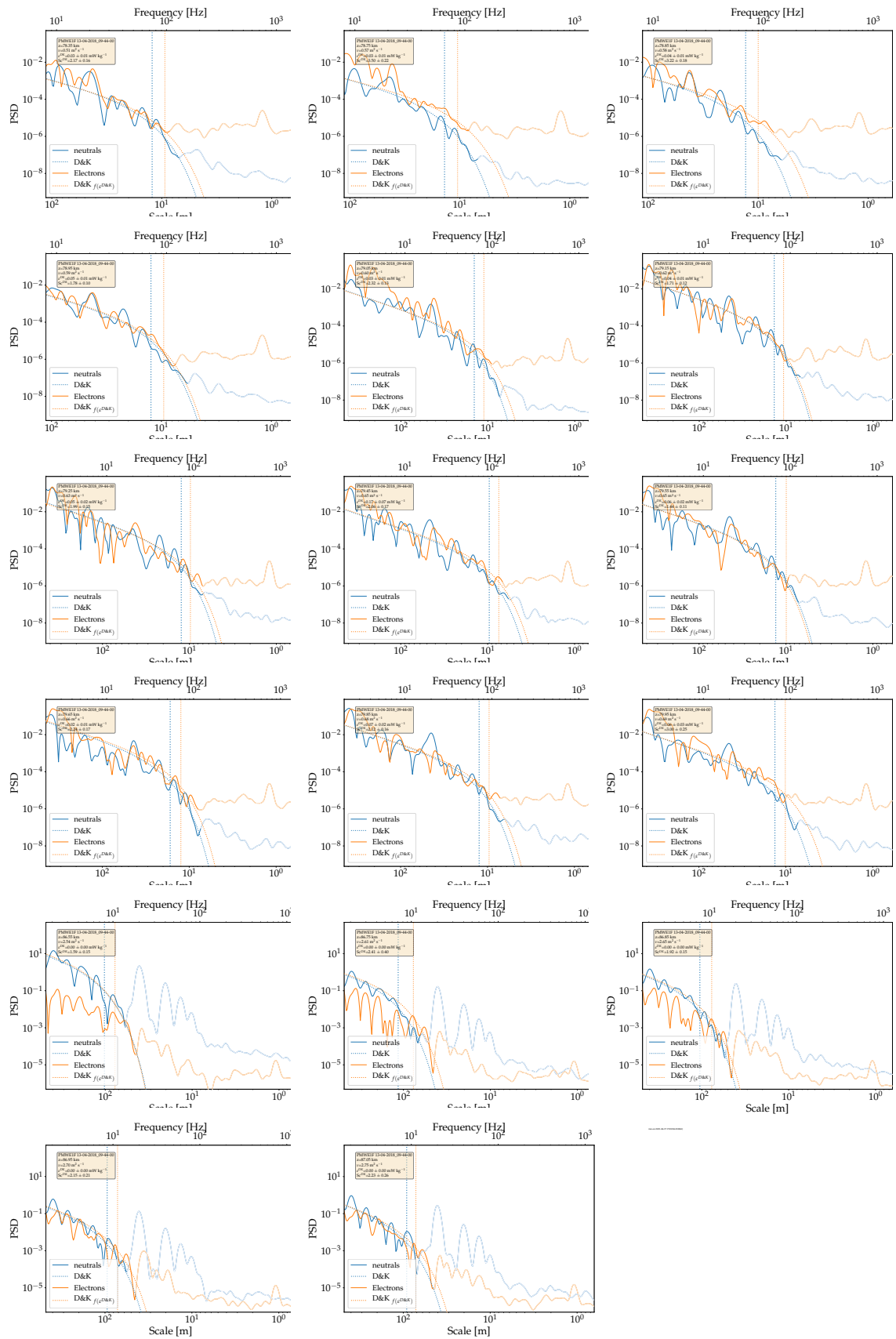


Figure F.4. Continued spectra from Fig. F.4 for altitude range from 78.35 to 87.05 km.



## F.2 PMWE1D spectra for neutral density fluctuations (Turb3D)

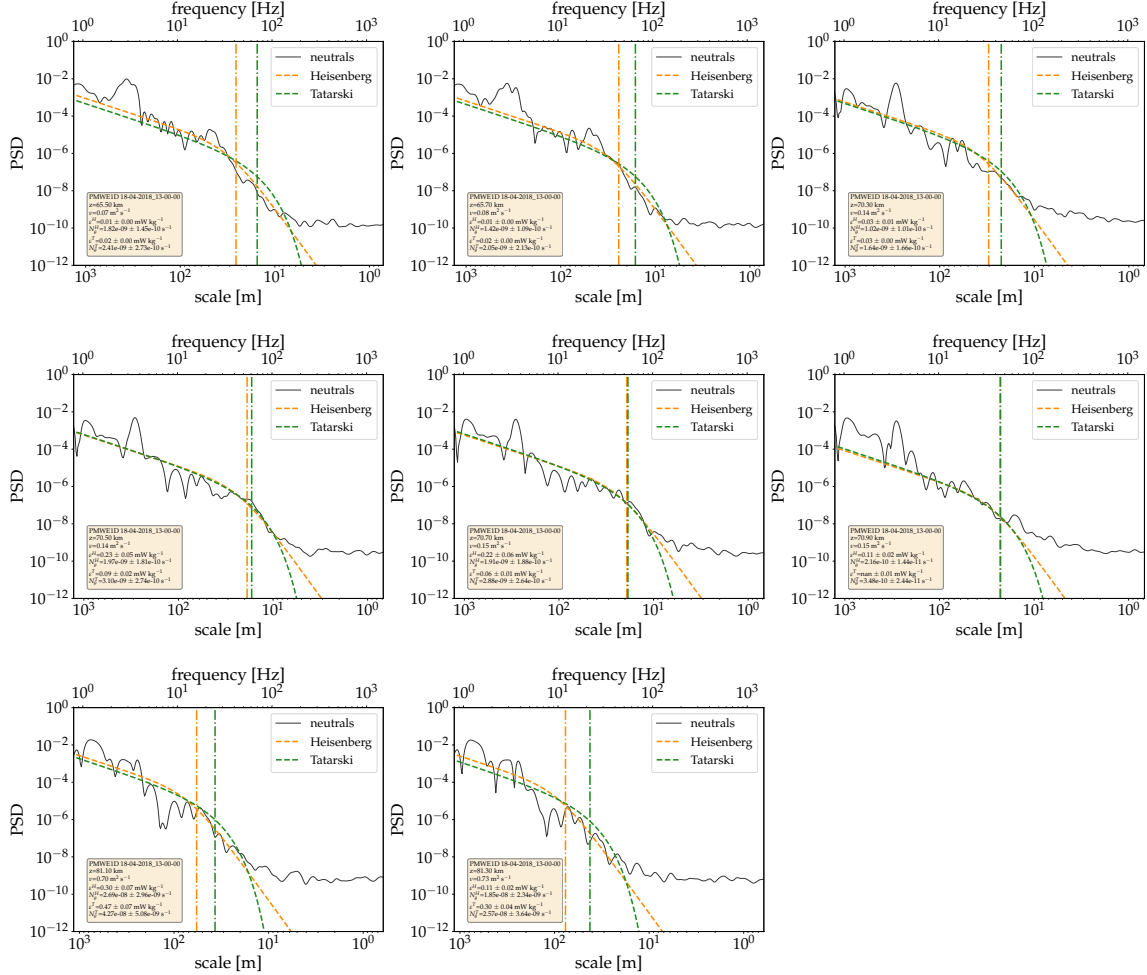


Figure F.5. PSD from neutral density fluctuations measured by Turb3D instrument onboard PMWE1D. Black graph reveals measured spectrum for 200 m altitude resolution. Orange and green dashed lines indicate model fit to measured spectrum for Heisenberg and Tatarski model, respectively. Vertical lines mark inner scale  $l_0$  for each model.



# Bibliography

- J. Allerge. The SR3 low density wind tunnel - Facility capabilities and research development. In *28th Joint Propulsion Conference and Exhibit*, Reston, Virginia, jul 1992. American Institute of Aeronautics and Astronautics. doi: 10.2514/6.1992-3972. URL <http://arc.aiaa.org/doi/10.2514/6.1992-3972>.
- E. V. Appleton. Wireless studies of the ionosphere. *Institution of Electrical Engineers - Proceedings of the Wireless Section of the Institution*, 7(21):257–265, sep 1932. ISSN 2054-0655. doi: 10.1049/pws.1932.0027. URL <https://digital-library.theiet.org/content/journals/10.1049/pws.1932.0027>.
- F. Arnold, D. Krankowsky, K. Marien, and W. Joos. A mass spectrometer probe for composition and structure analysis of the middle atmosphere plasma and neutral gas. *Journal of Geophysics Zeitschrift Geophysik*, 44:125–138, 1977. URL [https://gdz.sub.uni-goettingen.de/id/PPN1015067948\\_0044?tify=%7B%22pages%22:%5B138%5D,%22panX%22:0.541,%22panY%22:0.718,%22view%22:%22export%22,%22zoom%22:0.496%7D](https://gdz.sub.uni-goettingen.de/id/PPN1015067948_0044?tify=%7B%22pages%22:%5B138%5D,%22panX%22:0.541,%22panY%22:0.718,%22view%22:%22export%22,%22zoom%22:0.496%7D).
- H. Asmus. *In situ investigation of dusty plasmas in the polar E- and D-region*. Ph.d. thesis, University of Rostock, 2018.
- H. Asmus, B. Strelnikov, and M. Rapp. In situ measurements of charged mesospheric ice particles during the PHOCUS 2011 campaign and comparison of the results with a microphysical model. In *21st ESA Symposium on European Rocket and Balloon Programmes and Related Research*, pages 489–493, 2013.
- H. Asmus, T. Staszak, B. Strelnikov, F.-J. Lübken, M. Friedrich, and M. Rapp. Estimate of size distribution of charged MSPs measured in situ in winter during the WADIS-2 sounding rocket campaign. *Annales Geophysicae*, 35(4), 2017. ISSN 14320576. doi: 10.5194/angeo-35-979-2017.
- B. B. Balsley and K. S. Gage. *The MST Radar Technique: Potential for Middle Atmospheric Studies*. Technical report, 1980.
- B. B. Balsley, W. L. Ecklund, and D. C. Fritts. VHF Echoes from the High-Latitude Mesosphere and Lower Thermosphere: Observations and Interpretations. *Journal of the Atmospheric Sciences*, 40(10):2451–2466, oct 1983. ISSN 0022-4928. doi: 10.1175/1520-0469(1983)040<2451:VEFTHL>2.0.CO;2. URL [https://doi.org/10.1175/1520-0469\(1983\)040%3C2451:VEFTHL%3E2.0.CO;2](https://doi.org/10.1175/1520-0469(1983)040%3C2451:VEFTHL%3E2.0.CO;2)

[//journals.ametsoc.org/doi/abs/10.1175/1520-0469%281983%29040%3C2451%3AVEFTHL%3E2.0.CO%3B2](http://journals.ametsoc.org/doi/abs/10.1175/1520-0469%281983%29040%3C2451%3AVEFTHL%3E2.0.CO%3B2).

- G. K. Batchelor, I. D. Howells, and A. A. Townsend. Small-scale variation of convected quantities like temperature in turbulent fluid Part 2. The case of large conductivity. *Journal of Fluid Mechanics*, 5(01):134, 1959. ISSN 0022-1120. doi: 10.1017/S0022112059000106. URL [http://www.journals.cambridge.org/abstract\\_S0022112059000106](http://www.journals.cambridge.org/abstract_S0022112059000106).
- C. Baumann, M. Rapp, A. Kero, and C.-F. Enell. Meteor smoke influences on the D-region charge balance - Review of recent in situ measurements and one-dimensional model results. *Annales Geophysicae*, 31(11):2049–2062, 2013. ISSN 09927689. doi: 10.5194/angeo-31-2049-2013.
- C. Baumann, M. Rapp, and A. Kero. Secondary electron emission from meteoric smoke particles inside the polar ionosphere. *Annales Geophysicae*, 34(6):573–580, jun 2016. ISSN 1432-0576. doi: 10.5194/angeo-34-573-2016. URL <https://angeo.copernicus.org/articles/34/573/2016/>.
- G. Baumgarten, J. Fiedler, F.-J. Lübken, and G. von Cossart. Particle properties and water content of noctilucent clouds and their interannual variation. *Journal of Geophysical Research*, 113(D6):D06203, mar 2008. ISSN 0148-0227. doi: 10.1029/2007JD008884. URL <http://doi.wiley.com/10.1029/2007JD008884>.
- G. Baumgarten, J. Fiedler, J. Hildebrand, and F.-J. Lübken. Inertia gravity wave in the stratosphere and mesosphere observed by Doppler wind and temperature lidar. *Geophysical Research Letters*, 42:10,910–929,936, 2015. doi: 10.1002/2015GL066991.
- E. Becker. High Rossby-wave activity in austral winter 2002: Modulation of the general circulation of the MLT during the MaCWAVE/MIDAS northern summer program. *Geophysical Research Letters*, 31(24):L24S03, 2004. ISSN 0094-8276. doi: 10.1029/2004GL019615. URL <http://doi.wiley.com/10.1029/2004GL019615>.
- E. Becker. Dynamical Control of the Middle Atmosphere. *Space Science Reviews*, 168(1-4):283–314, jun 2012. ISSN 0038-6308. doi: 10.1007/s11214-011-9841-5. URL <http://link.springer.com/10.1007/s11214-011-9841-5>.
- E. Belova. The response time of PMSE to ionospheric heating. *Journal of Geophysical Research*, 108(D8):8446, 2003. ISSN 0148-0227. doi: 10.1029/2002JD002385. URL <http://doi.wiley.com/10.1029/2002JD002385>.
- E. Belova, S. Kirkwood, J. Ekeberg, A. Osepian, I. Häggström, H. Nilsson, and M. T. Rietveld. The dynamical background of polar mesosphere winter echoes from simultaneous EISCAT and ESRAD observations. *Annales Geophysicae*, 23(4):1239–1247, jun 2005. ISSN 1432-0576. doi: 10.5194/angeo-23-1239-2005. URL <https://angeo.copernicus.org/articles/23/1239/2005/>.

- E. Belova, M. Smirnova, M. T. Rietveld, B. Isham, S. Kirkwood, and T. Sergienko. First observation of the overshoot effect for polar mesosphere winter echoes during radiowave electron temperature modulation. *Geophysical Research Letters*, 35(3):L03110, feb 2008. ISSN 0094-8276. doi: 10.1029/2007GL032457. URL <http://doi.wiley.com/10.1029/2007GL032457>.
- E. Belova, S. Kirkwood, and T. Sergienko. EISCAT and ESRAD radars observations of polar mesosphere winter echoes during solar proton events on 11–12 November 2004. *Annales Geophysicae*, 31(7):1177–1190, jul 2013. ISSN 1432-0576. doi: 10.5194/angeo-31-1177-2013. URL <https://angeo.copernicus.org/articles/31/1177/2013/>.
- E. Belova, M. Kawne, I. Häggström, T. Sergienko, S. Kirkwood, and A. Tjulin. Tristatic observation of polar mesosphere winter echoes with the EISCAT VHF radar on 8 January 2014: a case study. *Earth, Planets and Space*, 70(1):110, dec 2018. ISSN 1880-5981. doi: 10.1186/s40623-018-0878-5. URL <https://earth-planets-space.springeropen.com/articles/10.1186/s40623-018-0878-5>.
- E. Belova, J. Kero, S. P. Näsholm, E. Vorobeva, O. A. Godin, and V. Barabash. Polar Mesosphere Winter Echoes and their relation to infrasound. In *EGU General Assembly 2020*, Vienna, 2020. doi: <https://doi.org/10.5194/egusphere-egu2020-5055>.
- F. Bennett, J. Hall, and P. Dickinson. D-region electron densities and collision frequencies from Faraday rotation and differential absorption measurements. *Journal of Atmospheric and Terrestrial Physics*, 34(8):1321–1335, aug 1972. ISSN 00219169. doi: 10.1016/0021-9169(72)90188-2. URL <https://linkinghub.elsevier.com/retrieve/pii/0021916972901882>.
- A. Biebricher and O. Havnes. Non-equilibrium modeling of the PMSE Overshoot Effect revisited: A comprehensive study. *Journal of Plasma Physics*, 78(3):303–319, jun 2012. ISSN 0022-3778. doi: 10.1017/S0022377812000141. URL [https://www.cambridge.org/core/product/identifier/S0022377812000141/type/journal\\_article](https://www.cambridge.org/core/product/identifier/S0022377812000141/type/journal_article).
- D. Bilitza, D. Altadill, Y. Zhang, C. Mertens, V. Truhlik, P. Richards, L.-A. McKinnell, and B. Reinisch. The International Reference Ionosphere 2012 – a model of international collaboration. *Journal of Space Weather and Space Climate*, 4:A07, feb 2014. ISSN 2115-7251. doi: 10.1051/swsc/2014004. URL <http://www.swsc-journal.org/10.1051/swsc/2014004>.
- D. Bilitza, D. Altadill, B. Reinisch, I. Galkin, V. Shubin, and V. Truhlik. The International Reference Ionosphere: Model Update 2016. In *EGU General Assembly Conference Abstracts*, Vienna, 2016. URL <https://ui.adsabs.harvard.edu/abs/2016EGUGA..18.9671B>.
- G. A. Bird. *Molecular Gas Dynamics and the Direct Simulation of Gas Flows*. Oxford University Press, Oxford, New York, 1994. ISBN 0-19-856195-4.

- G. A. Bird. *Molecular gas dynamics and the direct simulation of gas flows*. Clarendon Press, Oxford, oxford eng edition, 2003. ISBN 0198561954 | 0-19-856195-4.
- T. A. Blix, E. Thrane, and Ø. Andreassen. In situ measurements of the fine-scale structure and turbulence in the mesosphere and lower thermosphere by means of electrostatic positive ion probes. *Journal of Geophysical Research*, 95(D5):5533, 1990. ISSN 0148-0227. doi: 10.1029/JD095iD05p05533. URL <http://doi.wiley.com/10.1029/JD095iD05p05533>.
- T. A. Blix, E. Thrane, S. Kirkwood, and K. Schlegel. Plasma instabilities in the lower E-region observed during the DYANA campaign. *Journal of Atmospheric and Terrestrial Physics*, 56(13-14):1853–1870, nov 1994. ISSN 00219169. doi: 10.1016/0021-9169(94)90014-0. URL <https://linkinghub.elsevier.com/retrieve/pii/0021916994900140>.
- K. L. Bowles. Observation of Vertical-Incidence Scatter from the Ionosphere at 41 Mc/sec. *Physical Review Letters*, 1(12):454–455, dec 1958. ISSN 0031-9007. doi: 10.1103/PhysRevLett.1.454. URL <https://link.aps.org/doi/10.1103/PhysRevLett.1.454>.
- P. W. H. Bragg and W. L. Bragg. The reflection of X-rays by crystals. *Proceedings of the Royal Society of London. Series A, Containing Papers of a Mathematical and Physical Character*, 88(605):428–438, jul 1913. ISSN 0950-1207. doi: 10.1098/rspa.1913.0040. URL <https://royalsocietypublishing.org/doi/10.1098/rspa.1913.0040>.
- A. Brattli, T. A. Blix, Ø. Lie-Svendsen, U.-P. Hoppe, F.-J. Lübken, M. Rapp, W. Singer, R. Latteck, and M. Friedrich. Rocket measurements of positive ions during polar mesosphere winter echo conditions. *Atmospheric Chemistry and Physics*, 6(12):5515–5524, dec 2006. ISSN 1680-7324. doi: 10.5194/acp-6-5515-2006. URL <http://www.atmos-chem-phys.net/6/5515/2006/>.
- B. H. Briggs. *The analysis of spaced sensor records by correlation techniques*. SCOSTEP Secretariat, Dept. of Electr. Computer Eng., Univ of Illinois, Urbana, IL 61801, USA, 30, 1984. URL <https://play.google.com/books/reader?id=hto7oaA7BvMC&hl=de&pg=GBS.PP2>.
- K. Budden. Effect of electron collisions on formulas of magneto-ionic theory. *Journal of Research of the National Bureau of Standards, Section D: Radio Science*, 69D(2):191, feb 1965. ISSN 0502-2568. doi: 10.6028/jres.069D.028. URL [https://nvlpubs.nist.gov/nistpubs/jres/69D/jresv69Dn2p191\\_A1b.pdf](https://nvlpubs.nist.gov/nistpubs/jres/69D/jresv69Dn2p191_A1b.pdf).
- K. S. Carslaw, M. Wirth, A. Tsias, B. P. Luo, A. Dörnbrack, M. Leutbecher, H. Volkert, W. Renger, J. T. Bacmeister, and T. Peter. Particle microphysics and chemistry in remotely observed mountain polar stratospheric clouds. *Journal of Geophysical Research: Atmospheres*, 103(D5):5785–5796, mar 1998. ISSN 01480227. doi: 10.1029/97JD03626. URL <http://doi.wiley.com/10.1029/97JD03626>.

- F. H. Champagne, C. A. Friehe, J. C. LaRue, and J. C. Wynagaard. Flux Measurements, Flux Estimation Techniques, and Fine-Scale Turbulence Measurements in the Unstable Surface Layer Over Land. *Journal of the Atmospheric Sciences*, 34(3):515–530, mar 1977. ISSN 0022-4928. doi: 10.1175/1520-0469(1977)034<0515:FMFETA>2.0.CO;2. URL <http://journals.ametsoc.org/doi/abs/10.1175/1520-0469%281977%29034%3C0515%3AFMFETA%3E2.0.CO%3B2>.
- C. Chen and W. A. Scales. Electron temperature enhancement effects on plasma irregularities associated with charged dust in the Earth’s mesosphere. *Journal of Geophysical Research*, 110(A12):A12313, 2005. ISSN 0148-0227. doi: 10.1029/2005JA011341. URL <http://doi.wiley.com/10.1029/2005JA011341>.
- F. F. Chen. *Introduction to Plasma Physics and Controlled Fusion*. Springer International Publishing, Cham, 3rd edition, 2016. ISBN 978-3-319-22308-7. doi: 10.1007/978-3-319-22309-4. URL <https://link.springer.com/book/10.1007/978-3-319-22309-4> <http://link.springer.com/10.1007/978-3-319-22309-4>.
- P. B. Chilson, E. Belova, M. T. Rietveld, S. Kirkwood, and U.-P. Hoppe. First artificially induced modulation of PMSE using the EISCAT heating facility. *Geophysical Research Letters*, 27(23):3801–3804, 2000. ISSN 00948276. doi: 10.1029/2000GL011897.
- J. Y. Cho, T. M. Hall, and M. C. Kelley. On the Role of Charged Aerosols in Polar Mesosphere Summer Echoes. *J. Geophys. Res.*, 97:875–886, 1992.
- P. N. Collis, M. T. Rietveld, J. Röttger, and W. K. Hocking. Turbulence scattering layers in the middle-mesosphere observed by the EISCAT 224-MHz radar. *Radio Science*, 27(2):97–107, mar 1992. ISSN 00486604. doi: 10.1029/91RS02963. URL <http://doi.wiley.com/10.1029/91RS02963>.
- S. Corrsin. On the Spectrum of Isotropic Temperature Fluctuations in an Isotropic Turbulence. *Journal of Applied Physics*, 22(4):469–473, apr 1951. ISSN 0021-8979. doi: 10.1063/1.1699986. URL <http://aip.scitation.org/doi/10.1063/1.1699986>.
- P. Czechowsky and R. Rüster. VHF radar observations of turbulent structures in the polar mesopause region. *Annales Geophysicae*, 15(8):1028–1036, aug 1997. ISSN 1432-0576. doi: 10.1007/s00585-997-1028-8. URL <https://angeo.copernicus.org/articles/15/1028/1997/>.
- P. Czechowsky, R. Rüster, and G. Schmidt. Variations of mesospheric structures in different seasons. *Geophysical Research Letters*, 6(6):459–462, jun 1979. ISSN 00948276. doi: 10.1029/GL006i006p00459. URL <http://doi.wiley.com/10.1029/GL006i006p00459>.
- P. Czechowsky, I. M. Reid, R. Rüster, and G. Schmidt. VHF radar echoes observed in the summer and winter polar mesosphere over Andøya, Norway. *Journal of Geophysical Research*, 94(D4):5199–5217, 1989. ISSN 0148-0227. doi: 10.1029/JD094iD04p05199. URL <http://doi.wiley.com/10.1029/JD094iD04p05199>.

- R. J. Driscoll. A model for the turbulent energy spectrum. *Physics of Fluids*, 26(5):1228, 1983. ISSN 00319171. doi: 10.1063/1.864272. URL <http://link.aip.org/link/PFLDAS/v26/i5/p1228/s1&Agg=doihttps://aip.scitation.org/doi/10.1063/1.864272>.
- R. J. Driscoll and L. A. Kennedy. Spectral transfer and velocity derivative skewness equation for a turbulent velocity field. *Phys. Fluids*, 24(8):199–201, 1981.
- R. J. Driscoll and L. A. Kennedy. A model for the spectrum of passive scalars in an isotropic turbulence field. *Physics of Fluids*, 28(1):72–80, jan 1985. ISSN 0031-9171. doi: 10.1063/1.865128. URL <https://aip.scitation.org/doi/10.1063/1.865128>.
- M. Eberhart, S. Löhle, A. Steinbeck, T. Binder, and S. Fasoulas. Measurement of atomic oxygen in the middle atmosphere using solid electrolyte sensors and catalytic probes. *Atmospheric Measurement Techniques*, 8(9):3701–3714, 2015. doi: 10.5194/amt-8-3701-2015. URL <https://www.atmos-meas-tech.net/8/3701/2015/>.
- M. Eberhart, S. Löhle, B. Strelnikov, J. Hedin, M. Khaplanov, S. Fasoulas, J. Gumbel, F.-J. Lübken, and M. Rapp. Atomic oxygen number densities in the mesosphere–lower thermosphere region measured by solid electrolyte sensors on WADIS-2. *Atmospheric Measurement Techniques*, 12(4):2445–2461, apr 2019. ISSN 1867-8548. doi: 10.5194/amt-12-2445-2019. URL <https://amt.copernicus.org/articles/12/2445/2019/>.
- W. L. Ecklund and B. B. Balsley. Long-term observations of the Arctic mesosphere with the MST radar at Poker Flat, Alaska. *Journal of Geophysical Research: Space Physics*, 86(A9):7775–7780, sep 1981. ISSN 01480227. doi: 10.1029/JA086iA09p07775. URL <http://doi.wiley.com/10.1029/JA086iA09p07775>.
- L. Essen and K. D. Froome. The Refractive Indices and Dielectric Constants of Air and its Principal Constituents at 24,000 Mc/s. *Proceedings of the Physical Society. Section B*, 64(10):862–875, oct 1951. ISSN 0370-1301. doi: 10.1088/0370-1301/64/10/303. URL <https://iopscience.iop.org/article/10.1088/0370-1301/64/10/303>.
- J. Fiedler, G. Baumgarten, and F.-J. Lübken. NLC observations during one solar cycle above ALOMAR. *Journal of Atmospheric and Solar-Terrestrial Physics*, 71(3-4):424–433, mar 2009. ISSN 13646826. doi: 10.1016/j.jastp.2008.11.010. URL <https://linkinghub.elsevier.com/retrieve/pii/S1364682608003647>.
- J. Fiedler, G. Baumgarten, U. Berger, P. Hoffmann, N. Kaifler, and F.-J. Lübken. NLC and the background atmosphere above ALOMAR. *Atmospheric Chemistry and Physics*, 11(12):5701–5717, 2011. doi: 10.5194/acp-11-5701-2011. URL <https://www.atmos-chem-phys.net/11/5701/2011/>.
- W. L. Flock and B. B. Balsley. VHF Radar Returns from the D Region of Equatorial Ionosphere. *Journal of Geophysical Research*, 72(21):5537–5541, 1967.



- M. Friedrich. *Handbook of the Lower Ionosphere*. 2016. ISBN 978-3-85125-485-3. doi: 10.3217/978-3-85125-485-3. URL <http://www.tugraz-verlag.at/gesamtverzeichnis/elektrotechnik-und-informationstechnik/handbook-of-the-lower-ionosphere/>.
- M. Friedrich and M. Rapp. News from the Lower Ionosphere: A Review of Recent Developments. *Surveys in Geophysics*, 30(6):525–559, nov 2009. ISSN 0169-3298. doi: 10.1007/s10712-009-9074-2. URL <http://link.springer.com/10.1007/s10712-009-9074-2>.
- M. Friedrich and K. M. Torkar. High-latitude plasma densities and their relation to riometer absorption. *Journal of Atmospheric and Terrestrial Physics*, 45(2-3):127–135, feb 1983. ISSN 00219169. doi: 10.1016/S0021-9169(83)80017-8. URL <http://www.sciencedirect.com/science/article/pii/S0021916983800178><https://linkinghub.elsevier.com/retrieve/pii/S0021916983800178>.
- M. Friedrich, M. Rapp, T. A. Blix, U.-P. Hoppe, K. M. Torkar, S. Robertson, S. Dickson, and K. A. Lynch. Electron loss and meteoric dust in the mesosphere. *Annales Geophysicae*, 30(10):1495–1501, oct 2012. ISSN 1432-0576. doi: 10.5194/angeo-30-1495-2012. URL <http://www.ann-geophys.net/30/1495/2012/><https://angeo.copernicus.org/articles/30/1495/2012/>.
- K. O. Friedrichs. *Supersonic flow and shock waves*, volume 1 of *Pure and applied mathematics I*. Interscience Publ., New York, 4. printin edition, 1963.
- D. C. Fritts. Layering accompanying turbulence generation due to shear instability and gravity-wave breaking. *Journal of Geophysical Research*, 108(D8):1–13, 2003. ISSN 0148-0227. doi: 10.1029/2002JD002406.
- D. C. Fritts. Observations of extreme temperature and wind gradients near the summer mesopause during the MaCWAVE/MIDAS rocket campaign. *Geophysical Research Letters*, 31(24):L24S06, 2004. ISSN 0094-8276. doi: 10.1029/2003GL019389. URL <http://doi.wiley.com/10.1029/2003GL019389>.
- D. C. Fritts and M. J. Alexander. Gravity Wave Dynamics and Effects in the Middle Atmosphere. *Reviews of Geophysics*, 41(1):1–64, 2003. ISSN 8755-1209. doi: 10.1029/2001RG000106. URL <http://www.agu.org/pubs/crossref/2003/2001RG000106.shtml%5Cnhttp://www.agu.org/journals/rg/rg0301/2001RG000106/>.
- D. C. Fritts and L. Wang. Gravity Wave–Fine Structure Interactions. Part II: Energy Dissipation Evolutions, Statistics, and Implications. *Journal of the Atmospheric Sciences*, 70(12):3735–3755, dec 2013. ISSN 0022-4928. doi: 10.1175/JAS-D-13-059.1. URL <https://journals.ametsoc.org/doi/10.1175/JAS-D-13-059.1>.
- D. C. Fritts, L. Wang, G. Baumgarten, A. D. Miller, M. A. Geller, G. Jones, M. Limon, D. Chapman, J. Didier, C. B. Kjellstrand, D. Araujo, S. Hillbrand, A. Korotkov, G. Tucker, and J. Vinokurov. High-resolution observations and modeling of turbulence

- sources, structures, and intensities in the upper mesosphere. *Journal of Atmospheric and Solar-Terrestrial Physics*, 162(June 2016):57–78, 2017. ISSN 13646826. doi: 10.1016/j.jastp.2016.11.006.
- S. Fukao and K. Hamazu. *Radar for Meteorological and Atmospheric Observations*. Tokyo, 2014. ISBN 9784431543336. doi: <https://doi.org/10.1007/978-4-431-54334-3>.
- R. R. Garcia and S. Solomon. The effect of breaking gravity waves on the dynamics and chemical composition of the mesosphere and lower thermosphere. *Journal of Geophysical Research*, 90(D2):3850, apr 1985. ISSN 0148-0227. doi: 10.1029/JD090iD02p03850. URL <http://doi.wiley.com/10.1029/JD090iD02p03850>.
- C. H. Gibson and W. H. Schwarz. The universal equilibrium spectra of turbulent velocity and scalar fields. *Journal of Fluid Mechanics*, 16(3):365–384, 1963. ISSN 14697645. doi: 10.1017/S0022112063000835.
- J. Giebeler. *In-situ Messungen zur Untersuchung der Rolle von Turbulenz bei der Erzeugung von Radarechos in der polaren Mesosphäre im Sommer*. PhD thesis, Universität Bonn, 1995.
- J. Giebeler, F.-J. Lübken, and M. Nägele. CONE - A new sensor for in-situ observations of neutral and plasma density fluctuations. *Proceedings of the 11th ESA Symposium on European Rocket and Balloon Programmes and Related Research*, pages 311–318, 1993.
- J. Giebeler, F.-J. Lübken, and M. Nägele. CONE- A NEW PROBE FOR IN-SITU OBSERVATIONS OF NEUTRAL AND PLASMA DENSITY FLUCTUATIONS. *Proceedings of the 11th ESA Symposium on European Rocket and Balloon Programmes and Related Research*, 355(March):24–28, 1994.
- G. Giono, B. Strelnikov, H. Asmus, T. Staszak, N. Ivchenko, and F.-J. Lübken. Photocurrent modelling and experimental confirmation for meteoric smoke particle detectors on board atmospheric sounding rockets. *Atmospheric Measurement Techniques*, 11(9):5299–5314, sep 2018. ISSN 18678548. doi: 10.5194/amt-11-5299-2018. URL <https://amt.copernicus.org/articles/11/5299/2018/>.
- R. A. Goldberg. The MaCWAVE/MIDAS rocket and ground-based measurements of polar summer dynamics: Overview and mean state structure. *Geophysical Research Letters*, 31(24):L24S02, 2004. ISSN 0094-8276. doi: 10.1029/2004GL019411. URL <http://doi.wiley.com/10.1029/2004GL019411>.
- H. L. Grant, R. W. Stewart, and A. Moilliet. Turbulence spectra from a tidal channel. *Journal of Fluid Mechanics*, 12(02):241, 1962. ISSN 0022-1120. doi: 10.1017/S002211206200018X. URL [http://www.journals.cambridge.org/abstract\\_S002211206200018X](http://www.journals.cambridge.org/abstract_S002211206200018X).
- H. L. Grant, B. A. Hughes, W. M. Vogel, and A. Moilliet. The spectrum of temperature fluctuations in turbulent flow. *Journal of Fluid Mechanics*, 34(3):423–442, 1968. ISSN 14697645. doi: 10.1017/S0022112068001990.

- A. Grossmann and J. Morlet. Decomposition of Hardy Functions into Square Integrable Wavelets of Constant Shape. *SIAM Journal on Mathematical Analysis*, 15:723–736, 1984. doi: 10.1137/0515056.
- J. Gumbel. Aerodynamic influences on atmospheric in situ measurements from sounding rockets. *Journal of Geophysical Research: Space Physics*, 106(A6):10553–10563, jun 2001a. ISSN 01480227. doi: 10.1029/2000JA900166. URL <http://doi.wiley.com/10.1029/2000JA900166>.
- J. Gumbel. Rarefied gas flows through meshes and implications for atmospheric measurements. *Annales Geophysicae*, 19(5):563–569, 2001b. ISSN 09927689. doi: 10.5194/angeo-19-563-2001.
- J. Gumbel, G. Witt, D. P. Murtagh, P. J. Espy, A. Lundin, N. Wilhelm, and S. Sundin. Noctilucent clouds and odd oxygen: Results of the NLC-93 campaign. *European Space Agency, (Special Publication) ESA SP*, (397):483–488, 1997. ISSN 03796566.
- J. Gumbel, L. Megner, O. Martin Christensen, N. Ivchenko, D. P. Murtagh, S. Chang, J. Dillner, T. Ekebrand, G. Giono, A. Hammar, J. Hedin, B. Karlsson, M. Krus, A. Li, S. McCallion, G. Olentšenko, S. Pak, W. Park, J. Rouse, J. Stegman, and G. Witt. The MATS satellite mission-Gravity wave studies by Mesospheric Airglow/Aerosol Tomography and Spectroscopy. *Atmospheric Chemistry and Physics*, 20(1):431–455, 2020. ISSN 16807324. doi: 10.5194/acp-20-431-2020.
- A. Hauchecorne and M.-L. Chanin. Density and temperature profiles obtained by lidar between 35 and 70 km. *Geophysical Research Letters*, 7:565–568, aug 1980. doi: 10.1029/GL007i008p00565. URL <https://ui.adsabs.harvard.edu/abs/1980GeoRL...7..565H>.
- O. Havnes, J. Trøim, T. A. Blix, W. Mortensen, L. I. Naesheim, E. Thrane, and T. Tønnesen. First detection of charged dust particles in the Earth’s mesosphere. *Journal of Geophysical Research: Space Physics*, 101(A5):10839–10847, 1996. ISSN 01480227. doi: 10.1029/96JA00003. URL <http://doi.wiley.com/10.1029/96JA00003>.
- O. Havnes, A. Brattli, T. Aslaksen, W. Singer, R. Latteck, T. A. Blix, E. Thrane, and J. Trøim. First common volume observations of layered plasma structures and polar mesospheric summer echoes by rocket and radar. *Geophysical Research Letters*, 28(8): 1419–1422, apr 2001. ISSN 00948276. doi: 10.1029/2000GL012420. URL <http://doi.wiley.com/10.1029/2000GL012420>.
- O. Havnes, C. La Hoz, M. T. Rietveld, M. Kassa, G. Baroni, and A. Biebricher. Dust charging and density conditions deduced from observations of PMWE modulated by artificial electron heating. *Journal of Geophysical Research: Atmospheres*, 116(D24): n/a–n/a, dec 2011. ISSN 01480227. doi: 10.1029/2011JD016411. URL <http://doi.wiley.com/10.1029/2011JD016411>.
- O. Havnes, R. Latteck, T. W. Hartquist, and T. Antonsen. First Simultaneous Rocket and Radar Detections of Rare Low Summer Mesospheric Clouds. *Geophysical Research Letters*, 45(11):5727–5734, jun 2018. ISSN 19448007. doi: 10.1029/2018GL078218.

- J. Hedin, J. Gumbel, and M. Rapp. On the efficiency of rocket-borne particle detection in the mesosphere. *Atmospheric Chemistry and Physics*, 7(14):3701–3711, jul 2007. ISSN 1680-7324. doi: 10.5194/acp-7-3701-2007. URL <http://www.atmos-chem-phys.net/7/3701/2007/>.
- W. Heisenberg. Zur statistischen Theorie der Turbulenz. *Zeitschrift für Physik*, 124(7-12):628–657, jul 1948. ISSN 1434-6001. doi: 10.1007/BF01668899. URL <http://link.springer.com/10.1007/BF01668899>.
- M. E. Hervig, L. L. Gordley, L. E. Deaver, D. E. Siskind, M. H. Stevens, J. M. Russell, S. M. Bailey, L. Megner, and C. G. Bardeen. First satellite observations of meteoric smoke in the middle atmosphere. *Geophysical Research Letters*, 36(18), sep 2009. ISSN 00948276. doi: 10.1029/2009GL039737.
- R. J. Hill and S. F. Clifford. Modified spectrum of atmospheric temperature fluctuations and its application to optical propagation. *J. Opt. Soc. Am.*, 68(7):892–899, 1978. ISSN 0030-3941. doi: 10.1364/JOSA.68.000892. URL <http://www.opticsinfobase.org/abstract.cfm?URI=josa-68-7-892>.
- W. Hillert, F.-J. Lübken, and G. Lehmaner. TOTAL: a rocket-borne instrument for high resolution measurements of neutral air turbulence during DYANA. *Journal of Atmospheric and Terrestrial Physics*, 56(13-14):1835–1852, 1994. ISSN 00219169. doi: 10.1016/0021-9169(94)90013-2.
- J. O. Hinze. *Turbulence*. Mcgraw-hil edition, 1975. ISBN 0-07-029037-7.
- W. K. Hocking. *Investigations of the movement and structure of D-region ionospheric irregularities*. PhD thesis, University of Adelaide, 1981.
- W. K. Hocking. On the extraction of atmospheric turbulence parameters from radar backscatter Doppler spectra-I. Theory. *Journal of Atmospheric and Terrestrial Physics*, 45(2-3):89–102, 1983. ISSN 00219169. doi: 10.1016/S0021-9169(83)80013-0.
- W. K. Hocking. Measurement of turbulent energy dissipation rates in the middle atmosphere by radar techniques: A review. *Radio Science*, 20(6):1403–1422, nov 1985. ISSN 1944799X. doi: 10.1029/RS020i006p01403. URL <http://doi.wiley.com/10.1029/RS020i006p01403>.
- W. K. Hocking. *Target parameter estimation*, pages 228–268. SCOSTEP Secretariat, Dept. of Electr.Computer Eng., Univ of Illinois, Urbana, IL 61801, USA,30, 1989.
- W. K. Hocking. Evidence for viscosity, thermal conduction and diffusion waves in the Earth’s atmosphere (invited). *Review of Scientific Instruments*, 74(1 II):420–426, 2003. ISSN 00346748. doi: 10.1063/1.1516246.
- W. K. Hocking and J. Röttger. Studies of polar mesosphere summer echoes over EISCAT using calibrated signal strengths and statistical parameters. *Radio Science*, 32(4):1425–1444, 1997. ISSN 00486604. doi: 10.1029/97RS00716.

- W. K. Hocking, S. Fukao, M. Yamamoto, T. T. Tsuda, and S. Kato. Viscosity waves and thermal-conduction waves as a cause of “specular” reflectors in radar studies of the atmosphere. *Radio Science*, 26(5):1281–1303, sep 1991. ISSN 00486604. doi: 10.1029/91RS01661. URL <https://agupubs.onlinelibrary.wiley.com/doi/abs/10.1029/91RS01661><http://doi.wiley.com/10.1029/91RS01661>.
- W. K. Hocking, J. Röttger, R. D. Palmer, T. Sato, and P. B. Chilson. *Atmospheric Radar: Application and Science of MST Radars in the Earth’s Mesosphere, Stratosphere, Troposphere, and Weakly Ionized Regions*. Cambridge University Press, 2016. doi: 10.1017/9781316556115.
- P. Hoffmann, M. Rapp, J. Fiedler, and R. Latteck. Influence of tides and gravity waves on layering processes in the polar summer mesopause region. 26:4013–4022, 2008. doi: 10.5194/angeo-26-4013-2008.
- P. Hoffmann, E. Becker, W. Singer, and M. Placke. Seasonal variation of mesospheric waves at northern middle and high latitudes. *Journal of Atmospheric and Solar-Terrestrial Physics*, 72(14-15):1068–1079, sep 2010. ISSN 13646826. doi: 10.1016/j.jastp.2010.07.002. URL <https://linkinghub.elsevier.com/retrieve/pii/S1364682610001987>.
- J. R. Holton and M. J. Alexander. The role of waves in the transport circulation of the middle atmosphere. In *Geophysical Monograph Series*, volume 123, pages 21–35. 2000. ISBN 9781118668399. doi: 10.1029/GM123p0021. URL <http://doi.wiley.com/10.1029/GM123p0161><http://doi.wiley.com/10.1029/GM123p0021>.
- J. R. Holton and G. J. Hakim. Middle Atmosphere Dynamics. In *An Introduction to Dynamic Meteorology*, pages 413–452. Elsevier, 2013. doi: 10.1016/B978-0-12-384866-6.00012-X. URL <https://linkinghub.elsevier.com/retrieve/pii/B978012384866600012X>.
- U.-P. Hoppe, C. Hall, and J. Röttger. First observations of summer polar mesospheric backscatter with a 224 MHz radar. *Geophysical Research Letters*, 15(1):28–31, jan 1988. ISSN 00948276. doi: 10.1029/GL015i001p00028. URL <http://doi.wiley.com/10.1029/GL015i001p00028>.
- M. Horányi, J. Gumbel, G. Witt, and S. Robertson. Simulation of rocket-borne particle measurements in the mesosphere. *Geophysical Research Letters*, 26(11):1537–1540, jun 1999. ISSN 00948276. doi: 10.1029/1999GL900298. URL <http://doi.wiley.com/10.1029/1999GL900298>.
- D. W. Hughes. Meteors and cosmic dust. *Endeavour*, 21(1):31–35, jan 1997. ISSN 01609327. doi: 10.1016/S0160-9327(96)10030-2. URL <https://linkinghub.elsevier.com/retrieve/pii/S0160932796100302>.
- D. M. Hunten, R. P. Turco, and O. B. Toon. Smoke and Dust Particles of Meteoric Origin in the Mesosphere and Stratosphere. *Journal of the Atmospheric Sciences*, 37(6):1342–1357, jun 1980. ISSN 0022-4928. doi:

- 10.1175/1520-0469(1980)037<1342:SADPOM>2.0.CO;2. URL [http://journals.ametsoc.org/doi/abs/10.1175/1520-0469\(1980\)037%7B%25%7D3C1342:SADPOM%7B%25%7D3E2.0.CO%7B%25%7D3B2http://journals.ametsoc.org/doi/10.1175/1520-0469\(1980\)037%3C1342:SADPOM%3E2.0.CO;2](http://journals.ametsoc.org/doi/abs/10.1175/1520-0469(1980)037%7B%25%7D3C1342:SADPOM%7B%25%7D3E2.0.CO%7B%25%7D3B2http://journals.ametsoc.org/doi/10.1175/1520-0469(1980)037%3C1342:SADPOM%3E2.0.CO;2).
- C. H. Jackman and R. D. McPeters. Solar proton events as tests for the fidelity of middle atmosphere models. *Physica Scripta*, 1987(T18):309–316, 1987. ISSN 14024896. doi: 10.1088/0031-8949/1987/T18/031.
- D. Janches, C. J. Heinselman, J. L. Chau, A. Chandran, and R. Woodman. Modeling the global micrometeor input function in the upper atmosphere observed by high power and large aperture radars. *Journal of Geophysical Research*, 111(A7):A07317, 2006. ISSN 0148-0227. doi: 10.1029/2006JA011628. URL <http://doi.wiley.com/10.1029/2006JA011628>.
- N. Kaifler, G. Baumgarten, J. Fiedler, R. Latteck, F.-J. Lübken, and M. Rapp. Coincident measurements of PMSE and NLC above ALOMAR (69° N, 16° E) by radar and lidar from 1999-2008. *Atmospheric Chemistry and Physics*, 11(4):1355–1366, 2011. ISSN 16807316. doi: 10.5194/acp-11-1355-2011.
- A. J. Kavanagh, F. Honary, M. T. Rietveld, and A. Senior. First observations of the artificial modulation of polar mesospheric winter echoes. *Geophysical Research Letters*, 33(19), oct 2006. ISSN 00948276. doi: 10.1029/2006GL027565.
- M. C. Kelley. *The Earth's Ionosphere: plasma physics and electrodynamics*. Elsevier, Amsterdam, Boston, Heidelberg, London, New York, Oxford, Paris, San Diego, San Francisco, Singapore, Sydney, Tokyo, internatio edition, 2009. ISBN 9780120884254. URL <https://www.elsevier.com/books/the-earths-ionosphere/kelley/978-0-12-088425-4>.
- M. C. Kelley, J. C. Ulwick, J. Röttger, B. Inhester, T. M. Hall, and T. A. Blix. Intense turbulence in the polar mesosphere : rocket and radar measurements. *Journal of Atmospheric and Terrestrial Physics*, 52(10-11):875–891, 1990. ISSN 00219169. doi: 10.1016/0021-9169(90)90022-F.
- A. Kero, C.-F. Enell, A. J. Kavanagh, J. Vierinen, I. Virtanen, and E. Turunen. Could negative ion production explain the polar mesosphere winter echo (PMWE) modulation in active HF heating experiments? *Geophysical Research Letters*, 35(23):L23102, dec 2008. ISSN 0094-8276. doi: 10.1029/2008GL035798. URL <http://doi.wiley.com/10.1029/2008GL035798>.
- S. Kirkwood, V. Barabash, E. Belova, H. Nilsson, T. N. Rao, K. Stebel, U. Blum, A. Osepian, and P. B. Chilson. Polar Mesosphere Winter Echoes - by ESRAD, EISCAT and lidar. *British Astronomical Society*, 2002a. URL <https://www.diva-portal.org/smash/record.jsf?pid=diva2%3A989456&dswid=-7997>.
- S. Kirkwood, V. Barabash, E. Belova, H. Nilsson, T. N. Rao, K. Stebel, A. Osepian, and P. B. Chilson. Polar mesosphere winter echoes during solar proton events. *Advances in*

- polar upper atmosphere research*, 16:111–125, 2002b. ISSN 13451065. URL <http://ci.nii.ac.jp/naid/110000037475/en/>.
- S. Kirkwood, P. B. Chilson, E. Belova, P. Dalin, I. Häggström, M. T. Rietveld, and W. Singer. Infrasound - the cause of strong Polar Mesosphere Winter Echoes? *Annales Geophysicae*, 24(2):475–491, mar 2006. ISSN 1432-0576. doi: 10.5194/angeo-24-475-2006. URL <http://www.ann-geophys.net/24/475/2006/https://angeo.copernicus.org/articles/24/475/2006/>.
- S. Kirkwood, A. Osepian, E. Belova, and Y.-S. Lee. High-speed solar wind streams and polar mesosphere winter echoes at Troll, Antarctica. *Annales Geophysicae*, 33:609–622, 2015. doi: 10.5194/angeo-33-609-2015.
- S. Knappmiller, M. Rapp, S. Robertson, and J. Gumbel. Charging of meteoric smoke and ice particles in the mesosphere including photoemission and photodetachment rates. *Journal of Atmospheric and Solar-Terrestrial Physics*, 73(14-15):2212–2220, 2011. ISSN 13646826. doi: 10.1016/j.jastp.2011.01.008. URL <http://dx.doi.org/10.1016/j.jastp.2011.01.008>.
- A. N. Kolmogorov. The Local Structure of Turbulence in Incompressible Viscous Fluid for Very Large Reynolds Numbers. *Proceedings: Mathematical and Physical Sciences*, 434(1890):9–13, 1941. URL <http://www.jstor.org/stable/51980>.
- H. Körnich and E. Becker. A simple model for the interhemispheric coupling of the middle atmosphere circulation. *Advances in Space Research*, 45(5):661–668, 2010. ISSN 02731177. doi: 10.1016/j.asr.2009.11.001.
- L. S. G. Kovasznay. Spectrum of Locally Isotropic Turbulence. *Journal of the Aeronautical Sciences*, 15(12):745–753, dec 1948. ISSN 1936-9956. doi: 10.2514/8.11707. URL <https://arc.aiaa.org/doi/10.2514/8.11707>.
- C. La Hoz and O. Havnes. Artificial modification of polar mesospheric winter echoes with an RF heater: Do charged dust particles play an active role? *Journal of Geophysical Research Atmospheres*, 113(19):1–7, 2008. ISSN 01480227. doi: 10.1029/2008JD010460. URL <http://onlinelibrary.wiley.com/doi/10.1029/2008JD010460/abstract;jsessionid=790ED738724F42750E7C4D30656E9996.f04t03>.
- R. Latteck and J. Bremer. Long-term changes of polar mesosphere summer echoes at 69°N. *Journal of Geophysical Research: Atmospheres*, 118(18):10,441–10,448, sep 2013. ISSN 2169897X. doi: 10.1002/jgrd.50787. URL <http://doi.wiley.com/10.1002/jgrd.50787>.
- R. Latteck and I. Strelnikova. Extended observations of polar mesosphere winter echoes over Andøya (69°N) using MAARSY. *Journal of Geophysical Research: Atmospheres*, 120(16):8216–8226, 2015. ISSN 21698996. doi: 10.1002/2015JD023291.

- R. Latteck, W. Singer, and H. Bardey. The ALWIN MST radar - Technical design and performance. *European Rocket and Balloon Programmes and Related Research*, pages 179–184, 1999. URL <http://adsabs.harvard.edu/abs/1999ESASP.437..179L>.
- R. Latteck, W. Singer, R. J. Morris, W. K. Hocking, D. J. Murphy, D. A. Holdsworth, and N. Swarnalingam. Similarities and differences in polar mesosphere summer echoes observed in the Arctic and Antarctica. *Annales Geophysicae*, 26(9):2795–2806, sep 2008. ISSN 1432-0576. doi: 10.5194/angeo-26-2795-2008. URL <https://angeo.copernicus.org/articles/26/2795/2008/>.
- R. Latteck, W. Singer, M. Rapp, and T. Renkowitz. MAARSY – the new MST radar on Andøya/Norway. *Advances in Radio Science*, 8:219–224, oct 2010. ISSN 1684-9973. doi: 10.5194/ars-8-219-2010. URL <https://ars.copernicus.org/articles/8/219/2010/>.
- R. Latteck, W. Singer, M. Rapp, B. Vandeppeer, T. Renkowitz, M. Zecha, and G. Stober. MAARSY: The new MST radar on Andøya-System description and first results. *Radio Science*, 47(1):n/a–n/a, feb 2012. ISSN 00486604. doi: 10.1029/2011RS004775. URL <http://doi.wiley.com/10.1029/2011RS004775>.
- R. Latteck, T. Renkowitz, and B. Strelnikov. D region observations by VHF and HF radars during a rocket campaign at Andøya dedicated to investigations of PMWE. *Advances in Radio Science*, 17(November 2017):225–237, 2019. ISSN 16849973. doi: 10.5194/ars-17-225-2019.
- R. Latteck, T. Renkowitz, and J. L. Chau. Two decades of long-term observations of polar mesospheric echoes at 69°N. *Journal of Atmospheric and Solar-Terrestrial Physics*, 216 (November 2020):105576, 2021. ISSN 13646826. doi: 10.1016/j.jastp.2021.105576. URL <https://doi.org/10.1016/j.jastp.2021.105576>.
- M. Lesieur. *Turbulence in Fluids Fourth Revised and Enlarged Edition*. Dordrecht, 2008. ISBN 978-1-4020-6434-0.
- R. S. Lindzen. Turbulence and stress owing to gravity wave and tidal breakdown. *Journal of Geophysical Research*, 86(C10):9707, 1981. ISSN 0148-0227. doi: 10.1029/JC086iC10p09707. URL <papers://86db8c4a-2180-4f27-bae2-851576a2530f/Paper/p82http://doi.wiley.com/10.1029/JC086iC10p09707>.
- F.-J. Lübken. On the extraction of turbulent parameters from atmospheric density fluctuations. *Journal of Geophysical Research*, 97(D18):20385, 1992. ISSN 0148-0227. doi: 10.1029/92JD01916. URL <http://doi.wiley.com/10.1029/92JD01916>.
- F.-J. Lübken. *Experimental Results on the Role of Turbulence for the Heat Budget of the Upper Atmosphere*. Habilitation, Bonn, 1993.



- F.-J. Lübken. Seasonal variation of turbulent energy dissipation rates at high latitudes as determined by in situ measurements of neutral density fluctuations. *Journal of Geophysical Research: Atmospheres*, 102(D12):13441–13456, jun 1997. ISSN 01480227. doi: 10.1029/97JD00853. URL <http://doi.wiley.com/10.1029/97JD00853>.
- F.-J. Lübken. Thermal structure of the Arctic summer mesosphere. *Journal of Geophysical Research*, 104(D8):9135–9149, 1999. ISSN 0148-0227. doi: <https://doi.org/10.1029/1999JD900076>.
- F.-J. Lübken. Turbulent scattering for radars: A summary. *Journal of Atmospheric and Solar-Terrestrial Physics*, 107:1–7, jan 2014. ISSN 13646826. doi: 10.1016/j.jastp.2013.10.015. URL <https://linkinghub.elsevier.com/retrieve/pii/S1364682613002861>.
- F.-J. Lübken, W. Hillert, G. Lehmacher, and U. von Zahn. Neutral air turbulence during DYANA: First results. *Advances in Space Research*, 12(10):135–139, 1992. ISSN 02731177. doi: 10.1016/0273-1177(92)90455-7.
- F.-J. Lübken, W. Hillert, G. Lehmacher, and U. von Zahn. Experiments revealing small impact of turbulence on the energy budget of the mesosphere and lower thermosphere. *Journal of Geophysical Research*, 98(D11):20369, 1993. ISSN 0148-0227. doi: 10.1029/93JD02055. URL <http://doi.wiley.com/10.1029/93JD02055>.
- F.-J. Lübken, J. Giebeler, T. A. Blix, E. Thrane, W. Singer, and J. Bremer. In-situ measurement of the Schmidt number within a PMSE layer. *Geophysical Research Letters*, 21(15):1651–1654, jul 1994a. ISSN 00948276. doi: 10.1029/94GL01355. URL <http://doi.wiley.com/10.1029/94GL01355>.
- F.-J. Lübken, W. Hillert, G. Lehmacher, U. von Zahn, T. A. Blix, E. Thrane, H. U. Widdel, G. A. Kokin, and A. K. Knyazev. Morphology and sources of turbulence in the mesosphere during DYANA. *Journal of Atmospheric and Terrestrial Physics*, 56(13-14):1809–1833, 1994b. ISSN 00219169. doi: 10.1016/0021-9169(94)90012-4.
- F.-J. Lübken, M. Rapp, T. A. Blix, and E. Thrane. Microphysical and turbulent measurements of the Schmidt number in the vicinity of polar mesosphere summer echoes. *Geophysical Research Letters*, 25(6):893–896, mar 1998. ISSN 00948276. doi: 10.1029/98GL50479. URL <http://doi.wiley.com/10.1029/98GL50479>.
- F.-J. Lübken, M. J. Jarvis, and G. O. L. Jones. First in situ temperature measurements at the Antarctic summer mesopause. *Geophysical Research Letters*, 26(24):3581–3584, dec 1999. ISSN 00948276. doi: 10.1029/1999GL010719. URL <http://doi.wiley.com/10.1029/1999GL010719>.
- F.-J. Lübken, M. Rapp, and P. Hoffmann. Neutral air turbulence and temperatures in the vicinity of polar mesosphere summer echoes. 107, 2002.
- F.-J. Lübken, B. Strelnikov, M. Rapp, W. Singer, R. Latteck, A. Brattli, U.-P. Hoppe, and M. Friedrich. The thermal and dynamical state of the atmosphere during polar mesosphere winter echoes. *Atmospheric Chemistry and Physics*, 6(1):13–24, jan 2006. ISSN

16807324. doi: 10.5194/acp-6-13-2006. URL <http://www.atmos-chem-phys.net/6/13/2006/https://acp.copernicus.org/articles/6/13/2006/>.
- F.-J. Lübken, W. Singer, R. Latteck, and I. Strelnikova. Radar measurements of turbulence, electron densities, and absolute reflectivities during polar mesosphere winter echoes (PMWE). *Advances in Space Research*, 40(6):758–764, jan 2007. ISSN 02731177. doi: 10.1016/j.asr.2007.01.015. URL <https://linkinghub.elsevier.com/retrieve/pii/S0273117707000245>.
- V. S. L'vov. Universality of turbulence. *Nature*, 396(6711):519–521, dec 1998. ISSN 0028-0836. doi: 10.1038/24998. URL <http://www.nature.com/articles/24998>.
- J. Marti and K. Mauersberger. A survey and new measurements of ice vapor pressure at temperatures between 170 and 250K. *Geophysical Research Letters*, 20(5):363–366, mar 1993. ISSN 00948276. doi: 10.1029/93GL00105. URL <http://doi.wiley.com/10.1029/93GL00105>.
- J. D. Mathews. The incoherent scatter radar as a tool for studying the ionospheric D-region. *J. Atmos. Solar-Terr. Phys.*, 46(11):975–986, 1984. doi: [https://doi.org/10.1016/0021-9169\(84\)90004-7](https://doi.org/10.1016/0021-9169(84)90004-7).
- J. D. Mathews, S. J. Briczinski, D. D. Meisel, and C. J. Heinselman. Radio and Meteor Science Outcomes From Comparisons of Meteor Radar Observations at AMISR Poker Flat, Sondrestrom, and Arecibo. *Earth, Moon, and Planets*, 102(1-4):365–372, jun 2008. ISSN 0167-9295. doi: 10.1007/s11038-007-9168-0. URL <http://link.springer.com/10.1007/s11038-007-9168-0>.
- L.-A. McKinnell and M. Friedrich. A neural network-based ionospheric model for the auroral zone. *Journal of Atmospheric and Solar-Terrestrial Physics*, 69(12):1459–1470, aug 2007. ISSN 13646826. doi: 10.1016/j.jastp.2007.05.003. URL <https://linkinghub.elsevier.com/retrieve/pii/S1364682607001344>.
- E. Mechtly, S. Bowhill, and L. Smith. Changes of lower ionosphere electron concentrations with solar activity. *Journal of Atmospheric and Terrestrial Physics*, 34(11):1899–1907, nov 1972. ISSN 00219169. doi: 10.1016/0021-9169(72)90065-7. URL <https://linkinghub.elsevier.com/retrieve/pii/0021916972900657>.
- L. Megner, M. Rapp, and J. Gumbel. Distribution of meteoric smoke - sensitivity to microphysical properties and atmospheric conditions. *Atmospheric Chemistry and Physics*, 6:4415–4426, 2006. ISSN 1680-7324. doi: 10.5194/acp-6-4415-2006.
- C. J. Nappo. *An Introduction to Atmospheric Gravity Waves*. 2002. ISBN 0125140827.
- G. D. Nastrom and K. S. Gage. A Climatology of Atmospheric Wavenumber Spectra of Wind and Temperature Observed by Commercial Aircraft. *Journal of the Atmospheric Sciences*, 42(9):950–960, may 1985. ISSN 0022-4928. doi: 10.1175/1520-0469(1985)042<0950:ACOAWS>2.0.CO;2. URL <http://library1.nida.ac.th/termpaper6/sd/2554/19755.pdf>[http](http://):

[//journals.ametsoc.org/doi/abs/10.1175/1520-0469%281985%29042%3C0950%3AAC0AWS%3E2.0.CO%3B2](http://journals.ametsoc.org/doi/abs/10.1175/1520-0469%281985%29042%3C0950%3AAC0AWS%3E2.0.CO%3B2).

- T. Nishiyama, K. Sato, T. Nakamura, M. Tsutsumi, T. Sato, M. Kohma, K. Nishimura, Y. Tomikawa, M. K. Ejiri, and T. T. Tsuda. Height and time characteristics of seasonal and diurnal variations in PMWE based on 1 year observations by the PANSY radar (69.0S, 39.6E). *Geophysical Research Letters*, 42(7):2100–2108, apr 2015. ISSN 19448007. doi: 10.1002/2015GL063349.
- T. Nishiyama, K. Sato, T. Nakamura, M. Tsutsumi, T. Sato, Y.-M. Tanaka, K. Nishimura, Y. Tomikawa, and M. Kohma. Simultaneous Observations of Polar Mesosphere Winter Echoes and Cosmic Noise Absorptions in a Common Volume by the PANSY Radar (69.0°S, 39.6°E). *Journal of Geophysical Research: Space Physics*, 123(6):5019–5032, jun 2018. ISSN 21699380. doi: 10.1029/2017JA024717. URL <http://doi.wiley.com/10.1029/2017JA024717>.
- E. A. Novikov. Energy spectrum of a turbulent flow of incompressible fluid. *Doklady Akademii Nauk SSSR*, 139(2):331–334, 1961. URL <http://www.mathnet.ru/links/7867d720d9b2a90262aab4b96c3c772d/dan25253.pdf>.
- A. Obukhov. Structure of the temperature field in turbulent flow. *Izv. Akad. Nauk S.S.S.R., Ser. Geograf. Geofiz.*, 13:58–69, 1949.
- H. Ottersten. Atmospheric Structure and Radar Backscattering in Clear Air. *Radio Science*, 4(12):1179–1193, dec 1969a. ISSN 00486604. doi: 10.1029/RS004i012p01179. URL <http://doi.wiley.com/10.1029/RS004i012p01179>.
- H. Ottersten. Radar Backscattering from the Turbulent Clear Atmosphere. *Radio Science*, 4(12):1251–1255, dec 1969b. ISSN 00486604. doi: 10.1029/RS004i012p01251. URL <http://doi.wiley.com/10.1029/RS004i012p01251>.
- J. M. Picone, A. E. Hedin, D. P. Drob, and A. C. Aikin. NRLMSISE-00 empirical model of the atmosphere: Statistical comparisons and scientific issues. *Journal of Geophysical Research: Space Physics*, 107(A12):1–16, 2002. ISSN 21699402. doi: 10.1029/2002JA009430.
- J. M. C. Plane. Atmospheric Chemistry of Meteoric Metals. *Chemical Reviews*, 103(12): 4963–4984, 2003. doi: 10.1021/cr0205309. URL <http://dx.doi.org/10.1021/cr0205309>.
- J. M. C. Plane, R. W. Saunders, J. Hedin, J. Stegman, M. Khaplanov, J. Gumbel, K. A. Lynch, P. J. Bracikowski, L. J. Gelinis, M. Friedrich, S. Blindheim, M. Gausa, and B. P. Williams. A combined rocket-borne and ground-based study of the sodium layer and charged dust in the upper mesosphere. *Journal of Atmospheric and Solar-Terrestrial Physics*, 118:151–160, 2014. ISSN 13646826. doi: 10.1016/j.jastp.2013.11.008. URL <http://dx.doi.org/10.1016/j.jastp.2013.11.008>.
- S. B. Pope. *Turbulent flows*. Cambridge University Press, Cambridge, 2000. ISBN 9780521598866.

- L. Prandtl. 7. Bericht über Untersuchungen zur ausgebildeten Turbulenz. *ZAMM - Journal of Applied Mathematics and Mechanics / Zeitschrift für Angewandte Mathematik und Mechanik*, 5(2):136–139, 1925. ISSN 00442267. doi: 10.1002/zamm.19250050212. URL <http://doi.wiley.com/10.1002/zamm.19250050212>.
- L. Prandtl. *Prandtl - Führer durch die Strömungslehre*. Springer Fachmedien Wiesbaden, Wiesbaden, 2012. ISBN 978-3-8348-1918-5. doi: 10.1007/978-3-8348-2315-1. URL <http://link.springer.com/10.1007/978-3-8348-2315-1>.
- M. Rapp. Capture rates of electrons and positive ions by mesospheric aerosol particles. *Journal of Aerosol Science*, 31(11):1367–1369, nov 2000. ISSN 00218502. doi: 10.1016/S0021-8502(00)00030-6. URL <https://linkinghub.elsevier.com/retrieve/pii/S0021850200000306>.
- M. Rapp. Turbulence measurements and implications for gravity wave dissipation during the MaCWAVE/MIDAS rocket program. *Geophysical Research Letters*, 31(24):L24S07, 2004. ISSN 0094-8276. doi: 10.1029/2003GL019325. URL <http://doi.wiley.com/10.1029/2003GL019325>.
- M. Rapp and F.-J. Lübken. On the nature of PMSE: Electron diffusion in the vicinity of charged particles revisited. *Journal of Geophysical Research D: Atmospheres*, 108(8):1–13, 2003. ISSN 01480227. doi: 10.1029/2002jd002857.
- M. Rapp and F.-J. Lübken. Polar mesosphere summer echoes (PMSE): Review of observations and current understanding. *Atmospheric Chemistry and Physics*, 4(11/12):2601–2633, dec 2004. ISSN 1680-7316. doi: 10.5194/acp-4-2601-2004. URL <http://www.atmos-chem-phys.net/4/2601/2004/> <https://acp.copernicus.org/articles/4/2601/2004/>.
- M. Rapp and I. Strelnikova. Measurements of meteor smoke particles during the ECOMA-2006 campaign: 1. Particle detection by active photoionization. *Journal of Atmospheric and Solar-Terrestrial Physics*, 71(3-4):477–485, mar 2009. ISSN 13646826. doi: 10.1016/j.jastp.2008.06.002. URL <https://linkinghub.elsevier.com/retrieve/pii/S1364682608002071> <https://linkinghub.elsevier.com/retrieve/pii/S1364682608001521>.
- M. Rapp, J. Gumbel, and F.-J. Lübken. Absolute density measurements in the middle atmosphere. *Annales Geophysicae*, 19(5):571–580, may 2001. ISSN 1432-0576. doi: 10.5194/angeo-19-571-2001. URL <https://angeo.copernicus.org/articles/19/571/2001/>.
- M. Rapp, J. Gumbel, F.-J. Lübken, R. Latteck, and E. O. Hulburt. D region electron number density limits for the existence of polar mesosphere summer echoes. *Journal of Geophysical Research Atmospheres*, 107(14), 2002. ISSN 01480227. doi: 10.1029/2001JD001323.
- M. Rapp, I. Strelnikova, and J. Gumbel. Meteoric smoke particles: Evidence from rocket and radar techniques. *Advances in Space Research*, 40(6):809–817, 2007. ISSN 02731177. doi: 10.1016/j.asr.2006.11.021.

- M. Rapp, I. Strelnikova, R. Latteck, P. Hoffmann, U.-P. Hoppe, I. Häggström, and M. T. Rietveld. Polar mesosphere summer echoes (PMSE) studied at Bragg wavelengths of 2.8m, 67cm, and 16cm. *Journal of Atmospheric and Solar-Terrestrial Physics*, 70(7): 947–961, may 2008. ISSN 13646826. doi: 10.1016/j.jastp.2007.11.005. URL <http://linkinghub.elsevier.com/retrieve/pii/S1364682607004038>.
- M. Rapp, I. Strelnikova, B. Strelnikov, P. Hoffmann, M. Friedrich, J. Gumbel, L. Megner, U.-P. Hoppe, S. Robertson, S. Knappmiller, M. Wolff, and D. R. Marsh. Rocket-borne in situ measurements of meteor smoke: Charging properties and implications for seasonal variation. *Journal of Geophysical Research*, 115:D00I16, may 2010. ISSN 0148-0227. doi: 10.1029/2009JD012725. URL <http://doi.wiley.com/10.1029/2009JD012725>.
- M. Rapp, R. Latteck, G. Stober, P. Hoffmann, W. Singer, and M. Zecha. First three-dimensional observations of polar mesosphere winter echoes: Resolving space-time ambiguity. *Journal of Geophysical Research: Space Physics*, 116(A11):n/a–n/a, nov 2011a. ISSN 01480227. doi: 10.1029/2011JA016858. URL <http://doi.wiley.com/10.1029/2011JA016858>.
- M. Rapp, I. Strelnikova, B. Strelnikov, M. Friedrich, J. Gumbel, U.-P. Hoppe, T. A. Blix, O. Havnes, P. J. Bracikowski, K. A. Lynch, and S. Knappmiller. Microphysical Properties of Mesospheric Aerosols: An Overview of In Situ-Results from the ECOMA Project. In M. A. Abdu, , and D. Pancheva, editors, *Aeronomy of the Earth's Atmosphere and Ionosphere*, pages 67—74. Springer Netherlands, 2011b. ISBN 978-94-007-0326-1. doi: 10.1007/978-94-007-0326-1\_4. URL [https://doi.org/10.1007/978-94-007-0326-1\\_4](https://doi.org/10.1007/978-94-007-0326-1_4).
- M. H. Rees. Modelling of the Heating and Ionizing of the Polar Thermosphere by Magnetospheric Electron and Ion Precipitation. *Physica Scripta*, T18(T18):249–255, jan 1987. ISSN 0031-8949. doi: 10.1088/0031-8949/1987/T18/025. URL <https://iopscience.iop.org/article/10.1088/0031-8949/1987/T18/025>.
- T. Renkowitz, C. Schult, R. Latteck, and G. Stober. Validation of the radiation pattern of the VHF MST radar MAARSY by scattering off a sounding rocket's payload. *Advances in Radio Science*, 13:41–48, nov 2015. ISSN 1684-9973. doi: 10.5194/ars-13-41-2015. URL <https://ars.copernicus.org/articles/13/41/2015/>.
- T. Renkowitz, M. Tsutsumi, F. I. Laskar, J. L. Chau, and R. Latteck. On the role of anisotropic MF/HF scattering in mesospheric wind estimation. *Earth, Planets and Space*, 70:158, 2018. doi: 10.1186/s40623-018-0927-0. URL <https://doi.org/10.1186/s40623-018-0927-0>.
- T. Renkowitz, R. Latteck, I. Strelnikova, M. G. Johnsen, and J. L. Chau. Characterization of polar mesospheric VHF radar echoes during solar minimum winter 2019/2020. Part I: ionisation (accepted). *Journal of Atmospheric and Solar-Terrestrial Physics*, 2021.
- O. Reynolds. IV. On the dynamical theory of incompressible viscous fluids and the determination of the criterion. *Philosophical Transactions of the Royal Society of London*.

- (A.), 186:123–164, dec 1895. ISSN 0264-3820. doi: 10.1098/rsta.1895.0004. URL <https://royalsocietypublishing.org/doi/10.1098/rsta.1895.0004>.
- M. Rietveld, H. Kohl, H. Kopka, and P. Stubbe. Introduction to ionospheric heating at Tromsø—I. Experimental overview. *Journal of Atmospheric and Terrestrial Physics*, 55(4-5):577–599, mar 1993. ISSN 00219169. doi: 10.1016/0021-9169(93)90007-L. URL <https://linkinghub.elsevier.com/retrieve/pii/002191699390007L>.
- S. Robertson, M. Horányi, S. Knappmiller, Z. Sternovsky, R. Holzworth, M. Shimogawa, M. Friedrich, K. M. Torkar, J. Gumbel, L. Megner, G. Baumgarten, R. Latteck, M. Rapp, U.-P. Hoppe, and M. E. Hervig. Mass analysis of charged aerosol particles in NLC and PMSE during the ECOMA/MASS campaign. *Annales Geophysicae*, 27(3):1213–1232, mar 2009. ISSN 09927689. doi: 10.5194/angeo-27-1213-2009.
- S. Robertson, S. Dickson, M. Horányi, Z. Sternovsky, M. Friedrich, D. Janches, L. Megner, and B. P. Williams. Detection of meteoric smoke particles in the mesosphere by a rocket-borne mass spectrometer. *Journal of Atmospheric and Solar-Terrestrial Physics*, 118:161–179, 2014. ISSN 13646826. doi: 10.1016/j.jastp.2013.07.007. URL <http://dx.doi.org/10.1016/j.jastp.2013.07.007>.
- J. Rosinski and R. H. Snow. SECONDARY PARTICULATE MATTER FROM METEOR VAPORS. *Journal of Meteorology*, 18(6):736–745, dec 1961. ISSN 0095-9634. doi: 10.1175/1520-0469(1961)018<0736:SPMFMV>2.0.CO;2. URL [http://journals.ametsoc.org/doi/10.1175/1520-0469\(1961\)018%3C0736:SPMFMV%3E2.0.CO;2](http://journals.ametsoc.org/doi/10.1175/1520-0469(1961)018%3C0736:SPMFMV%3E2.0.CO;2).
- J. Röttger. Structure and dynamics of the stratosphere and mesosphere revealed by VHF radar investigations. *Pure and Applied Geophysics PAGEOPH*, 118(1):494–527, 1980. ISSN 00334553. doi: 10.1007/BF01586465.
- J. Röttger and M. F. Larsen. UHF/VHF Radar Techniques for Atmospheric Research and Wind Profiler Applications. In *Radar in Meteorology*, pages 235–281. American Meteorological Society, Boston, MA, 1990. doi: 10.1007/978-1-935704-15-7\_23. URL [http://link.springer.com/10.1007/978-1-935704-15-7\\_23](http://link.springer.com/10.1007/978-1-935704-15-7_23).
- J. Röttger and C. H. Liu. Partial reflection and scattering of VHF radar signals from the clear atmosphere. *Geophys. Res. Lett.*, 5(5):357–360, 1978. doi: <https://doi.org/10.1029/GL005i005p00357>.
- J. Röttger, P. K. Rastogi, and R. F. Woodman. High-resolution VHF radar observations of turbulence structures in the mesosphere. *Geophysical Research Letters*, 6(7):617–620, jul 1979. ISSN 00948276. doi: 10.1029/GL006i007p00617. URL <http://doi.wiley.com/10.1029/GL006i007p00617>.
- J. Röttger, C. La Hoz, M. C. Kelley, U.-P. Hoppe, and C. Hall. The structure and dynamics of polar mesosphere summer echoes observed with the EISCAT 224 MHz radar. *Geophysical Research Letters*, 15(12):1353–1356, nov 1988. ISSN 00948276. doi: 10.1029/GL015i012p01353. URL <http://doi.wiley.com/10.1029/GL015i012p01353>.

- O. Royrvik and L. G. Smith. Comparison of Mesospheric Vhf Radar Echoes and Rocket Probe Electron Concentration Measurements. *Journal of Geophysical Research*, 89 (A10):9014–9022, 1984. ISSN 01480227. doi: 10.1029/JA089iA10p09014.
- M. N. Saha. LIII. Ionization in the solar chromosphere. *The London, Edinburgh, and Dublin Philosophical Magazine and Journal of Science*, 40(238):472–488, 1920. ISSN 1941-5982. doi: 10.1080/14786441008636148.
- J. D. Sahr and B. G. Fejer. Auroral electrojet plasma irregularity theory and experiment: A critical review of present understanding and future directions. *Journal of Geophysical Research: Space Physics*, 101(A12):26893–26909, 1996. doi: 10.1029/96JA02404. URL <https://agupubs.onlinelibrary.wiley.com/doi/abs/10.1029/96JA02404>.
- H. Schlichting. *Grenzschichttheorie*. 2005.
- A. Schöch, G. Baumgarten, and J. Fiedler. Polar middle atmosphere temperature climatology from Rayleigh lidar measurements at ALOMAR (69°N). *Annales Geophysicae*, 26(7):1681–1698, 2008. doi: 10.5194/angeo-26-1681-2008. URL <https://www.ann-geophys.net/26/1681/2008/>.
- J. Schreiner, C. Voigt, A. Kohlmann, F. Arnold, K. Mauersberger, and N. Larsen. Chemical analysis of polar stratospheric cloud particles. *Science*, 283(5404):968–970, 1999. ISSN 00368075. doi: 10.1126/science.283.5404.968.
- G. J. Schulz. Characteristics of the bayard-alpert ionization gauge at pressures above 10-5 mm Hg. *Journal of Applied Physics*, 28(10):1149–1152, 1957. ISSN 00218979. doi: 10.1063/1.1722595.
- G. J. Schulz and A. V. Phelps. Ionization gauges for measuring pressures up to the millimeter range. *Review of Scientific Instruments*, 28(12):1051–1054, 1957. ISSN 00346748. doi: 10.1063/1.1715800.
- R. W. Schunk. Interactions between the polar ionosphere and thermosphere. *Physica Scripta*, 1987(T18):256–275, 1987. ISSN 14024896. doi: 10.1088/0031-8949/1987/T18/026.
- R. W. Schunk and A. F. Nagy. *Ionospheres, Physics, Plasma Physics, and Chemistry*. Cambridge University Press, Cambridge CB2 8RU, UK, second edi edition, 2009. ISBN 9780521877060. URL [www.cambridge.org/9780521877060](http://www.cambridge.org/9780521877060).
- A. Senior, M. T. Rietveld, M. J. Kosch, and W. Singer. Diagnosing radio plasma heating in the polar summer mesosphere using cross modulation: Theory and observations. *Journal of Geophysical Research: Space Physics*, 115(A9):n/a–n/a, sep 2010. ISSN 01480227. doi: 10.1029/2010JA015379. URL <http://doi.wiley.com/10.1029/2010JA015379>.

- A. Senior, A. Mahmoudian, H. Pinedo, C. La Hoz, M. T. Rietveld, W. A. Scales, and M. J. Kosch. First modulation of high-frequency polar mesospheric summer echoes by radio heating of the ionosphere. *Geophysical Research Letters*, 41(15):5347–5353, aug 2014. ISSN 00948276. doi: 10.1002/2014GL060703. URL <http://doi.wiley.com/10.1002/2014GL060703>.
- P. Shukla and A. Mamun. *Introduction to Dusty Plasma Physics*. CRC Press, may 2015. ISBN 9781420034103. doi: 10.1201/9781420034103. URL <https://www.taylorfrancis.com/books/9781420034103>.
- P. K. Shukla. A survey of dusty plasma physics. *Physics of Plasmas*, 8(5):1791–1803, may 2001. ISSN 1070-664X. doi: 10.1063/1.1343087. URL <http://aip.scitation.org/doi/10.1063/1.1343087>.
- W. Singer, R. Latteck, and D. A. Holdsworth. A new narrow beam Doppler radar at 3 MHz for studies of the high-latitude middle atmosphere. *Advances in Space Research*, 41(9):1488–1494, 2008. ISSN 02731177. doi: 10.1016/j.asr.2007.10.006.
- N. Sissenwine, M. Dubin, and H. Wexler. The U.S. Standard Atmosphere, 1962. *Journal of Geophysical Research*, 67(9):3627–3630, aug 1962. ISSN 01480227. doi: 10.1029/JZ067i009p03627. URL <http://doi.wiley.com/10.1029/JZ067i009p03627>.
- B. W. Skjelvan. EVALUATION OF MEASUREMENTS WITH A ROCKET-BORNE ELECTRON PROBE. *Diploma thesis, University of Trondheim*, 1994.
- E. Smith and S. Weintraub. The constants in the equation for atmospheric refractive index at radio frequencies. *Journal of Research of the National Bureau of Standards*, 50(1): 39, jan 1953. ISSN 0091-0635. doi: 10.6028/jres.050.006. URL [https://nvlpubs.nist.gov/nistpubs/jres/50/jresv50n1p39\\_A1b.pdf](https://nvlpubs.nist.gov/nistpubs/jres/50/jresv50n1p39_A1b.pdf).
- L. M. Smith and W. C. Reynolds. The dissipation-range spectrum and the velocity-derivative skewness in turbulent flows. *Physics of Fluids A: Fluid Dynamics*, 3(5): 992–994, may 1991. ISSN 0899-8213. doi: 10.1063/1.857979. URL <http://aip.scitation.org/doi/10.1063/1.857979>.
- S. Sommer, G. Stober, and J. L. Chau. On the angular dependence and scattering model of polar mesospheric summer echoes at VHF. *Journal of Geophysical Research*, 121(1):278–288, 2016. ISSN 21562202. doi: 10.1002/2015JD023518.
- T. Staszak, M. Brede, and B. Strelnikov. Open source software OpenFOAM as a new aerodynamical simulation tool for rocket-borne measurements. *European Rocket and Balloon Programmes and Related Research*, pages 201–208, 2015. URL <http://adsabs.harvard.edu/abs/2015ESASP.730..201S>.
- T. Staszak, H. Asmus, B. Strelnikov, F.-J. Lübken, and G. Giono. A new rocket-borne Meteor Smoke Particle (MSPD) for D-region ionosphere. In *23rd ESA Symposium on European Rocket and Balloon Programmes and Related Research*, ESA Special Publication, page 201, sep 2017.



- T. Staszak, B. Strelnikov, R. Latteck, T. Renkwitz, M. Friedrich, G. Baumgarten, and F.-J. Lübken. Turbulence generated small-scale structures as PMWE formation mechanism: Results from a rocket campaign. *Journal of Atmospheric and Solar-Terrestrial Physics*, 217:105559, jun 2021. ISSN 13646826. doi: 10.1016/j.jastp.2021.105559. URL <https://linkinghub.elsevier.com/retrieve/pii/S1364682621000237>.
- K. Stebel, U. Blum, K.-H. Fricke, S. Kirkwood, N. Mitchell, and A. Osepian. Joint radar/lidar observations of possible aerosol layers in the winter mesosphere. *Journal of Atmospheric and Solar-Terrestrial Physics*, 66(11):957–970, jul 2004. ISSN 13646826. doi: 10.1016/j.jastp.2004.03.008. URL <https://www.sciencedirect.com/science/article/pii/S1364682604000823?via%3Dihubhttps://linkinghub.elsevier.com/retrieve/pii/S1364682604000823>.
- G. Stober, R. Latteck, M. Rapp, W. Singer, and M. Zecha. MAARSY-the new MST radar on Andøya: First results of spaced antenna and Doppler measurements of atmospheric winds in the troposphere and mesosphere using a partial array. *Advances in Radio Science*, 10:291–298, 2012. ISSN 16849965. doi: 10.5194/ars-10-291-2012.
- B. Strelnikov. *In situ measurements of small scale neutral and plasma dynamics in the mesosphere/lower thermosphere region*. PhD thesis, University of Rostock, 2006.
- B. Strelnikov and M. Rapp. In Situ Measurements of Small-Scale Structures in Neutrals and Charged Aerosols. In *Aeronomy of the Earth's Atmosphere and Ionosphere*, pages 83–91. Springer Netherlands, Dordrecht, 2011. doi: 10.1007/978-94-007-0326-1\_6. URL [http://www.springerlink.com/index/10.1007/978-94-007-0326-1\\_6](http://www.springerlink.com/index/10.1007/978-94-007-0326-1_6).
- B. Strelnikov, M. Rapp, and F.-J. Lübken. Wavelet analysis applied to neutral density fluctuations measured in situ in the middle atmosphere. *European Rocket and Balloon Programmes and Related Research* *European Rocket and Balloon Programmes and Related Research*, 16(1):321–326, 2003. URL <https://ui.adsabs.harvard.edu/abs/2003ESASP.530..321S/abstract>.
- B. Strelnikov, M. Rapp, I. Strelnikova, N. Engler, and R. Latteck. Small-scale structures in neutrals and charged aerosol particles as observed during the ECOMA/MASS rocket campaign. *Annales Geophysicae*, 27(4):1449–1456, apr 2009a. ISSN 1432-0576. doi: 10.5194/angeo-27-1449-2009. URL <https://angeo.copernicus.org/articles/27/1449/2009/>.
- B. Strelnikov, M. Rapp, M. Zecha, T. A. Blix, M. Friedrich, and T. K. Yeoman. PMSE and E-region plasma instability: In situ observations. *Journal of Atmospheric and Solar-Terrestrial Physics*, 71(1):143–157, jan 2009b. ISSN 13646826. doi: 10.1016/j.jastp.2008.10.003. URL <https://linkinghub.elsevier.com/retrieve/pii/S1364682608002800>.
- B. Strelnikov, M. Rapp, and F.-J. Lübken. In-situ density measurements in the mesosphere/lower thermosphere region with the TOTAL and CONE instruments. In *An Introduction to Space Instrumentation*, pages 1–11. TERRAPUB, 2013. doi: 10.5047/

- aisi.001. URL [https://www.terrapub.co.jp/onlineproceedings/ste/aisi/abstract/aisi\\_001.html](https://www.terrapub.co.jp/onlineproceedings/ste/aisi/abstract/aisi_001.html).
- B. Strelnikov, F.-J. Lübken, M. Rapp, G. Krein, H. Henkel, and H.-J. Heckl. TURB3D: New Rocket-Borne Multi-Sensor System to Study Three-Dimensional Structures of Mesospheric Turbulence. In L. Ouwehand, editor, *22nd ESA Symposium on European Rocket and Balloon Programmes and Related Research*, volume 730, pages 101–106. ESA Special Publication, 2015. ISBN 978-92-9221-294-0. URL <https://ui.adsabs.harvard.edu/abs/2015ESASP.730..101S>.
- B. Strelnikov, A. Szewczyk, I. Strelnikova, R. Latteck, G. Baumgarten, F.-J. Lübken, M. Rapp, S. Fasoulas, S. Löhle, M. Eberhart, U.-P. Hoppe, T. Dunker, M. Friedrich, J. Hedin, M. Khaplanov, J. Gumbel, and A. Barjatya. Spatial and temporal variability in MLT turbulence inferred from in situ and ground-based observations during the WADIS-1 sounding rocket campaign. *Annales Geophysicae*, 35(3):547–565, apr 2017. ISSN 1432-0576. doi: 10.5194/angeo-35-547-2017. URL <https://www.ann-geophys.net/35/547/2017/https://angeo.copernicus.org/articles/35/547/2017/>.
- B. Strelnikov, M. Eberhart, M. Friedrich, J. Hedin, M. Khaplanov, G. Baumgarten, B. P. Williams, T. Staszak, H. Asmus, I. Strelnikova, R. Latteck, M. Grygalashvyly, F.-J. Lübken, J. Höffner, R. Wörl, J. Gumbel, S. Löhle, S. Fasoulas, M. Rapp, A. Barjatya, M. J. Taylor, and P.-D. Pautet. Simultaneous in situ measurements of small-scale structures in neutral, plasma, and atomic oxygen densities during the WADIS sounding rocket project. *Atmospheric Chemistry and Physics*, 19(17):11443–11460, 2019. doi: 10.5194/acp-19-11443-2019. URL <https://www.atmos-chem-phys.net/19/11443/2019/>.
- B. Strelnikov, T. Staszak, J. Gumbel, M. Rapp, and M. Others. PMWE sounding rocket project. *J. Atmos. Solar-Terr. Phys.*, pages submitted, this issue, 2020.
- B. Strelnikov, T. Staszak, R. Latteck, T. Renkowitz, I. Strelnikova, F.-J. Lübken, G. Baumgarten, J. Fiedler, J. L. Chau, J. Stude, M. Rapp, M. Friedrich, J. Gumbel, J. Hedin, E. Belova, M. Hörschgen-Eggers, G. Giono, I. Hörner, S. Löhle, M. Eberhart, and S. Fasoulas. Sounding rocket project “PMWE” for investigation of polar mesosphere winter echoes. *Journal of Atmospheric and Solar-Terrestrial Physics*, 218:105596, jul 2021. ISSN 13646826. doi: 10.1016/j.jastp.2021.105596. URL <https://linkinghub.elsevier.com/retrieve/pii/S1364682621000584>.
- I. Strelnikova and M. Rapp. Studies of polar mesosphere summer echoes with the EISCAT VHF and UHF radars: Information contained in the spectral shape. *Advances in Space Research*, 45(2):247–259, jan 2010. ISSN 02731177. doi: 10.1016/j.asr.2009.09.007. URL <http://dx.doi.org/10.1016/j.asr.2009.09.007https://linkinghub.elsevier.com/retrieve/pii/S0273117709006127>.
- I. Strelnikova and M. Rapp. Majority of PMSE spectral widths at UHF and VHF are compatible with a single scattering mechanism. *Journal of Atmospheric and Solar-*

- Terrestrial Physics*, 73(14-15):2142–2152, 2011. ISSN 13646826. doi: 10.1016/j.jastp.2010.11.025. URL <http://dx.doi.org/10.1016/j.jastp.2010.11.025>.
- I. Strelnikova and M. Rapp. Statistical characteristics of PMWE observations by the EISCAT VHF radar. *Annales Geophysicae*, 31(2):359–375, feb 2013. ISSN 1432-0576. doi: 10.5194/angeo-31-359-2013. URL <http://www.ann-geophys.net/31/359/2013/>.
- I. Strelnikova, M. Rapp, S. Raizada, and M. Sulzer. Meteor smoke particle properties derived from Arecibo incoherent scatter radar observations. *Geophysical Research Letters*, 34(15), aug 2007. ISSN 00948276. doi: 10.1029/2007GL030635. URL <http://doi.wiley.com/10.1029/2007GL030635>.
- I. Strelnikova, M. Rapp, B. Strelnikov, G. Baumgarten, A. Brattli, K. Svenes, U.-P. Hoppe, M. Friedrich, J. Gumbel, and B. P. Williams. Measurements of meteor smoke particles during the ECOMA-2006 campaign: 2. Results. *Journal of Atmospheric and Solar-Terrestrial Physics*, 71(3-4):486–496, mar 2009. ISSN 13646826. doi: 10.1016/j.jastp.2008.07.011. URL <https://linkinghub.elsevier.com/retrieve/pii/S1364682608002071>.
- I. Strelnikova, G. Baumgarten, and F.-J. Lübken. Advanced hodograph-based analysis technique to derive gravity-wave parameters from lidar observations. *Atmospheric Measurement Techniques*, 13(2):479–499, 2020. doi: 10.5194/amt-13-479-2020. URL <https://www.atmos-meas-tech.net/13/479/2020/>.
- J. Stude, H. Aufmhoff, H. Schlager, M. Rapp, F. Arnold, and B. Strelnikov. A novel rocket-borne ion mass spectrometer with large mass range: Instrument description and first-flight results. *Atmospheric Measurement Techniques*, 14(2):983–993, 2021. ISSN 18678548. doi: 10.5194/amt-14-983-2021.
- W. Sutherland. LII. The viscosity of gases and molecular force. *The London, Edinburgh, and Dublin Philosophical Magazine and Journal of Science*, 36(223):507–531, 1893. ISSN 1941-5982. doi: 10.1080/14786449308620508.
- A. Szewczyk. *Mesospheric Turbulence: The Role in the Creation of Mesospheric Inversion Layers and Statistical Results*. PhD thesis, University Rostock, 2015.
- V. I. Tatarski. *The effects of the turbulent atmosphere on wave propagation*. 1971. ISBN 9788578110796. doi: 10.1017/CBO9781107415324.004.
- V. I. Tatarski, R. A. Silverman, and N. Chako. Wave Propagation in a Turbulent Medium. *Physics Today*, 14(12):46–51, dec 1961. ISSN 0031-9228. doi: 10.1063/1.3057286. URL <http://physicstoday.scitation.org/doi/10.1063/1.3057286>.
- G. I. Taylor. Statistical theory of turbulenc. *Proceedings of the Royal Society A: Mathematical, Physical and Engineering Sciences*, 151(873):421–444, sep 1935. ISSN 1364-5021. doi: 10.1098/rspa.1935.0158. URL <https://royalsocietypublishing.org/doi/10.1098/rspa.1935.0158>.

- G. I. Taylor. The Spectrum of Turbulence. *Proceedings of the Royal Society A: Mathematical, Physical and Engineering Sciences*, 164(919):476–490, feb 1938. ISSN 1364-5021. doi: 10.1098/rspa.1938.0032. URL <https://royalsocietypublishing.org/doi/10.1098/rspa.1938.0032>.
- M. J. Taylor, E. H. Ryan, T. F. Tuan, and R. Edwards. Evidence of preferential directions for gravity wave propagation due to wind filtering in the middle atmosphere. *Journal of Geophysical Research: Space Physics*, 98(A4):6047–6057, 1993. doi: 10.1029/92ja02604.
- C. M. Tchen. Repeated cascade theory of homogeneous turbulence. *Physics of Fluids*, 16(1):13, 1973. ISSN 00319171. doi: 10.1063/1.1694158. URL <https://aip.scitation.org/doi/10.1063/1.1694158>.
- J. S. Theon, W. Nordberg, L. B. Katchen, and J. J. Horvath. Some Observations on the Thermal Behavior of the Mesosphere. *Journal of the Atmospheric Sciences*, 24(4):428–438, jul 1967. ISSN 0022-4928. doi: 10.1175/1520-0469(1967)024<0428:SOOTTB>2.0.CO;2. URL <http://journals.ametsoc.org/doi/abs/10.1175/1520-0469%281967%29024%3C0428%3ASOOTTB%3E2.0.CO%3B2>.
- E. Thrane and B. Grandal. Observations of fine scale structure in the mesosphere and lower thermosphere. *Journal of Atmospheric and Terrestrial Physics*, 43(3):179–189, 1981. ISSN 00219169. doi: 10.1016/0021-9169(81)90037-4.
- C. Torrence and G. P. Compo. A Practical Guide to Wavelet Analysis. *Bulletin of the American Meteorological Society*, 79(1):61–78, 1998. ISSN 00030007. doi: 10.1175/1520-0477(1998)079<0061:APGTWA>2.0.CO;2.
- J. C. Ulwick, K. D. Baker, M. C. Kelley, B. B. Balsley, and W. L. Ecklund. Comparison of simultaneous MST radar and electron density probe measurements during STATE. *Journal of Geophysical Research: Atmospheres*, 93(D6):6989–7000, jun 1988. ISSN 01480227. doi: 10.1029/JD093iD06p06989. URL <http://doi.wiley.com/10.1029/JD093iD06p06989>.
- U. Von Zahn, G. Von Cossart, J. Fiedler, K.-H. Fricke, G. Nelke, G. Baumgarten, D. Rees, A. Hauchecorne, and K. Adolfsen. The ALOMAR Rayleigh/Mie/Raman lidar: objectives, configuration, and performance. *Annales Geophysicae*, 18(7):815–833, jul 2000. ISSN 1432-0576. doi: 10.1007/s00585-000-0815-2. URL <https://angeo.copernicus.org/articles/18/815/2000/>.
- J. Weinstock. Vertical Turbulent Diffusion in a Stably Stratified Fluid, 1978. ISSN 0022-4928. URL [http://dx.doi.org/10.1175/1520-0469\(1978\)035%3C1022:VTDIAS%3E2.0.CO%5Cn2](http://dx.doi.org/10.1175/1520-0469(1978)035%3C1022:VTDIAS%3E2.0.CO%5Cn2).
- J. Weinstock. Energy Dissipation Rates of Turbulence in the Stable Free Atmosphere. *Journal of the Atmospheric Sciences*, 38(4):880–883, apr 1981. ISSN 0022-4928. doi: 10.1175/1520-0469(1981)038<0880:EDROTI>2.0.CO;2. URL [http://journals.ametsoc.org/doi/10.1175/1520-0469\(1981\)038%3C0880:EDROTI%3E2.0.CO;2](http://journals.ametsoc.org/doi/10.1175/1520-0469(1981)038%3C0880:EDROTI%3E2.0.CO;2).

- C. F. v. Weizsäcker. Das Spektrum der Turbulenz bei großen Reynoldsschen Zahlen. *Zeitschrift für Physik*, 124(7-12):614–627, 1948. ISSN 14346001. doi: 10.1007/BF01668898.
- H. G. Weller, G. Tabor, H. Jasak, and C. Fureby. A tensorial approach to computational continuum mechanics using object-oriented techniques. *Computers in Physics*, 12(6): 620, 1998. ISSN 08941866. doi: 10.1063/1.168744. URL <http://scitation.aip.org/content/aip/journal/cip/12/6/10.1063/1.168744>.
- R. F. Woodman and A. Guillen. Radar Observations of Winds and Turbulence in the Stratosphere and Mesosphere., 1974. ISSN 00224928.
- O. Zeller, M. Zecha, J. Bremer, R. Latteck, and W. Singer. Mean characteristics of mesosphere winter echoes at mid- and high-latitudes. *Journal of Atmospheric and Solar-Terrestrial Physics*, 68(10):1087–1104, jun 2006. ISSN 13646826. doi: 10.1016/j.jastp.2006.02.015. URL <https://linkinghub.elsevier.com/retrieve/pii/S1364682606000666>.



# Acknowledgements

I especially thank Dr. Boris Strelnikov for his ideas, prudence, many discussions, explanations, recommendations for literature, and introducing a mechanical engineer into the field of atmospheric physics with all its facets.

I also thank Prof. Franz-Josef Lübken in the department head position for giving me the chance to work in the sounding rocket group. Further, for forming an excellent environment to work on atmospheric science (personal, instrument, and infrastructure) in the position of the institute's director. I also thank Hans-Jürgen Heckl and Torsten Köpnick for building and preparing the instruments. I always appreciate the fruitful discussions and learned a lot.

Moreover, I have to thank Dr. Heiner Asmus and Dr. Carsten Baumann for bringing me in touch with the Leibniz Institute of Atmospheric Physics through their invitation to the student sounding-rocket project (Rexus) and also for being good friends.

Many thanks to the DLR MORABA for rewarding collaboration and bringing our instruments "up there". The same applies to the staff of Andøya Space (Center) and our american colleagues.

Also, I thank Prof. Martin Friedrich for his support with the Wave Propagation Experiment and discussions, explanations, and the handover of his unique expertise to IAP. Of course, I have to thank Dr. Ralph Latteck and Dr. Toralf Renkwitz for operating the radars and discussing and sharing their knowledge on PMWE.

Also, I thank Jens, Carsten, Sven, Svenja, Arvid, Francie for discussions on atmospheric physics and beyond, exquisite meals, and excellent frisbee matches.

I also thank Christian, Jens, and Sebastian for reading the thesis and giving me valuable feedback.

My wholehearted thanks go to Rosa and Kaspar, who have been so brave in these exceptional times. My loving thank is dedicated to Johanna, who managed most of the child care during the past months. She always had an ear for my thoughts and gave input from an outside perspective of a different scientific field. I could not imagine how to write this thesis without her great support. Also, I thank my parents and parents-in-law, for being wonderful parents and grandparents.

This work was supported by the Federal Ministry for Economic Affairs and Energy based on a decision by the German Bundestag on DLR grant 50OE1402, project PMWE.





# Declaration of authorship

Ich gebe folgende Erklärung ab:

- 1 Die Gelegenheit zum vorliegenden Promotionsvorhaben ist mir nicht kommerziell vermittelt worden. Insbesondere habe ich keine Organisation eingeschaltet, die gegen Entgelt Betreuerinnen/Betreuer für die Anfertigung von Dissertationen sucht oder die mir obliegenden Pflichten hinsichtlich der Prüfungsleistungen für mich ganz oder teilweise erledigt.
- 2 Ich versichere hiermit an Eides statt, dass ich die vorliegende Arbeit selbstständig angefertigt und ohne fremde Hilfe verfasst habe. Dazu habe ich keine außer den von mir angegebenen Hilfsmitteln und Quellen verwendet und die den benutzten Werken inhaltlich und wörtlich entnommenen Stellen habe ich als solche kenntlich gemacht.

Kühlungsborn, 16. August

2021

Ort, Datum

---

Tristan Staszak